ABSTRACT

STRUCTURAL, TRANSPORT, AND MAGNETIC STUDIES OF PEROVSKITE $Bi_{1-x}Ca_xMnO_3$

By
Hyungje Woo

This dissertation presents an investigation of the fundamental physics of the perovskite system $Bi_{1-x}Ca_xMnO_3$. This material belongs to a group of simple perovskites called the manganites which are of technological importance for magnetic device applications as read-head sensors.

The $Bi_{1-x}Ca_xMnO_3$ system is known to exhibit charge ordering (and high sensitivity to magnetic fields) for a much broader range of x than the well-characterized $La_{1-x}Ca_xMnO_3$ system. However, the properties of $Bi_{1-x}Ca_xMnO_3$ over the entire doping range are not well understood. Magnetization and resistivity measurements (up to 30T) as well as x-ray absorption and x-ray diffraction measurements on $Bi_{1-x}Ca_xMnO_3$ were performed to correlate the structural, transport, and magnetic properties. The system was found to be insulating and antiferromagnetic for the entire range of x studied ($x \geq 0.4$) except near $x \sim 0.875$ where glassy behavior was observed. Detailed magnetization measurements were performed as a function of field and temperature to explore the net moment on the Mn sites as a function of x. These measurements reveal the charge ordering and Néel temperatures. X-ray absorption measurements reveal significant structural distortions of the Mn-O bond distributions with increasing Bi content that correlates directly with increasing charge-ordering temperatures. Moreover, x-ray diffraction data reveal peak splittings consistent with lower symmetry cells as the Bi content increases. These structural-magnetic correlations point to the importance of Mn-O distortions in stabilizing the charge-ordered state in the manganites. A structural, transport and magnetic phase diagram over the complete range of x has been developed.

STRUCTURAL, TRANSPORT, AND MAGNETIC STUDIES OF PEROVSKITE $Bi_{1-x}Ca_xMnO_3$

By
Hyungje Woo

A Dissertation
Submitted to the Faculty of
New Jersey Institute of Technology and Rutgers,
The State University of New Jersey-Newark
in Partial Fulfillment of the Requirements for the Degree of
Doctor of Philosophy in Applied Physics

Federated Physics Department

August 2001

APPROVAL PAGE

STRUCTURAL, TRANSPORT, AND MAGNETIC STUDIES OF PEROVSKITE $Bi_{1-x}Ca_xMnO_3$

Hyungje Woo

Dr. Trevor A. Tyson, Dissertation Advisor — Date
Associate Professor of Physics, NJIT

Dr. Mark Croft, Committee Member — Date
Professor of Physics and Astronomy, Rutgers University, New Brunswick

Dr. Sang-Wook Cheong, Committee Member — Date
Professor of Physics and Astronomy, Rutgers University, New Brunswick

Dr. Earl Shaw, Committee Member — Date
Professor of Physics, Rutgers University, Newark

Dr. Gordon Thomas, Committee Member — Date
Distinguished Research Professor of Physics, NJIT

BIOGRAPHICAL SKETCH

Author: Hyungje Woo

Degree: Doctor of Philosophy

Date: August 2001

Undergraduate and Graduate Education:

- Doctor of Philosophy in Applied Physics, Federated Physics Department, New Jersey Institute of Technology, Newark, NJ, 2001 and Rutgers University, Newark, NJ, 2001
- Master of Science in Physics, Stevens Institute of Technology, Hoboken, NJ, 1993
- Bachelor of Science in Physics, Myongji University, Seoul, Korea, 1989

Major: Applied Physics

Publications:

Woo, H., T. A. Tyson, M. Croft, S-W. Cheong, and J. C. Woicik, "Correlations between the Magnetic and Structural Properties of Ca Doped $BiMnO_3$" Phys. Rev. B **63**, 134412 (2001).

Woo, H., T. A. Tyson, M. Croft, S-W. Cheong, and B. L. Brandt, "Evidence for Spin Clusters in Manganites: $Bi_{1-x}Ca_xMnO_3$ ($x \sim 0.875$)" to be submitted to Physical Review B

Woo, H., T. A. Tyson, M. Croft, S-W. Cheong, G. Popov, J. Bai, J. C. Woicik, "The Local and Long Range Structures of $Bi_{1-x}Ca_xMnO_3$ ($x \geq 0.8$)" manuscript in preparation.

Proceedings:

Woo, H., T. A. Tyson, M. Croft, S-W. Cheong, J. C. Woicik, and J. Bai, "Structure-Transport Correlations in Charge-Ordered $Bi_{1-x}Ca_xMnO_3$." March American Physical Society, Seattle, 2001, N24.007.

Carlo, J. P., T. A. Tyson, H. Woo, and J. Bai, "A Comparison of Local and Long-Range Structure in Bulk CMR Perovskite $La_{0.6}Y_{0.07}Ca_{0.33}MnO_3$." March American Physical Society, Seattle, 2001, N24.006.

Cui, C., T. A. Tyson, C. C. Kao, J. P. Carlo, and H. Woo, "High-Pressure Transport and Structural Studies of Manganites." March American Physical Society, Seattle, 2001, G24.010.

Woo, H., T. A. Tyson, M. Croft, S-W. Cheong, J. C. Woicik, and B. L. Brandt, "Transport, Magnetic and Structural Properties of $Bi_{1-x}Ca_xMnO_3$." March American Physical Society, Minnesota, 2000, T26. 12.

Cui, C., T. A. Tyson, H. Woo, and C. C. Kao, "Local Electronic and Atomic Structure of CMR Oxides Under High Pressure." March American Physical Society, Minnesota, 2000, F36. 13.

Woo, H., T. A. Tyson, M. Croft, and S-W. Cheong, "Magnetic and Local Structural Properties of Charge Ordered Manganites." March American Physical Society, Georgia, 1999, YC 05. 07.

Tyson, T. A., H. Woo, C. Dubourdieu, and J. P Senateur, "Correlations between Lattice Stain, Local Structure and Magneto-transport Properties of $LaMnO_3$ films." March American Physical Society, Georgia, 1999, XC05.05.

Woo, H., T. A. Tyson, M. Croft, S-W. Cheong, J. C. Woicik, and B. L. Brandt, " Magnetic and Local Structural Properties of Charge Ordered $Bi_{1-x}Ca_xMnO_3$(BCMO)." Fall Materials Research Society, Boston, 1999, JJ6.9.

Tyson, T. A., H. Woo, C. Dubourdieu, and J. P Senateur, "Evolution of the Mn-O Bond Asymmetry with Film Thickness in La_xMnO_3." Fall Materials Research Society, Boston, 1999, JJ3.5.

Woo, H., T. A. Tyson, M. Croft, and S-W. Cheong, "A Local Structure of Charge Ordered $Bi_{1-x}Ca_xMnO_3$ and $La_{1-x}Ca_xMnO_3$." Fall Materials Research Society, Boston, 1998, P3.9.

Woo, H. *et al.* "Energy Scaling of Plasma Focused Discharges with Enhanced Reactivity." IEEE Nuclear and Plasma Sciences Society, Canada, 1993, 93CH333-0.

To my lovely wife (변경아), *my parents* (우종국, 최종순), *and parents-in-law* (변용섭, 김경희) 님께 이 논문을 바칩니다.

특히 어렸을 때 아버님의 말씀 중에

"아는 것이 힘이다." (*Knowledge is stronger than a knife.*)

이 말씀이 저자를 깊이 있는 연구로 인도하였습니다.

그리고 누나들, 매형들, 처제, 동서, 우현정 (*Justin H. Woo*), 우민영 (*Jenny M. Woo*) 그밖에 가족, 친지들의 후원에 깊이 감사드립니다.

ACKNOWLEDGMENT

I wish to thank many people who helped in competing this thesis work. I would like to thank Dr. Trevor A. Tyson, my research advisor, for his support with valuable insight and intuition as well for critical points in fundamental physics. Special thanks go to Dr. Mark Croft for profound research insights and Dr. Sang-Wook Cheong for providing me with an excellent discussion about his research, samples and other resources. I also thank Dr. Gordon Thomas, Dr. Earl D. Shaw, and Dr. John Federici (proposal) as committee members for taking their time to review this dissertation. My friends, Dr. Sunghoon Kim, Mr. Alex Roh, Mr. Jangpyo Kim, and Mr. Keehong Um, fellow graduate students Mr. Congwu Cui, Mr. Lamine Dieng, Mr. Sungmin Maeng and Michael Deleon, undergraduate student Mr. Jeremy P. Carlo, post doctoral researchers Dr. Qing Qian and Dr. Alexander Ignatov also deserve recognition for their help.

I am deeply indebted to Dr. T. Y. Koo (Bell Labs. and Dept. of Physics, Rutgers University) for the significant effort expanded in the preparation of the $BiMnO_3$ sample; Dr. I. Fawcett (Dept. of Chemistry, Rutgers University) for assistance in x-ray diffraction, resistivity and magnetic measurements, Dr. B. G. Kim for assistance with sample preparation, and Dr. G. Hall (Dept. of Chemistry, Rutgers University) for assistance in XRF measurements to verify the purity of our $BiMnO_3$ high pressure sample. I also thank Dr. C. Segre of the Illinois Institute of Technology for assistance with the $BiMnO_3$ measurements at the Materials Research Collaborative Access Team (MR-CAT) in the Advanced Photon Source at Argonne National Laboratory (ANL).

I would like to note that following researchers: Dr. M. Uehara (Dept. of Physics, Rutgers University) for in assistance in sample preparation (x = 0.875); Mr. Guerman Popov (Dept. of Chemistry, Rutgers University) for assistance in DC magnetization measurements and GSAS refinement of XRD data; Mr. Gabriel Veith, and Dr. Siwen Li(Dept. of Chemistry, Rutgers University) for assistance in DC magnetization measurements. The author thanks Mr. S. Baily and Dr. M. Salaman (Dept. of Physics, University of Illinois at Urbana-Champaign) for useful discussion and AC susceptibility measurements. I am grateful to Dr. B. L. Brandt, Dr. D. Hall for assisting with the VSM and Dr. M. Whitton for assisting with resistivity measurements.

X-ray absorption measurements were performed at the National Synchrotron Light Source (Brookhaven National Laboratory), beamlines X11A, X18B, X19A and X23A2. The $BiMnO_3$ XANES spectra were collected at the MR-CAT facility in the Advanced Photon Source (Argonne National Laboratory). X-ray diffraction measurements were performed at X14A (the National Synchrotron Light Source (Brookhaven National Laboratory)). Magnetic measurements in high fields up to 30T were performed at the National High Magnetic Field Laboratory. This research was funded by DOE Grant DE-FG02-97ER45665 and the New Jersey Space Grant Consortium (NASA). Sample synthesis was supported in part by the NSF-DMR-9802513 (S-W. Cheong).

TABLE OF CONTENTS

TABLE OF CONTENTS
(Continued)

Chapter **Page**

TABLE OF CONTENTS
(Continued)

Chapter **Page**

LIST OF TABLES

LIST OF FIGURES

LIST OF FIGURES
(Continued)

Figure **Page**

LIST OF FIGURES
(Continued)

Figure **Page**

LIST OF FIGURES
(Continued)

Figure **Page**

LIST OF FIGURES
(Continued)

Figure **Page**

LIST OF FIGURES
(Continued)

Figure **Page**

CHAPTER 1

INTRODUCTION

1.1 MR/GMR/CMR Technology

1.1.1 A Brief History of Data Storage Technology

The idea of storing information magnetically is based on the fact that a reading sensor (called a read head) can be used to read the magnetization of local magnetic moments (called magnetic bits) whose direction codes for 0 or 1 on the magnetic disk. In order to enhance the capacity of storage devices, several steps can be taken such as: (1) reduction of the read head to magnetic disk distance, (2) enhancement of the sensitivity of the magnetic sensor, and (3) reduction of the magnetic bit size. Materials with large changes in resistance in response to magnetic fields (typically 0 gauss to 200 gauss) are an important aspect in enhancing storage density. Some of the existing sensor materials will be reviewed before focusing on the manganites. However, we now put the later development into a historical perspective.

In 1877, Edison invented a mechanical phonograph that operated with good sound quality for recordings lasting several minutes. In 1898, the Danish telephone and telegraph engineer Valdemar Poulsen invented the functioning magnetic recorder to record sound after Oberlin Smith had come up with the idea about 20 years before (see Fig. 1.1).

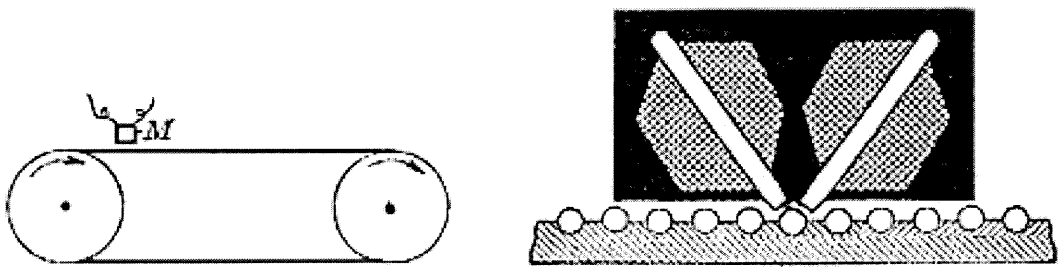

Fig. 1.1 The first telegraphone invented by Valdemar Poulsen. (a) The electromagnet "M" on a steel wire with endless steel wire traveled along and recorded or replayed sound. (b) Close-up of electromagnet M zoomed in from the figure (a).[1]

The mechanism of Valdemar Poulsen is based on the fact that the electromagnet "M" moves on a steel wire which can be magnetically polarized locally. If the exciting circuit through the magnet is alternatively opened and closed, the steel wire will be magnetized corresponding to the strength of the magnet during the periods when the circuit is closed. Therefore, the steel wire holds a permanent record of the magnetic chances. Running the electromagnet without a source read enabled one to read stored information. A patent for this idea was obtained by him.

His initial interest was to focus on leaving a message when people were not home (nowadays called an "answering machine"). Poulsen obtained a successful short recording along a piece of piano wire by moving the electromagnet and taking into the microphone. He played back the sound when the electromagnet was connected a telephone earpiece and moved along the wire in the same direction followed during the recording process On December 1, 1898, Poulsen designed a more complicated machine for his first patent application on magnetic storage. [2] It successfully recorded sound and was late called "Telegraphone".

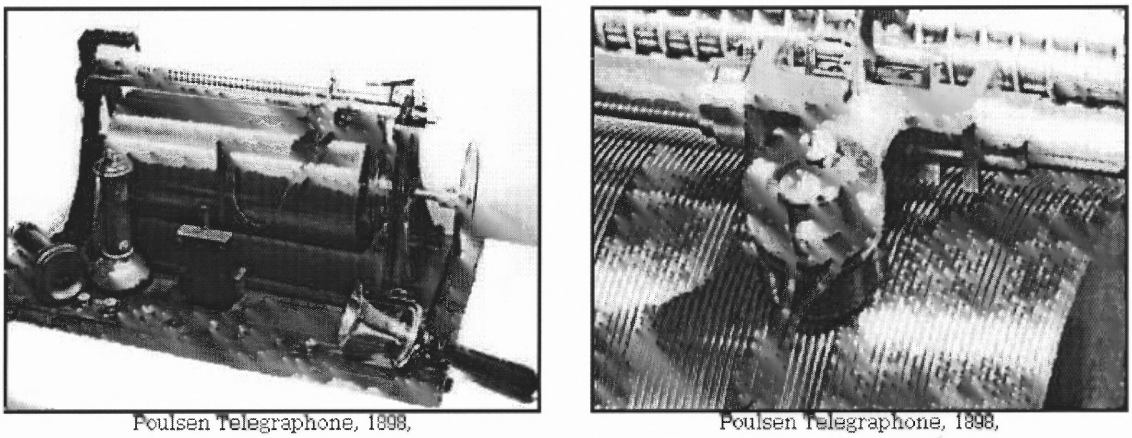

Poulsen Telegraphone, 1898, Poulsen Telegraphone, 1898,

Fig. 1.2 Valdemar Poulsen's first patent, a telegraphone. The telegraphone consists of a drum, wire and steel tape.[3]

At the time of the expiration of Valdemar Poulsen's patents (in 1918), the German electrical engineer Kurt Stille investigated the development of the telegraphone [see Fig. 1.2]. The telegraphone was a wrapped with wire around a drum and a recording/playback head that traveled by a screw thread on top.

In 1932, because of poor sales, Stille decided to contract with Ferdinand Schuchard AG to develop a totally new dictating machine, the Dailygraph magnetic wire recorder. But rights to the design were sold to International Telephone and Telegraph (ITT). In mid-1930s, ITT gave responsibility for magnetic recording to its subsidiary C. Lorenz AG which produced a variety of steel tape and wire-based recorders, called the Stahtonbandmaschine. Later, the wire and steel tape was replaced by thin plastic tape. In 1928, The Austrian inventor Fritz Pfleumer who lived in Dresden, Germany used a method for coating cigarette paper with small bronze particles for decorative purposes. Eventually, Pfleumer found that his coating technology could be applied to powdered magnetic material and created recording tape that was cheaper and easier to use than the solid steel wire or tape of previous machines. In 1932, the Allgemeine

Elektrizitatsgesellschaft (AEG) developed his idea and began manufacture of a machine calling the magnetophone.

Since the late 1940s, systems using magnetically coated tape, ring heads, and longitudinal magnetization have been developed. The first major application was for audio recording using linear analog methods based on ac biasing. The pursuit of high signal-to-noise ratios while increasing recording density, continued for audio and instrumentation applications at the leading edge of high-density magnetic recording technology. Further technological expansion led to the development of tape recording for the storage of digital data by using unbiased nonlinear recording. [4] This tape drive devices were pushed to operate at high tape speeds resulting in more rapid fast access to stored data. The demand for fast access made possible magnetic strips and loops, but these devices have problem of reliability. Even today, tape-drive systems remain the primary removable storage technology for digital data.

Tape storage was followed by an effort to move from stationary-head tape machines to video recording. This failed because of the requirement of excessive tape speed to record very high frequencies. In 1956, this problem was solved by using a scanning-head machine. This innovation was originally applied to professional video recording using high-speed transverse scanning of a slowly moving tape. Its subsequent development of helical scanning techniques produced lower-cost drives which were used in the commercial video-recording market. [5]

In 1957, the rotating rigid disk for digital data storage was introduced. [6] A read-write head significantly improved head-media velocity by employing an air bearing to support it. This enabled fast radial accessing over the disk in addition to high reliability

and high data access rate. The flexible-disk system in-contact recording became a primary product starting with the personal computer. [7] The low-cost storage technology uses a single coated plastic disk in a protective jacket. The removable, lightweight "diskette" led the market for small PCs.

A hard-disk drive is formed by stacking disk platters where each platter is a aluminum alloy or glass substrate that is coated with a magnetic material and protective layers. Read/write heads placed on the magnetic media store and retrieve data. The spindle motor rotates with a speed of between 3,600 and 10,000 revolutions per minute. [8] In 1956, IBM reported the first hard-disk drive, "the random access method of accounting and control (RAMAC)" that had only 50 aluminum platters that were 24 inches in diameter and coated with magnetic iron oxide. Not surprisingly, RAMAC could store only up to five million characters (character ~ byte) and weighed almost a ton and occupied the floor space of two modern refrigerators. Presently, desktop PCs have disk drives of over 70 Gb. The physical disks are getting smaller, disks are thinner, and the distance between head and platter are reduced (called the fly height, that is the order of 1 μin (= 25 nm) for 5 Gbits/in^2 in 1997) [9] while the cost of hard drives is dropping dramatically. Although heads were made of ferrite in previous years, in 1979 silicon chip-building technology successfully fabricated a thin film read-head. These heads were used to write data in tiny domains. In 1990s, IBM has produced a new technology called the magnetoresistive (MR) head, which is based on the variation of the electrical resistance of the read element by the magnetic field of the magnetic storage medium instead of just reading the alternating magnetic field on a disk. [see Fig. 1.3]

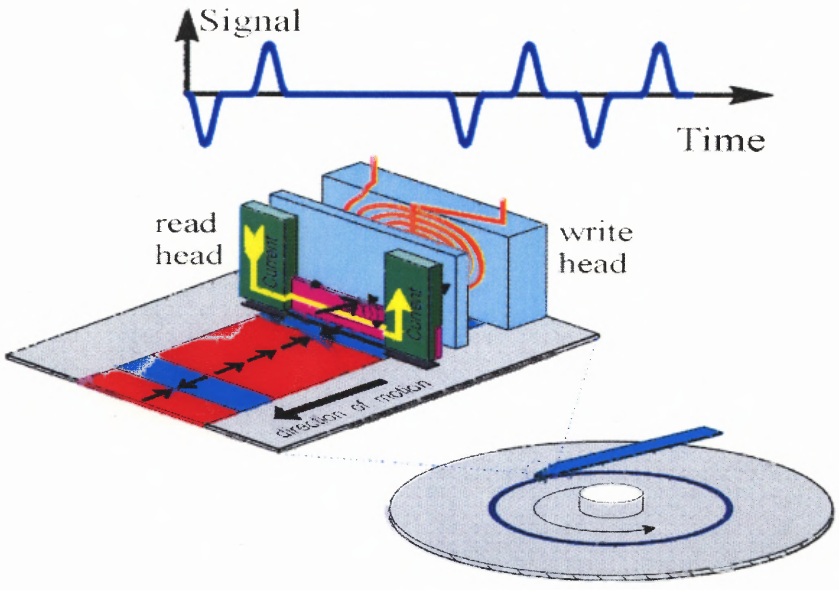

Fig. 1.3 IBM's merged read/write head design. The signals of magnetoresistance used to read the state of magnetic bits are shown in the upper curve.

Figure 1.3 illustrates a design to read and write the state of magnetic bits in advanced magnetic disk drives.[10] The read head consists of a MR sensor between two magnetic shields. The inductive heads write bits of information by magnetizing very small regions along concentric tracts. In the process of reading, the existence of a magnetic transition or flux reversal between bits causes the magnetic orientation in the MR sensor to change. Thus, this induces the resistance of the sensor to change. Large magnetoresistance materials are being developed to improve the sensitivity of read heads. The sensor's output voltage (or signal) is the product of the resistance change ($\Delta\rho$) and the read bias current. The output signal is amplified by low-noise electronics, and sent to the data detection electronics. The increasing sensitivity for storing data is decreased and far smaller drive sizes. This technology dominates the market. In 1997, an innovated technology was developed by IBM. The giant magnetoresistive (GMR) heads in built as a sandwich of magnetic and nonmagnetic materials layered in the read head improved

read head sensitivity. Currie Munce, director of storage systems and technology, announced the possibility that disk drives can store data at an aerial density more than 100 gigabits per square inch of platter space. The ultimate aim of storage technology is to reach atomic magnetic bit size.

At this point, further technology growth is questionable because of the limitation generated by the superparamagnetic effect (SPE). SPE is simply a physical situation where the holding energy of the magnetic spin in the atoms containing a bit (a 0 or 1), is increasing and is comparable to the ambient thermal energy. If this occurs, bits will be vulnerable because of the random "flipping" between 0's and 1's. Another approach to avoid thermal problems is to use rare earth and transition elements that are magnetically quite stable. Such metals are of a very high coercivity, called "hard." A laser is used for "softening" by heating before data is written (see Fig.1.4). One possibly serious problem

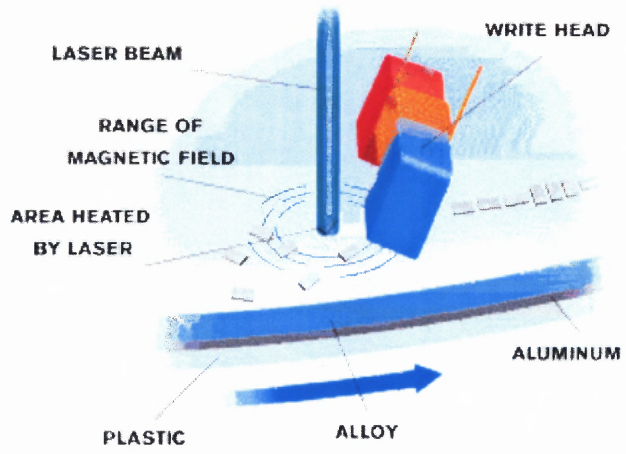

Fig. 1.4 Schematic design using a disk with grooves between the circular track (Seagate Technology).[11]

is an accidental heating adjacent to bits that contain old data. Recently, Seagate Technology has used a disk with grooves between the circular tracks of bits. Seagate

reported that technological difficulty is the potential problem of picking up unwanted noise during the reading process. In order to solve this they used a two-layer medium with a permanent storage layer positioned below a readout layer. If such a system works well, the Seagate technology could store 1,000 gigabits per square inch.

1.1.2 The Advent of GMR Materials

In 1986, the possibility of exchange interaction between ferromagnetic films across a nonmagnetic metallic interlayer was experimentally shown in Fe/Cr structures [12] and rare earth-based yttrium multilayers. [13] In MR heads, the output is directly proportional to the MR ratio. Scientists and engineers have been searching for the materials that show far larger changes in resistivity than the classic material permalloy (see Fig. 1-5 below).

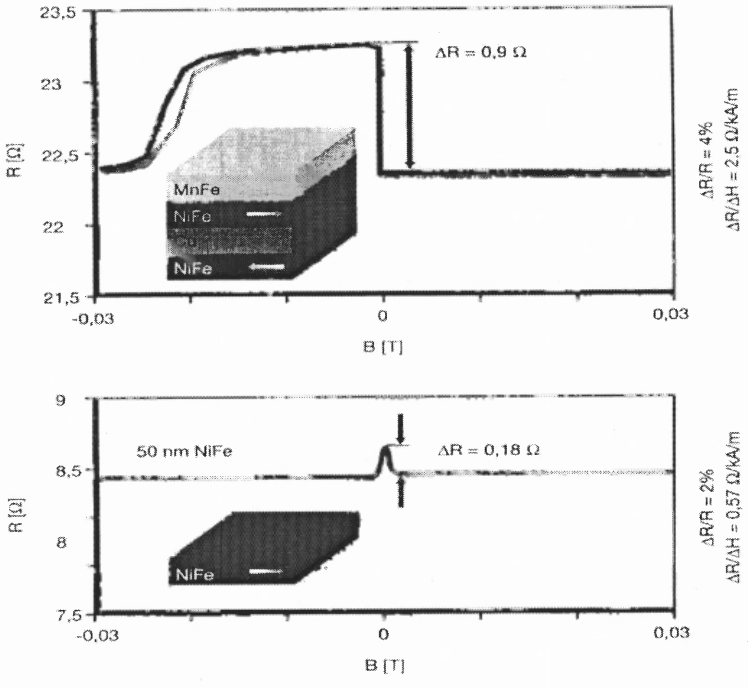

Fig. 1.5 Comparison mangnetic-field sensor outputs for GMR (top) and AMR (bottom) effects. [14] Note that the sensitivity, in GMR, which is defined as the slope, $s \equiv (\partial R/R)/\partial H$, is about 4.4 times larger than AMR.

Figure 1.5 shows that ΔR/R of the double layer GMR (4%) is better than that of the anisotropic magnetoresistance (AMR). The discovery of giant magnetoresistance (GMR) development of the antiferromagnetically coupled Fe/Cr systems [15,16,17,18] significantly stimulated the technology. In 1988, Fe/Cr magnetic superlattices (GMR) prepared by molecular beam epitaxy were first reported by Baibich *et al.* [15] In (Fe 3nm/Cr 0.9nm)$_{60}$ multilayers, a GMR ratio $\left(=\left(R_{ap}-R_{p}\right)/R_{p}\right)$ where R_{ap} and R_p are the resistance when magnetization is antiparallel and parallel respectively, was found to be ~ 85 % at 4.2 K. [19] In a $Co_{95}Fe_5$/Cu multiplayer, the GMR ratio was ~ 220 % at 4.2 K and ~ 100 % at 295 K respectively. [20] The GMR multilayers normally need a large saturation field to overcome the antiferromagnetic coupling of magnetic layers to show the large magneto resistance ratios.

In Co/Ru, Co/Cr, and Fe/Cr, Parkin *et al.* [16] reported the fact that the strength of the antiferromagnetic coupling is a periodic function of the nonmagnetic spacer. The origin of oscillatory antiferromagnetic coupling has been derived by the RKKY (Ruderman-Kittel-Kasuya-Yosida) theory [21] and by quantum well models. [22]

In fact, the field sensitivity of GMR multilayers is inferior to the AMR ratio of NiFe because of the huge saturation fields in the multilayers. For example, CoFe/Cu multilayers are not easy to implement in practical devices such as recording heads. Therefore, an alternative GMR structure with NiFe/Cu/NiFe/FeMn is considered (Fig.1-6). In the Fig. 1-6(a) the FeMn layer pins the magnetization of the top NiFe layer

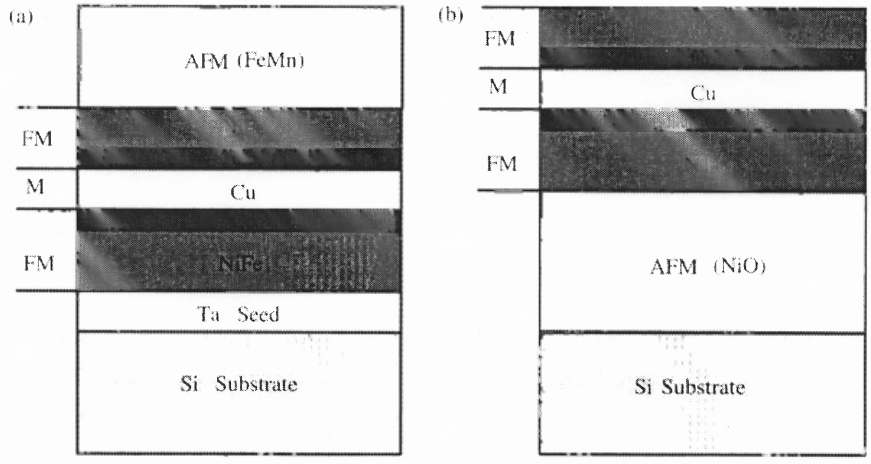

Fig. 1-6 Typical examples of schematic cross sections of a (a) top spin value, and a (b) bottom spin valve. Note that FM, M and AFM refer to ferromagnet, noble metal, antiferromagnet, respectively. [23]

through exchange anisotropy. [24] The FM (or antiferromagnetic) interaction between the FM, NiFe layers is much weaker than one in the GMR multilayer such that the bottom NiFe magnetization can switch under a small field, ~ 6 Oe only. These GMR sandwiches are called, "spin valves." The Si/Ta/NiFe(5 nm)/Co(2 nm)/Cu(2nm)/NiFe(3 nm)/FeMn(15 nm) spin valve shows a GMR ratio of ~ 9% where Co is the purpose of enhancement of interfacial spin-dependent scattering, and Ta seed layer is for promoting desirable film texture and morphology. The Si/NiO(75 nm)/NiFe(3 nm)Co(2 nm)/Cu(2nm)/NiFe(5 nm) spin valve shows a GMR ratio of ~ 12%. [25] Thereafter, a bottom pin valve structure of Si/NiO(50 nm)/Co(2.5 nm)/Cu(1.9 nm)/Co(3 nm) and a symmetrical spin valve structure of Si/NiO(50 nm)/Co(2.5 nm)/Cu(1.9 nm)/Co(4 nm)/Cu(1.9 nm)/Co(2.5 nm)/NiO(50 nm) achieve GMR ratios of 19% and 25% respectively. "Spectacular electron reflection" at outer surfaces was introduced by using a tiny amount of oxygen (~5 × 10^{-9} Torr) during ultrahigh vacuum (UHV) deposition chamber during spin valve growth. [26]

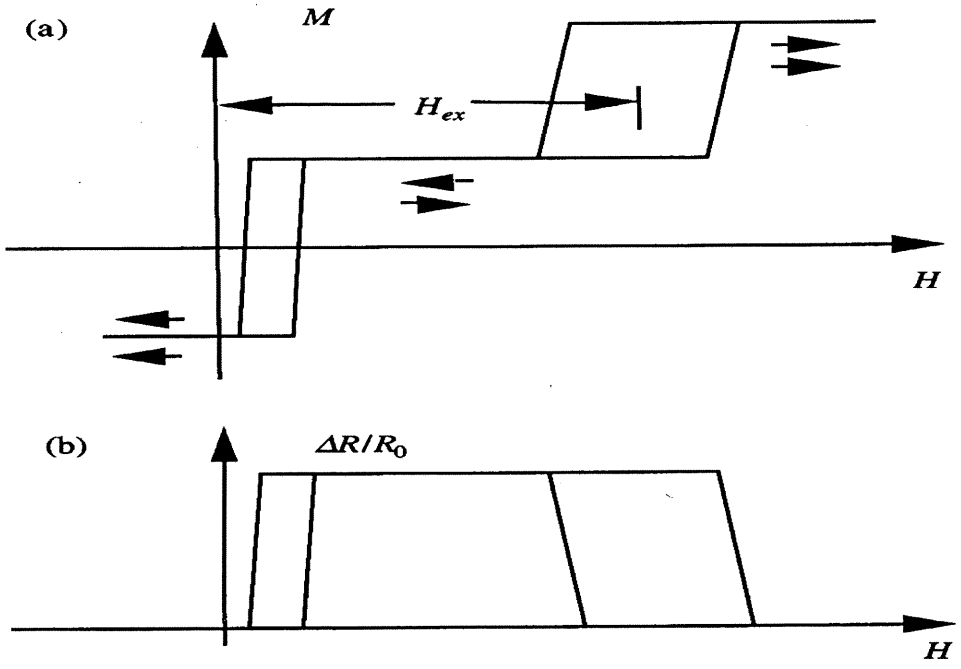

Fig. 1.7 The magnetic hysteresis loop and MR transfer curve of spin valves along the easy axis (EA). [27]

Figure 1-7 displays the magnetic hysteresis loop and subsequent MR in the free layer and pinned layer along the easy axis. The free-layer hysteresis loop is slightly shifted to the right due to a weak ferromagnetic coupling from the pinned layer. In this spin valve, the resistance is highest when top and bottom FM layers are antiparallel while it is lowest when parallel.

The definition of MR and GMR ratio varies according to emphasis of relative ratios of change in magnetoresistance. Magnetoresistance (MR) is defined as

$$MR(\%) = \frac{\rho(H) - \rho(0)}{\rho(0)} \times 100\%, \tag{1.1}$$

where ρ(H) and ρ(0) are resistivities due to the application of the magnetic field H and zero at a given temperature, respectively . MR can be positive or negative (see Table

1.3). General metals display a small MR (~ a few percent) while non-magnetic pure metals and alloys have a positive MR that depends on the square of the magnetic field, H. However, magnetic materials show negative MR owing to the suppression of spin disorder by the magnetic field. It is notable that highly resistive alloys also show negative MR due to the suppression of quantum mechanical interference between scatters (when electrons are localized over lots of impurity states, the localized states drastically overlapped in space on application of magnetic field). Heterogeneous ferromagnetic materials, such as thin-film multilayers and cluster-alloy compounds, exhibit giant magnetoresistance. These materials have different properties compared to classic GMR materials. Spin dependent scattering [28] (see Fig. 1.8) and intergrain tunneling [29] are known mechanisms of GMR. Spin-up electrons and spin-down electrons travel randomly inside the layers (see Fig. 1.5). In parallel magnetization arrangement (upper panel of Fig. 1.5), spin-down electrons are scattered but spin-up electrons travel freely inside layers. On the other hand, in the antiparallel magnetization arrangement (down panel of Fig. 1.5), electrons of both spin aligment are scattered.

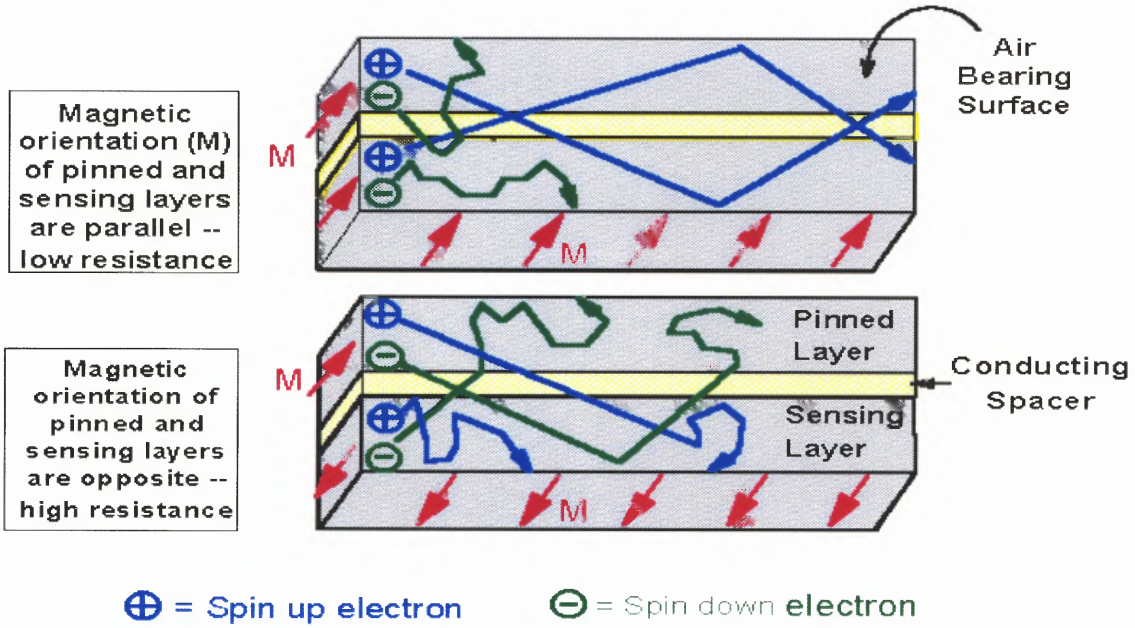

Fig. 1.8 Spin-Valve structure for a GMR read-head device. The schematic of spin-dependent scattering of the conduction carriers within the magnetic layers or at the boundaries of the magnetic layers is also shown. [30]

As shown in the figure 1.8, there is significant difference in resistance measured between the spin parallel and the spin anti-parallel arrangements. In case of strong and effective scattering process, the mean free path of an electron between scattering processes is shorter, and then the resistance becomes larger. A simplistic calculation of a significant difference in resistance was considered by using a resistor network (see Fig. 1.9).

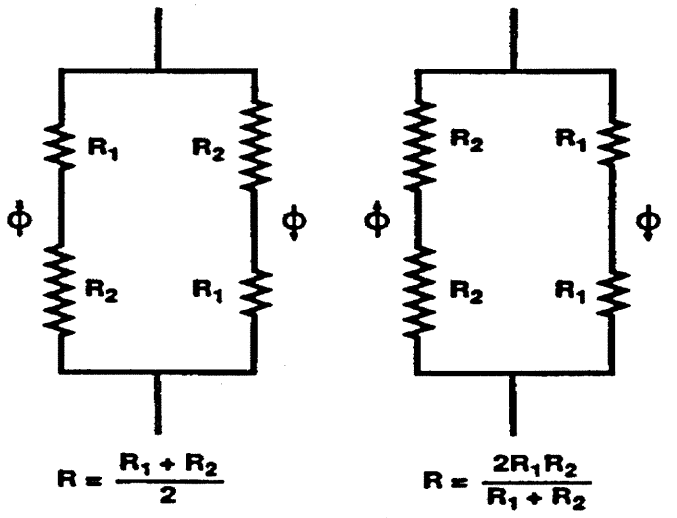

Fig. 1.9 A simplified equivalent resistor array displaying the GMR effect showing the high (left panel) and low (right panel) resistance states. [31]

1.1.3 Intergrain Tunneling

Hwang *et al.* [29] found that intergrain tunneling is induced by the scattering that stems from grain boundaries in polycrystalline samples. They found that in polycrystalline, the resistivity is ~ 10 times (at 1700 °C) and ~ 18 times (1300 °C) greater than a single crystal.[see Fig. 1.10(A)] However magnetization curves of polycrystalline samples and a single crystal seem very similar, implying that the intragrain properties reflect bulk intrinsic properties [see Fig. 1.10(C)]. The MR in the polycrystalline samples is dominated by transport across grain boundaries that are significantly sensitive to the application of magnetic field while the intrinsic negative MR in single crystal is due to the suppression of spin fluctuations. They suggested that spin-polarized intergrain tunneling was involved in their results. The original work of the MR in granular nickel

films were based on the tunneling of spin-polarized electrons between magnetic metallic particles. [32 ,33]

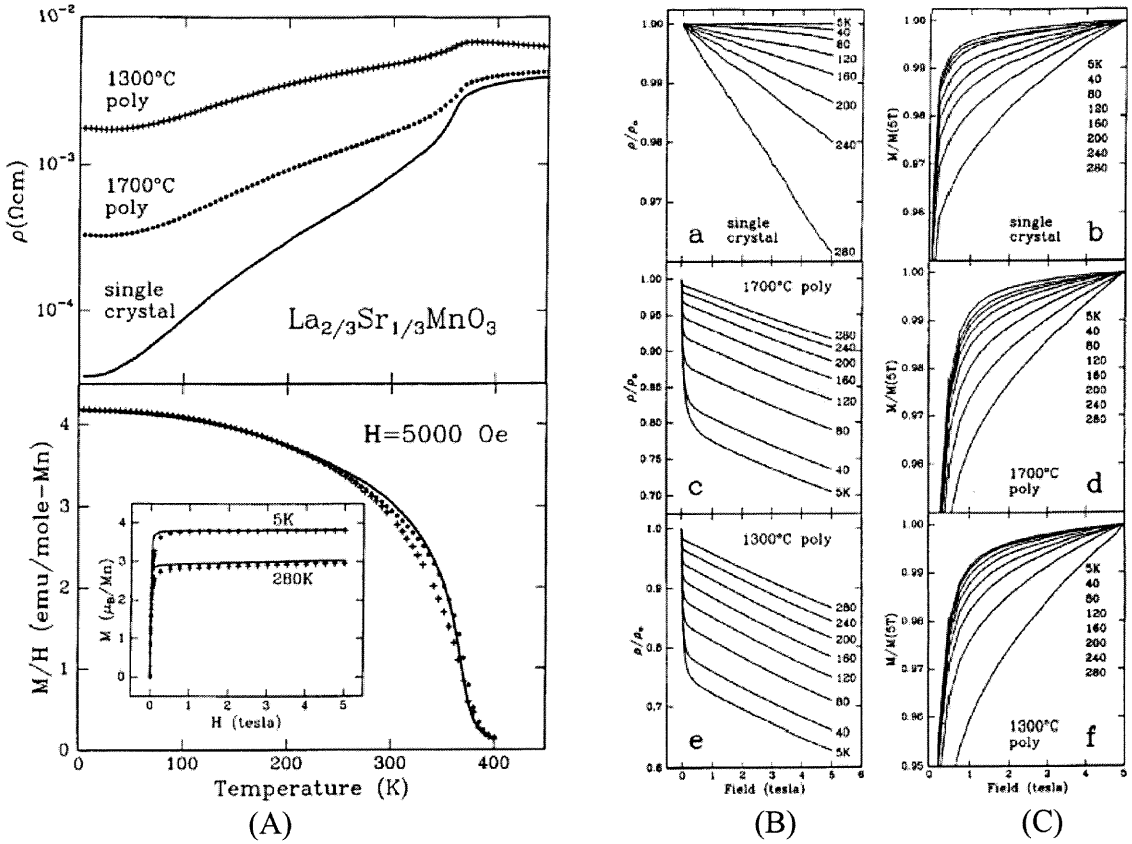

Fig. 1.10 Comparisons of resistivity-magnetization measurements of two polycrystalline samples and a single crystal $La_{2/3}Sr_{1/3}MnO_3$. (A) The top shows the resistivity vs. temperature curve of two polycrystalline samples with final sintering temperatures of 1300 °C and 1700 °C and a single crystal. The bottom shows the magnetization vs. temperature at H = 0.5T with an inset of M (μ_B/Mn) vs. H (T) at 5 and 280 K. (B) The normalized resistivity vs. H (T) and (C) the normalized magnetization vs. H (T) from 5K to 280K are shown

In the tunneling process with the conservation of the electron spin, an additional magnetic coupling energy was considered when the magnetic moments of the neighboring grains were not parallel. With the magnetic field dependence of this intergrain coupling energy, the first term in the high temperature expansion of the MR [33] is given by

$$\frac{\Delta\rho}{\rho} = -\frac{JP}{4k_B T}\left[m^2(H,T) - m^2(0,T)\right] \qquad (1.1)$$

where J is intergrain exchange constant, P is the electron polarization , and m is the magnetization normalized to the saturation value. In polycrystalline $La_{2/3}Sr_{1/3}MnO_3$, the sharp drop in resistance is correlated with the abrupt increase in magnetization. The MR is negative where J is positive, pointing to an antiferromagnetic intergrain interaction. The ferromagnetic alignment of the grains by an applied field increases electron tunneling-as in the case of spin valves.

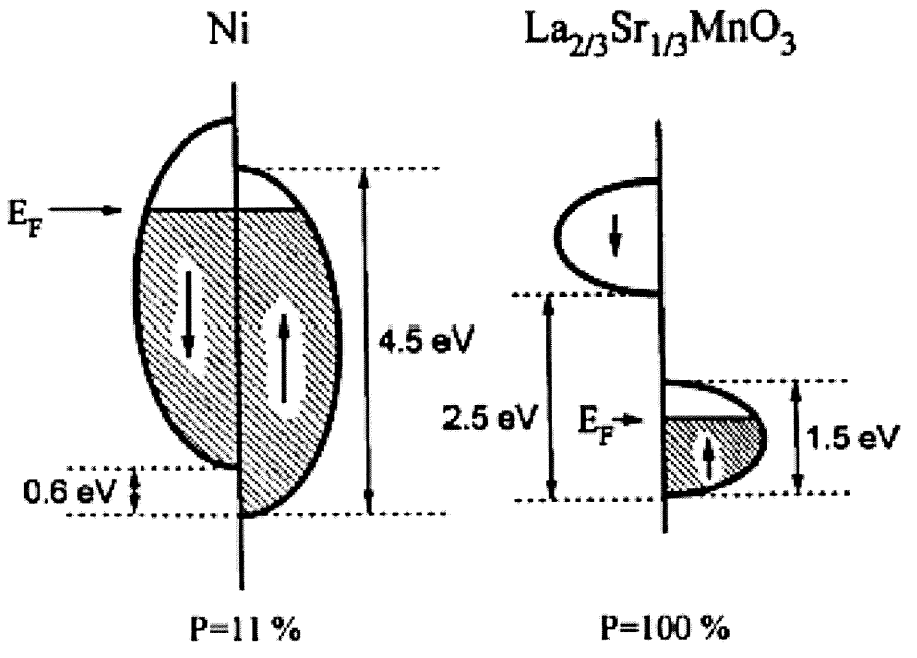

Fig. 1.11 Comparision diagram of energy levels of the conduction band of Ni with $La_{2/3}Sr_{1/3}MnO_3$.[34, 35]

Figure 1.11 shows energy level diagram of a normal itinerant ferromagnetic such as Ni with a very wide conduction band (~ 4.5 eV) which minority and majority carrier bands are shifted by a gap exchange energy (~ 0.6 eV), and a partial polarization of the electrons is about 11%.[35] On the other hand, in manganites, a relatively narrow majority carrier conduction band (~ 1.5 eV) is fully split from the minority band by a large Hund's

energy and exchange energy (~ 2.5 eV), resulting in a nearly complete polarization of the electrons. [34] Since the high degree of spin polarization in the perovskite manganites was shown [29, 36], spin-polarized transport effects have attracted much attention because of technological applications such as spin-polarization dependent phenomena and low field spin-valve MR.

1.1.4 Other Applications of GMR Materials

The giant magnetoresistance (GMR) effect shows in numerous ultra-thin multiplayer systems where thin magnetic films (~ order of a few tens of Å thickness) are sandwiched by non-magnetic metal films (~ order of tens of Å thickness). To get the GMR effect, the most important factor is the fact that the relative orientation of successive magnetic layers must be easily influenced and affected to change by the application of a magntetic field. The GMR effect is intensively attracted because of the potential perspective such as "read" heads in storage application.

The giant magnetoresistance (GMR) materials are possible to be built low cost sensors with superior operation such as temperature stability [37] and linearability over most of operating range; these can be measured up to 200 gauss. Wheatstone bridge structures with field concentrators that can be made very small by integration techniques are used. In memory cells, the resistance change depends on the angle between the magnetization in the two layers (GMR) instead of the angle between the sense current and the magnetization in normal anisotropic MR materials (AMR). Consequently, the resistance measurement of even small currents can be use to detect the state of the magnetization. For antiparallel configuration, a large current flows through stripe. An

accurate measurement for magnetoresistance in GMR memory cell is used by Wheatstone bridges. A bridge using 6% material gives a difference voltage of ± 0.15 volts under application of 5 volts. Magnetization states of bit "0" and "1" lead to high resistance (antiferromagnetically) and low resistance (ferromatically) respectively. GMR sensors detect signals that are 3 to 20 more sensitive than traditional Permalloy alloys (i.e. Fe/Ni) having much higher magnetic permeability than iron alone) magnetoresistive sensor. Magnetoresistive random-access memory (MRAM) is an integrated magnetic memory technology used in magnetic storage and magnetoresistive reading with semiconductor support circuits. [38]

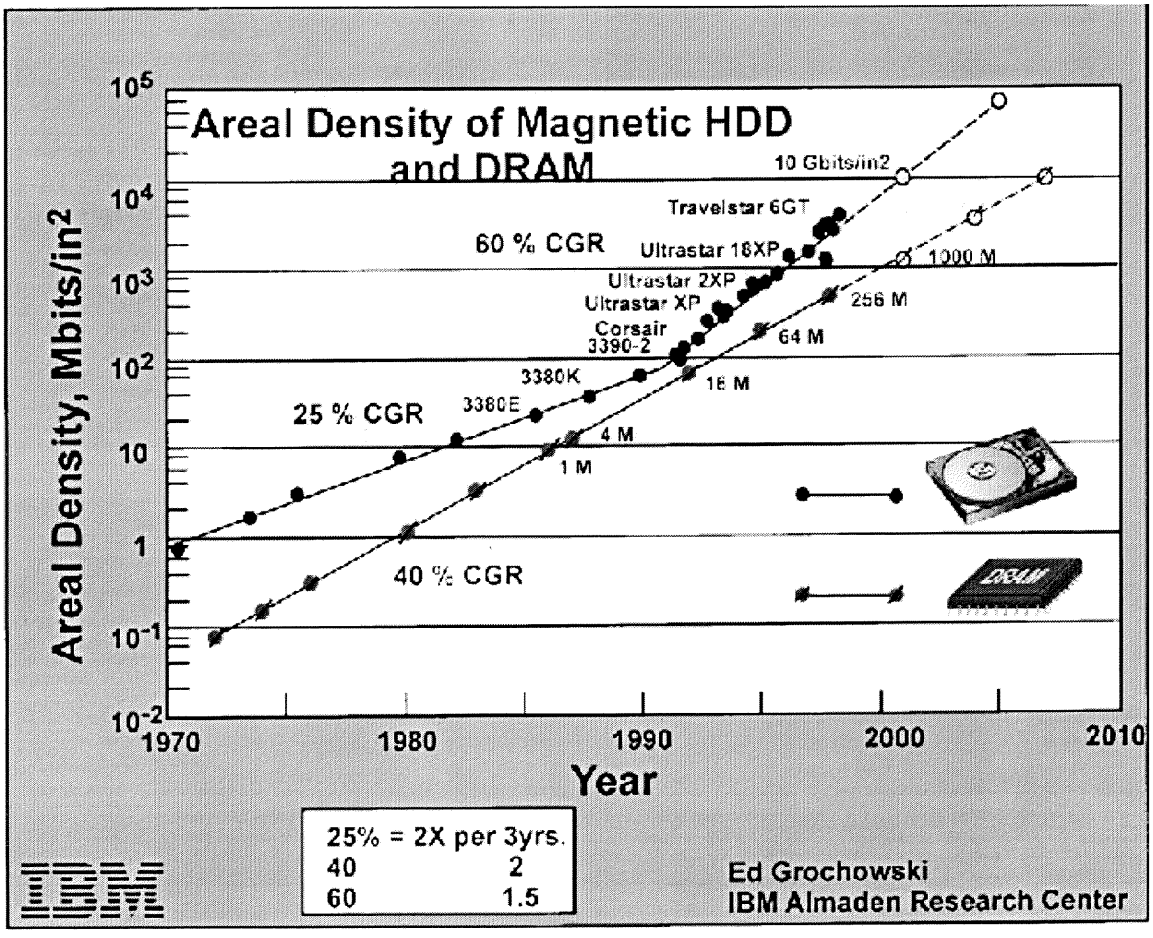

Fig. 1.12 The areal density advancements in IBMs hard disks. [39]

The MRAM consists of two parts: a magnetic sensing line and an orthogonal-insulated word line. The magnetic sensing line has a pair of thin magnetic films with their easy axes across the sense line and with interlayer sandwiched to break the exchange coupling between the magnetic layers. A current in the sense line generates a magnetic field parallel to the line with opposite direction between the top and bottom films. Therefore, a storage state indicates a clockwise or counterclockwise orientation of the magnetizations in the sandwich layers about the sense current. Thus, a "0" or "1" can be recorded into 2D array of these cells by a word current in the variation of designated polarity with a sense current. MRAM technology is essentially better than DRAM because of its inherent simplicity of processing, non-volatility, static storage, and nondestructive readout. GMR materials are used primarily in the computer hard-disk drive industry, but other emerging markets expand nonvolatile memory chips, magnetic field sensors, and ultrahigh speed isolators. GMR-based-magnetic sensors capable of probing the presence and motion of magnets and other iron-containing objects are superior to existing sensors, and can lead a market of applications. Further applications are in fields such as automation of factory production lines with position-sensing robots, antilock breaking systems for cars, "smart" shock absorbers, vehicle-counting systems, currency sorting and counting based on magnetic inks. [40]

1.2 Advances due to CMR

1.2.1 CMR Oxides

A large number of studies on manganites have been performed for the past decade since the giant magnetoresistance (GMR) effect and its technological applications were recognized.[41(a), (b)] The perovskite based manganese oxides (manganites) show unusual electronic magnetic properties, and they have attracted interest because of potential scientific and technological interest. The cubic manganites are represented as $A_{1-x}A'_xMnO_3$ where A is a rare-earth ion, i.e. La, Bi, Nd and A′ is a divalent ion, i.e. Ca, Sr, Ba, or Pb.

Since the late 1940s, various studies of the mixed-valence manganese perovskites for polycrystalline ceramic samples were characterized by Jonker *et al.* [42, 43, 44] Jonker and van Santen initiated the sample preparation, crystal structure and magnetic properties of the $La_{1-x}Ca_xMnO_3$ series with a brief introduction of the electrical resistivity. Other systems such as $La_{1-x}Ba_xMnO_3$ (only in $x < 0.5$) and $La_{1-x}Sr_xMnO_3$ (only in $x < 0.7$) were also reported. In 1954, magnetoresistance and other transport properties were first accounted by Volger. [45] Volger found that the magnetoresistance of $La_{0.8}Ca_{0.2}MnO_3$ shows negative with a peak near the Curie temperature.

On the other hand, in 1969 and 1970, flux-grown single crystals of $La_{1-x}Pb_xMnO_3$ ($0.2 < x < 0.44$) were studied by Searle and Wang, [46] Morrish *et al.*, [47] and Leung *et al.* [48] They reported metallic conductivity below the Curie point T_C and a large negative magnetoresistance (~ 20%) at 1T near T_C which is similar to polycrystalline La_{1-}

$_xSr_xMnO_3$. In the magnetization measurement, a fully spin-polarized d band is related to the ferromagnetic ordering process.

In 1990s, the mixed-valance manganites attracted again because of the preparation of high-quality thin films with large magnetoresistance by von Helmholt *et al.*, [49] and Chahara *et al.* [50] using a method employed for high-temperature superconductors into a structurally correlated manganites.

Comparatively, the MR value is +3% for permalloy (80%Ni-20%Fe) but -5% to –50% for GMR.[51, 52, 15, 24] Jin *et al.* [41(a)] founded that in La-Ca-Mn-O thin films (1000Å~2000Å epitaxial films, $La_{0.67}Ca_{0.33}MnO_x$ grown on (100) $LaAlO_3$ substrates by pulsed laser deposition), the MR was as large as 99.9% at T = 77K and H = 6T. For device applications, manganite materials must be developed, have high sensitivity at room temperature, and are sensitive to fields in the ~ 100 Oe range.

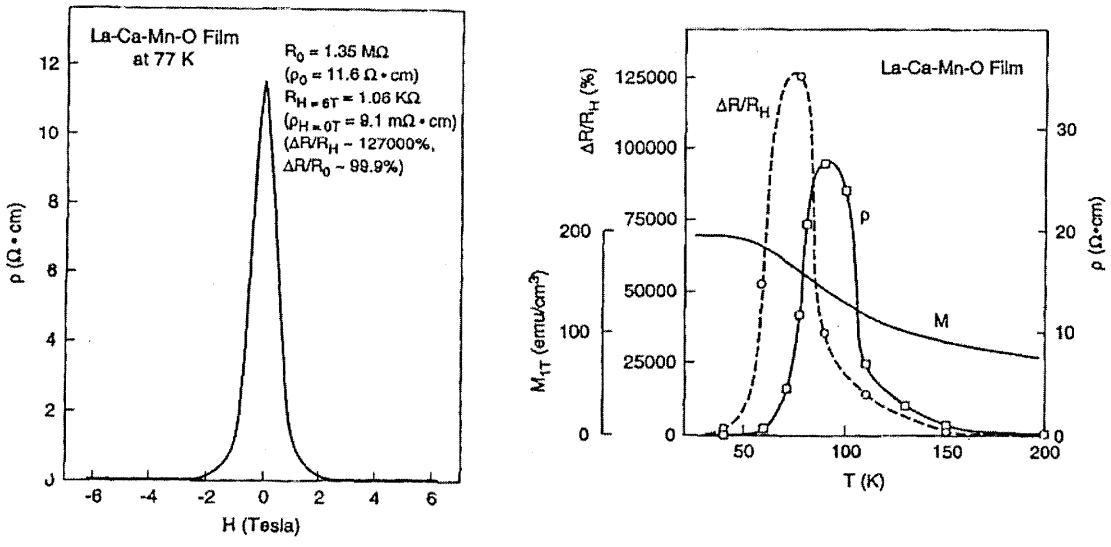

(a) (b)

Fig. 1.13 Colossal magnetoresistance (CMR) in epitaxial La-Ca-Mn-O films. (a) Resistivity vs. fields (H). (b) $\Delta R/R_H$(%), ρ, and M vs. Temperature. Note that [ρ(0)-ρ(H)]/ ρ(H) = 127,000% and [ρ(H)-ρ(0)]/ ρ(0) = 99.9%, respectively.

From this point, the term CMR has been accelerated to study manganites. CMR technology is only promised for large MR but sensitivity is still in high field (~ 6T) and low temperature. Surprisingly, the new oxide MR materials display a large MR called colossal magnetoresistance (CMR). On the other hand, charge ordering shows antiferromagnetic and insulating behavior with a significant changer than GMR. Therefore, charge ordering is a candidate for CMR. [41(d),53,54,55,56,57,58,59,60,61,62,63,64,65,66,67,68,69] It is worth noting that maximum charge ordering temperature (T_{CO}) for $Bi_{1-x}Ca_xMnO_3$ (BCMO) system is above room temperature while Maximum T_{CO} for $Bi_{1-x}Ca_xMnO_3$ (LCMO) system is only about 250 K. This is more suitable at room temperature application. If the future technology may improve this problem, then new technological application will be exploded.

1.3 Importance of Structure

An understanding of atomic structure is important in correlating the magnetic orders, transport, and structural (including local and long range) order. An ideal AMO_3 perovskite structure is cubic (see Fig.1.14) where in (a) B cation (or X atom) sits at origin, (b) A cation at origin, and (c) A cation at origin in hexagonal basis respectively.

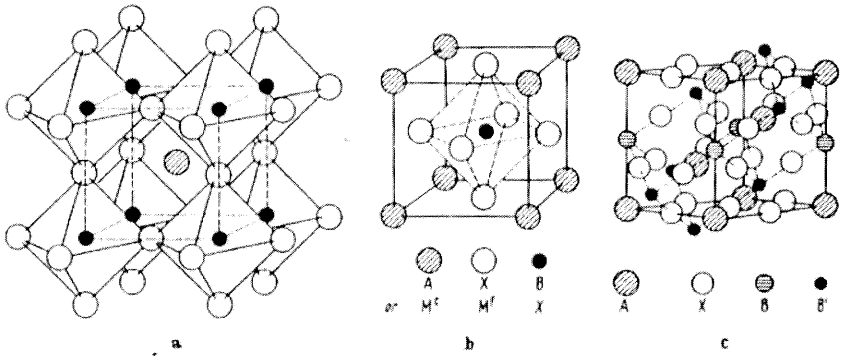

Fig. 1.14 Ideal perovskite structure ABX_3. (a) B cation (or X atom) at origin, (b) A cation at origin, (c) A cation at origin in hexagonal basis. [70]

The typical perovskite symmetry displays either orthorhombic or rhombohedral, depending on the relative ion sizes. [71]

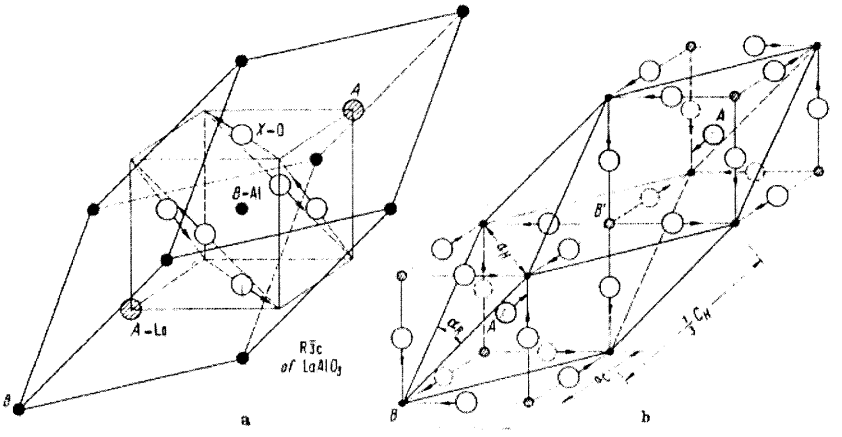

Fig. 1.15 Rhombohedral ABX_3 structures. (a) anion shifts for symmetry ($R\bar{3}c$), (b) the simplest ionic displacements according to symmetry ($R\bar{3}m$) for ordered $A_2BB'X_6$ structures having $r_{B'} > r_B$. [72]

Jonker and van Santen [42] found that a perovskite $La_{1-x}Sr_xMnO_3$ system in $0.2 \leq x \leq 0.5$ has a significantly reduced resistivity associated with ferromagnetism. Brown and Banks [73] also discovered a metallic conductivity in the perovskite system Na_xWO_3. Zener [74] proposed the double-exchange spin-spin interaction to understand the consequence of the mixed-valent character of the conducting perovskites. Wollan *et al.* [75] reported magnetic structures by using neutron diffraction. The $La_{1-x}Ca_xMnO_3$ system showed an anisotropic Type A antiferromagnetic order for x = 0, i.e. La MnO_3, ferromagnetic for x = 0.3, a complex Type CE order for x = 0.5, a Type C antiferromagnetic order for x = 0.75, and an isotropic Type G antiferromagnetic order for x = 1.0, i.e. $CaMnO_3$ respectively (see Fig. 1.16). Goodenough [76] proposed that the idea of orbital orderings at Mn^{3+} ions is based on the anisotropic magnetic coupling that is equivalent to Mn-O-Mn supberexchange pathways with the signs of the super-exchange coupling. Superexchange is based upon the exchange interaction between the moments (AF) on the transition-metal ions and is an indirect interaction through the intermediary

of the oxides. The process of interaction is that the spin of one transition-metal ion polarizes a neighboring oxygen and therefore, induces an interaction with a neighboring transition-metal ion.

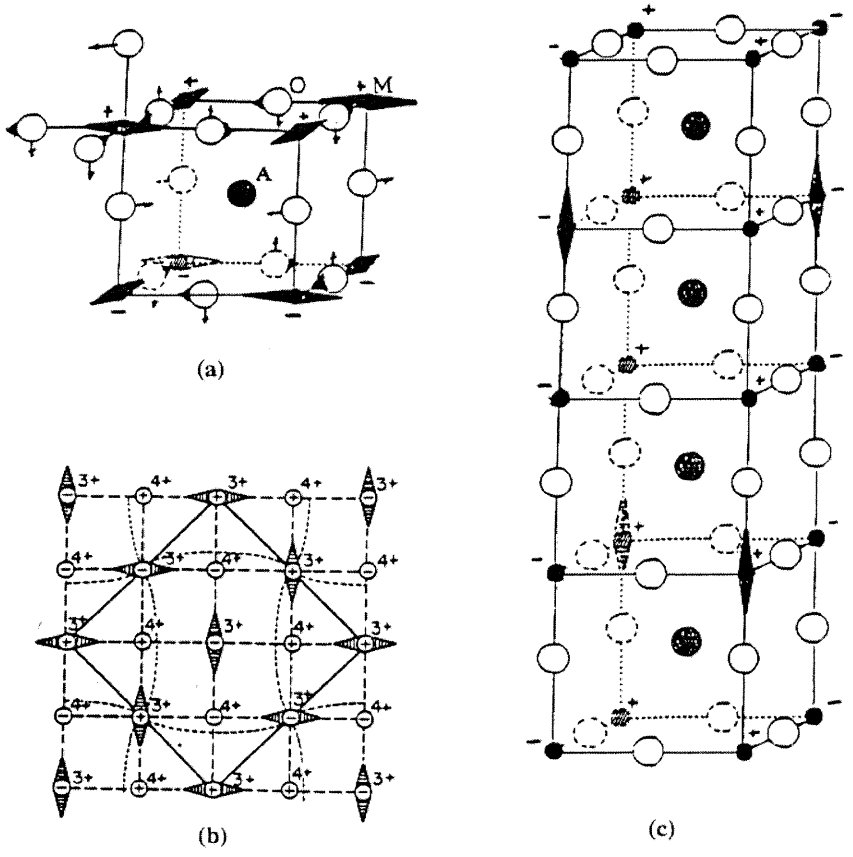

Fig. 1.16 Anisotropic antiferromagnetic orders and occupied e-orbital ordering in the $La_{1-x}Ca_xMnO_3$ system. Note that +/- signs indicate antiparallel spin directions. Figures show magnetic order (a) for x = 0, Type A, (b) for x = 0.5, Type CE, and for x = 0.75, Type C respectively.

In the AMO_3 perovskite structure (see Fig.1.14), the mismatch between the equilibrium A-O and M-O bond lengths is determined by a tolerance factor t,

$$t = \frac{(A-O)}{\sqrt{2}(M-O)} \tag{1.2}$$

A theoretical calculation is possible based on x-ray diffraction data. [77]

Table 1.1 Effective Ionic Radii in Perovskite Structure Oxides (Å). [78]

ION	CN [a]	IR [b]	ION	CN [a]	IR [b]
Al^{3+}	6	0.535	Mn^{4+}	6	0.53
Ba^{3+}	6	1.35	Mn^{3+}	6	0.58 [c]
	9	**1.47**			**0.645** [d]
	12	1.61			
Bi^{3+}	5	0.96	Nd^{3+}	6	0.983
	6	1.03		9	**1.163**
	8	**1.17**		12	1.27
Ca^{2+}	6	1.00	O^{2-}	2	1.35
	9	**1.18**		4	1.38
	12	1.34		6	**1.40**
Cd^{2+}	6	0.95	Pb^{2+}	6	1.19
	7	1.03		9	**1.35**
	8	**1.10**		12	1.49
	12	1.31			
Ce^{3+}	6	1.01	Pr^{3+}	6	0.99
	9	**1.196**		9	**1.179**
	12	1.34			
Co^{3+}	6	0.545 [c]	Sm^{3+}	6	0.958
		0.610 [d]		9	**1.132**
				12	1.240
Fe^{3+}	6	0.645 [d]	Sr^{3+}	6	1.18
				9	**1.31**
				12	1.44
Gd^{3+}	6	0.938	Tl^{3+}	6	0.885
	9	**1.107**		9	**0.75**
La^{3+}	6	1.032	Y^{3+}	6	0.900
	9	**1.216**		8	1.019
	12	1.360		9	**1.075**

[a] coordination number
[b] effective ionic radius
[c] low spin (LS), [d] high spin (HS)

The structure for $t > 1$ is known to either ferroelectric displacements ($BaTiO_3$) or the formation of hexagonal polytypes.[79] On the other hand, for $t < 1$ the perovskite structure

changes by a cooperative rotation of the MO_6 octahedra around a cubic [001] axis as in tetragonal $SrTiO_3$, [80] a cube [111] axis as in rthombohedral ($R\bar{3}c$) $LaNiO_3$, [81] a cubic [110] axis as in orthorhombic (Pbnm or Pnma) $GdFeO_3$, [82] and a cube [101] axis as in orthorhombic (Imma) $La_{0.7}Ca_{0.3}O_3$ only in $T \leq 100K$. These rotations reduce the Mn-O-Mn bond angle from 180°. Figure 1.16 shows the anisotropic antiferromagnetic order with the minimization of the elastic energy ordered the long axes of the distorted Mn(III) octahedra in the $La_{1-x}Ca_xMnO_3$ system. In $LaMnO_3$, a rotation along the [110] axis produced an O-orthorhombic axial ratio $c/a > \sqrt{2}$. In addition, orbital ordering changes for the O′-orthorhombic axial ratio $c/a < \sqrt{2}$. The O′-orthorhombic structure indicates the possibility of the existence of a static orbital ordering and O-orthorhombic structure may cause dynamic Jahn-Teller deformations (see Sec. 1.5 in detailed discussions). Figure 1.17 displays that with increasing the temperatures, the $x = 0.3$ perovskites change from a canted-spin ferromagnetic semiconductor in an phase for $t < 0.96$ to a ferromagnetic metal in a phase for $t \geq 0.98$. Interestingly, for $0.96 \leq t \leq 0.98$, a O phase, a sharp increase with t in the Curie temperature T_c occurs and a the CMR value reaches a maximum. [83]

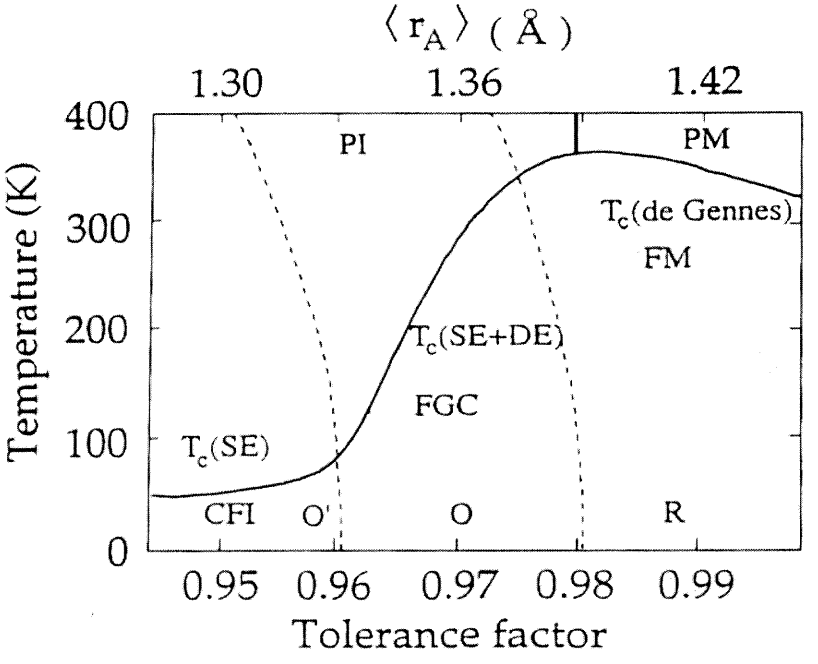

(a)

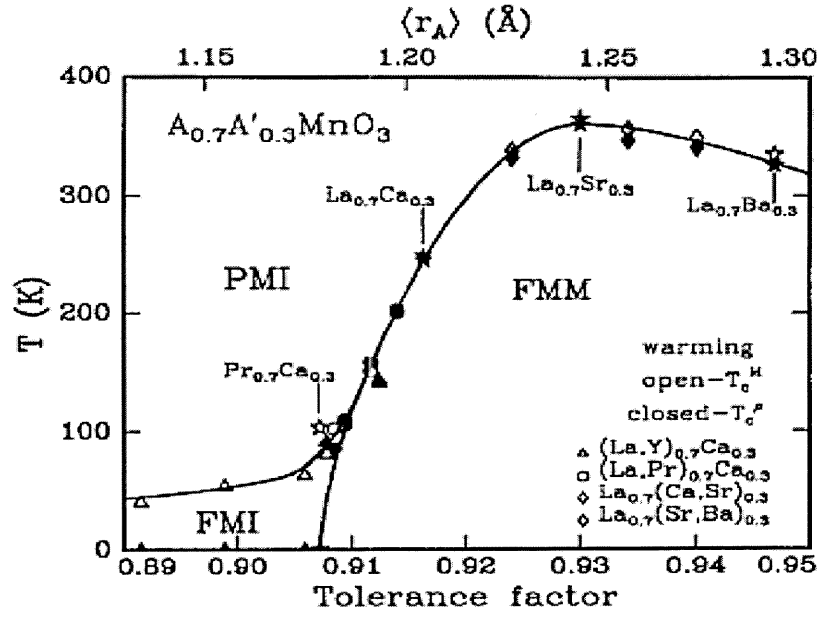

(b)

Fig. 1.17 Phase diagram of temperature vs. tolerance factor for (a) $Ln_{0.7}A_{0.3}MnO_3$ where Ln is lanthanide and A is Ca, Sr, or Ba. [84], and (b) $A_{0.7}A'_{0.3}MnO_3$ where A is La, Pr, or Y , and A′ is Ca, Sr, or Ba. [83]

Table 1.2 Structural data, ferromagnetic Curie temperatures (T_C), bond lengths (R_{MO}), and Mn-O-Mn bond angles in $La_{1-x}A_xMnO_3$ (A = Ca, Sr) and $La_{1-\delta}Mn_{1-\delta}O_3$. [85]

Composition	x or δ	Mn^{4+} (%)	T_C (K)	Crystal Structure *	Lattice Parameters (Å) or (°)	R_{MO} (Å)	Mn-O-Mn (°)
$La_{1-x}Ca_xMnO_3$	0.1	19	245	*R*	a = 5.480 α = 60.40	1.954	164
	0.2	25	260	*C*	a = 7.744	1.944	180
	0.3	33	260	*C*	a = 7.699	1.936	180
	0.4	39	240	*C*	a = 7.677	1.931	180
	0.5	44	240	*C*	a = 7.668	1.922	180
	0.9	86	100[i]				
$La_{1-x}Sr_xMnO_3$	0.1	27	260	*R*	a = 5.523 α = 60.60	1.964	164
	0.2	34	320	*R*	a = 5.482 α = 60.40	1.959	164
	0.3	37	360	*R*	a = 5.454 α = 60.14	1.953	164
	0.4	41	315	*C*	a = 7.721	1.939	180
	0.5	47	300	*C*	a = 7.714	1.932	180
$La_{1-\delta}Mn_{1-\delta}O_3$	0.02	12	240	*O*	a = 5.543 b = 5.594 c = 7.805	2.034	152
	0.04	24	230	*R*	a = 5.478 α = 60.55	1.957	167
	0.045	33	240	*C*	a = 7.788	1.948	180

* *O* is orthorhombic, *R* rhombohedral, and *C* cubic.
No peak in resistivity down to 4.2K.

Strong evidence for Electron-Spin-Lattice Coupling:

An interesting point is the fact that the application of magnetic fields induces structural phase transitions between rhombohedral and orthorhombic space groups in $La_{0.83}Sr_{0.17}MnO_3$ (see Fig. 1.18). [86]

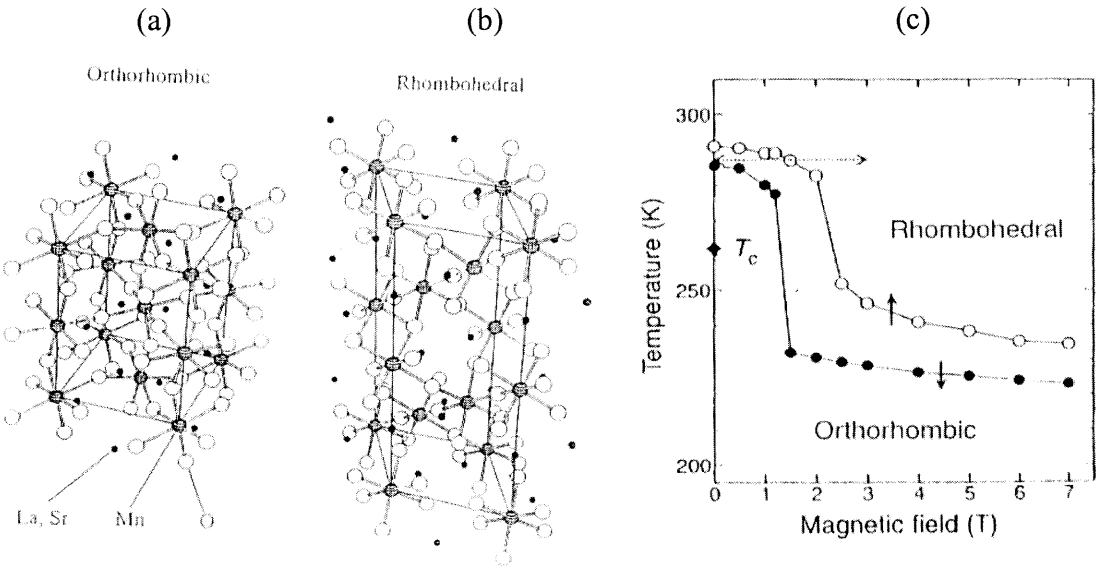

Fig. 1.18 Schematic crystal structures of crystal $La_{0.83}Sr_{0.17}MnO_3$ in (a) the orthorhombic phase (Pbnm), (b) the rhombohedral phase ($R\bar{3}c$), and (c) structural phase diagram in the T –H plane.

In addition, high magnetic fields have been found to destroy the highly resistive charge ordered state (insulator to metal transition). (See Fig. 1.19)

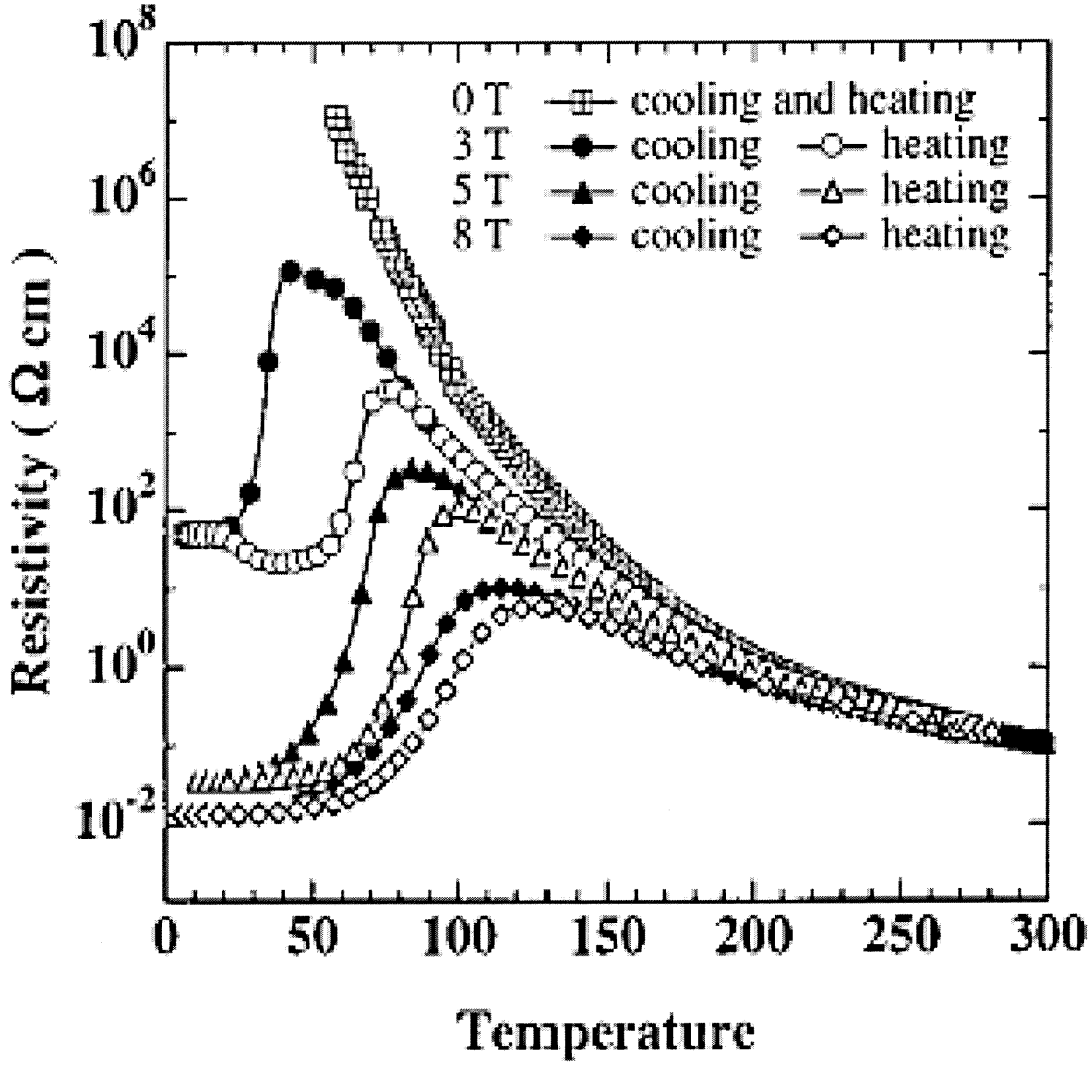

Fig. 1.19 Resistivity vs. temperature of $Pr_{0.7}Ca_{0.3}MnO_3$ in applied magnetic fields of 0, 3, 5, and 8T. Note that the filled symbols indicate cooling runs and opened symbols are for heating runs.

Table 1.3 Structural, Transport, and Magnetic Properties of MR/GMR/CMR Materials.

Materials	Structure	Electric features	Magnetic features*	T(K)	H(T)	MR (%)	Refs.
$La_{2/3}Ba_{1/3}MnO_x$ Thin films	perovskite like	semi-conductor to poor metal	FM	77	6	-99.9 $^{\delta}$	41(a), 87
$La_{2/3}Ba_{1/3}MnO_x$ Thin films	perovskite like	narrow gap semiconductor to poor metal	FM	300	7	60	41(b)
$La_{0.83}Ba_{0.45}CoO_{3-\delta}$ Thin films	perovskite	narrow gap semi-conductor to poor metal	FM	7	10	- 38	88
$Bi_{1-x}Ca_xMnO_3$ x = 0.875 Polycrystalline	perovskite	insulator	CG/ CAF	5	30	- 91	89
Sr_2FeMoO_6	double perovskite	semi-metal	FM	5 ~ 300	7	+ 20 5	90
$Tl_2Mn_2O_7$	pyrochlore	narrow gap semi-conductor to poor metal	FM	10 ~ 300	8	- 60	91
Metal multilayers	two dim-ensional	poor metal	FM / AF	4.2	2	-60	15
$(Zn_{1-x}Mn_x)_3As_2$ (x = 0.02) alloys	tetragonal	narrow gap Semi-conductor to metal	FM	4.2	2	-34	92
Fe/Cr(100)	super-lattices	insulator	AF	4.2	2.5	150 $^{\alpha}$	52

*FM = ferromagnetic, PM = paramagnetic, and AF = antiferromagnetic.

$^{\delta}$ $\Delta R/R_H = (R_H - R_0)/R_H = 127{,}000\%$

$^{\alpha}$ $\Delta\rho/\rho_s$ where ρ_s is the saturation resistivity.

1.4 Jahn-Teller Distortions

1.4.1 Basic Description of Jahn-Teller effect

Jahn-Teller distortions influence the transport properties in the manganite-oxides. The Jahn-Teller (JT) deformations of the MnO_6 octahedra in perovskite are known to cause a significant effect on their electrical and magnetic properties. The ground state of the cation is a degenerate state rather than just a Kramers' doublet. [93] A Kramers' doublet which can appear only when the molecule holds an odd number of electrons. The degeneracy is lifted by a local distortion to a lower symmetry state. [94] Kramers pointed out that an electric field without a magnetic field can fully remove the degeneracy only for a system with an integral value of the sum of the spins, while for the system with a half-integral value of the sum of the spins, all the levels applied to an arbitrary electric field must be doubly degenerate. In transition-metal materials, electrons in a partially filled cation shell are localized. In a somewhat similar situation, a high site symmetry in the cation may possibly be delocalized due to a deformation such as JT distortions. Since localized electrons are "atomic-like", the acting parameters should be considered strong ligand-fields which affect the symmetry of the lattice, the elastic coupling and the magnetic coupling between neighboring atoms. In a crystal, only d and f outer electrons are known to be localized.

Under a configurational distortion, the structural symmetry will be lowered and the energy level in the degeneracy will be shifted. In the case of a hydrogen atom, three p orbital states (p_x, p_y, p_z) are degenerate because the system has spherical symmetry, in which rotation about each axis by the nucleus makes the Hamiltonian invariant, i.e., switching the p functions into each other. This three-fold degeneracy keeps the same

degeneracy although a free atom lies in the external field generated by six charges that are located in an octahedral site surrounded by the nucleus. If the distortion such as extension or compression occurs in the octahedron along the z-axis, the structure transforms from cubic to tetragonal. Therefore, the degeneracy will be partially lifted as the electron energy becomes $E(p_z) \neq E(p_x) = E(p_y)$. Two-fold degeneracy in the tetragonal site can be distorted by orthorhombic perturbations.

In the sense of conservation of the energy, the energy level due to a distortion will be lifted while another will be lowered. Now a total distortion term for the system in the adiabatic form is considered to come form two parts as [95]

$$W(Q) \equiv U(Q) + E(Q) = \frac{kQ^2}{2} - VQ = k\left(Q - \frac{V}{k}\right)^2 - \frac{V^2}{2k}, \qquad (1\text{-}2)$$

where the elastic strain potential energy, $U(Q) = kQ^2/2$ where Q is the strain (distortion) and k is the corresponding force constant, and $E(Q) = -VQ$ where V is electron-strain coupling constant, is the lowest component potential of the split term. $W(Q)$ will reach a minimum when the term defined as Q_0 (= V/k), deviates from zero, i.e. initial highly symmetry position ($Q = 0$), and the distorting force exerted by the electrons on the nuclei is balanced by the elastic restoring force. An initial high symmetry state is unstable because distortion caused by displacement to the minimum $Q = Q_0$ makes a reduction by $\Delta E = V^2 / 2k$. The higher order term of $E(Q)$ rather than linear term is theoretically questioned.

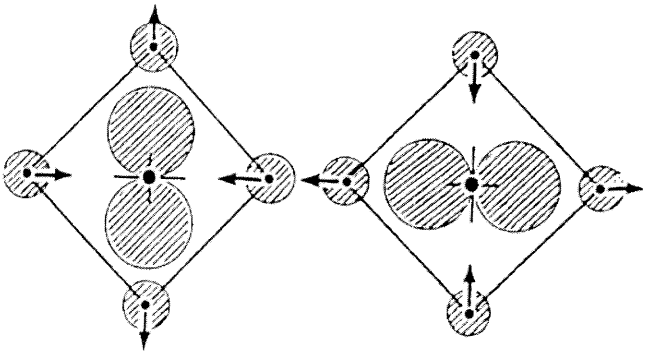

Fig. 1.20 Illustration of the two-fold (p_x, p_y) electronic degenerate state of the central atom in a surrounding with D_{4h} symmetry (square in the xy plane) group. Note that arrows indicate displacements of nuclei. [95]

Jahn and Teller's first publication [94] indicates that in a degenerate electronic state, the nuclear configuration of any nonlinear polyatomic system is unstable due to nuclear displacements that diminish the symmetry and remove the degeneracy. But this statement is not enough. The Jahn-Teller effect implies that for degenerate of the electronic term, the system itself distorts spontaneously and a distorted nuclear configuration should be observed. This is not true because even for a free molecular system, the distorted nuclear configuration may not be observable due to the JT dynamics and the degeneracy of the system is not entirely removed. In fact, the major effect of electronic degeneracy is a spatial coupling between the electronic and nuclear motion with the observable effects, called "JT vibronic coupling effect". [96]

Here is the mathematical proof. The Hamiltonian of the system is

$$H = H_r + H_Q + V(r,Q) \tag{1-3}$$

where H_r is the pure electronic part, denoting the electronic coordinates, H_Q is the nuclear kinetic energy, denoting Q symmetrized nuclear coordinates, and V(r,Q) is electron nuclear and nuclear-nuclear interactions. Now V(r,Q) can expand with respect to small nuclear displacement from the initial configuration $Q_\alpha = Q_{\alpha 0} = 0$, $\alpha = 1, 2, 3, ---, N$.

$$V(r,Q) = V(r,0) + \sum_{\alpha}\left(\frac{\partial V}{\partial Q_\alpha}\right)Q_\alpha + \frac{1}{2}\sum_{\alpha,\beta}\left(\frac{\partial^2 V}{\partial Q_\alpha \partial Q_\beta}\right)_0 Q_\alpha Q_\beta + \cdots \quad (1\text{-}4)$$

The vibronic coupling terms as a perturbation can be rewritten as

$$W(r,Q) = V(r,Q) - V(r,0) = \sum_{\alpha}\left(\frac{\partial V}{\partial Q_\alpha}\right)Q_\alpha + \frac{1}{2}\sum_{\alpha,\beta}\left(\frac{\partial^2 V}{\partial Q_\alpha \partial Q_\beta}\right)_0 Q_\alpha Q_\beta + \cdots \quad (1\text{-}5)$$

Now, the Schrodinger equation of this system is

$$H\Psi_i(r,Q) = \varepsilon_i \Psi_i(r,Q) \quad (1\text{-}6)$$

where ε_i and $\Psi_i(r,Q)$ are a set of energies and wave functions.

Ignoring the vibronic coupling, it can be rewritten as

$$[H_r + V(r,0)]\varphi_k(r) = \varepsilon'_{k_i}\varphi_k(r) \quad (1\text{-}7)$$

where a set of energies ε'_{k_i} and $\varphi_k(r)$ are a set of energies and wave functions for the given nuclear configuration depending the point $Q_\alpha = Q_{\alpha 0} = 0$. The goal here is to solve the Schrodinger equation with f-fold degenerate electronic term $\varepsilon'_k = \varepsilon_0, k = 1, 2, \cdots, f$ including a perturbation. One simple point is to understand how the solutions change due to nuclear displacements; the Schrodinger equation

$$(H - E)\Psi(r,Q) = 0 \quad (1\text{-}8)$$

must be solved. The wave function $\Psi(r,Q)$ is expanded as

$$\Psi(r,Q) = \sum_k \chi_k(Q)\varphi_k(r) \quad (1\text{-}9)$$

where $\chi_k(Q)$ are functions of the nuclear coordinates (Q) and $\varphi_k(Q)$ are the electronic functions. Combining two equations, the equation is

$$[H_Q + \varepsilon_k(Q) - E]\chi_k(Q) + \sum_{m\neq k}' W_{km}(Q)\chi_m(Q) = 0 \quad (1\text{-}10)$$
$$k, m = 1, 2, \cdots$$

where $W_{km}(Q)$ is the electronic matrix element of vibronic interactions, i.e. the part of the electron-nuclear interaction V (r, Q) in terms of Q [see Eq.1.5] and potential energy of the nuclei in the mean field of the electrons in state $\varphi_k(r)$ is

$$\varepsilon_k(Q) = \varepsilon_k^{'} + W_{kk}(Q). \tag{1-11}$$

The coupled system of equation (Eq.1.10) can be neglected if $W_{km}(Q) = 0$ for $k \neq m$); that is, coupling between these states vanishes. The equation of Eq.1.10 can be decomposed as

$$\left[H_Q + \varepsilon_k(Q) - E\right]\chi_k(Q) = 0 \tag{1-12}$$

It is worth noting that for a given k, Eq.1.12 indicates the nuclei moving in the mean field of the electron in state $\varphi_k(r)$. For a molecule of given N atoms, the number of vibrational degrees of freedom (the number of symmetrized displacements) are 3N – 6 (3N-5 for linear molecules). The normal coordinates can be established by means of symmetrized displacements that are collective nuclear displacements transforming according to one of their irreducible representations under the symmetry operation of the molecular point group by using group theory. [97] The f-fold degenerate representations (symmetry types), Γ , have f lines γ , in which the twofold degenerate representation Γ = E has two lines, $\gamma = \theta, \varepsilon$ and the threefold one Γ = T, $\gamma = \xi, \eta, \zeta$, and so on. Using normal coordinates, Eq.1.12 for nuclear motions splits into 3N - 6 (or 3N –5) equations of harmonic oscillators with the reduced mass μ_α of the αth normal vibration and frequency ω_α as

$$-\frac{\hbar^2}{2\mu_\alpha}\frac{\partial^2\chi_{n_\alpha}}{\partial Q_\alpha^2} + \frac{1}{2}\omega_\alpha^2 Q_\alpha^2 \chi_{n_\alpha} = E_{n_\alpha}\chi_{n_\alpha}, \qquad \alpha = 1, 2, \cdots, 3N-6 \tag{1-13}$$

The solutions of equation are written:[98]

$$E_{n_\alpha} = \hbar\omega_\alpha\left(n_\alpha + \frac{1}{2}\right), \qquad n_\alpha = 1, 2, \cdots, 3N-6 \tag{1-14}$$

$$\chi_{n_\alpha}(Q_\alpha) = \left(n!2^n\sqrt{\pi}\right)^{-1/2} H_n(Q_\alpha)\exp\left(-\frac{\mu_\alpha\omega_\alpha Q_\alpha^2}{2\hbar}\right), \tag{1-15}$$

where $H_n(Q_\alpha)$ are Hermite polynomials.

Two-fold degenerate electronic terms E interacting with a two-fold degenerate E vibration are simplest and most widespread JT problems: the E ⊗ e problem. Let the two electronic functions of the E term $|\theta\rangle$ and $|\varepsilon\rangle$ ($\theta \sim d_{z^2}$ and $\varepsilon \sim d_{x^2-y^2}$) respectively. In order to solve a f-fold degenerate electronic term, $\varepsilon_k^{'} = \varepsilon_0, k = 1, 2, \cdots, f$, including a perturbation[= vibronic coupling $W_{km}(Q)$], the secular equation of the adiabatic potential (AP) $\varepsilon_k(Q)$ for an f-fold degenerate electronic term Γ in extremely small nuclear displacements $Q_{\Gamma\gamma}$ can be solved as

$$\begin{vmatrix} W_{11}-\varepsilon & W_{12} & \cdots & W_{1f} \\ W_{21} & W_{22}-\varepsilon & \cdots & W_{2f} \\ \cdot & \cdot & & \cdot \\ \cdot & \cdot & & \cdot \\ \cdot & \cdot & & \cdot \\ W_{f1}-\varepsilon & W_{f2} & \cdots & W_{ff}-\varepsilon \end{vmatrix} = 0 \tag{1-16}$$

and

$$W_{\Gamma\gamma\Gamma\gamma'} = \sum_{\bar{\Gamma}\bar{\gamma}} F^{\Gamma\gamma\Gamma\gamma'}_{\bar{\Gamma}\bar{\gamma}} Q_{\bar{\Gamma}\bar{\gamma}} = \sum_{\bar{\Gamma}\bar{\gamma}} F^{\Gamma}_{\bar{\Gamma}} Q_{\bar{\Gamma}\bar{\gamma}} \left\langle \bar{\Gamma}\bar{\gamma}\Gamma\gamma' \middle| \Gamma\gamma \right\rangle \tag{1-17}$$

where the matrix elements of the linear terms F_θ and quadratic G_E, is ,have the linear vibronic coupling constant

$$F_\theta = \langle\theta\left\|\left(\frac{\partial V}{\partial Q_\theta}\right)_0\right\|\theta\rangle, \tag{1-18}$$

and

$$G_\theta = \langle\theta\left\|\left(\frac{\partial^2 V}{\partial Q_\theta \partial Q_\varepsilon}\right)_0\right\|\varepsilon\rangle \tag{1-19}$$

$$K_E = \langle\theta\left\|\left(\frac{\partial^2 V}{\partial Q_\theta^2}\right)_0\right\|\theta\rangle \tag{1-20}$$

where $|\theta\rangle$ and $|\varepsilon\rangle$ are the wave functions of two states of two degenerate states.

Not just solving Eq.1.7, the electronic term, i.e. Eq.1.7 from a degenerate electronic state at $Q_\alpha = 0$ is considered with vibronic coupling W(Q), a perturbation term. This term splits the degenerate term and yields ε_k^v with the harmonic (nonvibronic part) nuclear interaction term produce f branches of the adiabatic potential energy surface (APEC) that intersect at $Q_\alpha = 0$

$$\varepsilon_k(Q_\alpha) = \frac{1}{2}\sum_\alpha K_\alpha Q_\alpha^2 + \varepsilon_k^v(Q_\alpha) \qquad n_\alpha = 1, 2, \cdots, f \tag{1-21}$$

where K_α is the primary force constant. [see Eq.1.20]

In polar coordinates $Q_\theta = \rho\cos\phi$ and $Q_\varepsilon = \rho\sin\phi$, the APES is

$$\varepsilon_\pm(\rho,\phi) = \frac{1}{2}K_\alpha\rho^2 \pm \rho\left[F_E{}^2 + G_E{}^2\rho^2 + 2F_E G_E \rho\cos 3\phi\right]^{1/2} \tag{1-88}$$

If $G_E = 0$, the APES is the surface of revolution with $\varepsilon_\pm$ independent of ϕ, called "Mexican hat".

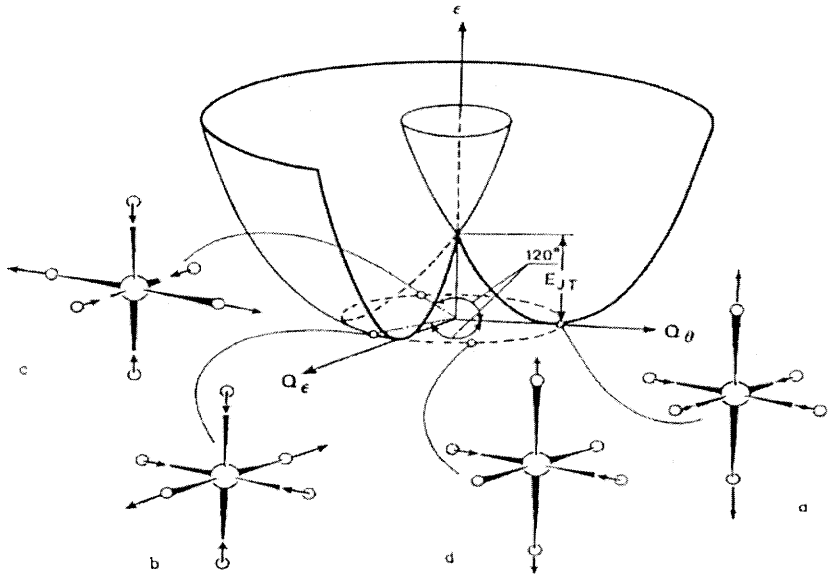

Fig. 1.21 The "Mexican hat" in the linear E⊗e problem with distortions of an octahedral system ML_6. (a, b, c) at $\phi = 0, 2\pi/3, 4\pi/3$, the octahedron is tetragonally distorted along the three 4-fold axes, respectively and (d) D_{2h} symmetry.[99]

In summary, to obtain a complete solution for Schrodinger equation, the electronic states $\varphi_k(r)$ can be solved by (Eq.1.10)) and used to determine the potential energy of the nuclei $\varepsilon_k(Q)$ from Eq.1.12. The wave function $\chi_k(Q)$ and energies E of nuclei part can be solved by (Eq.1.12). So the complete wave function is

$$\Psi(r,Q) = \varphi_k(r)\,\chi_k(Q). \qquad (1\text{-}22)$$

This is called the simple adiabatic approximation or the Born-Oppenheimer approximation.

The criterion for the simple adiabatic approximation is valid only when

$$\hbar\omega << \left|\varepsilon'_m - \varepsilon'_k\right| \qquad (1\text{-}23)$$

where $\hbar\omega$ is the energy quantum of vibrations in the electronic state in terms of k or m, and ε'_m and ε'_k are the electronic energy levels. Therefore, the vibronic mixing of

different electronic states i.e. Eq.1.10 (= perturbation) is extremely small $((m/M)^{1/2} \sim 10^{-2})$

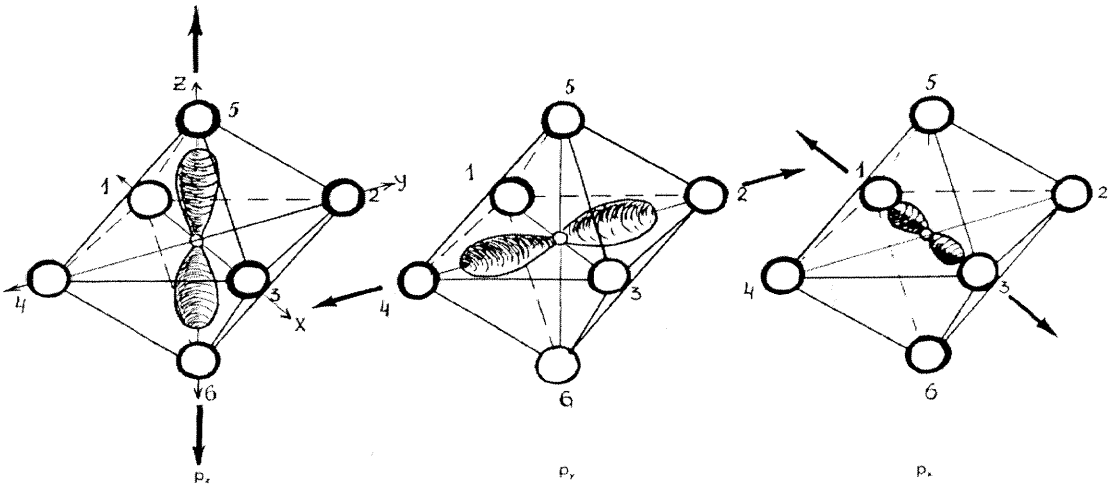

and neglected ($W_{km}(Q) = 0$).

Fig. 1.22 Simple diagram of the electrostatic origin of the Jahn-Teller effect for three-fold degeneracy. The electron of the central atom of an octahedral complex stretches out or pulls in resulting in tetragonal distortion of the octahedron shown as arrows. [100]

1.4.2 Cooperative Jahn-Teller Deformations

Van Vleck [101] showed that the two normal E_g vibrational modes would remove the e-orbital degeneracy of an electronic E_g configuration in the octahedral site. These two modes are associated with the orthorhombic and tetragonal deformations Q_2 and Q_3 (see Fig. 1.23). If they are defined as $Q_2 = \rho \cos\theta$ and $Q_3 = \rho \sin\theta$ in the polar coordinates, the ground state of an isolated octahedral MnO_6 is independent of θ because the only the first order in the coupling constant g between vibrational and electronic states is considered. [84] Therefore, the ground state can be thought a circle to any point with radius $\rho\left(= \delta = g/\sqrt{C}\right)$ where C is the stiffness constant related to vibrations.

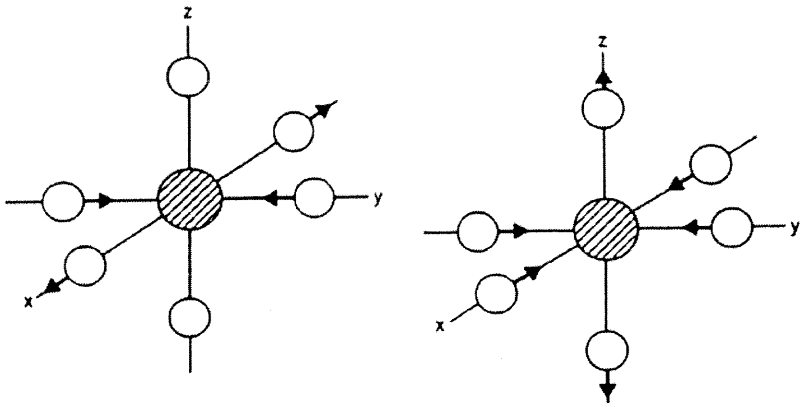

Fig. 1.23 Two E_g vibrational modes Q_2 (left) and Q_3 (right) in an octahedral site.

This forms a dynamic coupling of the e electrons to two E_g vibrational modes Q_2 and Q_3 which is referred to a dynamic JT stabilization of vibronic states. In a solid, static deformations may be affected by the symmetry of the crystalline lattice, and a Q_2-type local deformation. Consequently, the local JT deformations are cooperative in order to minimize the elastic energy. When more ions in the solid are JT distorted, these cooperative local distortions stimulate "a global, static displacive deformation" below an orbital-ordering temperature. For the case of lower concentration of JT ions, locally cooperative but dynamic JT deformations can cause anomalous physical properties.

1.4.3 Jahn Teller Effects in the CMR System

Millis *et al.* [102] developed a model with dynamic Jahn-Teller and double-exchange effects for colossal magnetoresistance in the doped rare-earth manganites, e.g. $La_{1-x}Sr_xMnO_3$. Hamiltonian for this model is

$$H_{eff} = H_{el} + H_{JT,} \tag{1.24}$$

where

$$H_{el} = -\sum_{ij\alpha} t_{ij}^{ab} d_{ia\alpha}^{+} d_{jb\alpha} + J_H \sum_{1a\alpha} \vec{S}_c^{\,i} \cdot d_{ia\alpha}^{+} \vec{\sigma} d_{ia\alpha} + \vec{h} \cdot \frac{\vec{S}_c}{S_c}, \tag{1.25}$$

and

$$H_{JT} = g\sum_{ja\sigma} d_{ja\sigma}^{+} \mathbf{Q}^{ab}(j) d_{jb\sigma} + \frac{k}{2}\sum_{j} \mathbf{Q}^{2}(j). \tag{1.26}$$

where t is the hopping matrix element, $d_{a\sigma}^{+}(i)$ is creating operator of an outer-shell d electron of spin σ in the a orbital on site i, J_H is coupling constant, S_c is spin angular moment, $\vec{h}$ is the external magnetic field, g is electron-phonon coupling, **Q** is the traceless symmetric matrix $\mathbf{Q} = r[\cos(\phi)\tau_x + \sin(\phi)\tau_x]$, and k is the phonon stiffness. For a limited density (density, i.e. n =1 only), they found that the interplay of electron-phonon coupling and double exchange correlates to the existence of a high T insulating phase and CMR effect at T_c, and the sensitivity to magnetic field. Mechanism that is not appeared in the double-exchange model, must relate to significantly diminish the electron kinetic energy K at $T \approx T_c$. In fact, double exchange itself can not explain the the reisistivity as a function of temperature. Millis *et al.* proposed a polaron effect due to a gigantic electron-phonon coupling resulting from a Jahn-Teller splitting of the Mn^{3+} ion which is supported by Kusters *et al.*' work [103] (magnetic polaron picture). Thus, the

standard double-exchange Hamiltonian does not include magnetic polaron effects since the Jahn-Teller coupling appears too strong while the effective carrier-spin interaction is so weak. The extensive work [104] was studied by using the dynamical mean-field method to investigate a model of electrons Jahn-Teller coupled to localized classical oscillators and ferromanetically coupled to "core spins". Millis *et al.* argued that the model contains the fundamental physics of the CMR manganites, $Re_{1-x}A_xMnO_3$ where Re means a rare-earth element, that is, La or Nd etc. and A is Sr or Ca etc. They suggest the idea that the basic physics of the CMR manganites, $Re_{1-x}A_xMnO_3$ relates the interplay between a strong electron-phonon coupling and the double exchange effect of magnetic order on the electronic kinetic energy. They suggested that different doped materials have different intrinsic electron hopping with probably different electron-phonen couplings but the variation of the electron kinetic energy with x is very sufficient to sweep the effective coupling through the critical value at some x between 0.1 and 0.5. In particular, when they applied electron-phonon coupling in a variety of models without double exchange, the results have a similarity with the metallic state in the ground state in the Ca concentration, $0.2 < x < 0.5$.

In addition to Millis, Zang *et al.* [105] studied Jahn-Teller electron-phonon-coupling effects in the CMR perovskite compounds in $La_{1-x}A_xMnO_3$ in somewhat different point of view. The long-ranged Jahn-Teller order was presumed to occur at low T. They investigated the combined effect of orientational fluctuations of the Jahn-Teller distortion and double exchange on the resistivity in the metallic phase below T_C. They found that the carriers are electrons without associated static Jahn-Teller distortion. An appropriate JT coupling strength can lift the double degeneracy of e_g orbitals by finite static JT

distortions. Therefore, the JT distortion fluctutions will cause magnetoresistance at somewhat and high temperatures as the function of the temperature dependence. These further scattering effects of the JT distortion will be increased when in the inhomogeneous insulating phase above T_C with the localization of small magnetic polarons.

Roder *et al.* [106] investigated the combined influence of spin double exchange and Jahn-Teller lattice coupling to hole-doped manganites, $La_{1-x}A_xMnO_3$ where A is Ca, Sr, Ba. They found that the lattice effects reduce the magnetic transition temperature and furthermore result in the maximal value of the transition temperature as a function of dopant concentration x depending on the Jahn-Teller coupling strength.

Satpathy[107] employed a single Mn-O-Mn bond to understand dynamical Jahn-Teller effect on double exchange (DEX) interaction and the isotope shift. It depends sharply upon the electron hopping parameter t. He proposed that these stem from the coupling of the motion of the bridging oxygen atom to the Mn electrons.

Recently, Zou *et al.* [108] reported the spin diffusion dynamics of the double exchange model including Jahn-Teller distortion for manganites, i.e. the CMR effect. Because of the trapping of composite polarons in the magnetic transition regime, the spin diffusion dynamics becomes important. The composite polarons relate to the itinerant character as well as the localization character. An anomalous spin diffusion peak [109] near T_C in perovskite manganaties is explained by the competition between both characters. They proposed that this competition in the FM transition regime causes the CMR effect, and two characters manifest the composite polarons crossover from itinerancy to localization in the magnetic and transport properties of CMR materials.

From the theoretical point of view, many issues still remain unsolved as follows: [104] (a) the origin of the experimentally observed chemical and doping dependence, (b) the degree of "fine-tuning" of essential parameters, (c) calculations of models in different electron concentrations, (d) quantum fluctuations of the phonons, and (e) other omitted interactions.

1.5 Magnetic Order

1.5.1 A Theoretical Background of Magnetism

Magnetism (even superconductivity) in solids is related to "cooperative phenomena" that are directly stemmed from the interaction between the electrons, not just a single electron problem. In the quantum mechanical treatment, the origin of ferromagnetism was thought of the exchange interaction which is mathematically difficult to solve the problem and phenomenologically represented. Now suppose that nuclei are fixed like a point charge. The Hamiltonian with the wavefunction $\Psi(\mathbf{r}_1, \mathbf{r}_2, \cdots, \mathbf{r}_N)$ of the coordinates of all N electrons [110] can be written as

$$\left[-\frac{\hbar^2}{2m}\sum_i \nabla_i^{\,2} + \sum_i V(\mathrm{r}_i) + \frac{1}{2}\sum{}' \frac{e^2}{|\mathrm{r}_i - \mathrm{r}_j|}\right]\Psi(\mathrm{r}_1, \mathrm{r}_2, \cdots \mathrm{r}_N) = E\Psi(\mathrm{r}_1, \mathrm{r}_2, \cdots \mathrm{r}_N) \qquad (1.27)$$

where the first term is the individual electronic kinetic energies, the 2nd term is the interaction between the i^{th} electron and the nuclei, and the 3rd term is the interaction between electrons. Due to the electron-electron interaction, the equation cannot be separated to obtain independent equations in the coordinates of the individual electrons.

In the Hartree-Fock approximation, we must consider linear combinations of such the product wavefunctions where the entire wavefunction changes sign under the interchange

of any two electrons. The antisymmetric wavefunctions may be taken as a Slater determinant,

$$\Psi(r_1, r_2, \cdots r_N) = \frac{1}{N!}\begin{vmatrix} \psi_1(r_1) & \psi_1(r_2) & \cdots & \psi_1(r_N) \\ \psi_2(r_1) & \psi_2(r_2) & \cdots & \psi_2(r_N) \\ \cdots & \cdots & \cdots & \cdots \\ \psi_N(r_1) & \psi_N(r_2) & \cdots & \psi_N(r_N) \end{vmatrix} \tag{1-28}$$

When we postulate a N-electron system and it acts like variational calculation on Eq. 1.27 (Hartree approximation), this may write the optimized one-electron problem, the Hartree-Fock equations:

$$\left[-\frac{\hbar^2}{2m}\nabla^2 + V(r) + \sum_j e^2 \int \frac{\psi_j^*(r')\psi_j(r')d\tau'}{|r-r'|}\right]\psi_i(r) - \sum_j e^2 \psi_j(r) \int \frac{\psi_j^*(r')\psi_i(r')d\tau'}{|r-r'|} = \varepsilon_i \psi_i(r). \tag{1-29}$$

This is very approximate solutions to the initial equation but an complete solution would require an infinite series of Slater determinants. The last term i.e.,

$$-\sum_j e^2 \psi_j(r) \int \frac{\psi_j^*(r')\psi_i(r')d\tau'}{|r-r'|} \tag{1-30}$$

is called "exchange interaction" which is different from the 3rd term i.e., direct interaction. The exchange interaction term is purely coulombic at origin and develops from the correlated motion of the electrons due to the antisymmetry of the wavefunction. Using annihilation operators, c and creation operator, c^+, the Slater determinant can be rewritten as

$$|\Psi\rangle = c_{k_N}{}^+ c_{k_{N-1}}{}^+ \cdots c_{k_2}{}^+ c_{k_1}{}^+ |0\rangle \tag{1-31}$$

and

$$\langle\Psi| = \langle 0| c_{k_1} c_{k_2} \cdots c_{k_{N-1}} c_{k_N} \tag{1-32}$$

where $\langle 0|$ is vacuum state. The electron Hamiltonian H_e with eigenstates k_i of energy ε_{k_i}, in the second-quantized form, can be written as

$$H_e = \sum_k \varepsilon_k c_k^{+} c_k \tag{1-33}$$

When we introduce a potential, V, by each of the electrons, the potential forms

$$V(r) = \sum_{k,k'} \langle k'|V|k\rangle c_k^{+} c_k \tag{1-34}$$

where the number $\langle k'|V|k\rangle$ is the matrix components of the potential between the one-electron eigenstates,

$$\langle k'|V|k\rangle = \int \psi_{k'}^{*}(r) V(r) \psi_k(r) d^3r \tag{1-35}$$

The diagonal terms, $\mathbf{k}' = \mathbf{k}$, sum to the zero-order energies, ε_k while the off-diagonal matrix components relate many electron wavefunctions where one of the electrons has changed its state. The interaction between electrons in 2nd quantized form can be written as

$$V(r_1 - r_2) \rightarrow \frac{1}{2} \sum_{\substack{k_1,k_2 \\ k_3,k_4}} \langle k_4, k_3|V|k_2, k_1\rangle c_{k_4}^{+} c_{k_3}^{+} c_{k_2} c_{k_{13}} \tag{1-36}$$

where $\mathbf{k}_i$ are quantum numbers for any complete set of one-electron states which may or may not be plane waves, and spin quantum number.

Now for many-electron system, if we approximate the true state of the system with a single Slater determinant $|\Psi\rangle = \prod_{k_i} c_{k_i}^{+} |0\rangle$, from the Hartree-Fock approximation the energy of the electron-electron interaction is

$$\frac{1}{2}\langle\Psi|V(r_1-r_2)|\Psi\rangle=\frac{1}{2}\prod_{k_i}\langle 0|c_{k_i}\sum_{k,k'}{}'\left(\begin{array}{l}\langle k',k|V|k',k\rangle c_{k'}{}^{+}c_k{}^{+}c_{k'}c_k \\ \quad+\langle k',k|V|k',k\rangle c_{k'}{}^{+}c_k{}^{+}c_{k'}c_k\end{array}\right)c_{k_i}{}^{+}|0\rangle.$$

(1-37)

The direct interaction $\langle k',k|V|k',k\rangle$ can be included with the external potential. The term, $\langle k',k|V|k',k\rangle$, is the exchange energy and appears only if **k** and **k**′ have the same spin. Thus,

$$\langle k',k|V|k',k\rangle=\int\psi^*_{k'}(r_1)\psi^*_k(r_2)V(r_1-r_2)\psi_{k'}(r_2)\psi_k(r_1)d^3r_1d^3r_2 \qquad (1\text{-}38)$$

This matrix term is crucial term to be considered how exchange interaction may form magnetism. For example, for parallel spin, the exchange term gives rise to reduce the energy since $\langle k',k|V|k',k\rangle$ is positive and $c_{k'}{}^{+}c_k{}^{+}c_{k'}c_k=-n_{k'}n_k$ is negative.

If we consider the spin-dependent interaction between single electrons, the Hamiltonian, H_{ex}, is

$$H_{ex}=-\sum_{i>j}J_{ij}S_i\cdot S_j. \qquad (1\text{-}39)$$

where J_{ij} are called exchange integrals which is related to matrix elements in Hartree-Fock approximation, and the sum is over all pairs of electrons.

It is of great interest that if the two states are two electronic states in the free atom, for parallel spins by Hund's rule the sign of J tends to appear "positive"(FM spin alignment) and for antiparallel spins the one of J does to be "negative" (AF).

The spin operators of two-electron spin states can be written by a normalized by vectors, $\begin{pmatrix}1\\0\end{pmatrix}$ for spin-up and $\begin{pmatrix}0\\1\end{pmatrix}$ for spin-down. Pauli spin matrices are also

$$S_i^x = \frac{1}{2}\sigma_x = \frac{1}{2}\begin{pmatrix} 0 & 1 \\ 1 & 0 \end{pmatrix}_i, S_i^y = \frac{1}{2}\sigma_y = \frac{1}{2}\begin{pmatrix} 0 & -i \\ i & 0 \end{pmatrix}_i, S_i^z = \frac{1}{2}\sigma_z = \frac{1}{2}\begin{pmatrix} 1 & 0 \\ 0 & -1 \end{pmatrix}_i$$

Therefore,

$$S_i \cdot S_j = S_i^x S_j^x + S_i^y S_j^y + S_i^z S_j^z \tag{1-40}$$

For example, with $S_i^x = \begin{pmatrix} 1 \\ 0 \end{pmatrix}_i = \frac{1}{2}\begin{pmatrix} 0 \\ 1 \end{pmatrix}_i$,

$$S_i \cdot S_j \begin{pmatrix} 1 \\ 0 \end{pmatrix}_i \begin{pmatrix} 1 \\ 0 \end{pmatrix}_j = \frac{1}{4}\begin{pmatrix} 0 \\ 1 \end{pmatrix}_i \begin{pmatrix} 0 \\ 1 \end{pmatrix}_j - \frac{1}{4}\begin{pmatrix} 0 \\ 1 \end{pmatrix}_i \begin{pmatrix} 0 \\ 1 \end{pmatrix}_j + \frac{1}{4}\begin{pmatrix} 1 \\ 0 \end{pmatrix}_i \begin{pmatrix} 1 \\ 0 \end{pmatrix}_j = \frac{1}{4}\begin{pmatrix} 1 \\ 0 \end{pmatrix}_i \begin{pmatrix} 1 \\ 0 \end{pmatrix}_j$$

$$S_i \cdot S_j \begin{pmatrix} 1 \\ 0 \end{pmatrix}_i \begin{pmatrix} 0 \\ 1 \end{pmatrix}_j = \frac{1}{4}\begin{pmatrix} 0 \\ 1 \end{pmatrix}_i \begin{pmatrix} 1 \\ 0 \end{pmatrix}_i + \frac{1}{4}\begin{pmatrix} 0 \\ 1 \end{pmatrix}_i \begin{pmatrix} 1 \\ 0 \end{pmatrix}_i - \frac{1}{4}\begin{pmatrix} 1 \\ 0 \end{pmatrix}_i \begin{pmatrix} 0 \\ 1 \end{pmatrix}_j$$

As the x and y components of the dot product have flipped both spins and orthogonality properties use, the z component alone appears to expectation values as

for parallel spins,

$$\left\langle \begin{pmatrix} 1 \\ 0 \end{pmatrix}_j \begin{pmatrix} 1 \\ 0 \end{pmatrix}_i \middle| H_{ex} \middle| \begin{pmatrix} 1 \\ 0 \end{pmatrix}_i \begin{pmatrix} 1 \\ 0 \end{pmatrix}_j \right\rangle = -\frac{1}{4} J_{ij} \tag{1-41}$$

and for antiparall spins,

$$\left\langle \begin{pmatrix} 0 \\ 1 \end{pmatrix}_j \begin{pmatrix} 1 \\ 0 \end{pmatrix}_i \middle| H_{ex} \middle| \begin{pmatrix} 1 \\ 0 \end{pmatrix}_i \begin{pmatrix} 0 \\ 1 \end{pmatrix}_j \right\rangle = +\frac{1}{4} J_{ij} \tag{1-42}$$

To solve the many-electron problem, these matrix elements with exchange in Hartree-Fock approximation must be identified with the exchange integral <ij|V|ij> and an additional direct term given by Heisenberg exchange.

To get the spin Hamiltonian, at first consider a two-electron system where each individual electron spin operator satisfies $S_i^2 = \frac{1}{2}\left(\frac{1}{2}+1\right) = \frac{3}{4}$, and the total spin **S** is

$$S = (S_1 + S_2)^2 = \frac{3}{2} + 2S_1 \cdot S_2. \quad (1\text{-}43)$$

The eigenvalue of the operator $S_1 \cdot S_2$ is –3/4 in the singlet (S = 0) state and +1/4 in the triplet (S = 1) states. The following spin Hamiltonian is

$$H^{spin} = \frac{1}{4}(E_s + 3E_t)^2 - (E_s - E_t)S_1 \cdot S_2 \quad (1\text{-}44)$$

where E_s is eigenvalue in the singlet state, and E_t is eigenvalue in the triplet states. To redefine the zero of energy, the constant $(E_s + 3E_t)/4$ common to all four states may be ignored. The spin Hamiltonian can be rewritten as

$$H^{spin} = -JS_1 \cdot S_2, \quad J = E_s - E_t. \quad (1\text{-}45)$$

Because H^{spin} is the scalar product of the vector spin operators $\mathbf{S_1}$ and $\mathbf{S_2}$, there are parallel spin arrangements if J is positive and antiparallel ones if J is negative. Of course the signs of J depend upon the energy level of E_s and E_t, implying that the spins are parallel in the triplet state and antiparallel in the singlet. For a large number of spins system, the spin Hamiltonian for the two-spin case can be summed over all pairs of ions as

$$H^{spin} = -\sum J_{ij} S_i \cdot S_j.$$

1.5.2 Molecular-Field Approximation and the Ferromagnetic Transition

In 1907, Weiss investigated ferromagnetism, called the molecular-field approximation (MFA). [111] He was trying to understand how MFA originates from Heisenberg exchange. The exchange Hamiltonian in a self-consistent field can be written as

$$H_{ex} = -\sum_{i>j,j} J_{ij} S_i \cdot S_j \approx -\sum_k \left(\sum_{i>k} J_{ik} \langle S_i \rangle \cdot S_k + \sum_{j<k} J_{kj} S_k \cdot \langle S_j \rangle \right)$$
$$= -\sum_k S_k \cdot \sum_i {}' J_{ik} \langle S_j \rangle \qquad (1\text{-}46)$$

where $\langle \mathbf{S}_j \rangle$ is the expectation value of the spin $\mathbf{S}_j$ and in a FM, it is a vector parallel to the total spin of the system; in a AF, it will be a vector parallel to the total spin of the system.

Now, it is of interest that the interaction between the magnetic moment of the ion and a magnetic field ($H \sim -\mu \cdot \mathbf{H}$ where μ is the magnetic moment for an ion), is $g\mu_0 \mathbf{S}$ where $\hbar$ is Planck constant, g is the gyromagnetic ratio (g = 2 for a free electron), and Bohr magneton, $\mu_0 = e\hbar/2mc$. Let's consider an effective magnetic field H_I, called the molecular field (or internal field). The exchange energy in the z-axis along $\langle \mathbf{S}_j \rangle$ is

$$H_{ex} = -\sum_i \left(g\mu_0 S_i^{\,z} \right) H_I \qquad (1\text{-}47)$$

where $H_I = \frac{1}{g\mu_0} \sum_j {}' J_{ij} \left(S_j^{\,z} \right)$ and is proportional and parallel to the magnetization per unit volume, $M_z = g \langle S_j^{\,z} \rangle \mu_0 / \Omega_0$.

With an applied field along z direction, the Hamiltonian is

$$H = -\sum_i \mu_i^{\,z} (H + H_I) \qquad (1.48)$$

where $\mu_i^{\,z} = -g\mu_0 S_i^{\,z}$.

To calculate the magnetization (magnetic susceptibility) in the function of the temperature and applied field, the magnetization summing over a unit volume is

$$M = \sum_i \mu_i^{\,z} = N \langle \mu^z \rangle \qquad (1\text{-}49)$$

where N is the number of ions per unit volume.

Using (1.48) and (1.49) with ordinary statistical mechanics,

$$\langle \mu^z \rangle = \frac{\sum_{\mu_z} \mu_z e^{(H_I+H)\mu_z/kT}}{\sum_{\mu_z} e^{(H_I+H)\mu_z/kT}} \tag{1-50}$$

where k is Boltzman constant and the sum over μ^z represents over possible spin orientations. Let's defind $y \equiv (H + H_I)/kT$.

$$\langle \mu^z \rangle = \frac{\sum_{\mu_z} \mu_z e^{\mu_z y}}{\sum_{\mu_z} e^{\mu_z y}},$$

It can be written as

$$\langle \mu^z \rangle = \frac{\partial}{\partial x}\left(\ln \sum_{-J}^{J} e^{\mu_z y} \right)$$

$$= \frac{\partial}{\partial x}\left(\ln \sum_{-J}^{J} e^{-Jx}\left(1 + e^{x} + e^{2x} + \cdots + e^{2Jx}\right) \right)$$

Using $\sinh x = (e^x - e^{-x})/2$, it can rewrite

$$\langle \mu^z \rangle = \frac{\partial}{\partial x}\left(\ln e^{-Jx} \frac{1 - e^{(2J+1)x}}{1 - e^{x}} \right)$$

$$= \frac{\partial}{\partial x}\left(\ln \frac{\sinh[(2J+1)/2]x}{\sinh(x/2)} \right)$$

$$\langle \mu^z \rangle = J\left[\frac{2J+1}{2J} \coth\left(\frac{2J+1}{2J} \right) y - \frac{1}{2J} \coth \frac{y}{2J} \right]$$

$$= JB_J(y)$$

where $y = J(H_I+H)/kT = Jx$ and $B_J(y)$ is called the Brillouin function. [112]

Therefore, the magnetization over a unit volume is

$$M = NJB_J(y).$$

For the simple example case of S = ½ and g = 2 system, $\mu^z = \pm \mu_0$ and

$$\langle \mu^z \rangle = \mu_0 \tanh \frac{(H_I + H)\mu_0}{kT}. \tag{1-51}$$

In no applied field, i.e. $H_I = 0$, the magnetization is

$$\begin{aligned} M &= N\mu_0 \tanh \frac{H\mu_0}{kT} \\ &\approx \frac{N\mu_0^2}{kT} H \end{aligned} \tag{1-52}$$

where last term is approximated for small field H (or high temperature). The susceptibility, χ is

$$\chi \approx \frac{N\mu_0^2}{kT} \tag{1-53}$$

When we write $\langle \mu^2 \rangle = (2\mu_0)^2 S(S+1) = 3\mu_0^2$, this equation can be the Curie law for magnetic susceptibility,

$$\chi = \frac{N\langle \mu \rangle^2}{3kT} \tag{1-54}$$

This is good for mild response in the application, such as paramagnetic susceptibility. Finally, if we include the molecular field, $H_I = \lambda M$, the magnetization can be combined as

$$M = N\mu_0 \tanh \frac{(H + \lambda M)\mu_0}{kT}. \tag{1-55}$$

For a small H, the susceptibility is

$$\chi = \frac{N\mu_0^2}{kT - N\mu_0^2 \lambda}. \tag{1-56}$$

This leads the Curie-Weiss law in terms of $\langle \mu \rangle^2$ as follows,

$$\chi = \frac{N\langle \mu^2 \rangle}{3k(T-\theta)} \tag{1-57}$$

where the Curie temperature θ is $\chi = \frac{N\langle \mu^2 \rangle \lambda}{3k}$ and this is a good expression for the magnetic susceptibility of ferromagnetic materials above θ where the magnetization is small.

1.5.3 Magnetic Phenomena (Experimental Observations)

In the broad sense, doped transition metals have two interesting parts: First, non-interacting or very dilute 3d-magnetic impurities (= doped) embedded in a non-magnetic host, can exhibit the Kondo effect in which a localized antiferromagnetic interaction of the isolated impurities spins with the surrounding conduction electrons. Second, the impurity spin-spin interactions give a large arrangement of moments, called ferromagnetism (FM); and lesser amount of moments are antiferromagnetism (AF), paramagnetism, canted ferromagnetism (CAF), cluster glass (CG) and spin glass (SG) [see Fig. 1.24 and Fig. 25].

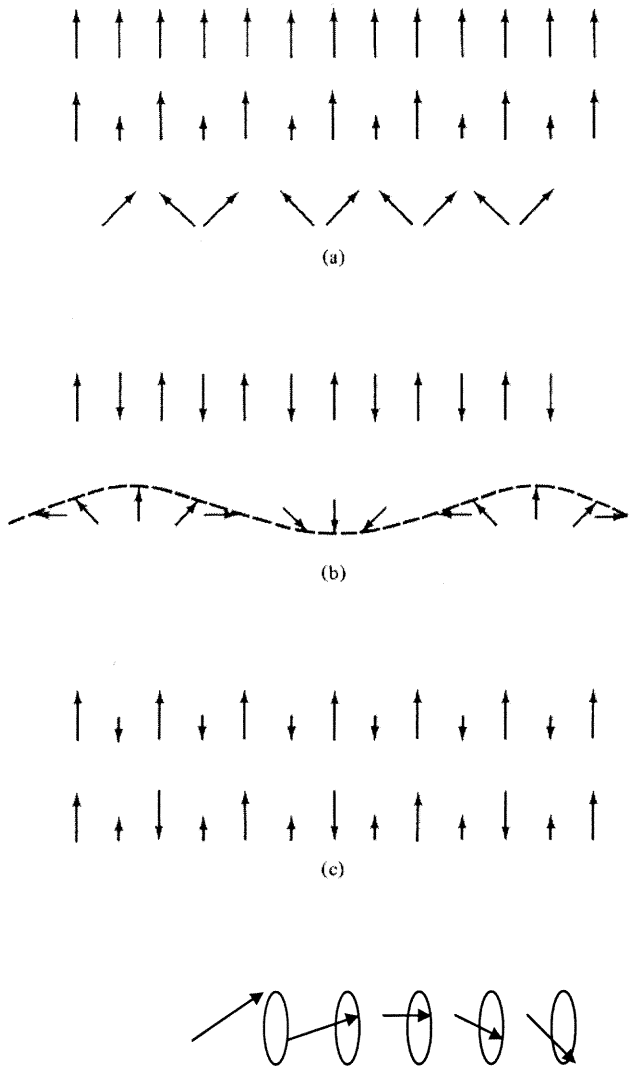

Fig. 1.24 Magnetic spin arrangements. The general 1-dimensional diagrams are shown for (a) ferromagnetic (b) antiferromagnetic, (c) ferromagnetic orderings, and hellical spin arrays. [113]

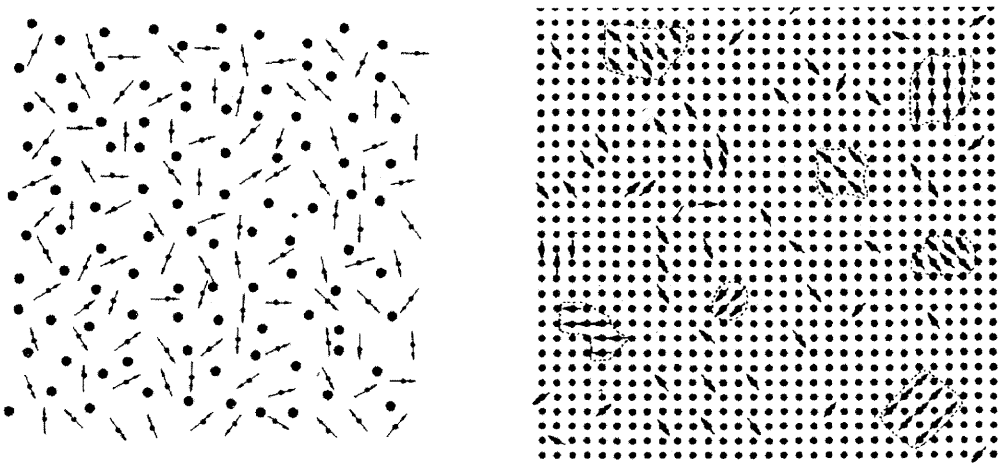

Fig. 1.25 Two dimensional schematic diagram for spin glass and cluster glass. (a) spin glass with 50% occupied magnetic moments (left side) (b) cluster glass (mictomagnet) (right side).[114]

These magnetic properties depend significantly on the conduction electrons to propagate the magnetic interactions over large distances. The difference states from FM to SG are governed by the magnetic behavior of these itinerant electrons. For smaller concentrations-longer distances between impurities, the interaction has an oscillatory nature and SG ordering will probably dominate rather than ferromagnetic ordering with large concentrations. For each system, a percolation limit exists at a critical concentration above a long range ordering. When the percolation limit is increasing, then magnetic clusters are formed and randomly freeze out at critical temperatures, i.e. mictomagnetism or cluster glass.

A property exhibited by materials, whose atoms or ions tend to assume an ordered but nonparallel arrangement in zero applied field below a certain characteristic temperature known as the Néel temperature. Usually within a magnetic domain, a substantial net magnetization results from the antiparallel alignment of neighboring nonequivalent sublattices. The macroscopic behavior is similar to ferromagnetism.

Above the Néel temperature, these substances become paramagnetic. The Néel temperature defines the temperature at which ferrimagnetic and antiferromagnetic materials become paramagnetic (see Fig. 1.26). The Curie temperature defines the temperature above which a ferromagnetic material loses its permanent magnetism. In minerals, lightening often flash-heats minerals above their Curie temperatures, effectively resetting the magnetic fields trapped in lava flows.

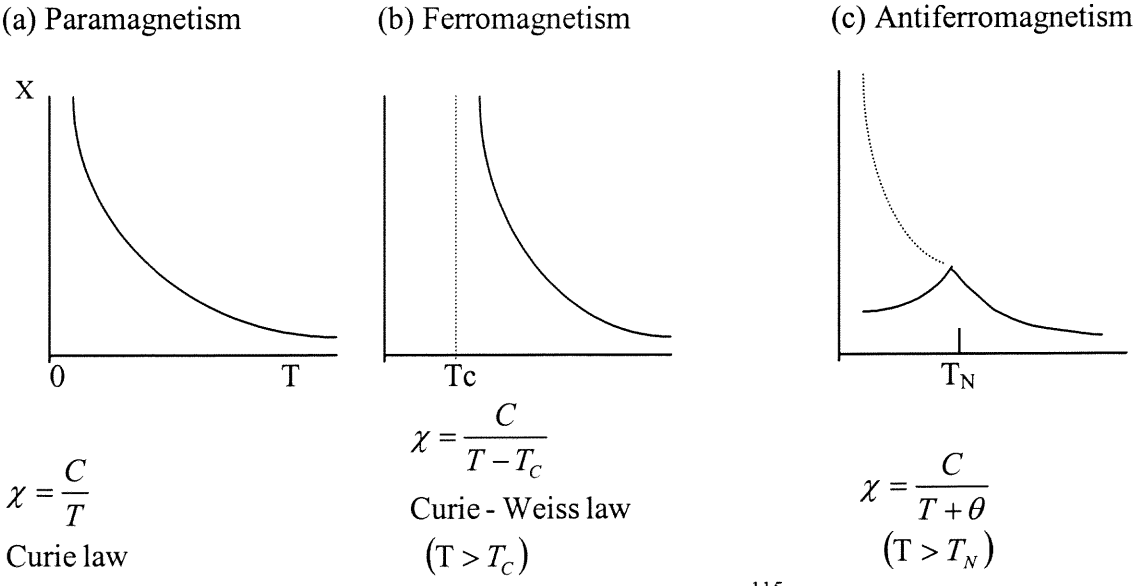

Fig. 1.26 Susceptibility vs. T in paramagnetism, FM, AF. [115]

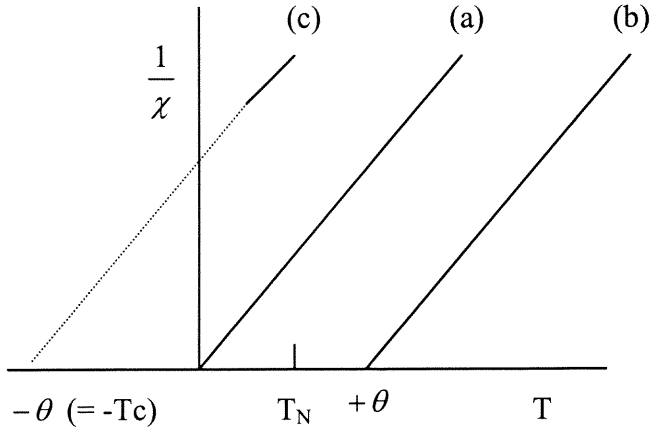

Fig. 1.27 Schematic diagram $1/\chi$ versus temperature. Note that the line (a) shows $\chi = C/T$ (Curie's law), the line (b) shows $\chi = C/(T - T_C)$ (Curie-Weiss law), and the line (c) displays $\chi = C/(T + \theta)$. [116]

1.5.4 Spin Glass/Cluster Glass

Magnetic systems exhibit different kinds of ordering as a function of the temperature and external magnetic field. Spin glasses have been heavily studied but are not well understood for a theoretical perspective. The simplest model for a spin glass is a collection of spins (i.e. magnetic moments) with random alignment at low temperature (see Fig. 1.25). There may be competition among the different interactions between the moments, in the sense that no single configuration of the spins in uniquely favored by all interactions (this is commonly called `frustration'). Second, these interactions must be at least partially random. Spin glass behavior has been seen in virtually every kind of systems which satisfies these requirements.

Experimentally, spin glasses (SG) exhibit a classic set of properties: (a) the low-field, low-frequency ac susceptibility $\chi_{a.c.}(T)$ show a cusp at a temperature T_g and this cusp becomes flattened with a field as small as 50 Gauss. The nonlinear susceptibility diverges. (b) No sharp anomaly is shows in the specific heat. (c) below T_g, the magnetic response is history-dependent. In other words, the susceptibility measured in a field-cooled sample is higher than in a zero-field cooled. (d) below T_g, the magnetization decreases slowly as a function of time. (e) below T_g, a hysteresis curve shifted from the origin appears, (f) below T_g, no magnetic Bragg scattering, which is the characteristic of long-range order (LRO), is observed in neutron scattering experiments, thereby demonstrating the absence of LRO. (g) susceptibility begins to deviate from the Curie law at temperatures $T >> T_g$. [117]

The group of SG systems composes the noble metal alloys and transition metal alloys.. The classical) spin glasses are $Cu_{1-x}Mn_x$ and $Au_{1-x}Fe_x$. These noble-metal alloys

are usually called canonical spin glasses. Other compounds which are spin glasses are $Eu_xSr_{1-x}S$ (a semiconductor) and $La_{1-x}Gd_xAl_2$ (a metal).

On the other hand, the spin glass region in AuFe alloys usually exists in under about 10% of impurities. For higher concentration, there is an increasing statistical probability of on impurity having another as a first or second nearest neighbors. Therefore, there is a tendency to form magnetic clusters due to concentration fluctuations in the alloy and this region is known as the mictomagnetic, cluster spin glass, or cluster glass (CG). [118] Detailed identifications between SG and CG will be discussed in introduction of Chapter 7.

CHAPTER 2

BACKGROUND INFORMATION AND PHYSICS OF CMR SYSTEMS

2.1 Background Information on CMR Systems

As a function of temperature, pressure, doping, and A^{3+}/A'^{2+}-site ionic radius, perovskite mixed-valent manganites $A^{3+}_{1-x}A'^{2+}_{x}MnO_3$ (A^{3+} = Bi, La, Pr, Nd, etc., and A'^{2+} = Ca, Sr, Ba, Pb, etc.) show intriguing properties such as structural transformations, charge ordering (CO), metal-insulator transitions, and magnetic ordering (ferromagnetic (FM) - antiferromagnetic (AF)) transformations. [41, 42, 43, 119] In addition to the rich basic physics exhibited by these materials, there is also much interest from the technological perspective because they are known to exhibit "colossal" magnetoresistance (CMR). [87]

By virtue of the total miscibility of its end point compounds, the $La_{1-x}Ca_xMnO_3$ system has been widely studied.[44,75,76,120,121,122] A schematic phase diagram for this system is reproduced in Fig. 2-1. [123]

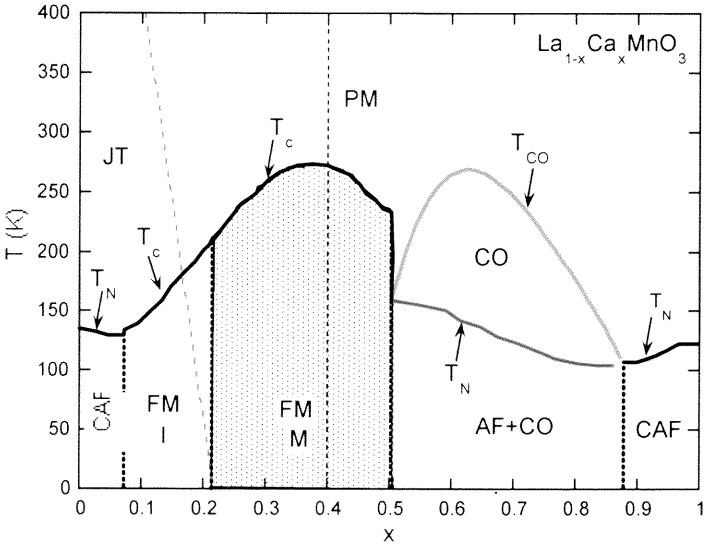

Fig. 2.1 Phase diagram of $La_{1-x}Ca_xMnO_3$.

The heavy dashed line indicates the low-x limit of the static Jahn-Teller ordered (JTO) regime. Despite the low concentration disappearance of this particular JTO phase, dynamic JT interactions and the incorporation of static JT ordered components are important over most of the phase diagram. An extended phase diagram [see Fig.2-5] of the prototypical $La_{1-x}Ca_xMnO_3$ (LCMO) system has been developed and structural, magnetic, and transport measurements have been performed. [1, 124]

Evidence [53] of change ordered [Mn^{3+} and Mn^{4+} cation ordering, see Fig. 2-2 and 2-3] stripes in $La_{0.33}Ca_{0.67}MnO_3$ [see Fig. 2-2] and in $La_{0.5}Ca_{0.5}MnO_3$ (see Fig. 2-3) was also observed.

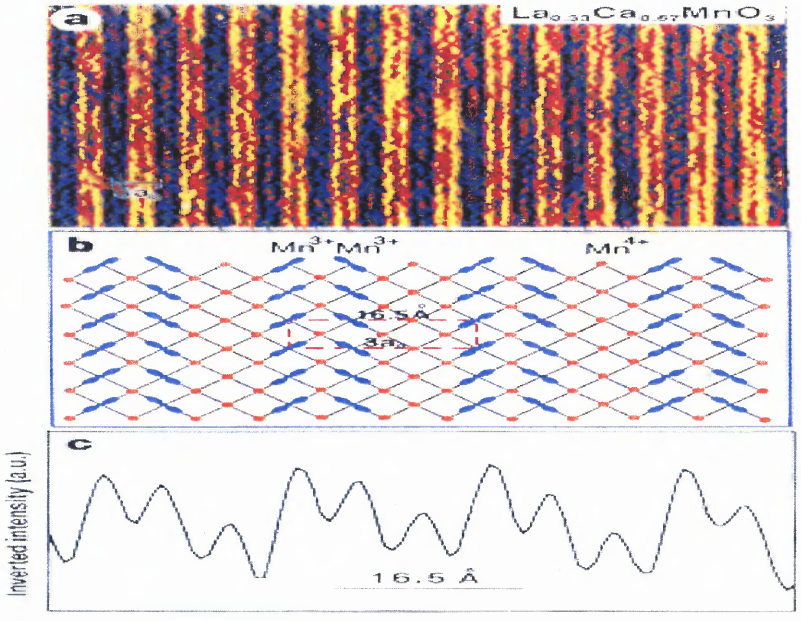

Fig. 2.2. Evidence of charge-ordered stripes in $La_{0.33}Ca_{0.67}MnO_3$ (a) A [001] zone-axis high-resolution lattice image obtained at 95K showing $3a_0$ pairing of Jahn-Teller stripes (JTS). (b) Schematic model in the a-b plane displaying the pairing of d_{z2} stripes on Mn^{3+} in orange. (c) Inverted intensity scan from a selected area in (a) (arbitrary units) where pairs of the strongest peaks are identified as $Mn^{3+}O_6$ JTS and the weaker peaks and valleys as $Mn^{4+}O_6$ stripes. [53]

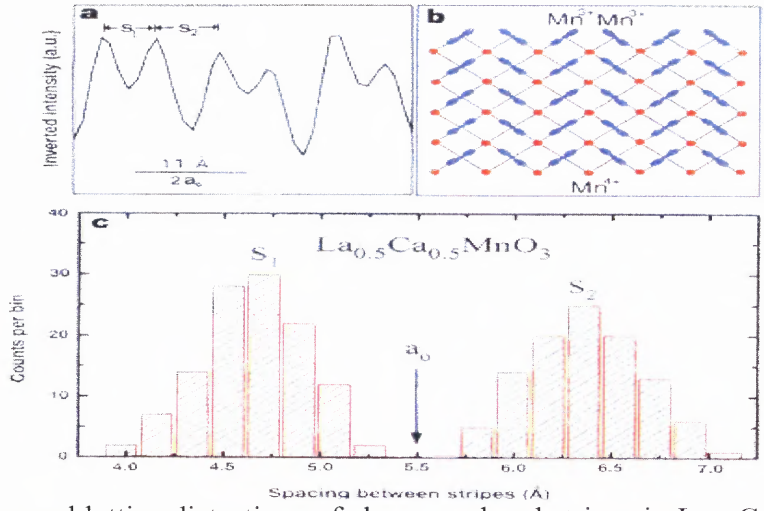

Fig. 2.3 Pairing and lattice distortions of charge-ordered stripes in $La_{0.5}Ca_{0.5}MnO_3$ [5]. (a) Inverted intensity scan, (b) schematic model showing ordering of JTS, (c) a histogram of two distinct spacings, S_1 for paired stripes (contractions) and S_2 for non-paired stripes are respectively displayed.

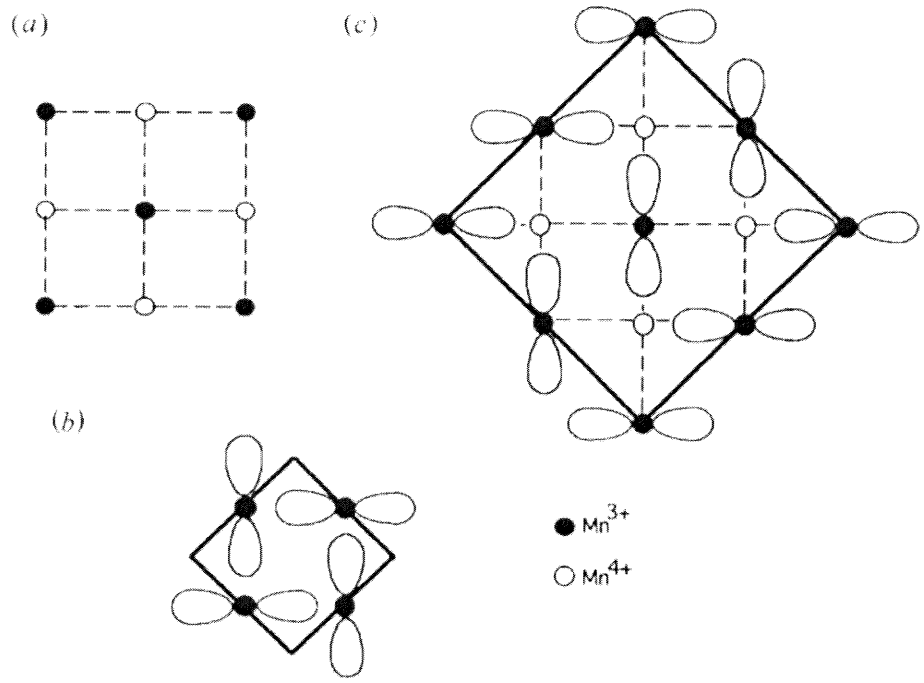

Fig. 2.4 (a) Charge ordering of Mn^{3+} and Mn^{4+} in half mixed crystal (x = ½). (b) Orbital ordering of the d_{z^2}. [125]

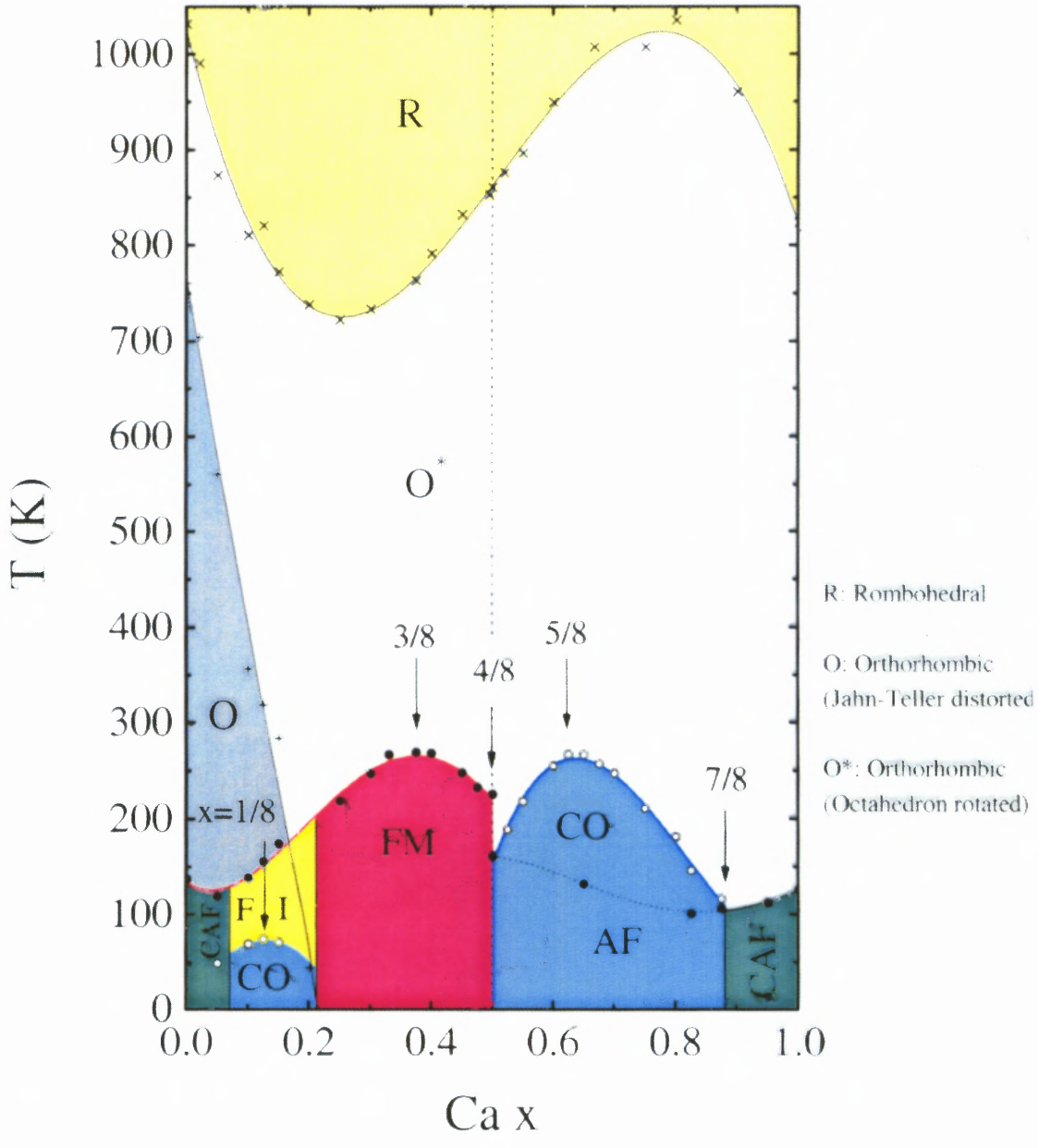

Fig. 2.5 Extended phase diagram of $La_{1-x}Ca_xMnO_3$. [12]

For $0 < x < \sim 0.21$, the system is an insulator (I) with a canted antiferromagnetic (CAF) or ferromagnetic ground state. For the range, $\sim 0.21 < x < 0.5$, a ferromagnetic metallic (FM) ground state occurs and undergoes a concomitant metal-to-insulator (MI) and FM-to-paramagnetic (PM) transformation in the temperature range 150 K-250 K. [42, 44, 120]

Near $x = 0.5$, a competition between a higher temperature AF-M phase and a lower temperature CO-AF-I phase results in a first order transition.[121,122,75] In the $0.50 < x < 0.875$ region, the materials are insulators with a charge/orbital (CO) ordered and AF ordered ground state which, upon increasing the temperature, first loses its AF ordering (at T_N) and then, at a higher temperature (T_{co}), its CO ordered. [69,121] Above $x \sim 0.875$ it is believed that these materials are canted antiferromagnets (CAF). Recently Neumeier *et al.*[126] [see Fig. 2-6] suggested that electron-doped $CaMnO_3$ in $0.8 \leq x \leq 1.0$ of $La_{1-x}Ca_xMnO_3$ exhibits magnetic phase segregation with strong competition between local FM and G-type AF regions. Assuming the orbital angular momentum is quenched, the moments have a spin $S_{3+} = 2$ for Mn^{3+} in the orientation opposite to the $S_{4+} = 3/2$ for Mn^{4+}, which leads to in equivalent magnetic sites in a localized region, or a local ferromagnetic region with the AFM background. The lower line in Fig. 2-6-region I of a net ferromagnetic saturation moment per Mn ion at T = 0K is modeled by considering

$$M_{sat}(OK) = g\,(S_{3+} - S_{4+})\mu_B x = 2\times(2-3/2) = \mu_B x$$

where g is 2. [127] On the other hand, the upper line of the strongly Hund's coupled mobile electron is

$$M_{sat}(OK) = g\,(S_{3+} - S_{4+})\mu_B x = g(2 + 3/2)\mu_B x = g(7/2)\mu_B x.$$

while the a 180°-spin-flip is based on removing n Mn^{4+} moments from an AFM lattice out of N Mn^{4+} moments: $M_{sat}(OK) = g\,(6/2)\mu_B(n/M)$.

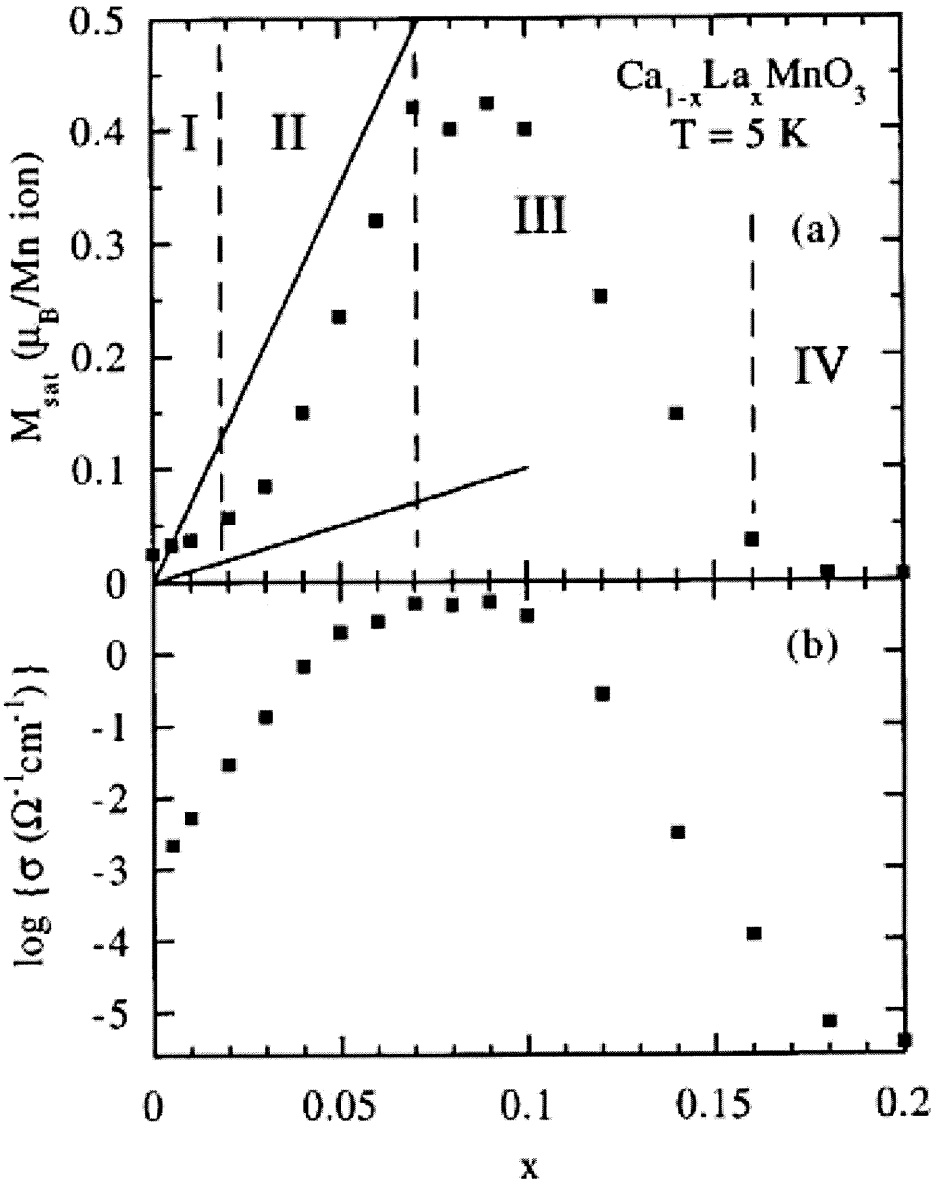

Fig. 2.6 Magnetic saturation moment at 5 K versus La doping x. Note that region I shows G-type AFM and local ferrimagnetism, region II indicates local FM regions with G-type AFM, and region IV displays C-type AFM. [126]

Since the seminal work of Goodenough [76] the interesting charge/orbital ordered phases of these materials have been an area of continually evolving experimental and theoretical work in terms of: the degree of Mn^{3+}/Mn^{4+} order; the orbital orientational ordering of the

Mn^{3+}-like Jahn-Teller distorted sites; and the detailed incorporation of these local distortions into the long range ordered state.

As noted above, the x ~ 0.5 region of this system is particularly interesting because of the existence of the CO-AF-I and FM-M phase competition. [54] Charge/orbital ordering has also been observed in many other systems such as; $Pr_{0.5}Sr_{0.5}MnO_3$,[54 128] $Pr_{0.5}Ca_{0.5}MnO_3$, [129] $Pr_{0.7}Ca_{0.3}MnO_3$, [129] $Nd_{0.62}Ca_{0.38}MnO_3$, [59] $Nd_{0.5}Sr_{0.5}MnO_3$, [60] $Tb_{0.5}Ca_{0.5}MnO_3$,[61] $La_{0.5}Sr_{1.5}MnO_4$, [62] $La_{1-x}Sr_xMnO_3 (0.11 \le x < 0.15)$, [63] as well as in broader regions of $La_{1-x}Ca_xMnO_3$, [64,120, 41(d)] $(Nd_{1-y}Sm_y)_{1/2}Sr_{1/2}MnO_3$, [66] $Pr_{1-x}Sr_xMnO_3$, [67] and $Nd_{1-x}Sr_xMnO_3$. [68]

From the experimental perspective, weak peaks in the electron diffraction images of $La_{0.5}Ca_{0.5}MnO_3$ are found on crossing (with temperature) into the charge ordered region. [64] The charge ordered regions are seen in dark-field images from superlattice peaks (resulting from differences in strain) that order in stripes. [76,128,64,69] In the strong charge ordering region of LCMO system, i.e. for $0.63 < x \le 0.67$, charge ordering is associated with significant increases in the sound velocity at 260 K. [69] These observations suggest a connection between the magnetic and charge ordering and the local structure (Mn-O bond distribution and Mn-Mn correlations) of charge ordered materials.

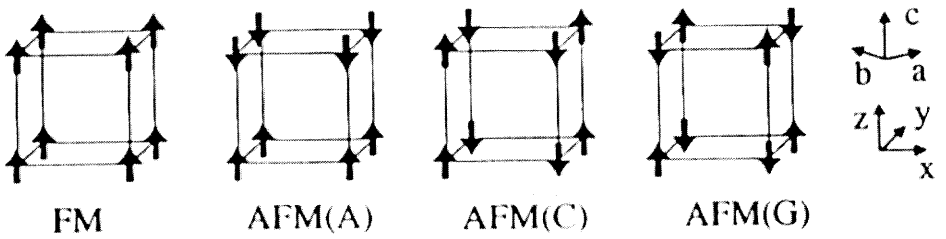

Fig. 2.7 Typical magnetic structure of the perovskite-type oxides AFM. The oxygen atoms have been left out for clarity. [130]

The fundamental origin of the magneto-structural properties of these materials is still evolving. The first model of magnetism in these materials was developed by Kramers [131], Zener. [132] Zener modeled an indirect exchange, called "double exchange" in which the e_g electron hops from a Mn^{3+} site to the neighboring oxygen site concomitant with a transfer of one electron for the oxygen site to a Mn^{4+} site, along the same chain.

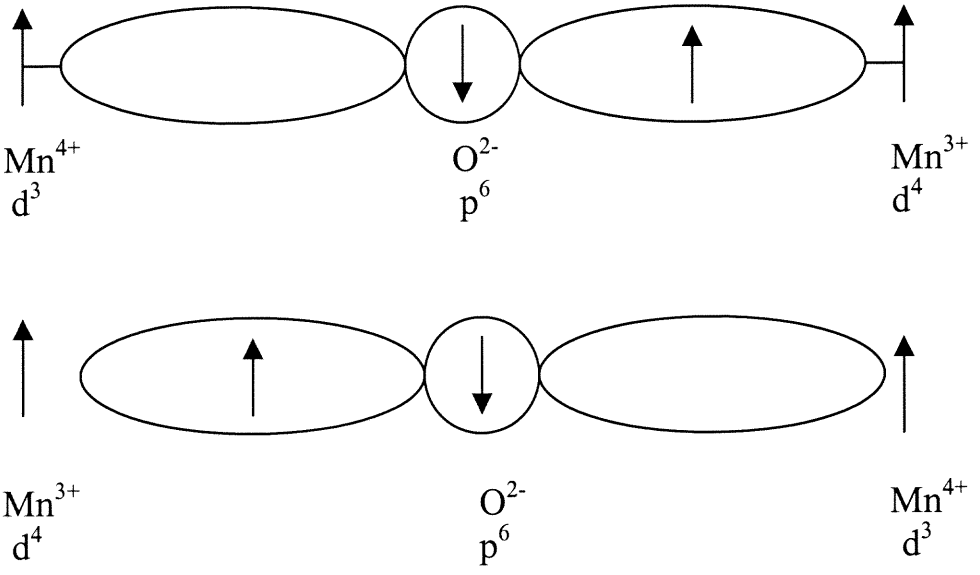

Fig. 2.8 Schematic configurations of the double-exchange meachanism. [133]

Kramers proposed an indirect "superexchange" which leads to an antiferromagnetic alignment of spins in the absence of Mn^{3+}/Mn^{4+} hopping. Millis *et al.*[102] pointed out the importance of local structural deformation (dynamic Jahn-Teller distortions) in the PM phase along with the quenching of these distortions in the FM-M phase.

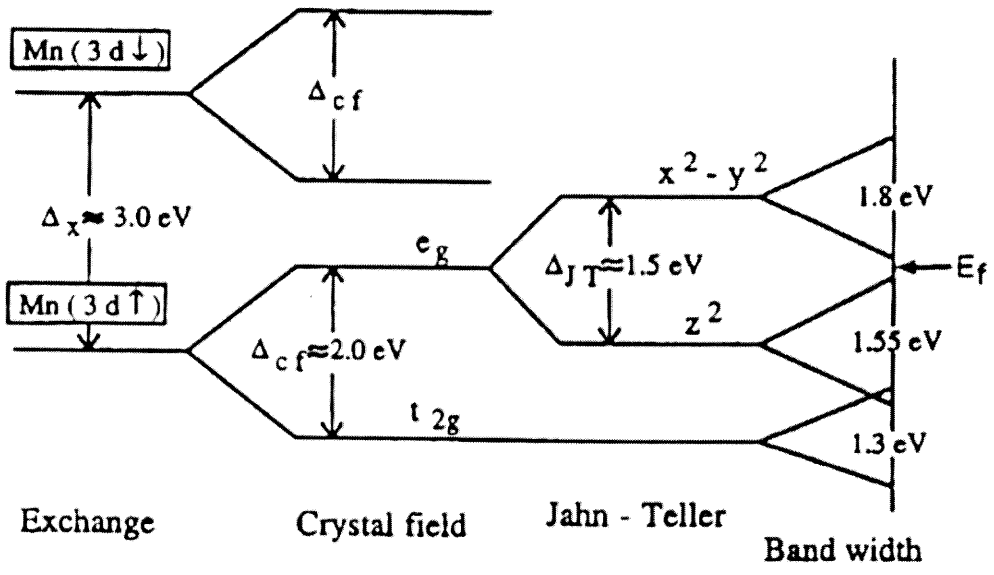

Fig. 2-9 Level splitting of the Mn(3d) orbitals for $LaMnO_3$ as obtained from the density-functional calculation (LDA).[134]

Millis showed that double exchange alone does not adequately predict the transport and magnetic properties of these materials. Many local structural studies have now been performed revealing strong correlations between the transport and magnetism on the ferromagnetic region of the manganites. [135] However, not much work has been done in the charge ordered and insulating regions.

2.2 Other Phase Diagrams

A systematic study of a broad range of materials in the system $L_{1-x}A_xMnO_3$ (L = Pr, Sm; A = Ca, Sr) was performed by Martin, Hervieu, and Raveau.[136] The properties of the manganites are known to vary with the manganese valence, and are also significantly affected by chemical factors such as ionic radii.[83,137] From the Table 1.1, we show the atomic radii of La, Pr, Bi, Sm, Ca and similar ionic radii. [see Fig. 2-10 and Fig. 2-11] The Sr atom is relatively large.[see Fig. 2-12] It was discovered that $Sm_{1-x}Ca_xMnO_3$ (SCMO) and $Pr_{1-x}Ca_xMnO_3$ (PCMO) fall into the class of manganites, which are insulators over the entire doping region while $Pr_{1-x}Sr_xMnO_3$ mimics the behavior of the classic $La_{1-x}Ca_xMnO_3$ system. The small-Ca-ion doped systems $Sm_{1-x}Ca_xMnO_3$, $Pr_{1-x}Ca_xMnO_3$ and $La_{1-x}Ca_xMnO_3$ all show a peak in low temperature magnetization near x ~ 0.9. The high net moments in these systems were attributed to cluster glass formation based on ac susceptibility measurements. It should be emphasized, however, that neutron scattering measurements on the material clearly showed the presence of G-type AF order coexisting with the FM-cluster glass behavior. Interestingly, even in the end-member, $CaMnO_3$, weak ferromagnetism is observed a long with G-type AF order.[138] The material $Bi_{1-x}Ca_xMnO_3$ (BCMO) was also found to exhibits a large moment near x ~ 0.875. A systematic study of the BCMO study will be carried out in this thesis.

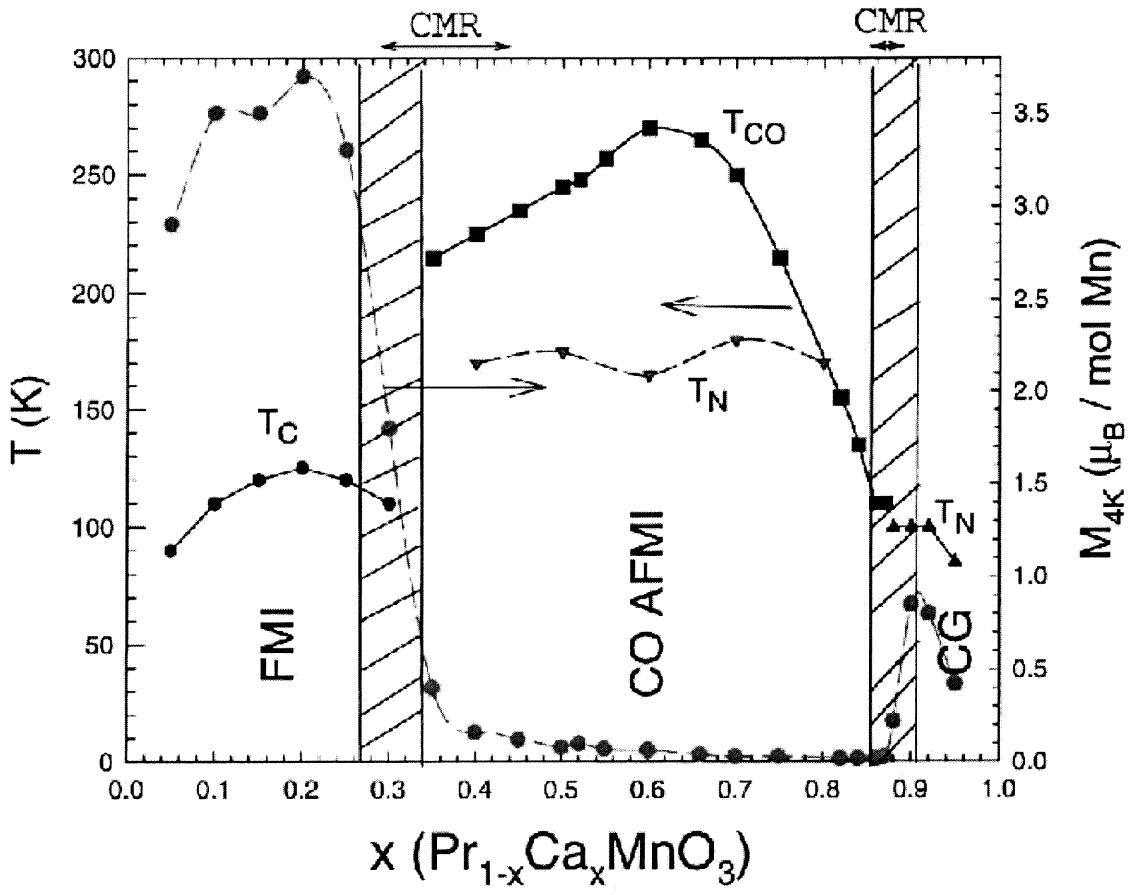

Fig. 2.10 Magnetic phase diagram of the $Pr_{1-x}Ca_xMnO_3$ system. [136]

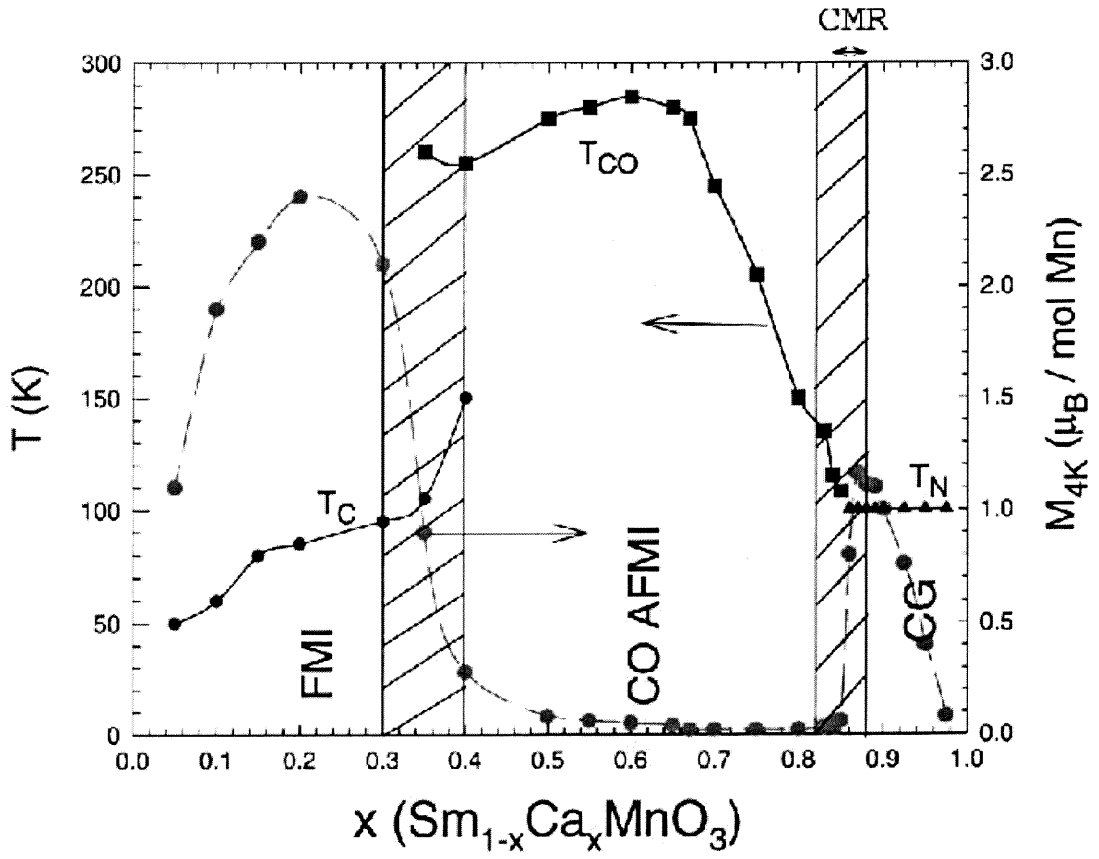

Fig. 2.11 Magnetic phase diagram of the $Sm_{1-x}Ca_xMnO_3$ system. The gray symbols and dashed line indicate the magnetization values at 4.2K in 1. 45T. The slashed regions are the intermediate phase transition area, and CMR region is labeled near x ~ 0.875. [136]

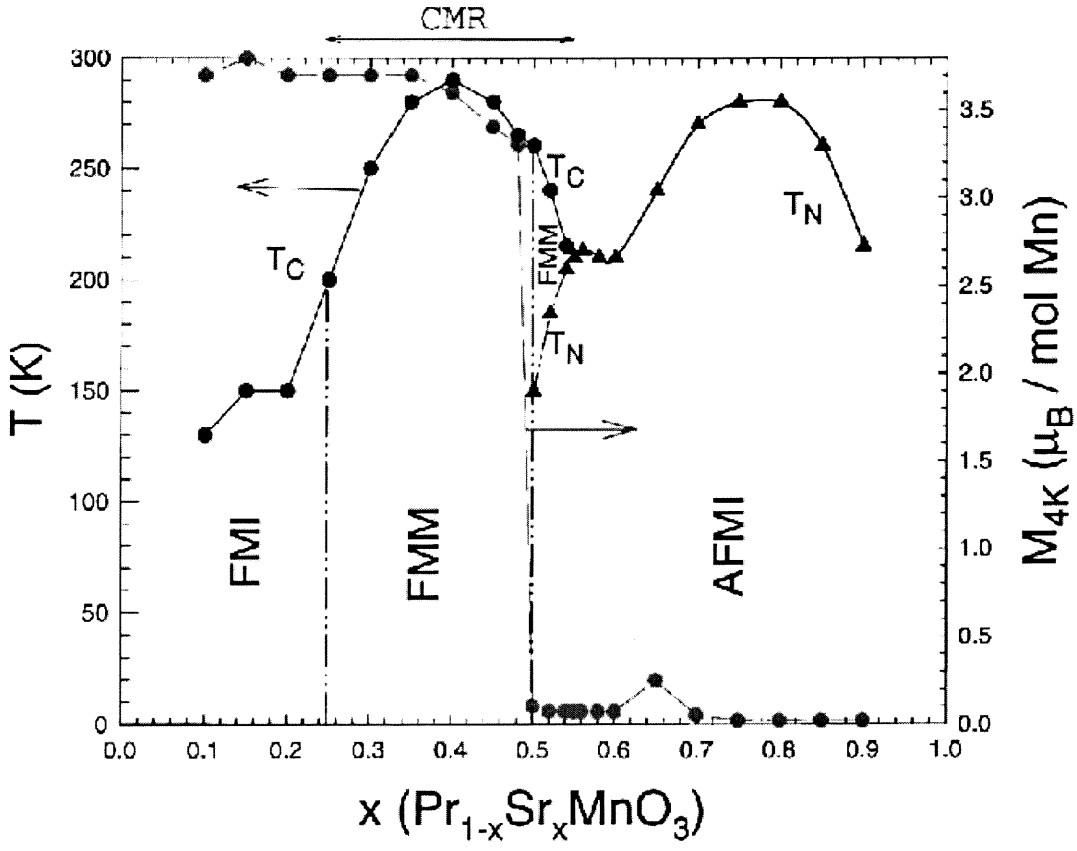

Fig. 2.12 Magnetic phase diagram of the $Pr_{1-x}Sr_xMnO_3$ system. [136]

CHAPTER 3

PREVIOUS WORK ON $Bi_{1-x}Ca_xMnO_3$ AND MAGNETIC-TRANSPORT PROPERTIES

3.1 PREVIOUS WORK ON $Bi_{1-x}Ca_xMnO_3$

A large, but somewhat scattered, body of work has been performed on the doped BCMO system. This work is summarized in this chapter.

Bokov *et al.* [139] studied the structural, magnetic and resisivity properties of the of BCMO system for $0.2 \leq x \leq 1.0$. Their phase included: two monoclinic phases and one orthorhombic phase as a function of temperature for $x < 0.4$; one of the monoclinic phases disappears for x above ~ 0.4; for $0.4 \leq x \leq 0.83$ a high temperature cubic phase transforms to a monoclinic low-temperature phase; and above $x \sim 0.83$ the more distorted monoclinic phase gives rise to a higher symmetry orthorhombic phase. Their magnetic measurements showed a FM-like Curie constant (θ) at high temperatures for all $x < 0.9$. For $x < 0.4$, the lattice parameter b is larger than the lattice parameter a, i.e., $b > a$, but for $x > 0.4$, $b < a$. Above this value the (θ_p) crosses over the Néel temperature and vanishes at $x = 1$. They suggested that for $x > 0.8$, because the Mn^{3+}concentration are relatively low, the resultant exchange interaction must be antiferromagnetic. Charge ordering was suggested to occur between $x = 0.2$ and $x = 0.4$. From resistivity measurements on $x = 0.4$, 0.5 and 0.7, a dramatic increase of resistivity at low temperature with Bi content was found. Consistent with the work of Chiba *et al.* [140], the reduction in resisivity occurs near the point where the net magnetization per Mn site is largest $x \sim 0.9$.

Chiba *et al.* [141] contrasted the magnetic, electrical and magnetoresistance properties of (Bi, AE)MnO_3 (AE = Ca, Sr) with those of LCMO in the highly substituted,

$x \geq 0.8$ regime. They noted that while the Bi- and Ca- based systems had the same crystal symmetry and weak ferromagnetism in this Ca-rich region, the magnetic moments in the Bi-system were larger than those in the La-system at the same Ca content. ($CaMnO_3$ was found to exhibit semi-conductor type behavior and is antiferromagnetic [142]) Chiba *et al.* [141] found that, the low temperature resistivity drops continuously when $CaMnO_3$ is doped with Bi^{3+} (electron doping) and reaches a minimum at $x = 0.875$, and exhibits a weak temperature dependence. At $x = 0.875$, the resistivity exhibits a very weak temperature dependence. At $x = 0.85$, a sharp increase in resistivity was found and suggested an anomalous magnetic transition temperature. The Néel temperature was found to be almost constant for $0.875 \leq x \leq 0.95$, while the paramagnetic Curie temperature decreased with increasing Ca doping. At $x = 0.875$, the Néel temperature approaches the paramagnetic Curie temperature and a saturation magnetization of $1.1\mu_B$ per Mn site is obtained (which is almost 1/3 of the fully aligned value, i.e., $3.1\mu_B$, suggesting spin canting). The maximum moment is achieved at this value of x.

Cheong and Hwang [143] expanded on the magnetic phase diagram of Chiba *et al.* by including the charge ordered temperatures for $0.5 < x < 0.7$. For this range, the charge ordered temperature is always above 300K. The maximum charge ordering temperature of 332 K was found to occur at $x \sim 0.63$. In addition, they also observed the same behavior of the charge ordering temperature in the LCMO system.

Bao *et al.* [119] performed neutron scattering, electron diffraction, and bulk magnetic measurements on single crystal BCMO ($0.74 \leq x \leq 0.82$). For $x = 0.82$, at the charge ordering temperature $T_{co} = 210$ K, a structural transition was found in which the lattice parameters change abruptly. This coincides with the transition from orthorhombic

to monoclinic II found by Bokov *et al.* [139] Above T_{co} ferromagnetic spin fluctuations were found by neutron diffraction. These fluctuations switch over to antiferromagnetic fluctuations below T_{co}. Strong competition between FM double exchange charge ordering and AF superexchange occurs in this system. The Néel temperature was found to be 160 K. The same trends were also found in earlier neutron diffraction measurements by Turkevich and Plakhtii [144] on $Bi_{0.15}Ca_{0.85}MnO_3$. They found the signature of the onset of antiferromagnetic Mn – Mn interactions at low temperatures as evidenced by appearance of {110} and {211} superstructure lines.

Optical conductivity measurements by Liu *et al.* [145] divide the phase diagram of this system into three distinct temperature regions. For $T > T_{co}$ ferromagnetic correlations exist, for $T_N < T < T_{co}$ phase separation into CO (AF) and ferromagnetic regions coexist and for $T < T_N$ a charge gap develops a long-range antiferromagnetism is observed.

Murakami *et al.* [146] found evidence for charge ordering in $Bi_{0.2}Ca_{0.8}MnO_3$ concomitant with 32- and 36-fold periodicity. The charge ordering temperature, T_{CO}, was found to be ~160 K and below T_{CO} the magnetic structure was transformed from paramagnetic to antiferromagnetic phase. Long-period structures with 32- and 36-fold periodicity associated with charge ordering in $Bi_{0.2}Ca_{0.8}MnO_3$ were found.

Utilizing high-pressure synthesis, Sugawara *et al.* [147] obtained the end member, $BiMnO_3$. It was found that, unlike $LaMnO_3$, $BiMnO_3$ is ferromagnetic with a Curie temperature of 103 K. The saturation magnetization was observed to be ~ $4\mu_B$ per Mn site. A distorted perovskite structure with a triclinic pseudo-unit cell was found.

In oxygen K-edge EELS measurement, Murakami *et al.* [148] explored changes in the near edge structure with temperature and doping. They associate the main line

transition with a 1s to hybridized O(2p)-Mn(3d) transition. The reduction in the main line intensity in going into the charge ordered region was associated with weakening of the O(2p)-Mn(3d) hybridization due to a distortion of the Mn-O-Mn bond angle resulting from charge ordering. The charge ordering was also detected by electron diffraction. The broad array of interesting properties suggests a deep correlation between the local structure and the magnetic and transport trends in the BCMO system.

High temperature structural studies of $BiMnO_3$ were recently performed by Faqir *et al.* [149] They reported that $BiMnO_3$ has structural phase transition from triclinic to tetragonal structure at 490°C in air and a ferromagnetic transition temperature (T_C) of 108 K. $BiMnO_3$ was found to decompose into Bi_2O_3 and $Bi_2O_3 \cdot 2Mn_2O_3$ at ~600°C .

Matsumoto *et al.* [150] measured a single phase region in $0.08 \leq x \leq 0.12$ of the 9R(= 9 layer rhombohedral structure) structure for the $Ba_{1-x}Bi_xMnO_3$ system. They concluded that the concentration at $x = 0.05$ obtained the optimal stabilization of 9R structure from the correlation between the average ionic radius of the Ba/Bi cation in the A site and Bi content.

Recently, Atou *et al.* reported powder neutron diffraction measurements of the structure of the ferromagnetic perovskite $BiMnO_3$ formed under high pressure. A distorted perovskite structure was found with monoclinic C2 space group symmetry. They suggested that, the distortions were caused by the polarized Bi $6s^2$ lone pairs. [147] The combined Jahn-Teller instability (Mn^{3+}) and lone pair induced distortions result in a highly disordered $BiMnO_3$ system with a range of Mn-O bonds between 1.78 and 2.32 Å. The origin of the ferromagnetic tendency is uncertain.

Recently, Ohshima *et al.* [151] prepared films of $BiMnO_3$ on $SrTiO_3$ substrates. Although the films exhibited the ferromagnetic behavior seen in the corresponding bulk material, the saturation moment of thick films ($M = 2.8\mu_B$) fell short of the bulk value ($M = 3.6\mu_B$). In addition, a strong dependence of the saturation moment on film thickness was found. Also, unlike the bulk material strong hysteresis was found in the film samples.

The broad array of interesting properties suggests a deep correlation between the long-range and local structure and the magnetic and transport trends in the BCMO system.

CHAPTER 4

FUNDAMENTALS OF TRANSPORT IN OXIDES

4.1 METAL-INSULATOR TRANSITIONS (MIT)

The distinguishing characteristic between a metal and an insulator can be established only at absolute zero temperature because when the temperature is not zero, thermal excitations allow an insulator to carry a current. It is natural that the ground state determines the metal and insulator states. Above T = 0K, the positive gradient of the temperature, i.e. dR/dT determines "metallic-like" and the negative one is "insulator-like". The MIT can be truly a transition between two distinct ground states forced by parameters. [152]

Metal-insulator transitions occur with large resistivity changes (greater than tens of orders of magnitude). These phenomena have been attracted because of intriguing phenomena and technological importance. A key issue to understanding MIT is the fact that there are phase transitions forced by a strongly correlated electron-electron interaction. The insulating state forced by the correlation effects is classified as the Mott Insulator. [153] Particularly near the phase-transition region, the metallic state displays fluctuations and orderings in the spin, charge, and orbital degrees of freedom. One interesting debate is related to interplay among spin, charge, and orbitals. There are several theoretical attempts such as Fermi-liquid theory that treats correlations connected adiabatically in the noninteracting picture. [154] For strong-coupling models that do not require Fermi-liquid theory, the Hubbard model and t-J models are scaling theory [155] of the transition are applied.

A theoretical understanding of the transition between the Mott insulator and metals was attempted by a simplified lattice fermion models, called "Hubbard model". [156] Mott took a lattice model with a single electronic orbital on each site. If there are no electron-electron interactions, the atomic orbitals of a single band could be overlapped. When two electrons with spin-up and spin-down occupy each site, the band becomes full. But if two electrons occupy the same site, then they might feel a significant Coulomb repulsion. Thus, Mott proposed the splitting of the band. The lower band electrons occupied in an empty site and the upper band electrons that occupied a site are already taken by another electrons, for example, when one electron is in a site, the lower band is full [see Fig. 4.1]. Then the system becomes an insulator. Figure 4.1 shows the representation of the intrinsic properties of materials such as insulator (usually above10^{14}ohm-cm), metal (~10^{-10} ohm-cm at T = 1K), semimetal, and semiconductor (10^{-2} to 10^{9} ohm-cm at room temperature) and details show the difference of energy bands gapped by certain range, called energy gaps or band gaps, in which no wavelike electron orbitals exist.

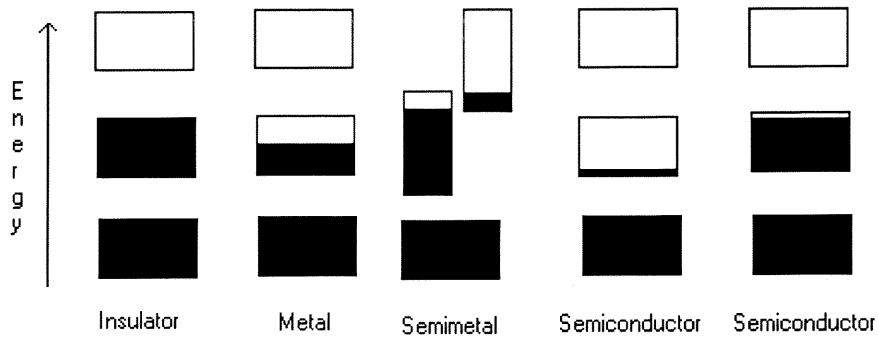

Fig. 4.1 Electron occupancy of allowed energy bands: insulator, metal, semimetal, semiconductors. [157] Note that for a semimetal (bismuth), a middle band is almost filled while the upper band is mostly empty at absolute zero. At absolute zero temperature a pure semicoductor (silicon etc.) shows an insulator. On the right-hand side, i.e. left of two semiconductor is the thermally excited state of carriers in a finite temperature. The last semiconductor exhibits the state of electron deficiency due to impurities. An orbital at energy ε Fermi energy at T = 0 K.

For an insulator, the Fermi level E_F is located at the middle of the valence band (lower) and the conduction band (upper). For the doped material, extra electrons are bound to conduction band, and the Fermi level shifts upward to the localized states near conduction band. The localized electron wave functions are overlapped and broaden. Then the Fermi level is inside the "impurity band", and therefore, the system becomes metallic.

Abnormal transport properties of the metallic state near the insulator transition are mostly found in transition metal oxides d-electron systems such as high T_C superconductivity in cuprates and colossal magnetoresistance (CMR) in manganites. Generally speaking, the theoretical parameters such as strong spin and orbital fluctuations, mass renormalization effects, incoherence of charge dynamics, and phase transitions in mainly varying band filling, bandwidth, and dimensionality are related to

experiment parameters for example, chemical composition, doping, pressure, temperature, and magnetic fields. Basically two distortion mechanisms from the ideal crystals are "disordered" and mesoscopic (= sub-micron) systems. The fluctuations are significantly increasing and diverging as the temperature decreases down to zero. Theoretically, Bloch's theorem itself could not explain it.

The disorder and electron-electron interaction are crucial factors in understanding MIT. Two models are initiated in electron localization. Mott [16(a)] proposed that a metal-insulator transition occurs only as a result of Coulomb repulsion among electrons when the potential energy of the electrons is greater than their kinetic energy. The phenomenon of Anderson localization [158] was founded for such a disorder system in the electrostatic potential caused by random impurities. This disorder state changes a system of non-interacting electrons into an insulating state. Anderson localization is based on the fact that the more disorder rises, the slower the diffusion of electrons gets until it suddenly stops completely. Such a transport is due to the tunneling of electrons through a barrier, and the resistance is known to change exponentially rather than just inversely as the length. The problem of coexistance of both disorder and interaction-induced effects is still unclear.

The theory implies that this phenomenon is involved in the quantum states of the system that localized electrons in some regions of the system, not just allowing extended states that characterized the diffusion regime. The phenomenon is known to metal insulator transition which attracts physical properties such as phase transitions, solid-liquid or ferromagnetic-paramagnetic and so forth.[159] The bands of d-electron systems are strongly affected by anisotropic crystal fields in solids. In the transition-metal, the

overlap indirect between d orbitals bridging ligand p orbitals (oxygen atom) [see Fig. 4.2].

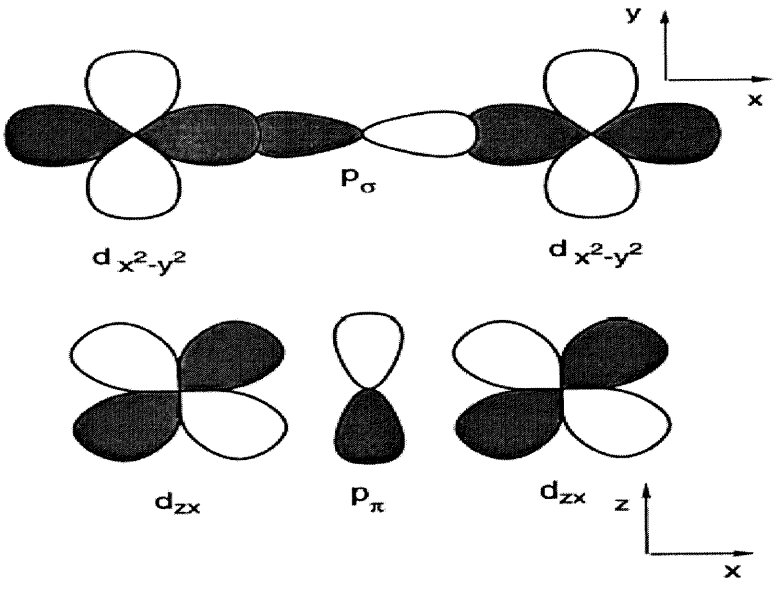

Fig. 4.2. Transition-metal 3d orbitals bridging with ligand p orbitals.

The bandwidth is determined by the overlap. Since the angular moment of the 3d orbital is $L = 2$, five-fold degeneracy is possible i.e., $L_z = 0, \pm1, \pm2$ for each spin. However, there are ten-fold degeneracy for spins. Figure 4.3 shows 4 fold for e_g such as $d_{x^2-y^2}$ and $d_{3z^2-r^2}$ and 6 fold degenerate for t_{2g}.as d_{yz}, d_{zx}, d_{yz}. [160] Following additional interesting figures [see Fig. 4.4 through Fig. 4.7] are shown.

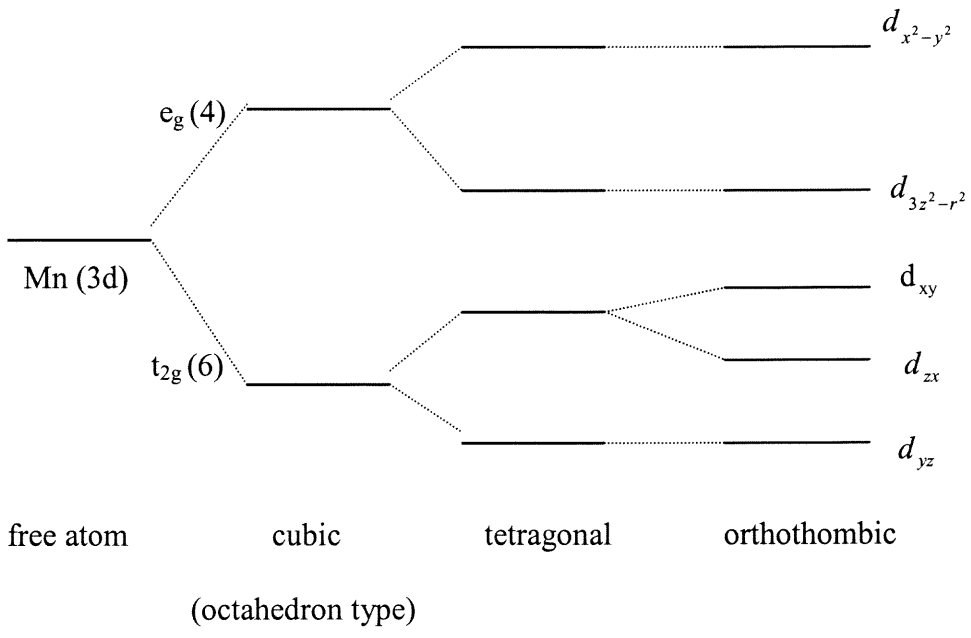

Fig. 4.3 Crystal –field splitting of 3d orbitals in cubic, tetragonal, and orthothombic crystals. Note that there are 10 different degeneracies with spins in 3d orbital.

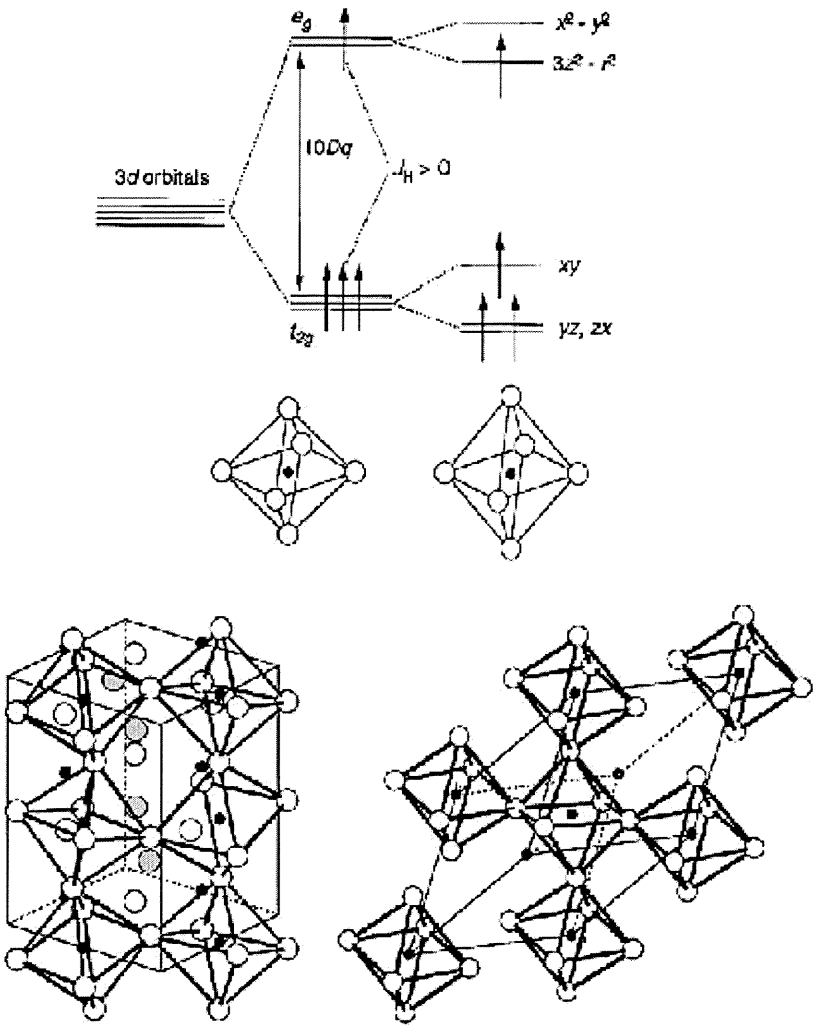

Fig. 4.4 Schematic diagrams: Top: crystal-field splitting of five-fold degenerate atomic 3d levels (lower t_{2g} (triply degenerate) and higher e_g (doubly degenerate) levels). Jahn-teller distortion of MnO_6 octahedron results more splitting onto orbitals such as x^2-y^2, $3z^2$-r^2, xy, yz, and zx. Bottom: Structural distortion of perovskite manganites between orthorhombic(left) and rhombohedral (right). [41(e)]

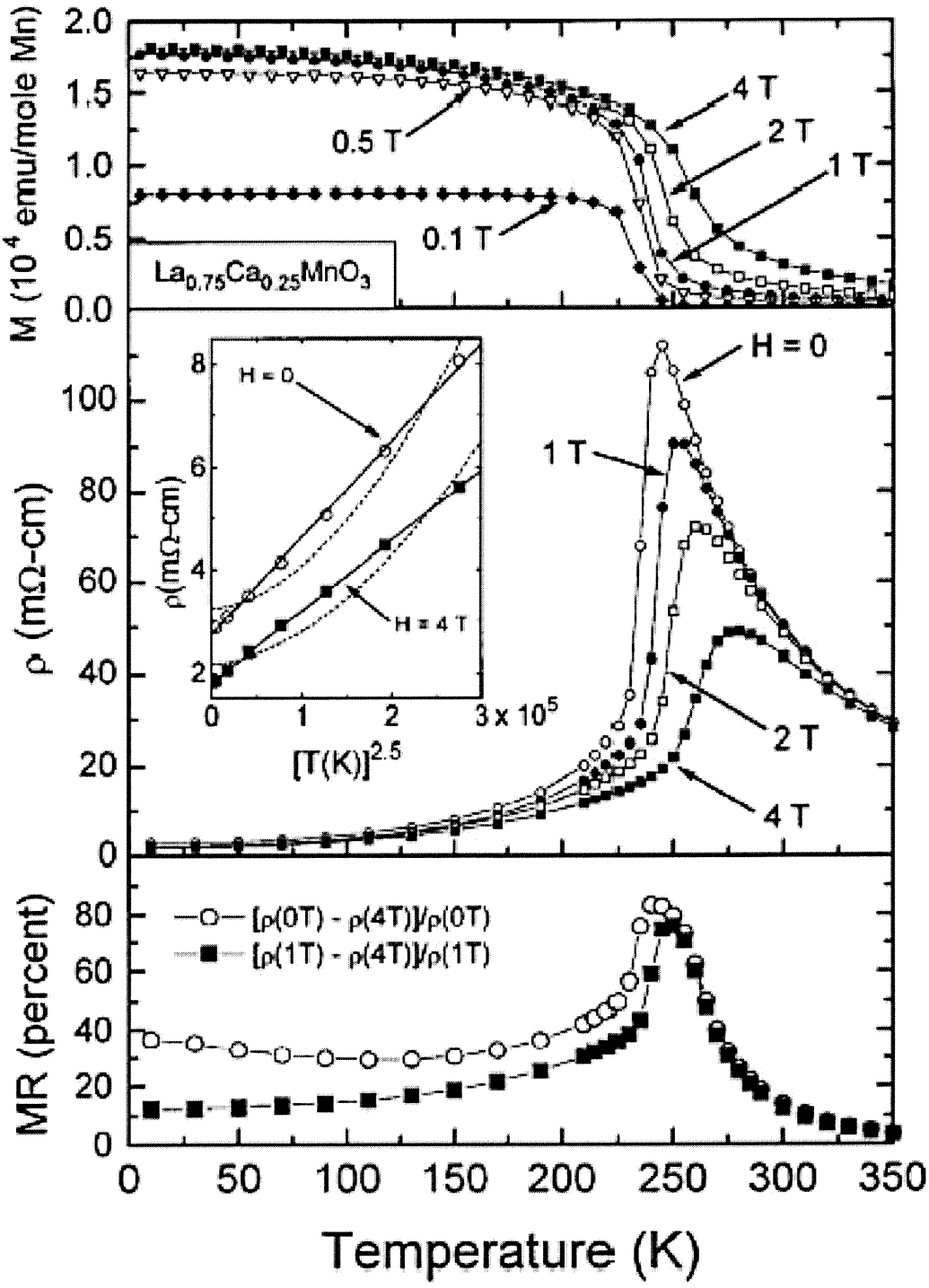

Fig. 4.5 Magnetoresistance in $La_{0.75}Ca_{0.25}MnO_3$.

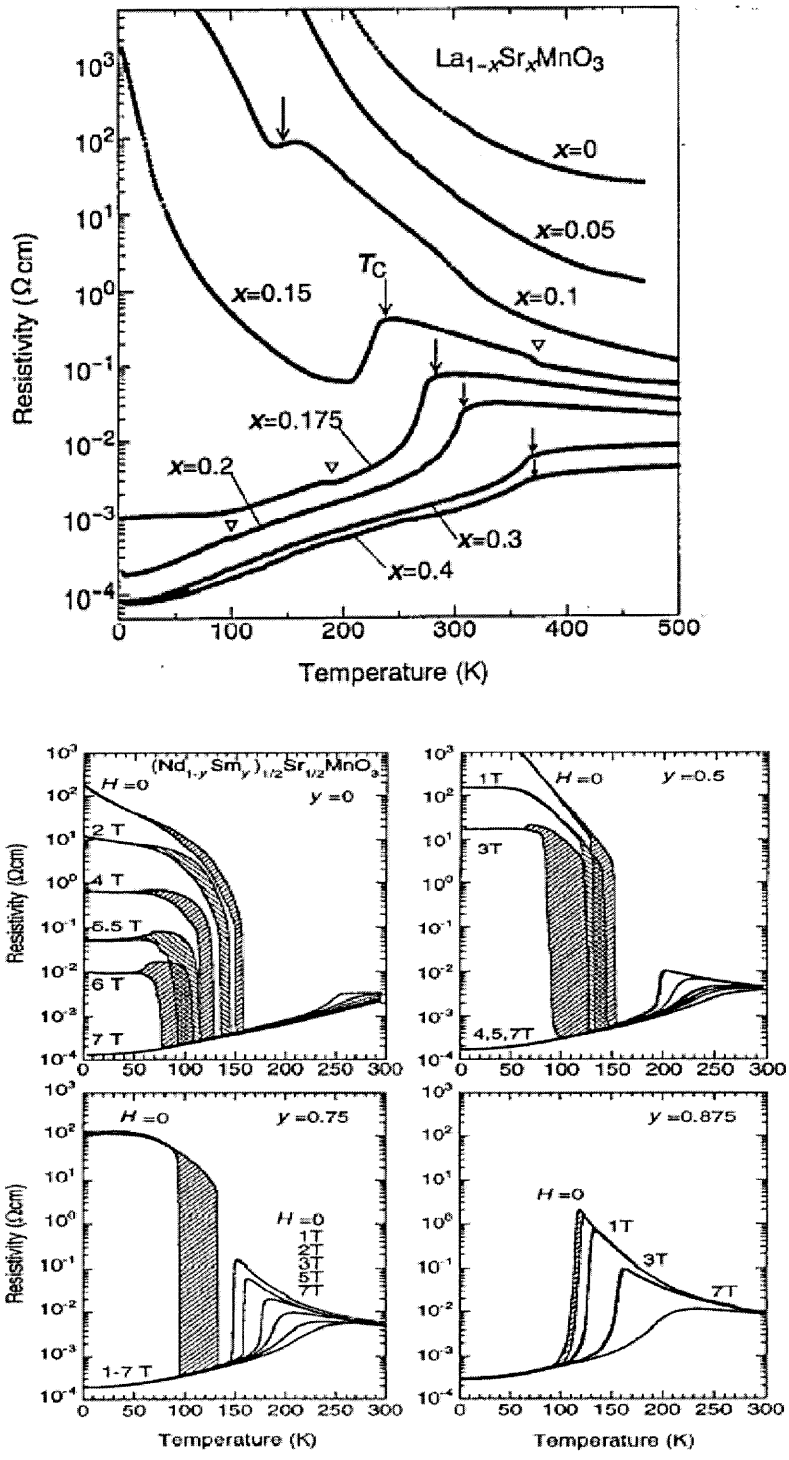

Fig. 4.6 Magnetic field-induced resistivity for $(Nd_{1-y}Sm_y)_{1/2}Sr_{1/2}MnO_3$ in y = 0, 0.5, 0.75, and 0.875. Each field measured a thermal hysteresis(slashed area) in the cooling and warming runs. [161]

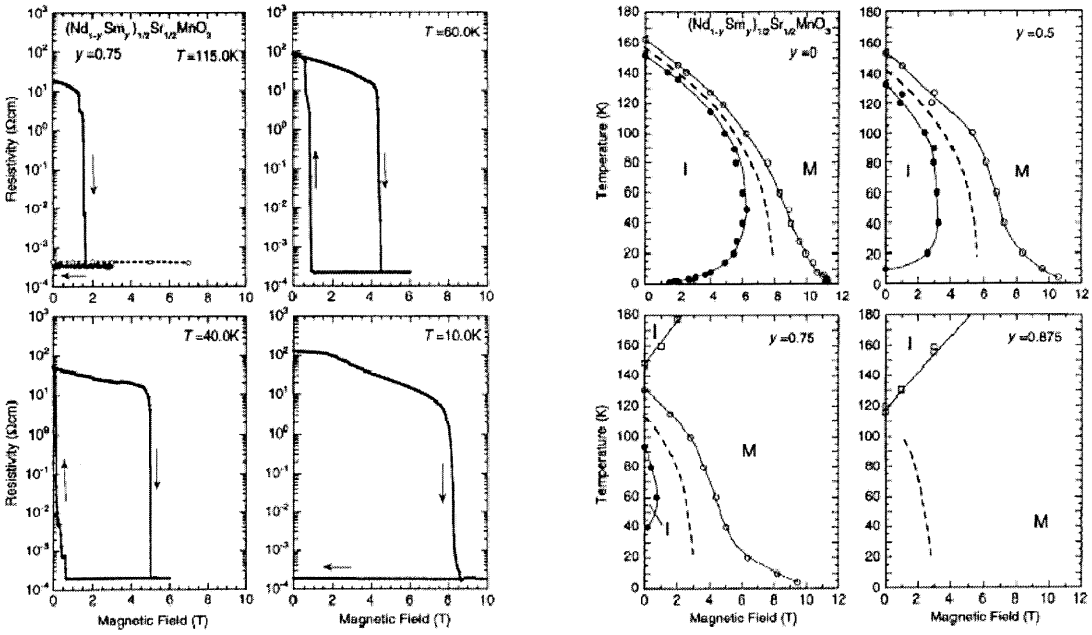

(a) (b)

Fig. 4-7 (a) Isothermal magnetoresistance with its hysteretic behavior, which indicates the metallic state(a dotted line) at 115K and the insulating state(a solid line) cooling firstly below 90K and then warming. (b) The metal insulator phase diagrams in temperature vesus magnetic field (right 4 panels) with $(Nd_{1-y}Sm_y)_{1/2}Sr_{1/2}MnO_3$ in y = 0, 0.5, 0.75, and 0.875. Open and closed circles exhibits the critical magnetic fields with the transitions from charge-ordered antiferromagnetic insulator to ferromagnetic metal and vice versa. For y = 0.75 and 0.875, open squares show the first-order phase change to the ferromagnetic metallic state accompanying a change in lattice parameters.

4.2 Models of ρ vs. T (Variable Range Hopping)

Goodenough [76] proposed that as the conduction electron enters an antibonding orbital, it will look for the lowest energy one. It notes that the lowest antibonding energy indicates the outmost bonding energy with the longest bond distance. A localized state caused from the electron phonon interaction is called a small polaron. The variable range hopping conduction (VRH) is described by the conduction mechanism of one electron by way of intermediately localized orbitals in a random potential. The conductivity in the n dimensions is written as

$$\sigma \propto \exp\left(-\frac{T_0}{T}\right)^{1/(n+1)}$$

where n is the dimension of the conduction path. [162] For example, one dimensional organometallic substances such as NMP-TCNQ [163] is known for n = 1, i.e., $T^{-1/2}$ and the two dimensional materials polycrystalline oxide YFe_2O_4 [164] is known for n = 2, i.e., $T^{-1/3}$ and the third dimensional materials is known for n = 3, i.e., $T^{-1/4}$. The sample $Bi_{0.1}Ca_{0.9}MnO_3$ has been reported in this case of n = 3, i.e., $T^{-1/4}$. This will be described compared with our result in details in the chapter 6.

CHAPTER 5

EXPERIMENTAL METHODS

5.1 Sample Preparation

5.1.1 Standard Method

We have prepared a series of BCMO ($x > 0.2$) polycrystalline samples using the standard solid-state reaction method. Stoichimetric mixtures of Bi_2O_3, $CaCO_3$ and MnO_2 were mixed, ground, and pressed into pellets which were calcined at 900 °C. After calcination, the samples ($x > 4.0$) were reground and sintered at 1000 °C in air. The samples for $x < 0.4$ were sintered at 1050 °C in air. This was repeated one more time. This method was used for samples with $x > 0.25$.

5.1.2 High Pressure Synthesis

$BiMnO_3$ was synthesized under high pressure (25 kbar (2.5 GPa)) at 800 °C by using a cylinder-piston-type pressure furnace, from Depths of the Earth Company. A 1:1-mixture of Bi_2O_3 and Mn_2O_3 was mixed, ground, pressed into pellets, held in gold capsules for 1 hour heated. The purity of $BiMnO_3$ was checked by x-ray fluorescence spectroscopy. The furnace assembly is shows in Fig. 5.1. The detailed steps follow.

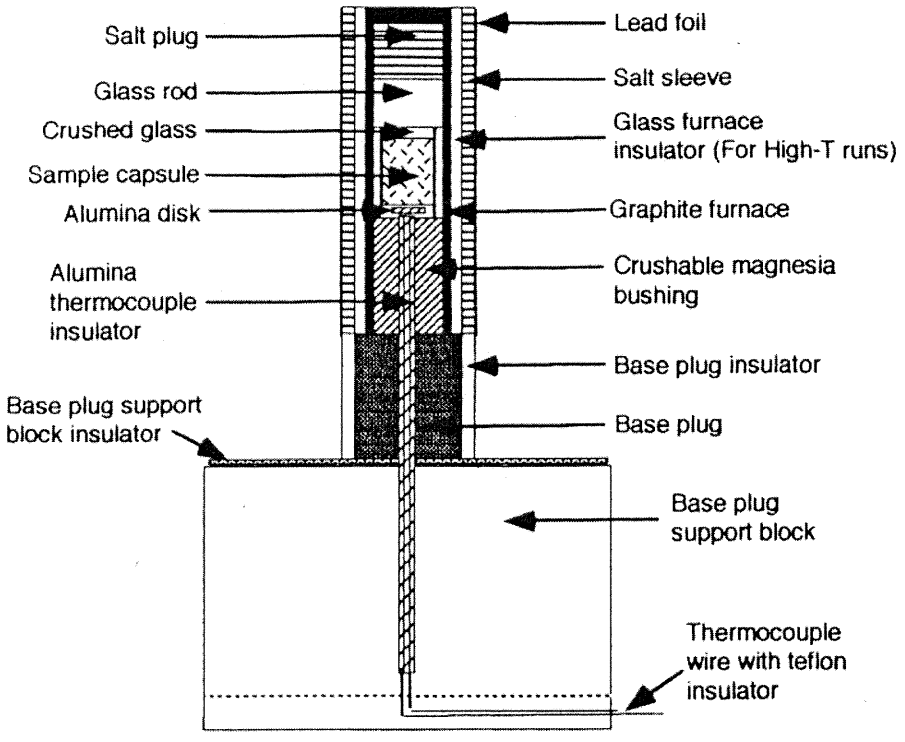

Fig. 5.1 High-pressure furnace assembly for high-temperature experiments.[165]

Step 1. The assembly stands on the base plug support block.

Step 2. On top of the support block an insulator ring that is built of gasket paper

Step 3. The insulated thermocouple wires (Tungsten-Rhenium alloys W26Re and W5 Re; Chromel-Alumel) is rapped in Teflon insulation and put into Alumina insulation. A flat surface is desirable.

Step 4. The thermocouple securely slides through a pyrex glass tubing insulator over the base plug.

Step 5. A crushable magnesia tube over the thermocouple is positioned and fixed. The tube stands on the base plug, and the thermocouple top is flush with the magnesia tubing. Note that the thermocouple can be reused several times.

Step 6. An alumina disk (similar to size of sample) placed over the opening of the magnesia bushing and thermocouple top is glued by using Al_2O_3 cement.

Step 7. The graphite furnace on the assemblage is put in place and is directly connected to the base plug.

Step 8. The sample capsule is inserted into the furnace.

Step 9. The empty space between the sample capsule and the furnace is filled with pyrex (or MgO or Al_2O_3 wire, etc.) solid or powder. A solid wire or piece of disk is better than power because the powder may block the flowing of current between graphite and base plug. This should be checked by an ohmmeter.

Step 10. A cylindrical segment of pyrex rod is placed in the furnace.

Step 11. A salt rod is cut off and aligned with the top margin. An important point concerning the assembly is that the fit should be snug to preventing cracking the furnace.

Step 12. To operate the temperature above 1000°C a glass-salt furnace insulator is needed.

Step 13. A furnace lid (graphite cap) is placed on the furnace tube.

Step 14. The salt cell should slide over the glass insulator or graphite furnace and the top edge of the salt cell must be flush with the furnace lid. For the case of a tightly fitting salt cell, it can be heated before it is incorporated into the furnace assembly.

Step 15. A 0.001 ~ 0.003 thick lead foil is wrapped around the salt cell.

This method was attemped for samples for $x < 0.25$ for which the standard solid state reaction method failed. In addition to BiMnO3, $Bi_{0.9}Ca_{0.1}MnO_3$, and $Bi_{0.8}Ca_{0.2}MnO_3$ preparation was attempted.

5.2 Extended X-ray Absorption Fine Structure (EXAFS)

XAFS spectroscopy is broadly applied to physics, materials science, chemistry (in particular catalysis and coordination chemistry), biology, geochemistry and environmental science. The extended x-ray absorption fine structure (EXAFS) is the fine structure of the x-ray absorption coefficient from an absorption edge up to 1 to 2 keV. EXAFS measurements are able to extract local atomic structure about specific atomic species by tuning across the characteristic absorption edges.

EXAFS is attracted by following properties: (A) Synchrotron radiation sources are now available which are tunable and with higher resolution and significantly higher intensities (10^3) than the standard x-ray tube sources. (B) long-range order is not required, haence both crystalline and non crystalline solids can be considered on the same basis. (C) The local atomic structure can be determined with a great resolution (~ 0.005 Å) for distinct elements.

Absorption of an x-ray photon (typically to 40 keV) causes ejection of a bound electron from a core level. X-ray absorption resulting in the ejection of the 1s, $2s_{1/2}$, $2p_{1/2}$, and 2p3/2 correspond to the K-, L_1, L_2 and L_3 edges, respectively. Classically, the outgoing photoelectron wave backscatters off the neighboring sites and interferes with the incoming wave to produce oscillation as a function of energy- the EXAFS oscillations. The frequency of the oscillations is related to the absorber-neighbor distance and the amplitude is related to the coordination number.

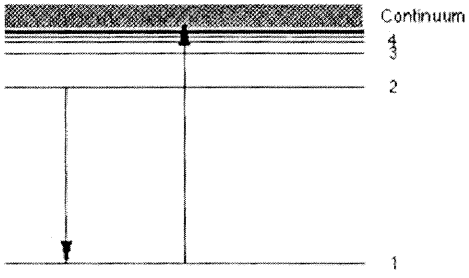

Fig. 5.2 Schematic diagram (left to right) for K-edge x-ray photon absorption followed by K_α decay.

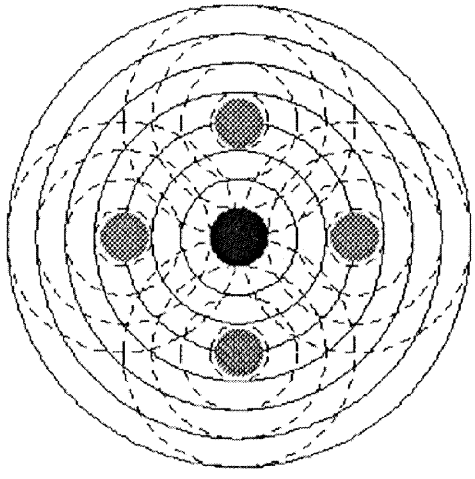

Fig. 5.3 QualitativeThe outgoing waves (solid circles) and the backscattered waves (dashed circles). [166]

The wave number of the spherical outgoing wave is

$$k = \frac{2\pi}{\lambda} = \sqrt{(2m/\hbar^2)(E - E_0)}$$

where λ is the wavelength of photoelectron related by de Broglie $\lambda = \frac{h}{p}$, $E = h\nu$ where h is Planck's constant, i.e., x-ray energy and E_0 is the binding energy of the photoelectron .

The EXAFS function is related to the absorption length (and absorption cross section) which can be calculated quantum mechanically using Fermi's Golden Rule [167] as

$$\mu(E) \propto \left| \left\langle f \left| \hat{\varepsilon} \cdot \vec{r}\, e^{i\vec{K}\cdot\vec{r}} \right| i \right\rangle \right|^2$$

where the K is the wave vector and the labels *i* and *f* refer to the initial and final states of the photoelecton respectively. (Note that $\frac{I}{I_0} = e^{-\mu(E)x}$ and $\mu(E)x = \mathrm{Ln}\left(\frac{I_0}{I}\right)$.)

A general multiple-scattering (MS) scheme [168] can be used to quantitatively describe the absorption process Their derivation is stemmed from the solution of the Dyson equation with a complex self-energy of the Hedin-Lundqvist type for the single particle Green's function describing the propagation of the excited photoelectron through the system.

An unpolarized photoabsorption cross section for photons with energy ω is expressed by

$$\sigma(\hbar\omega) = 4\pi^2\alpha\hbar\omega \sum_{if} \left| \left\langle \Psi^f \left| \hat{\varepsilon} \cdot \vec{r} \right| \Psi^i_{core} \right\rangle \right|^2 \delta(\hbar\omega + E_i - E_f)$$

$$\sigma(\hbar\omega) = 4\pi^2\alpha\hbar\omega \sum_{if} \left\langle \Psi^i_{core} \left| \hat{\varepsilon} \cdot \vec{r}\, \delta(\hbar\omega + E_i - E_f) \right| \Psi^f \right\rangle \left\langle \Psi^f \left| \hat{\varepsilon} \cdot \vec{r}' \right| \Psi^i_{core} \right\rangle,$$

Using the identity,

$$\lim_{\eta\to 0^+} \frac{1}{x \pm i\eta} = P\frac{1}{x} \mp i\pi\delta(x),$$

$$\begin{aligned} \delta(\hbar\omega + E_i - E_f)\left|\Psi^f\right\rangle &= \delta(\hbar\omega + E_i - H_0)\left|\Psi^f\right\rangle \\ &= -\frac{1}{\pi}\lim_{\eta\to 0^+} \mathrm{Im}\left[\frac{1}{\hbar\omega + E_i - H_0 + i\eta}\right]\left|\Psi^f\right\rangle \\ &= \mathrm{Im}\left[-\frac{1}{\pi}G^+(E)\right]\left|\Psi^f\right\rangle, \end{aligned}$$

where $E = \hbar\omega + E_i$.

$$\sigma(\hbar\omega) = 4\pi^2\alpha\hbar\omega\sum_i \mathrm{Im}\left\langle \Psi^i_{core}\left|\hat{\varepsilon}\cdot\vec{r}\left[-\frac{1}{\pi}G^+\left(\vec{r},\vec{r}';E\right)\right]\hat{\varepsilon}\cdot\vec{r}'\right|\Psi^i_{core}\right\rangle$$

$$= 4\pi^2\alpha\hbar\omega\sum_i \mathrm{Im}\left\{\iint d^3r\,d^3r'\Psi^i_{core}\left(\vec{r}\right)\hat{\varepsilon}\cdot\vec{r}\left[-\frac{1}{\pi}G\left(\vec{r},\vec{r}';E\right)\right]\hat{\varepsilon}\cdot\vec{r}'\,\Psi^i_{core}\left(\vec{r}'\right)\right\},$$

where the Green's function satisfies an effective one-particle Schrodinger equation,

$$H_0G^+\left(\vec{r},\vec{r}',E\right) = \left[\nabla^2 + E - V\left(\vec{r}\right)\right]G^+\left(\vec{r},\vec{r}',E\right) = \delta\left(\vec{r}-\vec{r}'\right),$$

In the case of a muffin-tin type of potentials with non-overlapping spheres-, the Green's function is given by

$$-\frac{1}{\pi}\left[G^+\left(\vec{r},\vec{r}',E\right)\right]^{ij}_{LL'} = \sum_{LL'}R^i_L\left(\vec{r}\right)\tau^{i\,j}_{LL'}R^j_L\left(\vec{r}'\right) - \sum_L \delta_{ij}R^i_L\left(\vec{r}_<\right)S^j_L\left(\vec{r}_>\right),$$

where $\vec{r}$ and $\vec{r}'$ are centered on the absorber's sphear defined as

$$\vec{r}_< \equiv \begin{cases}\vec{r} \text{ for } r < r' \\ \vec{r}' \text{ for } r' < r,\end{cases}$$

Fort inner-shell excitations, the form reduces to

$$-\frac{1}{\pi}\left[G^+\left(\vec{r},\vec{r}',E\right)\right] = \sum_{LL'}R^0_L\left(\vec{r}\right)\tau^{0\,0}_{LL'}R^0_L\left(\vec{r}'\right) - \sum_L R^0_L\left(\vec{r}_<\right)S^0_L\left(\vec{r}_>\right),$$

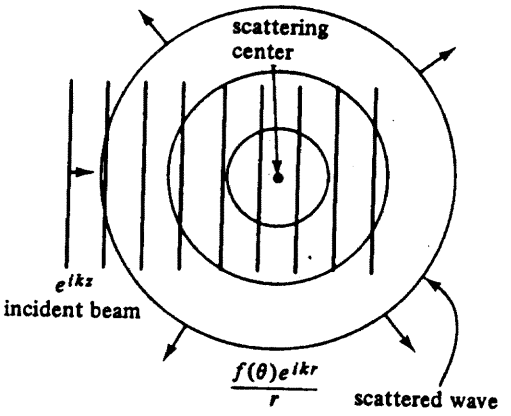

Fig. 5.4 Schematic diagram of scattering of incident plane wave and scattered outgoing spherical wave. [169]

In the scattering process from incident plane wave and scattered outgoing spherical wave with a fixed scattering center through the central potentral V(r), a phase shift δ_l with the l^{th} partial wave occurs if V(r) decreases faster than r^{-1}. In this model the effect of scattering by spherical atomic potentials is accounted for by the scattering amplitude, t_l^i, of the atom located at site with angular momentum l [170]

$$t_l^i = \exp(i\delta_l^i)\sin(\delta_l^i).$$

For a cluster of atoms this becomes the matrix

$$\left(T_a^{-1}\right)_{LL'}^{ij} = \left[\left(t_l^i\right)^{-1}\right]\delta_{ij}\delta_{LL'}$$

The amplitude of propagation from site i with angular momentum L to site j with angular momentum L' is given by the function $G_{LL'}^{ij}$. Hence the scattering path above becomes

$$\tau_{l\,m\;lm}^{0\,0} = \left\{\left[1 - T_a G_0\right]^{-1} T_a\right\}_{l\,m\;lm}^{0\,0},$$

and can be expanded into successive terms representing scattering of the photoelectron off various centers. For the convenience purpose, we drop subscript on G

$$\tau = \left\{\left[1 - T_a G\right]^{-1} T_a\right\} = \sum_n \left(T_a G\right)^n T_a.$$

where the last expansion is valid only where the spectral radius $\rho(T_a G)$ (maximum modulus of the eigenvalues) of the matrix $T_a G$ is less than unity.

For n = 2,

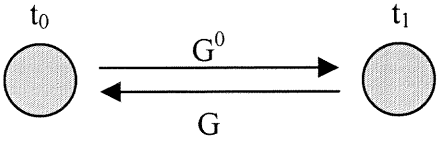

For n = 3,

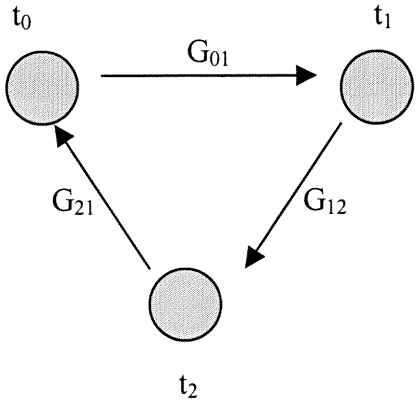

Fig. 5.5 Schematic diagram for a single scattering for n = 2 (TOP) and for multiple scattering for n = 3 respectively.

$$\sigma_l^n(\hbar\omega) \cong \sigma_{l_i+1}^n(\hbar\omega)$$

$$\cong \frac{8}{3}\pi^2\alpha\hbar\omega(l_i+1)\left\{\mathrm{Im}\left[\sum_m M_{l_i l}^2 \frac{1}{2l+1}\left[(T_a G)^n T_a\right]_{lm\,lm}^{0\;0}\right]\right\} l = l_i + 1$$

and

$$\sigma_l^0(\hbar\omega) \cong \sigma_{l_i+1}^0(\hbar\omega)$$

$$\cong \frac{8}{3}\pi^2\alpha\hbar\omega(l_i+1)\left\{\mathrm{Im}\left[\sum_m M_{l_i l}^2 t_l^0 - \tilde{M2}_{lil}\right]\right\} l = l_i + 1,$$

The total fine structure due to an excitation channel l is

$$\chi_1(\hbar\omega) = \frac{\sigma_1(\hbar\omega) - \sigma_1^0(\hbar\omega)}{\sigma_1^0(\hbar\omega)}$$
$$= \frac{\sum_{n=2}^{\infty} \sigma_1^n(\hbar\omega)}{\sigma_1^0(\hbar\omega)},$$

In other words, we have

$$\chi_1(\hbar\omega) = \frac{\sigma_1^2(\hbar\omega)}{\sigma_1^0(\hbar\omega)} + \frac{\sigma_1^3(\hbar\omega)}{\sigma_1^0(\hbar\omega)} + \frac{\sigma_1^4(\hbar\omega)}{\sigma_1^0(\hbar\omega)} + \cdots$$
$$= \chi_1^2(\hbar\omega) + \chi_1^3(\hbar\omega) + \chi_1^4(\hbar\omega) + \cdots,$$

Using the plane wave limit for G and assuming real potentials

$$G^{i\ i}_{LL'} = -4\pi i(1-\delta_{ij}) \sum_{L''} i^{l-l'+l''} C_{L\ L'}^{\ L''} h_{l''}^{+}(\kappa R_{ij}) Y_{L''}\left(\hat{R}_{ij}\right)$$
$$\approx 4\pi Y_L\left(\hat{R}_{ij}\right) Y_{L'}\left(\hat{R}_{ij}\right) \frac{e^{i\kappa R_{ij}}}{\kappa R_{ij}},$$

where $\kappa \equiv \sqrt{E - V_{II}}$ and $t_1^0(\kappa) \equiv e^{i\delta_1^0(\kappa)} \sin\left(\delta_1^0(\kappa)\right)$.

We obtain the form of the single scattering signal

$$\chi_2^1(\hbar\omega) = \frac{\sigma_1^2(\hbar\omega)}{\sigma_1^0(\hbar\omega)}$$
$$\cong \frac{\frac{8}{3}\pi^2 \alpha \hbar\omega (l_i + 1)}{\sigma_1^0(\hbar\omega)} \left\{ \mathrm{Im}\left[\sum_m M_{l_i l}^2 \frac{1}{2l+1} \left[T_a G T_a G T_a\right]^{0\ 0}_{lm\,lm} \right] \right\} l = l_i + 1$$
$$\cong \left\{ \frac{1}{\sin^2\left(\delta_1^0\right)} \frac{1}{2l+1} \mathrm{Im}\left[\sum_{\substack{m \\ l'm' \\ r}} t_1^0 G^{0\,r}_{1\,m\ \ l'm'} t_1^r G^{r\ 0}_{l'm'\ \ lm} t_1^0 \right] \right\} l = l_i + 1$$
$$\cong \mathrm{Im}\left\{ (-1)^l e^{i 2\delta_1^0} \sum_r \frac{e^{i 2\kappa R_{0r}}}{\kappa R_{0r}^2} \sum_{l'} \frac{t_{l'}^r (2l'+1) P_{l'}(\cos(\pi))}{\kappa} \right\} l = l_i + 1$$
$$\cong (-1)^{l_i+1} \sum_r \sin\left\{ 2\delta_{l_i+1}^0(\kappa) + 2\kappa R_{0r} + \arg\left[f(\pi,\kappa)\right] \right\} \frac{\left|f(\pi,\kappa)\right|}{\kappa R_{0r}^2},$$

The third order signal is of the form

$$\mathrm{Im}\left[\sum_{\substack{m\\ r\,l'\,m'\\ s\,l''\,s''}} t_1^0 G_{1m\,l'\,m'}^{0r}\, t_{l'}^r G_{l'\,m'\,l''\,m''}^{rs}\, t_{l''}^r G_{l''\,m''\,1m}^{rs}\, t_1^0\right],$$

Yielding a structure of the type

$$\sin\left\{2\delta_{l_i+1}^0(\kappa)+\kappa\left[R_{0r}+R_{rs}+R_{s0}\right]+\arg\left[F(\kappa)\right]\right\}\frac{\left|F(\kappa)\right|}{\kappa R_{0r}R_{rs}R_{s0}},$$

and so on for higher order signals. The most general form of the n-th order signal is:

$$\chi_n^{l_i+1}=\sin\left\{2\delta_{l_i+1}^0(\kappa)+\kappa P_{\mathrm{total}}+\arg\left[F(\kappa)\right]\right\}\frac{\left|F(\kappa,R_{0r},R_{rs},R_{st},\cdots,R_{v0})\right|}{\kappa R_{0r}R_{rs}R_{st}\cdots R_{v0}},$$

In the experiments, the background signal extraction was carried out using AUTOBK.[171] The fine structure signals were extracted from the spectra as the difference between the normalized spectra and an adjustable spline function fit through the post-edge region normalized by the absorbance decrease with energy, the parameters of which were adjusted to minimize low frequency region ($R < 1$ Å) in the Fourier transform. After comparison, two to ten individual scans were averaged. Representative data are given in the inset in Fig. 5.6.

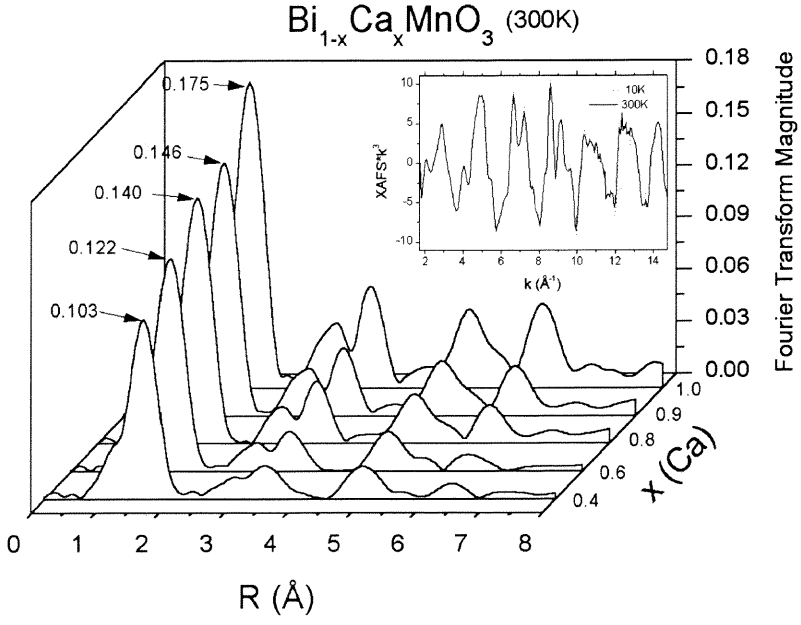

Fig. 5.6 Magnitude of the Fourier transform of XAFS*k^3 (2.5 Å^{-1} ≤ k ≤ 12.3 Å^{-1}) for the system $Bi_{1-x}Ca_xMnO_3$ at 300 K. The first peak (~ 2 Å) corresponds to the Mn - O bond distribution. The second (~ 2.5 Å) and third peaks (~ 3.3 Å) contain the Mn - Ca /Bi and Mn - Mn correlations, respectively. The inset displays raw XAFS*k^3 data for x = 0.9 at 300 K (solid line) and 10 K (dotted line). Note that the temperature dependent changes in amplitude are quite small. [172]

Information about the Mn-O bond distributions was obtained by fitting the k^3 weighted raw data over the range 2 < k < 12.3 Å^{-1} ($k = \sqrt{(2m/\hbar^2)(E - E_0)}$). Fitting was made using the functional form,

$$\chi_{\text{model}}(k) = \sum_{i}^{\text{shells}} S_0^2 \frac{N_i}{kR_i^2} f_i(\pi, k, R_i) \exp\left(-2\sigma_i^2 k^2 + \frac{2}{3} C_{4i} k^4\right) \times \sin\left(2kR_i - \frac{4}{3} C_{3i} k^3 + \phi_i(\pi, k, R_i)\right), \quad (5.1)$$

where S_0^2 is the scale factor for the multielectron effects, N_i is coordination number of the i - shell, R_i is radius of the i - shell, σ^2 is mean square radial displacement or Debye-Waller factor, f_i is backscattering amplitude of the photoelectron due to the atoms of i - coordination shell, C_3, and C_4 are cumulants [173, 174] of a distribution to model anharmonic effects and/or non - Gaussian disorder [175], and ϕ_i is phase shift, respectively.

The inhomogeneously broadened (fine structure) χ based on the statistical ensemble of scattering path lengths [176] is written as

$$\langle \chi(k;R) \rangle = \int dR\, P(R) \chi(k;R), \quad (5.2)$$

In the cumulant approach to distributions, one represents the Fourier transform of a distribution by its moments. For small deviations from a Gaussian distribution a rapidly

$$\ln \int_0^\infty P(r,\lambda) e^{2ikr} dr = C_0 + \sum_{n=1}^{\infty} \frac{(2ik)^n}{n!} C_n, \quad (5.3)$$

converging series makes possible a description by a small number of parameters. For the effective distribution we have

where

$$P(r,\lambda) = \rho(r)\frac{e^{-2r/\lambda}}{r^2}.$$

The leading cumulants (C_n) are

$$\begin{aligned}
C_1 &= \langle R \rangle, \\
C_2 &= \sigma^2 = \langle R^2 \rangle - \langle R \rangle^2, \\
C_3 &= \langle R^3 \rangle - 3\langle R^2 \rangle \langle R \rangle + 2\langle R \rangle^3, \\
C_4 &= \langle R^4 \rangle - 4\langle R^3 \rangle \langle R \rangle - 3\langle R^2 \rangle^2 + 12\langle R^2 \rangle \langle R \rangle^2 - 6\langle R \rangle^4. \qquad (5.4)
\end{aligned}$$

For an effective Gaussian distribution, cumulants (C_n) higher than the second vanish. In a convergent series the C_3 and C_4 parameters are related to asymmetry and flatness of the distribution, respectively. [see Eq.5.4] We performed fits with parameters up to C_4. Photoelectron scattering factors utilized in these fits were obtained using the code FEFF7.[177] These complex phase shifts included the electron damping. By defining the coordination numbers, N, as the values known for perovskite systems, average bond lengths, R, and Debye-Waller factors, σ, were extracted from the fits as well as C_3 and C_4 for the Mn-O (first shell) bond distribution. The errors in these parameters were estimated based on the statistical spread found for fits to individual scans.

X-ray absorption spectra were measured at Brookhaven National Laboratory's National Synchrotron Light Source (NSLS) beam lines X11A, X18B, X19A and X23A2. Si(111) monochromator crystals were used on X18B and X19A while Si(311) crystals were used on X23A2. Spectra were taken in transmission mode using N_2-filled ion chambers. The reduction of the x-ray absorption measurements was performed using

standard procedures. [167(b)] Calibration was accomplished by defining the first inflection point in a simultaneous Mn foil as 6539 eV, the ionization threshold. Consistency between different beamlines was checked by using a MnO_2 powder reference sample over the complete data range. Bi spectra were collected at the Bi L_3 edge 13419 eV.

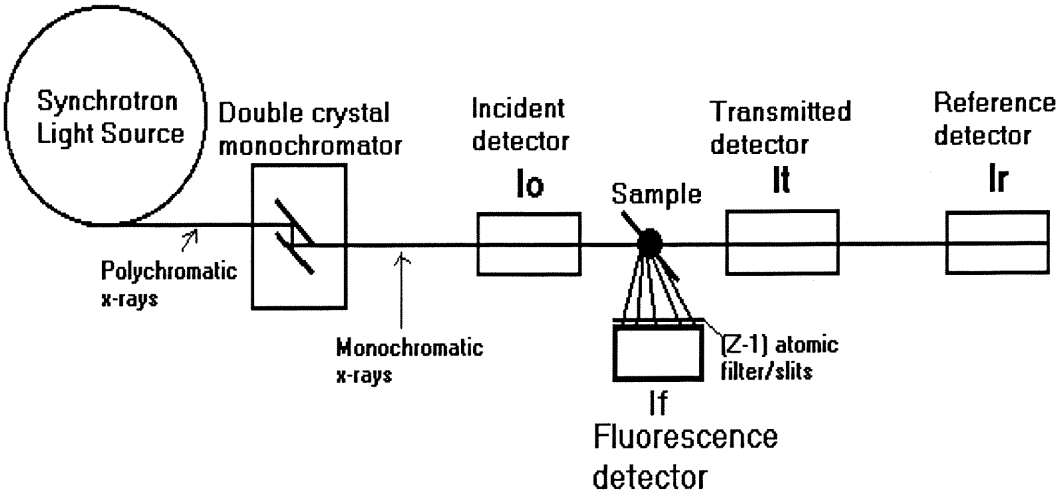

Fig. 5.7 Schematic transmission and fluorescence experimental set-ups.

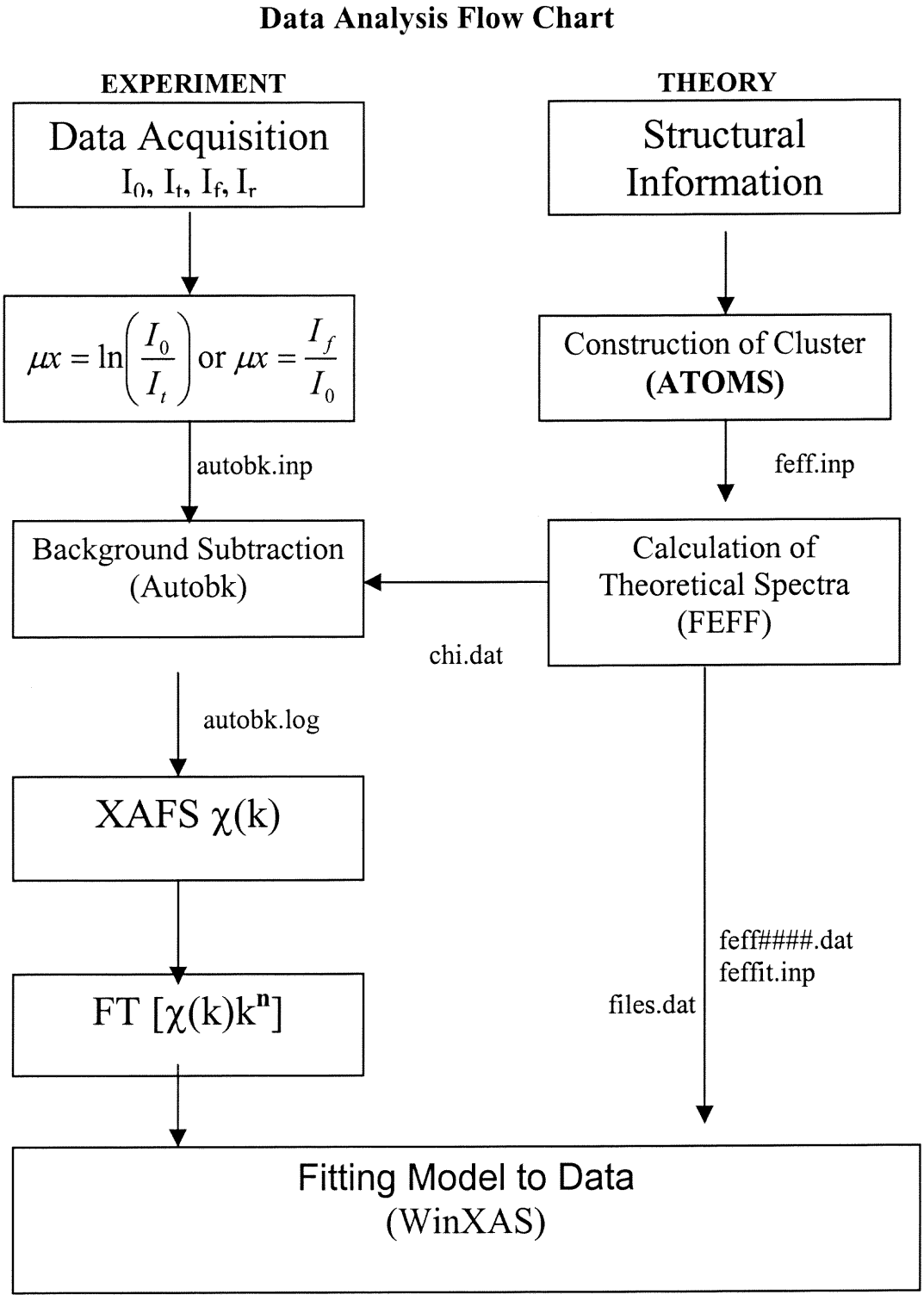

Fig. 5.8 EXAFS flow chart.

Procedures of EXAFS analysis are as follows:

1. Run ATOMS from http://millenia.cars.aps.anl.gov/cgi-bin/atoms/atoms.cgi
   In order to run ATOMS, we need structural information: Space Group; Rmax (Usually 6); Edge; Output (feff6.inp); Shift: 0, 0, 0; Lattice parameters: a, b, c; alpha only (beta, gamma sometimes); Choose center atom.
   Atoms-program will generate feff.inp.
   Need to change as follows because of printing format:
   From: "* mphase,mpath,mfeff,mchi
   CONTROL 1 1 1 1
   PRINT 1 0 0 **0**"

   To:
   "* mphase,mpath,mfeff,mchi
   CONTROL 1 1 1 1
   PRINT 1 0 0 **3**"

2. Run Feff7.exe:
   Need an input file from step 1: feff.inp
   Will generate "files.dat"
3. Fitting with "files.dat" in WinXAS 97,
   Convert to Fourier transform magnitude taken from χ vs k data.
   A. Click EXAFS-fit from XAFS menu.
   B. Check "Experimental Phases" with K-, L1-edge or L2-, L3- edge
   C. Check "Feff-Fit" and then chick "files.dat".
   D. Choose feff0001.dat with highest ratio and nleg 2, Reff ~2
   E. In EXAFS-fit windows- Check "Use current phases+amplitudes keep parameters from simulation or previous fit" and add 3rd and 4th cumulant parameters only if needed. Use k-weight with 2 or 3 (as in EXAFS data) and number of shells, R-space (refinement to FT), and to set border, check G and choose a node and a node you wish to fit. Click OK.
   F. New window, enter parameter for XAFS Fit. Set initial values: S0^2 ~1, N, R, sigma^2 = 0.005, and E0 shift = 10 (oxides), 3rd cumulant = 0.0001, 4th cumulant = 0.00001.
   G. Fitting data analysis (good/bad)
      Bad: negative sigma^2, S0^2, Residual greater than about 10.
      Good: Residual lower than 2. S0^2 = coordination number with atoms and low E0 near 0 and small cumulant factors.
      Convergence check: For use of the cumulant expansion we must have: $k^4C_4 << k^3C_3 << k^2\sigma^2$.

Table 5.1 Quantitative Comparative of Beamline Parameters.

Beam Lines	Energy Range (KeV)	Crystal Type	Resolution ($\Delta E / E$)	Flux (photons/sec) @monochrom. Bandpass (100 mA, 2.5 GeV)	Spot-Size Unfocused (mm)	Total Horizontal Angular Acceptance (mradians)
X11A [α]	4.5 ~ 26	Si(111)	2×10^{-4}	~1.0×10^{10} (@ 10keV)	10H×0.5V	0.5 (unfocused)
	8 ~ 35	Si(311)	2×10^{-4}	~5.0×10^{8} (@ 25 keV)	10H×0.5V	0.5 (unfocused)
X14A [α]	3.5 ~ 40	Si(111)	2×10^{-4}	~9.0×10^{11} (@ 8 keV) (223mA,2.5GeV)	1.5H×1.0V	5
X18B [α]	5.8 ~ 40	Si (111)	2×10^{-4}	1.0×10^{10} (@ 8 keV)	25H×1.5V	1.0 (unfocused)
X19A [α]	2.1 ~ 8 3.4~12.9 4.0~15.2	Si(111) Si(220) Si(311) low	[a]8.1 - 0.7\u*\d 12 - 0.8	~1.0×10^{11} (@ 5 keV)	40H × 5V (unfocused) ~1mm diam. focused	2.4 (unfocused) 1.3 (focused)
	7.7~13.4 12.5~23 14.6~25.6	Si(111) Si(220) Si(311) high	[a]8.1 - 0.7 12- 0.8	~5.0×10^{11} (@ 11 keV)	40H × 5V (unfocused) ~1mm diam. focused	2.4 (unfocused) 1.3 (focused)
X23A2 [α]	5.4 ~ 30	Si(311)	2×10^{-4}	1.0×10^{10} (@10 keV)	25H×1.0V	4.0 (unfocused)
X23B [α]	3 ~ 11	Si(111)	3×10^{-4} (@5.8 keV ,measured)	6.9×10^{10} (@7.4 keV, measured) (Ref. of 178)	1.0H×3.0V (measured)	6
MRCAT [β]	4.8 ~ 30	Si(111)	1.0×10^{-4}	~ 3.0×10^{13} (100 mA, 7 GeV)	5mm×2mm	(Undulator)[b]

Note that all data above are not compared with the same experimental conditions.

[a] Resolution \(*De(ev) @8 keV, Si(111) @12keV, Si(220).

\u\dLargest value corresponds to 2 mm slit. Small value is for 0.1 mm slit.

The data above were taken from http://www.nsls.bnl.gov/BeamLine/pages/XrayBls.html and http://www.aps.anl.gov/xfd/communicator/useroffice/.

[b] This is an undulator, the acceptance is irrelevant since we get all of the beam on the monochromator crystal.

[α] National Synchrotron Light Source (NSLS), Brookhaven National Laboratory (BNL).

[β] Advanced Photon Source (APS), Argonne National Laboratory (ANL).

OPTICAL CONFIGURATION

Table 5.2 Beamline Descriptions (National Synchrotron Light Source (NSLS), Brookhaven National Laboratory).

Beamlines	Descriptions
X11A	Monochromator: Double flat crystal; non-fixed exit; hutch table tracks with beam height; first crystal is cooled; Bragg angle range from 5 deg. to 80 deg.; located 12 meters from the source.
X14A	Mirror: Platinum coated flat single-crystal silicon mirror cylindrical in design, 700 mm long x 100 mm wide; variable vertical focusing or collimation. Radius adjustable from flat to 1km; incident angles between 1 and 7 mradians; located 7.5 meters from the source; can be removed for high energy operation. Monochromator: Horizontally focusing double crystal monochromator; adjustable focal point from 13.3 - 30 meters from source; first crystal is water-cooled and flat; second crystal is conically bent; located 9.3 meters from the source.
X18B	Monochromator : Si(111) channel cut monochromator with detuning and some deglitching capabilities. Beam walk < few microns during typical scan. Monochromator in ultra high vacuum 18 m from the source. Sample at ~ 20 m from the source.0.1, 0.2, 0.3, 0.5, 1.0 and 1.5 mm vertical slits at ~ 17 m from the source.
X19A	Monochromator: NSLS boomerang-type double flat crystal monochromator; fixed exit geometry; first crystal is water-cooled; operates at UHV; two presettable Bragg angle ranges of 14.4 - 70 deg (low) and 8.5 - 15 deg (high) located 9.3 meters from the source. Though able to reach energies up to 20keV with the current complement of crystals, the beamline specializes in the energy range between 2.12 and 8.0 keV (P to Fe in the periodic table) using a Si(111) (low) focused configuration Mirrors: A recently replaced spherical front mirror immediately downstream of the shield wall collimates light in the vertical direction; and a toroidal mirror after the monochromator focuses the beam to a ~0.8 mm x 0.8 mm beam spot in the hutch. The 60 cm length of this last optic limits the horizontal acceptance angle to roughly 1.5 mradians. Windows: Beamline is UHV and windowless up to an 8 mil Be window located inside the experimental hutch.
X23A2	Monochromator: Upwards reflecting, fixed exit Golovchenko-Cowan design; piezo-feedback stabilized.
X23B	Mirror No. 1: Platinum coated flat silicon collimating mirror; 400 mm long by 70 mm wide; collimation achieved by four point bending; high energy cutoff is 11 keV; angle of incidence is 7.15 mradians; located 7.9 meters from the source. Monochromator: Fixed exit position double crystal monochromator (Cowan type); two ranges of incident angle are 8 - 15 degrees and 13.5 - 70 degrees;located 9.2 meters from the source.

Table 5.3 Beamline Description (Advanced Photon Source (APS), Argonne National Laboratory).

Beamlines	Descriptions
MRCAT	Monochromator: The line is equipped with a Si (111) monochromator consisting of a cryo-cooled first crystal designed by the IIT Center for Synchrotron Radiation Research and Instrumentation (CSRRI) and a 200mm long second crystal which provides an energy range of 4.8keV to 30keV from the fundamental reflection. This monochromator has been measured to deliver in excess of 10^{13} photons/second to the experimental station. Harmonic Rejection and Focussing Mirrors: All of the MRCAT mirrors reside in the experimental station and are intimately connected to the general positioning system that we have developed for the beamline. Currently, there is a positionable flat harmonic rejection mirror with Pt and Rh stripes.

Flux Calculation:

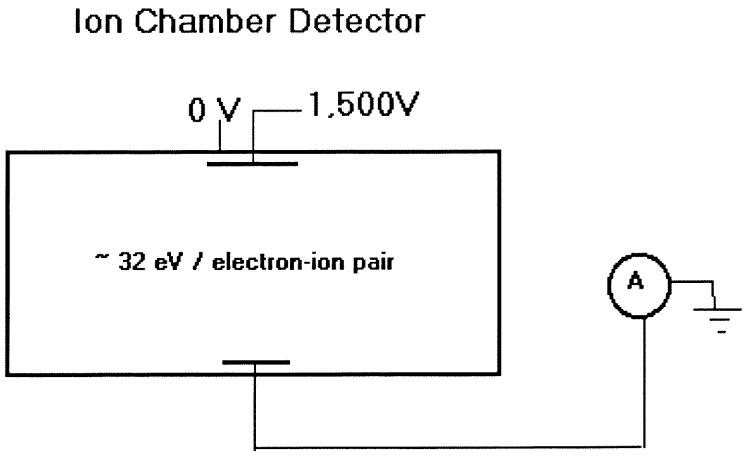

Fig. 5.9 Ion chamber detector.

~32eV per Electron-ion pair

$I_0 \sim 3$ volts. ((@6600eV) in 20% He and 80% N_2)
Gain = 10^6
6600 eV / 32eV = 206 electron-ion pairs

I = flux [photons/sec] · (photon energy[eV]/32eV/e^{-1}) · ($1.6 \cdot 10^{-19}$ [C / e^{-1}]) · V ·10^6[V/A]
Current from ion chamber

I [C/Sec] =N(1-$e^{-\mu x}$)·(E [eV]/32 [eV/ e^{-1}]) ·$1.6 \cdot 10^{-19}$ [C / e^{-1}]
Where x is the chamber length.

We have $3 \cdot 10^{-6}$Amps (gain is 10^6[V/A])

N = $3 \cdot 10^{-6}$A/(0.1·6600 eV / 32eV) ·$1.6 \cdot 10^{-19}$ [C / e^{-1}] = $3 \cdot 10^{10}$ photons/sec

5.3 X-ray diffraction

The following is based significantly on Rietveld Analysis: R. A. Young, "Using the Rietveld method", version 5, School of Physics, Georgia Institute of Technology, Atlanta, GA 30332, 1995.

The Rietveld method [179] is a powerful tool to refine crystal structures (not just profiles) using x-ray and neutron diffraction data until a good agreement between observed and calculated observations is obtain. Ultra-high resolution synchrotron sources [180] have been utilized in solid state chemistry/physics. Materials may be distorted by a variety of defects such as concentration variation, macrostrain, microstrain, size stacking fault, antiphase domains which possibly affect the shape and width of the powder diffraction pattern reflections. [181]

Methodologically the process of the Rietveld method is based on the least-squares refinements until the optimum fit is obtained between the entire observed powder diffraction pattern taken as a whole and the whole calculated pattern established on the simultaneously refined models with desired input parameters: the crystal structure(s), diffraction optics effects, instrumental factors, and other specimen characteristics (e.g., lattice parameters).

Data are Collected with the intensity value, y_i, at equal increments (steps) depends on scattering angle (2θ), some energy parameter such as velocity for time-of-flight (TOF) neutron data (energy dispersion via velocity discrimination data) or fixed wavelength for X-ray data. The Rietveld method is basically the same approach in both X-ray and

neutron data. The differences among data sources are whether the steps are in angle or energy and the required instrumental parameters.

The residual, S_y, is the minimized value in the least-squares refinement

$$S_y = \sum_i w_i (y_i - y_{ci})^2$$

where $w_i = 1/y_i$, and y_i is observe d(gross) intensity at the i^{th} step, and y_{ci} is calculated intensity at the i^{th} step. There are useful often-used numerical criteria for the quality of the fit: First, "R-pattern", R_p, is

$$R_p = \frac{\sum_K |y_i(obs) - y_i(calc)|}{\sum_K y_i(obs)},$$

and "R-weighted pattern", R_{wp}, is

$$R_{wp} = \frac{\sum_K w_i (y_i(obs) - y_i(calc))^2}{\sum_K w_i (y_i(obs))^2}.$$

where K is the K^{th} Bragg reflection. In addition, the "Goodness-of-Fit" indicator, S, is defined as

$$S = \left(\frac{S_y}{N - P} \right)^{3/2} = \frac{R_{wp}}{R_e} \approx \text{chi}\hat{}2$$

where N is the number of observations (data points), P is the number of constraints, and "R-expected", R_e, is $R_e = \left((N - P) / \sum_i w_i y_{io} \right)^{1/2}$. Typically a good fit yields R_p and R_{wp} are about 10% or less and χ^2 is as small as possible not less than 1.

The software package developed at Los Alamos National Laboratory, Generalized Structure Analysis System (GSAS) [182] was adopted to fit our materials.

5.4 Resistivity Measurements

Resistivity measurements were measured by standard technique, i.e. the four point probe.

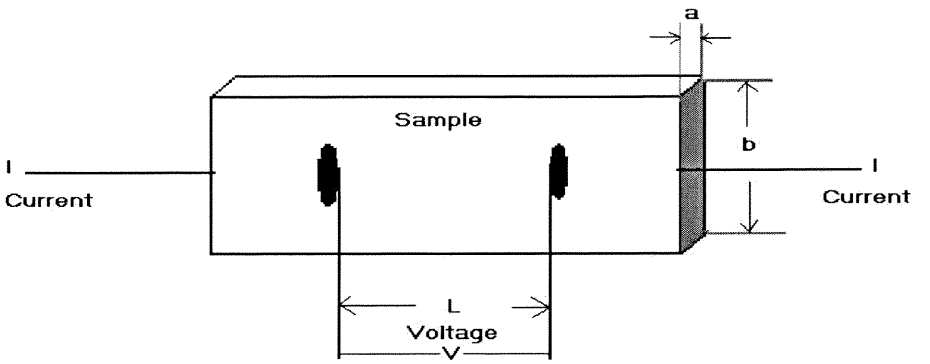

Fig. 5.10 Standard four point probe method with sliver paste or paint used to adhere wires.

Gold wire (usually 12 ~ 50 μm) and the sample was contacted with the silver print conductive paint. Resistivity can be calculated as follows:

$$\rho = \frac{V}{I} \cdot \frac{ab}{L} [\Omega \cdot cm]$$

where V is voltage measured, I is the current, l is the length in voltage-contact, and a, b are cross-sectional sides.

5.5 Magnetic Measurements

There are numerous commercial magnetic sensors such as Search-Coil Magnetometer, Flux-Gate Magnetometer, Optically Pumped Magnetometer, Hall-Effect Sensor, Magnetoresistive Magnetometer, Magnetodiode, Magnetotransistor, Fiber-Optic Magnetometer, Magneto-Optical Sensor, and SQUID Magnetometer. [183] Detailed descriptions for those are described in a review article. [184] These sensitivities, power requirements and frequency limits are vary. SQUIDs are able to measure magnetic fields as small as $\sim 10^{-10}$ gauss but their disadvantages are the required low temperature condition. On the other hand magnetoresistive sensors with flux collectors enable frequencies to execute up to 10^8 Hz with only 100 mille watts of power.

5.5.1 SQUID Measurements

The superconducting quantum interference device (SQUID) is the most sensitive (10^{-10} G ~ 10^{-4} G) for measuring a magnetic field (see Fig. 5.11). The key idea is based on extraordinary interactions of electric currents and magnetic fields measured when materials are cooled down below a superconducting transition temperature. In this temperature, the materials become superconductors.

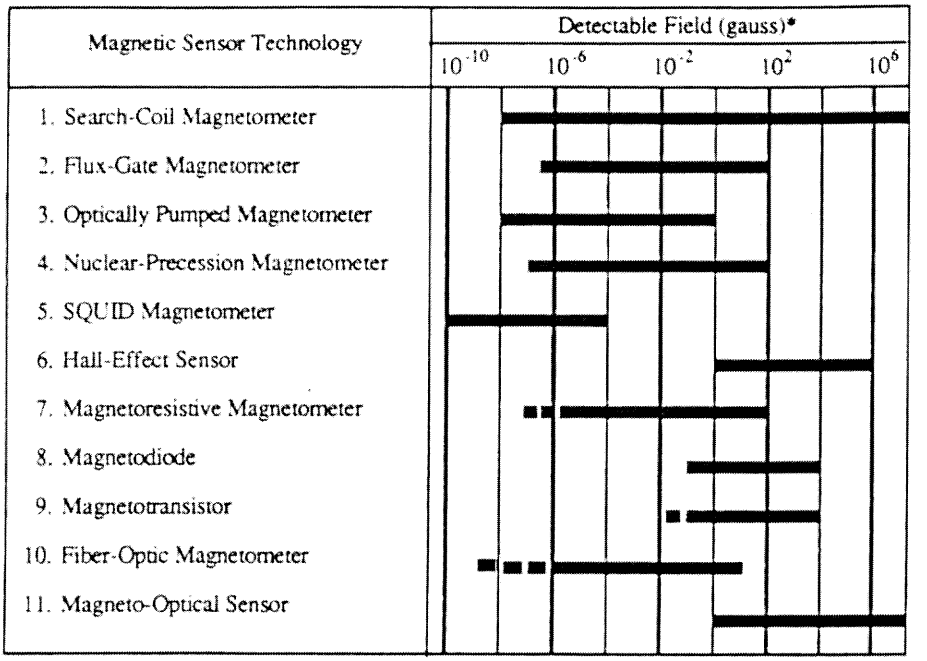

* Note: $1T = 10^4 G$

Fig. 5.11 Magnetic sensor comparison. [185]

If a superconducting ring is interrupted by a line of magnetic flux, a current is induced into the ring. This magnitude of the induced current is very sensitive indicator of the flux density. In fact, the ring can detect a tiny change in the field from a single quantum unit of magnetic flux.

The device wass originally proposed by Brian D. Josephson in 1962, who was a graduate student at the University of Cambridge. His basic interest was in what could happen in a superconducting ring interrupted by a "weak-link", either a thin layer of insulator or an area where the superconductor itself narrows to a very small cross section. He discovered that a supercurrent can penetrate the weak link, but it is an oscillating function of the magnetic field intensity in which the supercurrent has a peak and dies out periodically. This situation is very similar pattern as the interference fringes generated by the diffraction of light.

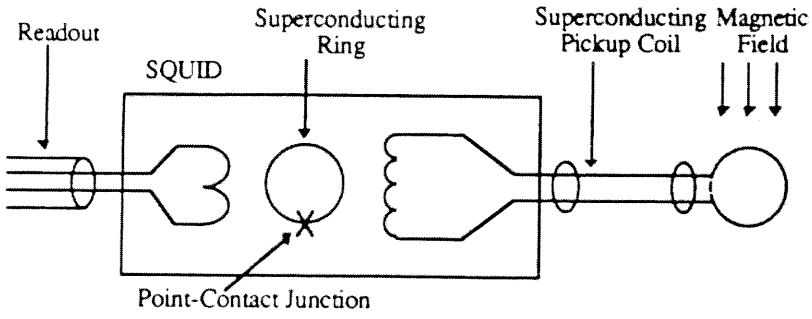

Fig. 5.12 Schematic diagram of components in a SQUID magnetometer.

In a SQUID, there are three major parts: the SQUID ring, the radio-frequency coil, and the large antenna loop. These parts should be cooled to be a superconducting state by using the liquid helium. Periodic variations of output signals are used to measure the current in the ring and ambient magnetic field. This ring is coupled to a radio-frequency circuit that gives a known bias field and serves as the detector output. Consequently changes in the ring vary the resonant frequency of the circuit, and from this result the output signal changes periodically as the field varies. Variations in the field can be observed by counting the peaks and valleys which are similar to count fringes in an interference pattern. A feedback loop can be alternatively used to lock the radio-frequency circuit onto a single peak and continuously regulate the bias field to compensate for changes in the external field. This feedback current is a measure of the ambient field.

Typically a SQUID can be formed by two Josephson junctions in the ring. In a situation that the two weak links are matched properly through design, the current in the ring gets a dc response to the flux going through it.

The superconducting ring in a SQUID is a toroid with a few millimeters in diameter (Pb/Nd). Sensitivity is improved by coupling the ring to a larger superconducting loop or coil without a weak link, which effectively acts like a magnetic

"antenna" or dc search coil, gathering flux over an area of several square centimeters. A dc transformer between the sense loop and the SQUID readout can be obtained with advantages of using superconducting properties. Therefore the SQUID ring eventually operates like a very accurate ammeter, which can measure the current in the pickup coil. A null level can be set by adjusting the bias field of the radio-frequency circuit rather than the average terrestrial magnetic field. Superconducting sense loop has a dc response to magnetic fields. The gradient of the external field in nine directions ($\delta B_x/\delta x$, $\delta B_x/\delta y$, etc.) can be measured, and it is called a high-sensitivity "gradiometer". The SQUID usually consumes only several watts to operate the radio-frequency electronics.

DC magnetization measurements were performed with a Quantum Design SQUID magnetometer (MPMS-XL) between 4.2 K and 400 K. AC susceptibility was measured by a Quantum Design MPMS (1 Tesla model with ultra-low field options).

5.5.2 High Field Measurements

The high field magnetization and resistivity measurements (up to 30 T DC) were performed using the Cell #8 32 mm bore magnet at the National High Magnetic Field Laboratory (NHMFL), Florida. A vibrating sample magnetometer was used for magnetization measurements and the standard four-probe method for resistivity was employed.

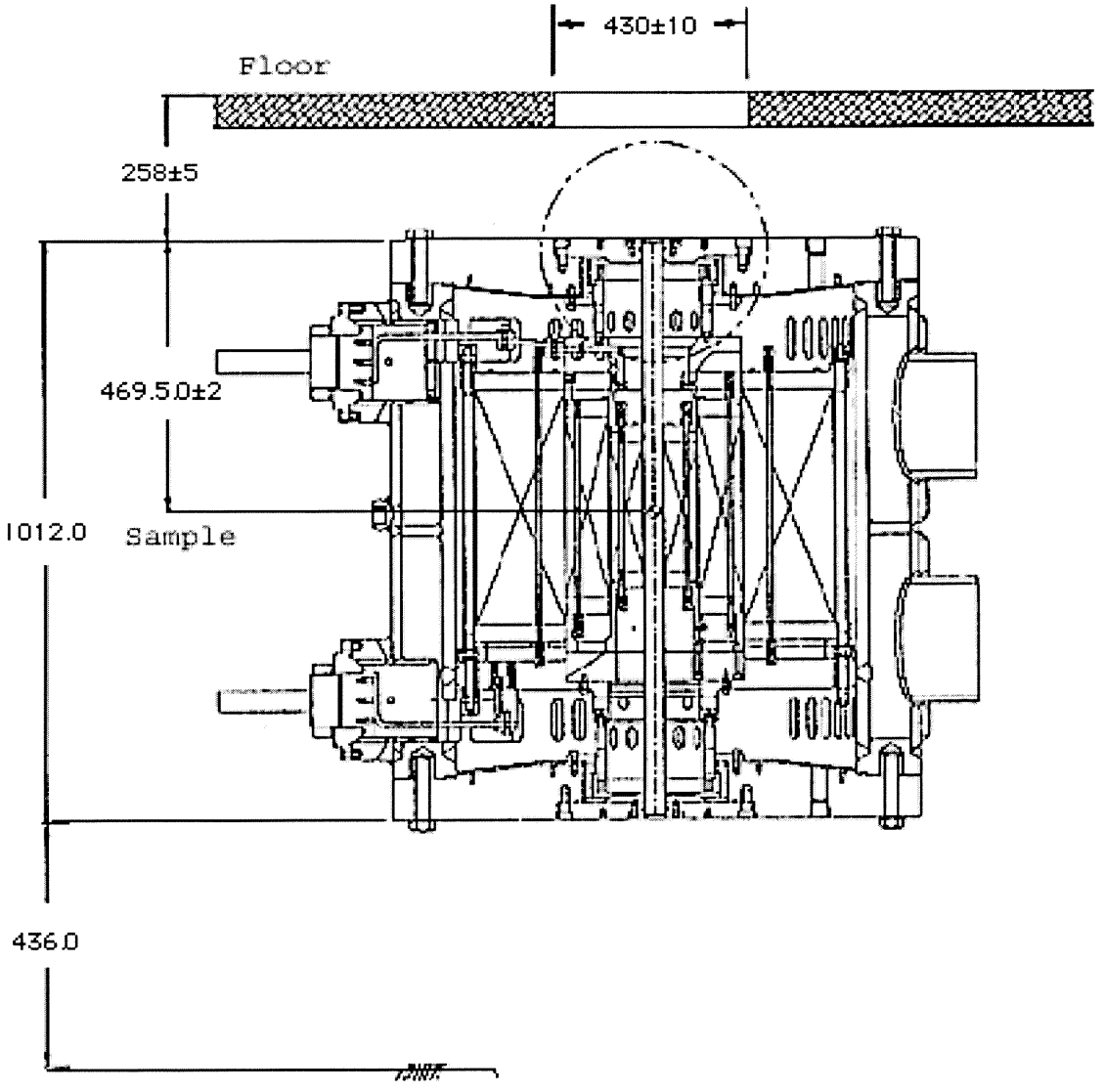

Fig. 5.13 32 mm Bore magnet user interface side view. [186]

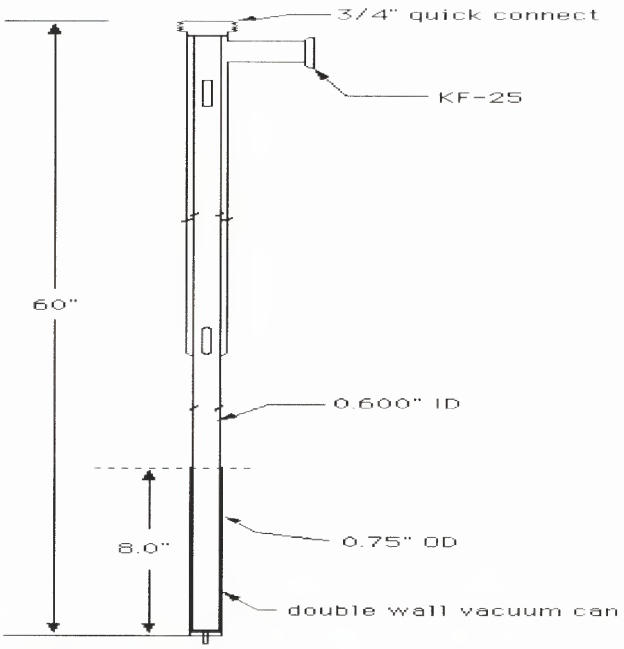

Fig. 5.14 Vacuum can for 32 mm bore magnet.

Fig. 5.15 High Magnetic Field Apparatus in National High Magnetic Field Laboratory (NHMFL). Note that a person in left side is author and Dr. Bruce L. Brandt stands in the right side.

Vibrating Sample Magnetometer (VSM):

To measure the magnetization in high magnetic laboratory, we used a VSM that can be used by large samples up to 6 mm diameter and 8 mm long, and can detect the magnetization with a resolution of 10^{-3} emu. Temperature in the VSM can varies from 1.2K to 300K and fields up to 33T. Figure 4-15 demonstrates the actual set-up of VSM. Sample was mounted inside the plastic tube (like a straw to drink soda). We used the Lake Shore's Vibrating Sample Magnetometer systems with vibrating frequencies of 82 Hz.

Fig. 5.16 Experimental set up of the VSM. [187]

In some figures we report the magnetization in Bohr Magnetons (μ_B)/Mn ion of $Bi_{1-x}Ca_xMnO_3$. This is derived by starting with the magnetization in emu units. Using the weight of the sample we then obtain the magnetization in emu/mole. We then carry out the following multiplication:

emu/mole $Bi_{1-x}Ca_xMnO_3$ * (1 mole /6.022 x 10^{23} molecules) x (1 μ_B/9.27332 10^{-23} emu)

$\Rightarrow \mu_B$/Mn ion.

CHAPTER 6

CORRELATIONS BETWEEN THE MAGNETIC AND STRUCTURAL PROPERTIES OF Ca DOPED $BiMnO_3$

6.1 X-RAY DIFFRACTION MEASUREMENTS

Figure 6.1 shows representative room temperature X-ray diffraction profiles for the x = 0.4, 0.6, 0.8 and 0.9 materials. A reduction of symmetry (space group) from orthorhombic to triclinic occurs on going from high to low calcium contents.

The x = 0.9 material was indexed with the orthorhombic ($\alpha = \beta = \gamma = 90^{\circ}$) perovskite structure and the extracted lattice parameters were a = 5.314Å, b = 7.480Å, and c = 5.297Å. On the other hand, the x = 0.4 pattern was indexed with a triclinic (nearly monoclinic) cell with the structural parameters of a = 3.848Å, b = 7.655Å, c = 3.855Å, $\alpha = 90.166^{\circ}$, $\beta = 90.877^{\circ}$, and $\gamma = 89.997^{\circ}$. This is consistent with the splitting of the a, b, and c, lattice parameters founded by Bokov et al. [139] The x = 0.6 exhibited a similar triclinic structure but with the triclinic splittings much reduced. The x = 0.8 assumes a structure with lattice parameters similar to that for x = 0.9. Hence, reduced Ca content coincides with reduced space group symmetry.

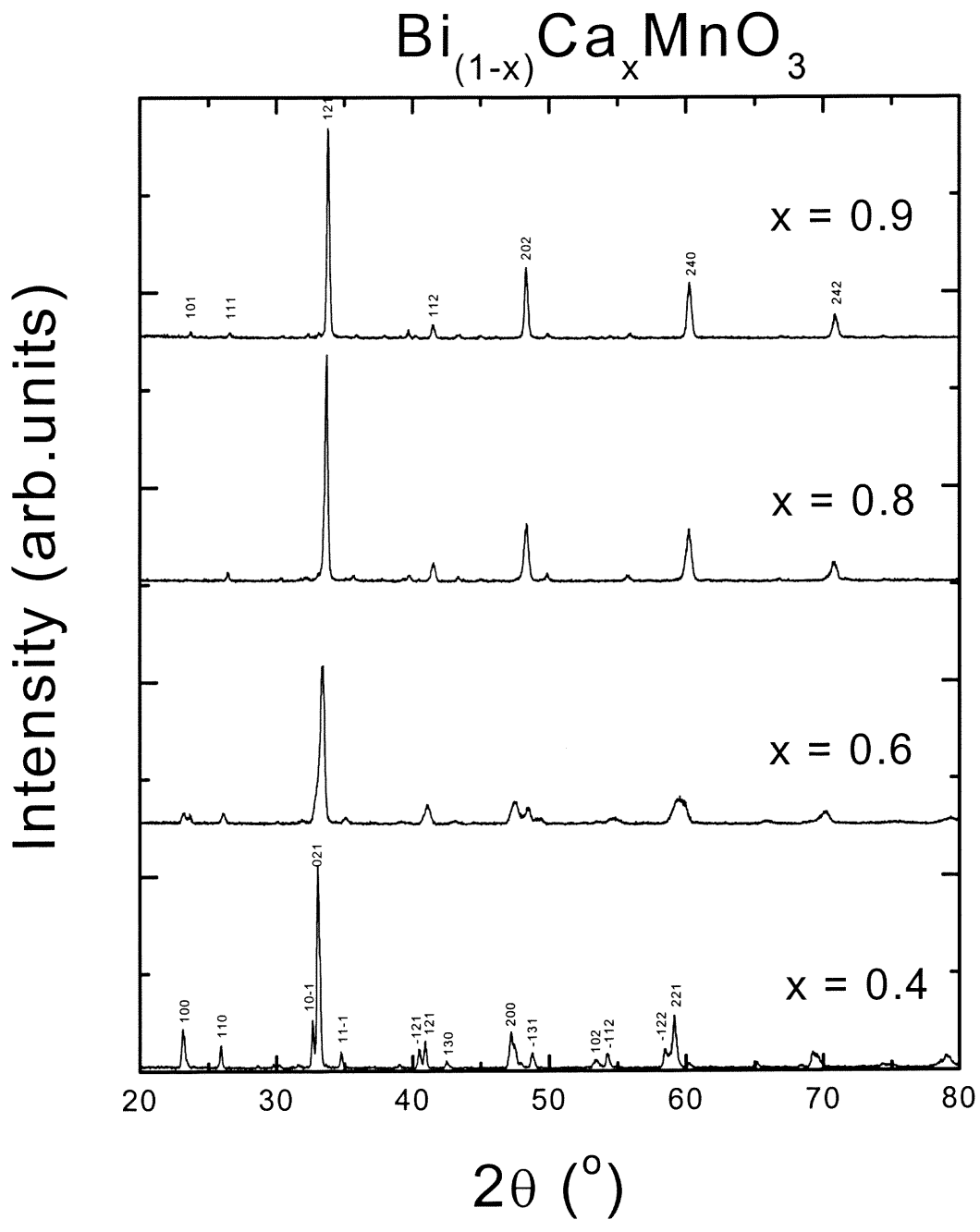

Fig. 6.1 Powder x-ray diffraction curves for x = 0.4, 0.6, 0.8 and 0.9. The splitting and broadening of the x = 0.4 peaks are indicative of a lower space group symmetry. The region above 60°(= 2θ) for the x = 0.4 pattern manifests closely spaced multiple reflections and the indices have been omitted.

6.2 RESISTIVITY MEASUREMENTS

The BCMO system is insulating for $x \geq 0.4$ except near $x \sim 0.9$. We noticed that the resistivity curves jump at the charge ordering temperatures (T_{co}) at 315K, 330K, and 190K for x = 0.4, 0.6, and 0.8 respectively. At the Néel temperature the x = 0.4 sample shows a little dip indicating phase transition.

Zeng *et al.* [188] have reported an activated variation of the resistivity ($\rho = \rho_o e^{To/T}$) with T_0 = 778 K and ρ_o = 12.3 Ω cm for $CaMnO_3$. In the bottom of Fig. 6.2 we compare the logarithmic resistivity variation for the x = 0.9, BCMO material plotted versus (1/T) and $(1/T)^{1/4}$. Unlike the pure x = 0.0 system, the strong curvature of the x = 0.9 material in the 1/T-plot indicates that: (1) its resistivity can not be characterized as activated and (2) a simple crossover between two activation regions appears untenable. On the other hand the $(1/T)^{1/4}$-plot manifests a wide range of high temperature linearity crossing over rather sharply to a low temperature linear range. Fitting the data to the form ($\rho = \rho_o \exp(T_0/T)^{1/4}$) yield T_0 and ρ_o values of 1.42 MK and 1.19 μΩ cm at higher temperatures and 5470K and 0.0136 Ω cm at lower temperatures.

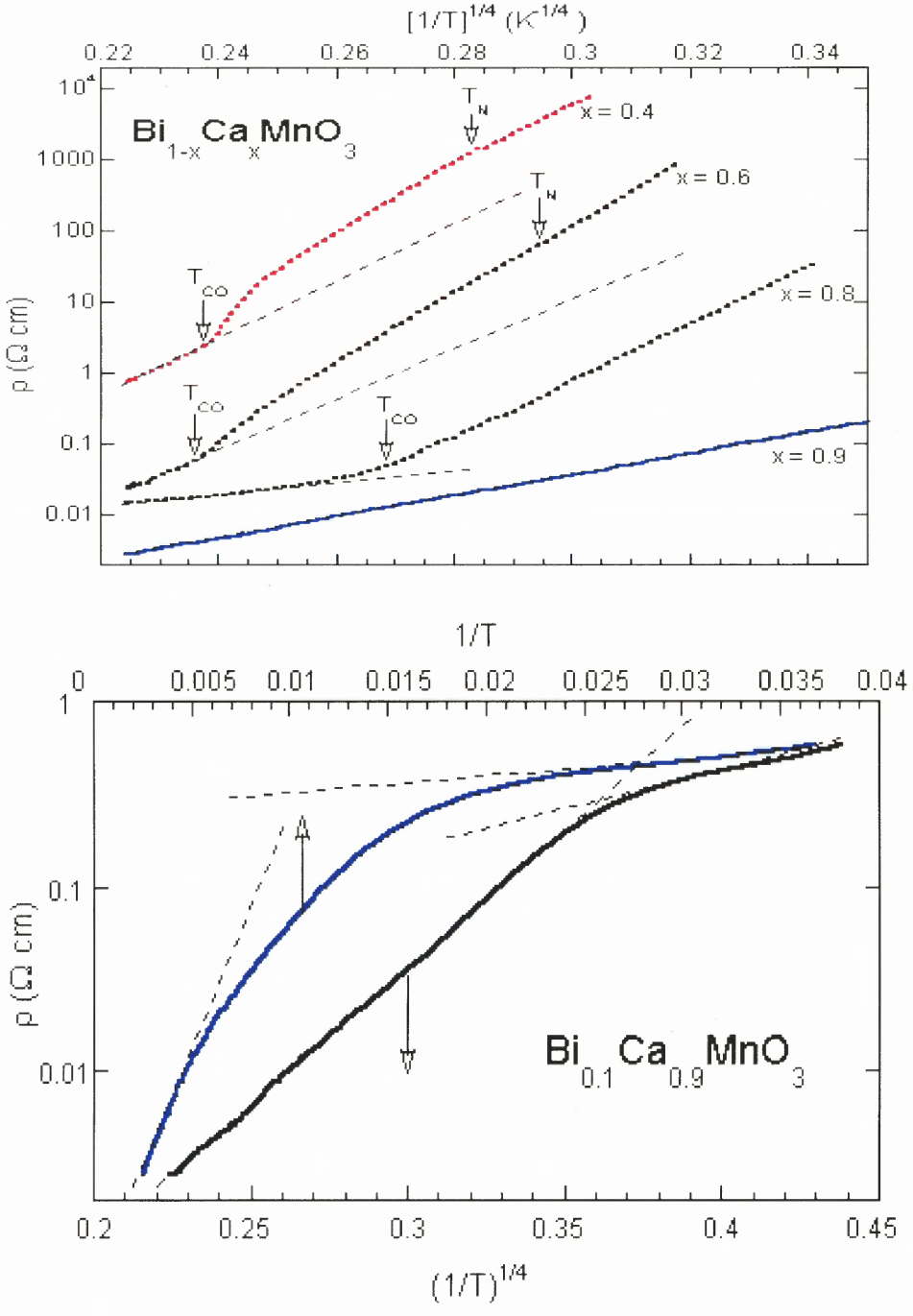

Fig. 6.2 Temperature dependence ($1/T^4(K^{-4})$) of the electric resistivity for x = 0.4, 0.6, 0.8, and 0.9, respectively. Note that there are anomalies at T_{co} = 315K, 330K, and 190K for x = 0.4, 0.6, and 0.8 respectively. T_N = 160K and 130K for x = 0.4, and 0.6. In the lower panel we compare the logarithmic resistivity variation for the x = 0.9, $Bi_{1-x}Ca_xMnO_3$ material plotted versus 1/T (upper curve) and $1/T^{1/4}$ (lower curve).

We performed resistivity measurements for x = 0.4, 0.6, 0.8, and 0.9 (See Fig. 6.2-top panel).

As discussed below, at high temperatures these doped manginites manifest FM-correlations. Models of these materials picture the FM correlations as local-polarons randomly distributed and fluctuating. [41] In this picture, the carrier hopping between FM fluctuations would involve disordered and potentially variable range hopping. In view of this, Fontcuberta *et al.* [189] used the $(T_0/T)^{1/4}$ dependence of the log of the resistivity data to characterize manganite system results. Varma *et al.* [190] argued in favor of a $(T_0/T)^{1/2}$ type behavior for manganite systems due to the importance of electron interactions in the localization. This provides some motivation for trying the 3-D variable range hopping form ($\rho = \rho_o \exp(T_0/T)^{1/4}$) as an ansatz for plotting the data. At this juncture, however, we prefer to view the $(1/T)^{1/4}$ display of the data simply as an empirically useful method of characterizing the high temperature variation of the resistivity.

In Fig. 6.2 (upper panel) the logarithmic variation of the resistivities of the x = 0.4, 0.6, 0.8, and 0.9 materials is plotted versus $(1/T)^{1/4}$. In the smaller range of this plot the x = 0.9 variation is quite linear. The x = 0.4, 0.6, and 0.8 material resistivities can also be well approximated by a ($\rho = \rho_o \exp(T_0/T)^{1/4}$) form for $T > T_{co}$ (the charge/orbital ordering temperatures). For the high temperature region materials the values of ρ_o and T_0 are given by: 3.3 nΩ cm, and 53 MK at x = 0.4; 0.30 nΩ cm, and 43 MK at x = 0.6; 176 μΩ cm and 0.15 MK at x = 0.8. The onset of the charge-ordered phase is characterized by a clear increase in the resistivity for all of the materials (see top of Fig. 6.2). This is consistent with the suppression of the carrier hopping associated with the charge-ordered

phase. No clear resistivity anomalies, associated with the AF ordering temperatures (T_N), were observed.

It is worth noting for later reference that the magnitude of the resistivity at 300 K versus composition (see Fig. 6.5(b)), from our and previous work, [140] shows a distinctive dip (of nearly 2.5 orders of magnitude) in the $0.8 < x < 0.95$ range. A similar drop in the localization energy scale parameters (T_o) is evident from our data. The low-x side of this dip is associated with the suppression of CO correlations whereas the rise, approaching $CaMnO_3$ is related to the crossover to insulating behavior with the disappearance of doped carriers.

6.3 MAGNETIC MEASUREMENTS

Magnetization measurements (see Figs. 6.3(a) - 3(d)) were performed with magnetic fields of 1T, 2T and 4T for $x = 0.4$, 0.6, and 0.8, and 0.01T, 0.1T, and 1T for $x = 0.9$.

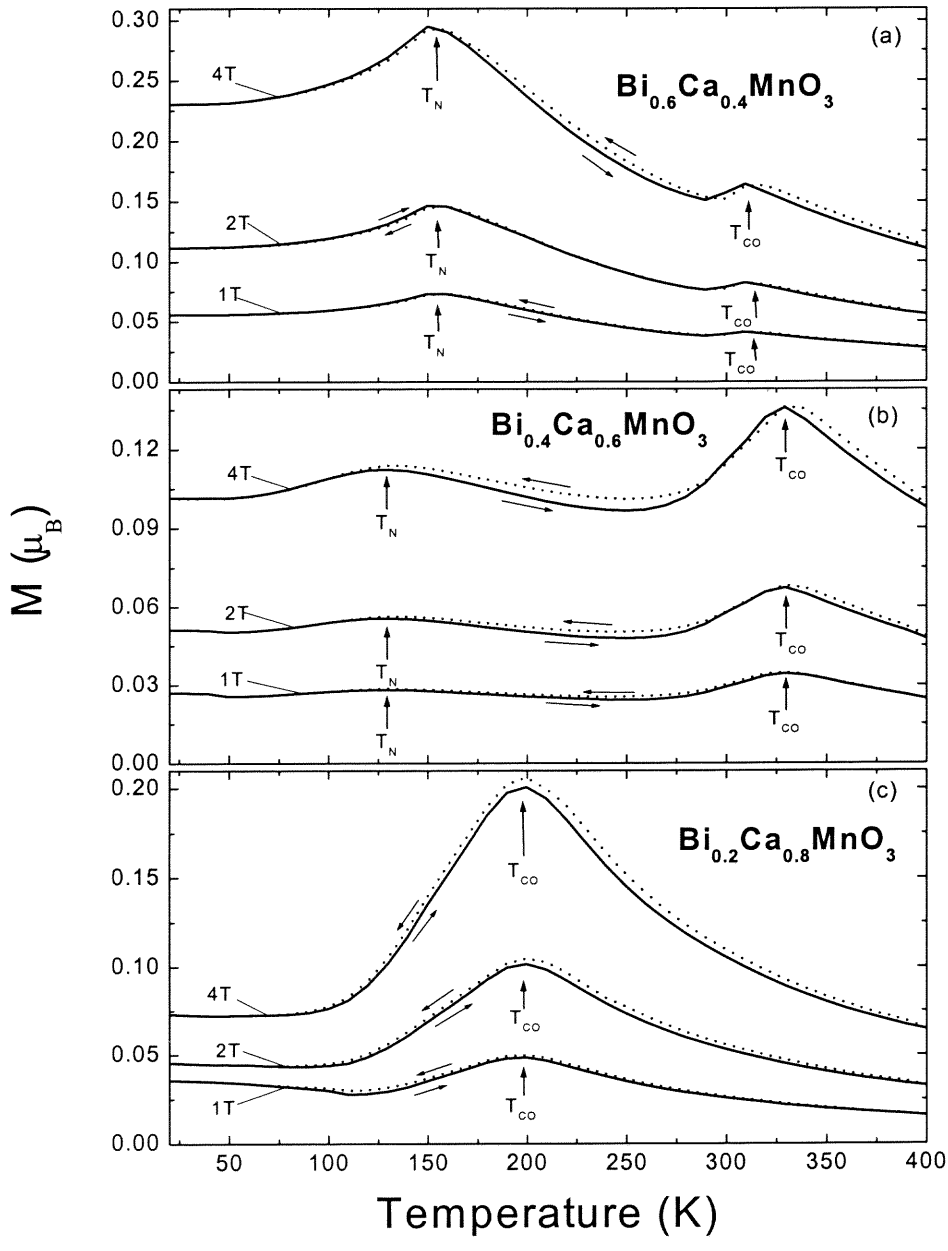

Fig. 6.3(a)-(c) Temperature dependence of the magnetization for x = 0.4, 0.6, 0.8, and 0.9 as (a), (b), and (c). The magnetization measurements at x = 0.4, 0.6, and 0.8 were taken with magnetic fields of 1T, 2T, and 4T for cooling down and warming up.

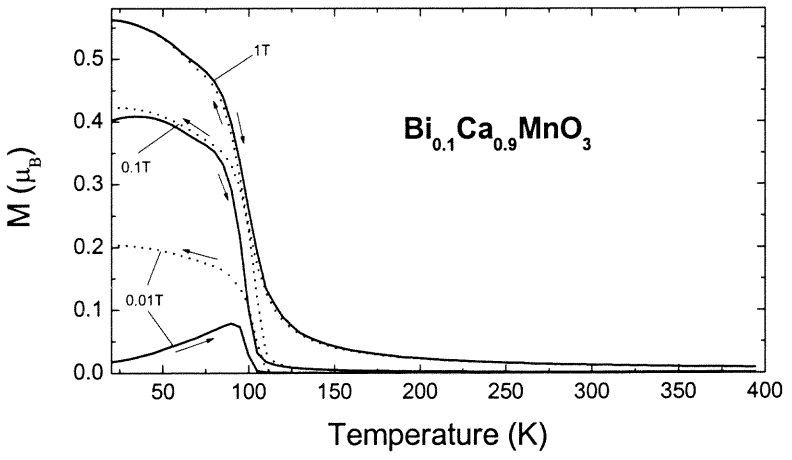

Fig. 6.3(d) For x = 0.9 measurements were made with magnetic fields at 0.01T, 0.1T, and 1T.

The magnetic susceptibility at the high temperatures showed Curie-Weiss type behavior [$\chi = C/(T+\theta)$] with a FM-like (i.e. negative) θ-value over the $0.4 \leq x \leq 0.95$ as illustrated in Fig. 6.5(a). Here the Curie-Weiss behavior is for temperatures above the c ordering and antiferromagnetic transition temperatures. Thus this high temperature range appears to be dominated by local ferromagnetic fluctuations (FMF) that are presumably mediated by Mn^{3+}/Mn^{4+} hopping-induced double exchange interactions. With decreasing temperature our x = 0.4, 0.6, and 0.8 magnetization curves (see Figs. 6.3(a) - 3(d)) exhibit distinct maxima at the charge ordering temperatures (T_{co}) indicated. The neutron scattering results of Bao *et al.* [119] and Turkevich and Plakhtii [191] (on a x = 0.82 material) have nicely correlated such maxima with the suppression of the FMF when the charge ordering freezes out the hopping mechanism. In the charge-ordered phase, AF superexchange interactions dominate, leading to an AF ordering at a temperature (T_N) in the 129K-171K range. T_N is identified with a lower temperature local-magnetization maximum. In the x = 0.8 material the signature of the AF-ordering is perceptible only as

a subtle shoulder on the low temperature side of the CO related peak in the magnetization (see Fig. 6.3(c)).

The CO phase is suppressed for x values above ~ 0.85. Our x = 0.9 magnetization curves, for example, reflect the development of a robust net moment, which depends on the field strength, below a magnetic ordering temperature near 110K. The onset of AF type order in this temperature range is common to materials with $0.85 < x \leq 1.0$ in this system as is the appearance of a net FM moment in a magnetic field. This FM moment has been attributed in the past to FM-interaction induced moment canting. However the magnitude and nonlinear field onset of the FM moment varies strongly in this $0.85 < x \leq 1.0$ range as illustrated by the H = 1T moment variation vs. x (from our and other work) in Fig. 6.5(b). [140] The rapid rise in the FM moment as x increases through 0.85 marks the exit from the CO-AF state. The similarly rapid magnetization drop near x = 0.95 correlates with the suppression of a FM-θ value (high-T FMF) in the same range. As has been noted previously, the θ value of the x = 1.0 material is several folds larger than the AF-T_N, suggesting possible low energy scale nonmagnetic (covalency) effects in the pure Ca material.

The nonlinear field dependence of the magnetization in $CaMnO_3$ and its response to electron doping has been touched upon, (although too briefly) in the literature. The roles of magnetic frustration, AF-domain-spin-canting,[188] homogeneous canted antiferromagnetic (CAF) order, and (most recently) local scale FM/AF coexistence have all been brought up in this regard,[126] In Fig. 6.4 we illustrate a subtle field dependent behavior in these BCMO materials which may reflect a competing FM component in the CO/AF state of this system.

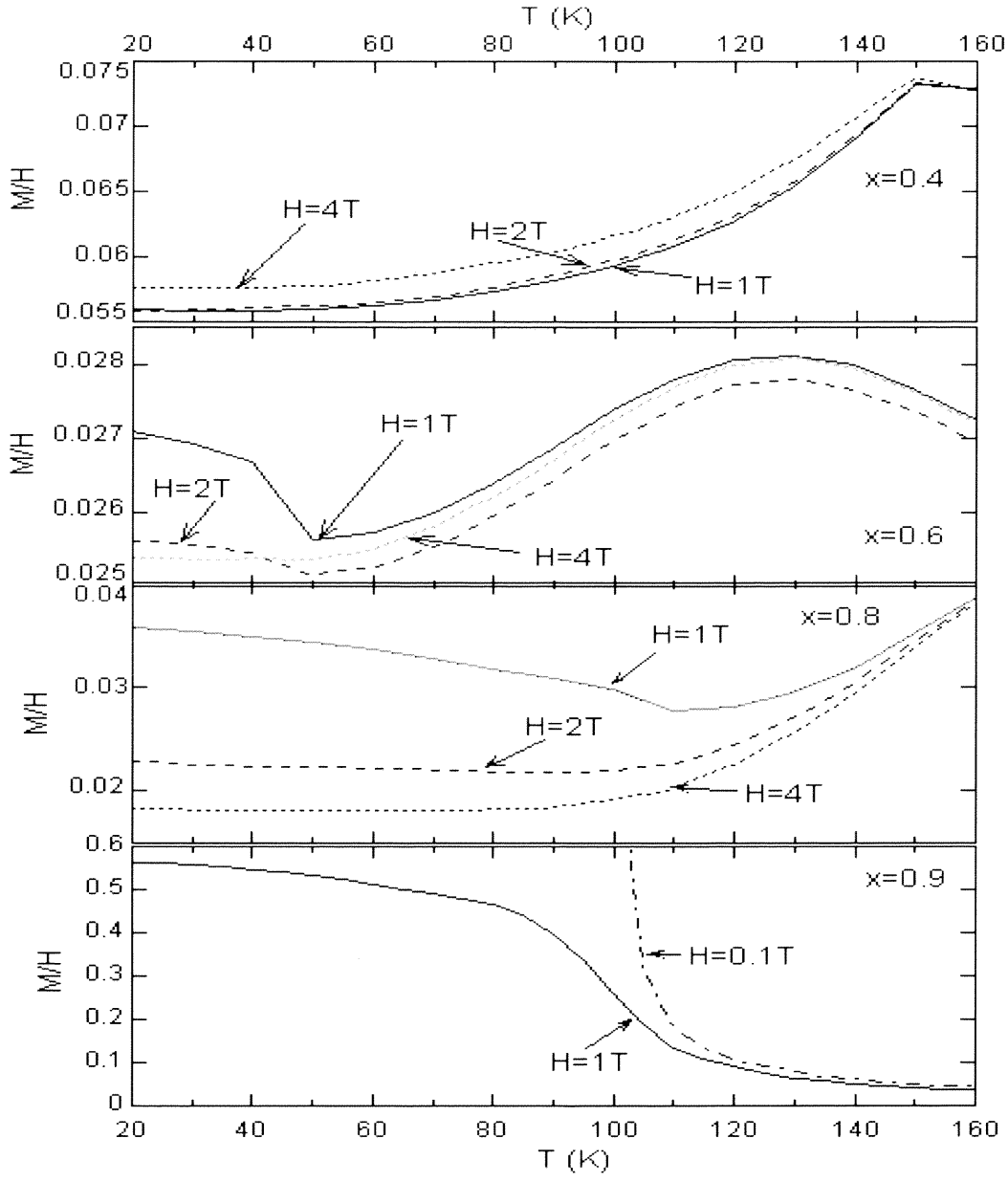

Fig. 6.4 The finite field susceptibility (M/H) in units of emu· mol^{-1}· T^{-1} in the low temperature ordered phase of the x = 0.4, 0.6, 0.8 and 0.9 materials. Note the nonlinear saturation effects that occur in field (see text).

The M/H curves in Fig. 6.4 represent the finite field susceptibility (as opposed to the differential susceptibility dM/dH) and help to highlight field dependent saturation effects in the magnetic response. For the x = 0.9 material (Fig. 6.4(d)) the M/H curves at

low field (e.g. H = 0.1T) manifest a tremendous response at the ordering temperature. The H = 1T, M/H curve shows a typical FM component response below T_N and its smaller magnitude simply indicates that the FM response saturated at a much smaller field. This type of behavior is the basis for CAF or locally-coexisting FM/AF order proposed for such x > 0.85 range materials.

In a simple AF system, where the field energy is much less than T_N, the field response should be small and M/H would be expected to increase with increasing field (at least until spin flop effects saturate). The M/H curves of the x = 0.4 material in Fig. 6.4 (a) illustrate this type of behavior.

In Fig. 6.4(c) the M/H curves within the CO-AF phase of the x = 0.8 material are shown. There is a small but clear nonlinear field response below about 100-120K in the 1T curve which is saturated in the higher field curves. Comparison of Fig. 6.4(c) and Fig. 6.4(d) shows that this field-effect in the x = 0.8 material is similar in thermal variation, although much smaller in magnitude, to that in the x = 0.9 material. Again in the M/H results for x = 0.6 (Fig. 6.4) a similar (albeit quite small) low – T, low field increase in the response can be seen. For x = 0.6 the energy scale for this effect has moved down to about 50K. If one refers to the 1T susceptibility results of Chiba *et al.* [140], one notes the presence of low temperature FM – moment response in the x = 0.8 and x = 0.85 materials in their CO/AF states. Whether these effects are related to local composition fluctuations, CO/AF – domain interface, or FM-like impurity site effects are at present unclear and further work on these effects is warranted.

6.4 PHASE DIAGRAM

In Fig. 6.5 we summarize our results and previous magnetic results for the BCMO system as a phase diagram. Here the previous work on this system focused either on restricted temperature or composition ranges. Our results augment the previous work and we have carefully attempted to draw together both our and previous results. The high temperature phase is a paramagnet (PM) with ferromagnetic fluctuations (FMF) for the range $x < 0.95$. The loss of FM correlations, approaching the $x = 1.0$ (pure-Ca) material is marked by a dotted line. For the $x < 0.85$ range the Mn^{3+}/Mn^{4+} hopping, supporting the FMF, is quenched upon crossing a line of charge ordering transitions (Tco). With further cooling, in the $x < 0.85$ range, a transformation to a antiferromagnetic (while still CO ordered) ground state occurs below a line of temperatures T_N (in the $110 \sim 160$K range).

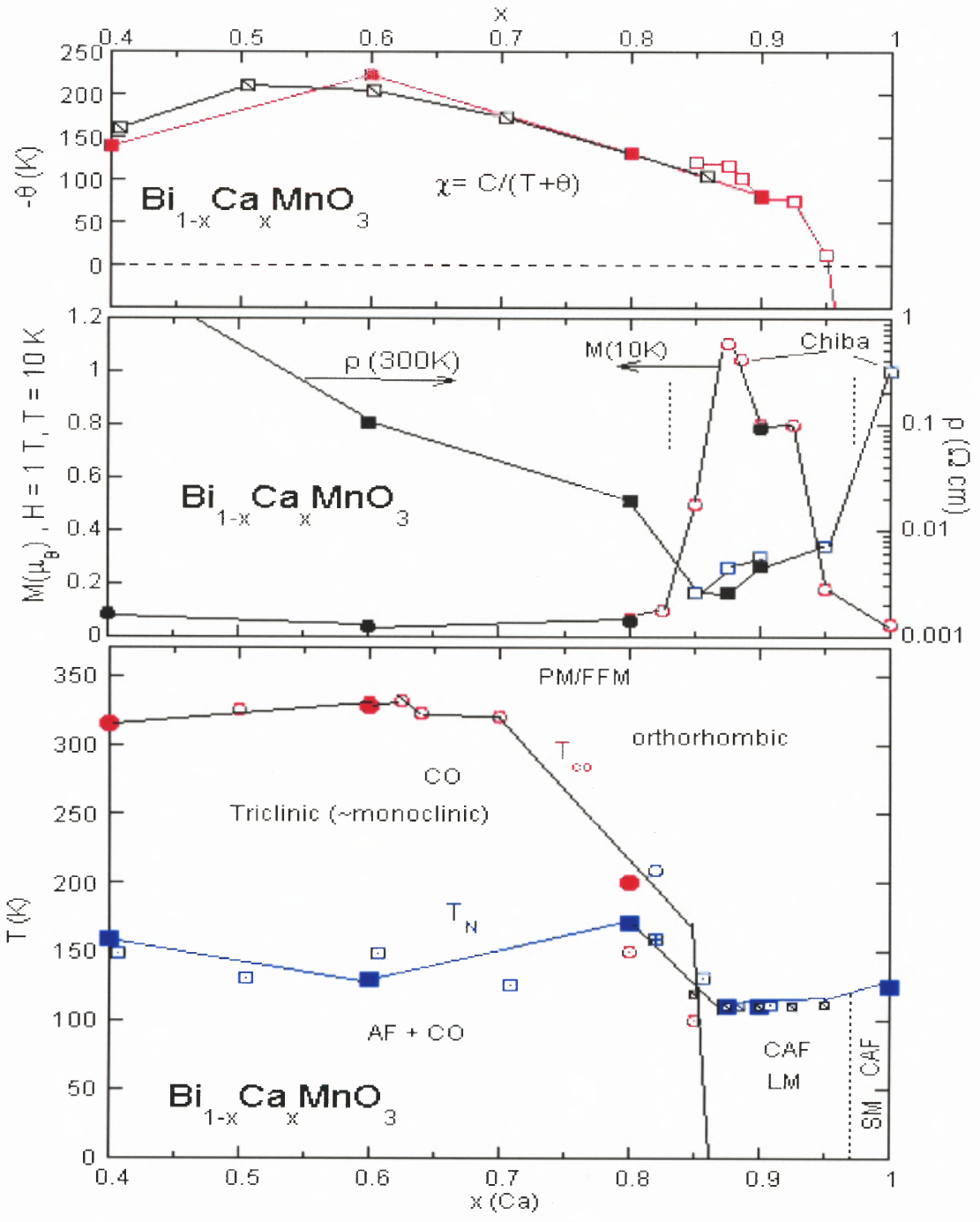

Fig. 6.5 (a) The high temperature Curie-Weiss temperature variation versus x in the BCMO system from our work (filled squares) and from that of Chiba *et al.* (open squares) [140] and Bokov *et al.* (back-slashed squares). [139] Note that the susceptibility ϑ values from our group (and from Chiba *et al.* [140]) were determined for T< 400K (in the PM phase) and from Bokov *et al.* [139] in the 400K < T < 700K range.
(b) The low temperature magnetization (at H = 1 T) and room temperature resistivity variation versus x in the BCMO system from our work (filled squares and filled circles) and from Chiba *et al.* [140] (open squares and open circles) are presented.

(c) A summary phase diagram of the BCMO system. We indicate phases including: the AF ordering temperatures and AF phase, canted AF (CAF) phase with large moment (LM), canted AF (CAF) phase with small moment (SM), high temperature range supporting ferromagnetic fluctuations (FMF) charge/orbital ordered phase and its ordering temperature. Note that the data comes from our work (filled triangles and filled squares), Chiba *et al.* [140] (open squares and open inverted triangles), Bokov *et al.* [139] (back-slashed squares) and Bao *et al.* [119] (open triangle with vertical bar and squares with cross).

It is worth noting that the charge-ordered phase of this system is stable over a wider range of compositions and temperatures than in any of the other manganite systems. In the case of the LCMO system, for example, in the $0.4 < x < 0.5$ range a FM metallic phase has replaced the charge ordering state found here as the ground state. Moreover, in none of the other systems does the CO ordered state persist above room temperature.

The loss of CO correlations for $x > 0.8$ appears to enable the Mn^{3+}/Mn^{4+} hopping and FMF to persist to room temperature, and below, as evidenced by a wider FM Curie-Weiss range for the susceptibility and the strongly reduced resistivity in this x-range. Moreover, a FM component (peaking near $x = 0.875$) also appears to be incorporated into the AF ground state in this range as reflected by the magnetization at 10 K variation versus x in Fig. 6.5(c).

6.5 Mn-K Near Edge XAS

Previous work has shown the Mn-K near edge spectra to be useful in chronicling the Mn-valence/configuration change in the LCMO system. [188] In Fig. 6.6 the main edge (and pre-edge in the inset) spectra for, x = 0.0, 0.5, and 1.0 in this system are shown. It should be noted that: the peak feature, B, shifts markedly between the formally Mn^{3+} and Mn^{4+} compounds with x = 0.0 and x = 1.0; the x = 0.5 material has an intermediate chemical shift while preserving a quite sharp B-feature. Indeed, it has been noted by several authors that the intermediate spectra in this series (e.g. see the x = 0.5 spectrum) are far too sharp to be a superposition of the end point spectra, despite conventional discussions of the systems of magnetic properties in terms of dynamic Mn^{3+}/Mn^{4+} mixtures. [192] This quandary is underscored and compounded by noting that the structure of the x = 0.5 main-edge spectrum changes only very slightly upon entering its low temperature "charge/orbital ordered state". [193]

The Mn-K pre-edge feature spectral strength in this system has also been shown to track the Mn-valence/configuration change. The increase in the pre-edge feature strength, with increasing x, is illustrated in the inset of Fig. 6.6. The presence of three identifiable features a1/a2/a3 in the pre-edge of $CaMnO_3$ has been found to be characteristic of such Mn^{4+} compounds. [188] The cross over to a bimodal a1/a2 structure in $LaMnO_3$ is also clear in the Fig. 6.6-inset.

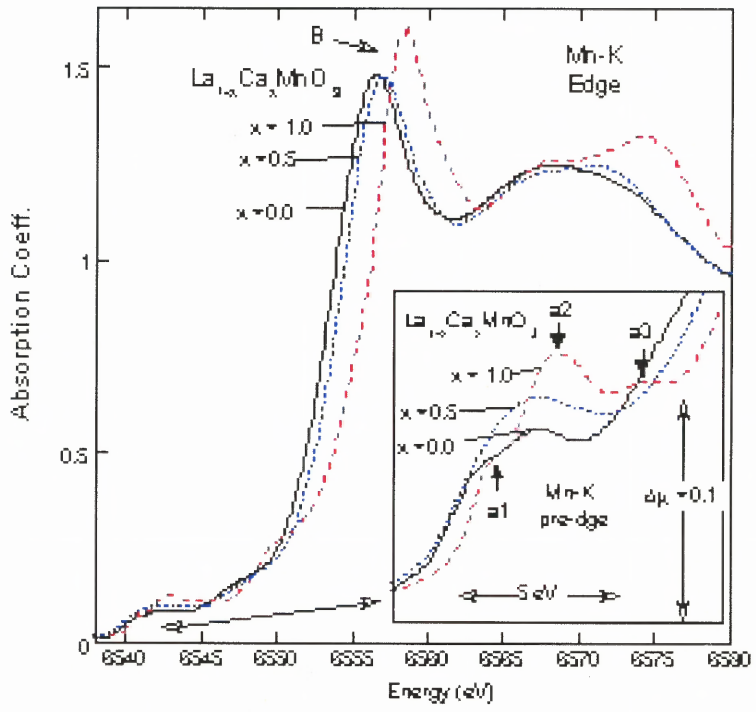

Fig. 6.6 The Mn K-near-edge spectra for the extensively studied $La_{1-x}Ca_xMnO_3$ system, for x = 0.0, x = 0.5, and x = 1.0.

The main-edge spectra of the BCMO series shown in Fig. 6.7 sharply contrasts with these previous results (the differing crystal structure of the x = 0.0 material motivates its separate consideration). While the B-feature of the BCMO series does shift systematically to lower energy with decreasing x, the B-feature also rapidly broadens, and loses intensity to the region of the spectrum labeled A in Fig. 6.7. Interestingly, plotting the B-feature energy position versus x for the (Bi,Ca)-system (see Fig. 6.7-inset lower right) reveals a quite good correlation with the (La,Ca)-system despite the dramatically different edge-structural evolution in the two.

In Fig. 6.7, upper-left, the pre-edge spectra of the BCMO series are shown. The spectral strength of these pre-edges decreases with decreasing x. This is consistent with

the previous results on the LCMO system and with the decreasing Mn-valence. The shift of intensity away from the a2 to the a1 portion of the spectrum is also consistent with that observed in the (La,Ca) system, with decreasing x and with decreasing Mn-valence. The formation of a particularly sharp pre-edge feature in the $BiMnO_3$ is worth noting. In previous studies by our group on defected perovsites, the appearance of such features has correlated with the formation of non-centrosymmetric MnO_6 octahedra. [188] Such local deviations from centrosymmetry would be consistent with the proposed "ferroelectric" distortions in of $BiMnO_3$. [194]

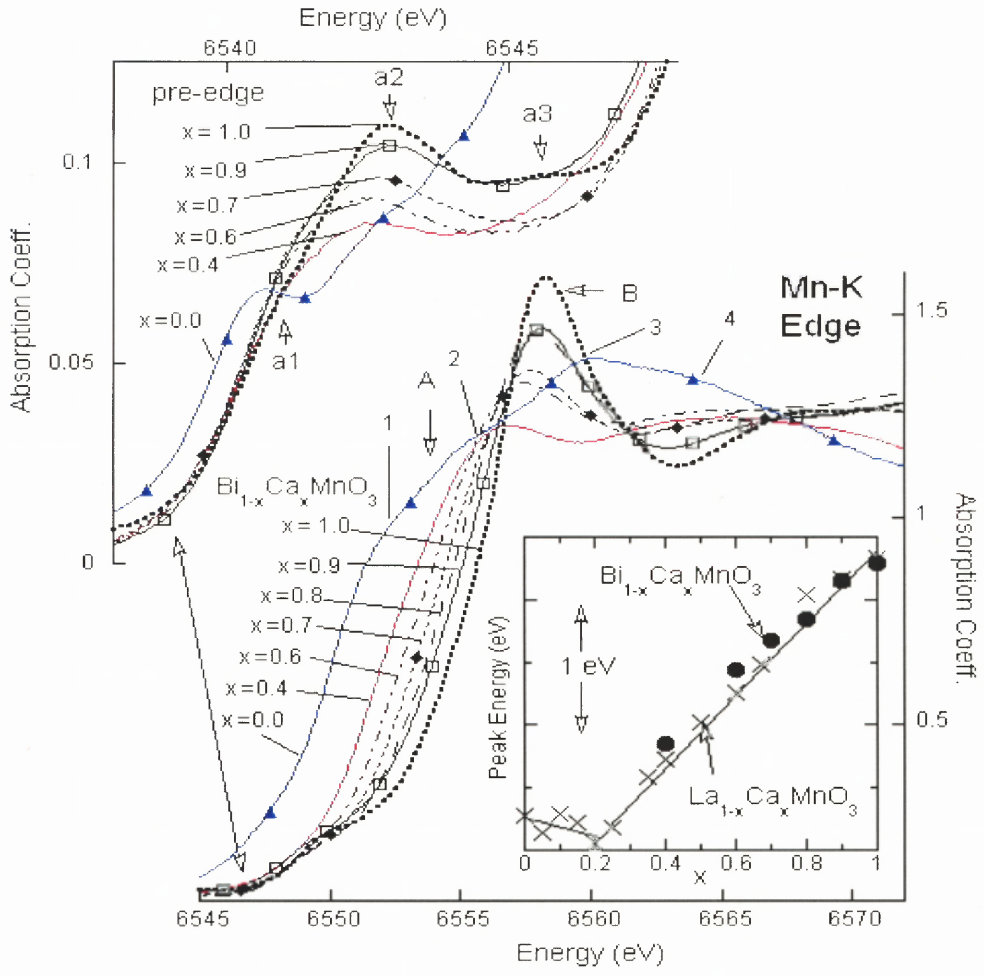

Fig. 6.7 The Mn K-near-edge spectra showing the evolution in the $Bi_{1-x}Ca_xMnO_3$ system with doping. Note the changes in pre-edge and main line amplitudes. The inset shows the evolution position of the main line (B feature) as a function of x in both $Bi_{1-x}Ca_xMnO_3$ (solid circles) and $La_{1-x}Ca_xMnO_3$ (x's) indicating similar changes in valence with doping.

The crystal structure of $BiMnO_3$ is highly distorted. [195] Indeed, it has been suggested that this material is in fact ferroelectrically/ferrodistortively distorted. [194] The Mn-K main-

edge spectrum for $BiMnO_3$ (see Fig. 6.7) displayed multiple unresolved features at the edge (see the labeled features 1-4 in Fig. 6.7). Ti-K edge studies of the $ATiO_3$ (A = Ca, Sr, Ba, Pb) systems [196] have shown that the multiplicity and splitting of the main edge features increase with the increasing distortion in these ferro-distortive/electric perovsites. These main edge splittings persist far above the ferroelectric transition temperatures in these Ti-based materials leading authors to propose reinterpretation of the ferroelectricity as an order-disorder transition of the local distortions. [197] The exceptionally large distortions in $PbTiO_3$ and $BiMnO_3$ have been attributed to the polarizability of the Pb/Bi $6s^2$ states and their incorporation into covalent bonding with the O. [194,195] The pronounced splitting of the Mn-K main edge features is consistent with such local distortion effects.

It is tempting to associate the large modifications of the Mn main edge (upon Bi substitution into $CaMnO_3$) with disordered local distortions of the same sort that lead to the ferroeclectricity in $BiMnO_3$. That such local distortions would persist at x values far from the pure ferroelectric x = 0.0 material is not unexpected in view of the local stability of distortions in the Ti-compounds at temperatures far above the ferroelectric transition. [197] To empirically test this notion, we have formed the difference spectra $\Delta\mu$ = [I(x)-x I(1.0)]/x for the BCMO series where I(x) is the Mn-K edge spectrum at a given x (Fig. 6.8). This procedure "subtracts off " a fraction, x, of sites assumed to remain $CaMnO_3$-like. While the authors believe that the $CaMnO_3$-like sites must in fact also evolve substantially with x, this method does provide a means of identifying subtle features in the B-feature broadening process.

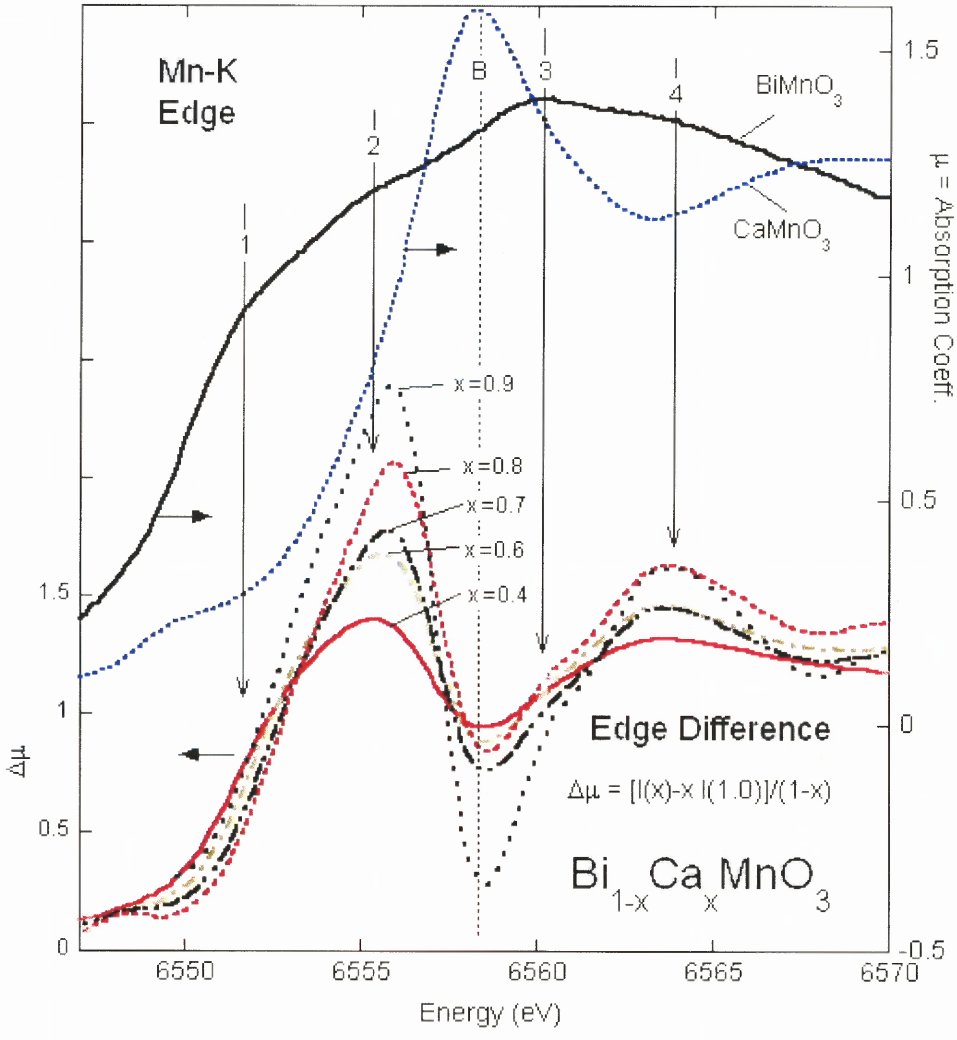

Fig. 6.8 The Mn K-near-edge spectra for $BiMnO_3$ and $CaMnO_3$. Lower set of curves give the difference spectra, $\Delta\mu$, for $Bi_{1-x}Ca_xMnO_3$ at x = 0.4, x = 0.6, x = 0.7, x = 0.8 and x = 0.9. Here $\Delta\mu(E,x) = [I(E,x)\text{-}x\ I(E,x = 1)/(1\text{-}x)]$ was formed to approximate the spectrum of "Bi-modified" sites by subtracting off the fraction (x) of "$CaMnO_3$-like" sites and renormalizing. In doing so the authors only wish to qualitatively highlight the subtle Bi-induced local-modifications and do not intend to imply the actual admixture of two such simple unmodified endpoint states.

Figure 6.8 displays the $CaMnO_3$ and $BiMnO_3$ spectra along with a series of $\Delta\mu$ difference spectra. As alluded to above, the subtraction procedure appears over zealous in the energy region of the $CaMnO_3$ B-feature peak (i.e. the "$CaMnO_3$-like" sites should

not be x-independent). Nevertheless, there are strong structures in the $\Delta\mu$ spectra at energies close to the features labeled 2 and 4 in the $BiMnO_3$ spectrum. There is also a distinct shoulder at the feature-3 energy despite the fact that it rides on the over-subtracted, B-feature dip. At the highest concentration ($x = 0.4$) the buildup of intensity in the feature-1 region is also apparent. Thus our Mn-K main edge XAS appears consistent with the notion that Bi-substitution introduces locally distorted Mn-sites into the BCMO system that are similar to those which lead to the ferroelectric distortion in $BiMnO_3$.

Work by Bridges *et al.* [198] has shown modest but clear temperature dependences in the pre-edge spectra of the LCMO system in the ferromagnetic $0.2 < x < 0.5$ range. Recently, Qian *et al.* [193] have confirmed this effect and also discovered a different thermal dependence accompanying the onset of robust charge/orbital ordering for $0.5 \leq x \leq 0.8$ in the LCMO system.

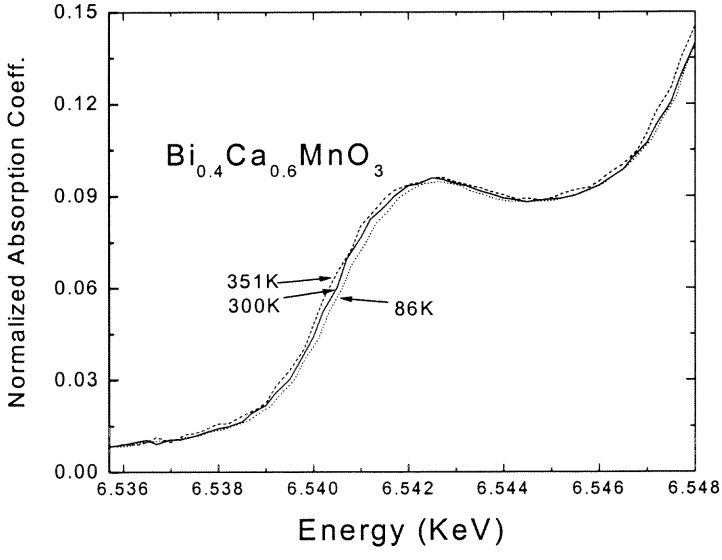

Fig. 6.9 Temperature dependent pre-edge spectra of $Bi_{0.4}Ca_{0.6}MnO_3$. Note that the same trend occurs for $x = 0.4$ and $x = 0.8$.

Figure 6.9 illustrates the variation of the Mn-K pre-edge features of the 0.6 material from above to below the charge/orbital ordering temperature. As observed by Qian *et al.* [193] (for the La-Ca system) the spectral intensity in the lowest energy portion of the pre-edge (the a1-feature region) is reduced modestly in the CO phase. The same effect was seen in the x = 0.8 system but with a much smaller change presumably due to the much weaker charge ordering near the phase's stability limit. The interpretation of these modest charge/orbital ordering induced that spectral changes are unclear at present, but two suggestions will be made here to motivate theoretical calculations. A small increase in the degree of Mn^{4+} admixture accompanying the loss of ferromagnetic interactions upon entering the charge-ordered phase would at least be qualitatively consistent with the pre-edge feature change (i.e. the a1 feature is weakened/shifted-up with increasing Mn-valence). A second possibility involves the orbital component, at the more-Mn^{3+} sites, of the charge-ordered phase. Specifically, the static orbital alignment at these sites should be accompanied by a Jahn-Teller energy up-shift in the unoccupied e_g -states. Since the a1 feature involves such e_g states, the charge-ordered induced degradation of the low energy side of the a1-feature would be reasonable. Clearly the emergence of consistent pre-edge feature changes accompanying the phase changes in these materials should stimulate theoretical calculations of these spectral features.

6.6 Mn-K EXAFS

In order to compare the local structure unique of BCMO samples with LCMO samples, we have performed Mn K-Edge x-ray absorption spectra measurements. Representative raw x-ray absorption spectra data are shown in Fig. 6.10 (Fig. 5.6 shown again for comparison) as the inset for x = 0.9. Note that only small changes in amplitude occur with temperature.

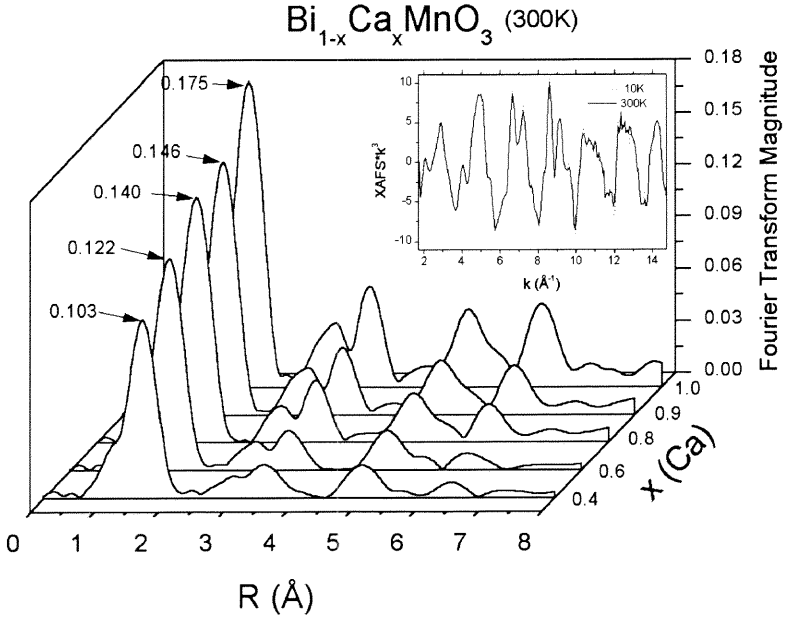

Fig. 6.10. Magnitude of the Fourier transform of XAFS*k^3 (2.5 Å^{-1} ≤ k ≤ 12.3 Å^{-1}) for the system $Bi_{1-x}Ca_xMnO_3$ at 300 K. The first peak (~ 2 Å) corresponds to the Mn - O bond distribution. The second (~ 2.5 Å) and third peaks (~ 3.3 Å) contain the Mn - Ca /Bi and Mn - Mn correlations, respectively. The inset displays raw XAFS*k^3 data for x = 0.9 at 300 K (solid line) and 10 K (dotted line). Note that the temperature dependent changes in amplitude are quite small.

In Fig. 6.10, we show the magnitude of the Fourier transform of the XAFS*k^3 spectra for selected materials in the BCMO system at 300K. The first peak (1 - 2 Å) corresponds to the Mn - O bond distribution. The second (~ 2.5 Å) and third peaks (3.3 Å) contain the Mn - Ca/La and Mn - Mn correlations, respectively. The higher coordination peaks should also be noted. The corresponding curves for the LCMO system at 300K are shown in Fig. 6.11.

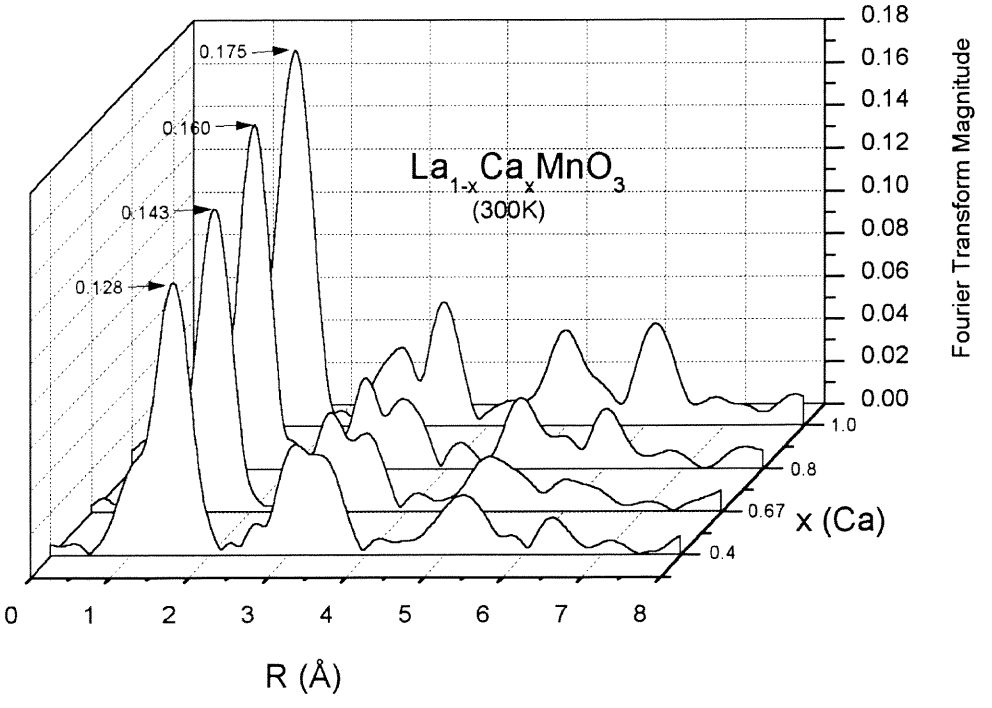

Fig. 6.11 Magnitude of the Fourier transform of XAFS*k^3 (2.5 $Å^{-1} \leq k \leq 12.3$ $Å^{-1}$) for the system $La_{1-x}Ca_xMnO_3$ at 300 K. The first peak (~ 2 Å) corresponds to the Mn - O bond distribution. The second (~ 2.5 Å) and third peaks (~ 3.3 Å) contain the Mn - Ca /La and Mn - Mn correlations, respectively.

The position of the first peak is related to the average Mn-O bond distance and its width is related to the spread in Mn-O bond distances. The amplitude of this peak is

characterized by a Debye-Waller factor type reduction due to static and thermal disorder effects. Thus the Mn-O first shell in the Bi substituted system appears to be disordered on a local scale relative to the LCMO system. The Bi-induced onset of charge/orbital ordering correlations could contribute to this effect; however, work in our group has shown that the first Mn-O shell feature in the $La_{0.5}Ca_{0.5}MnO_3$ spectra do not show significant change upon entering the ordered state. The spectra above and below the charge ordering temperature for the $Bi_{0.2}Ca_{0.8}MnO_3$ material also does not reveal an appreciable first shell modification (Table 6.1). Thus the local distortions in the Mn-O shell in the BCMO system appear to be related to the local effect of the Bi-substitution and not to the longer range charge/orbital ordering distortions. In fact, in systematic temperature dependent on x-ray absorption spectra measurements of the 0.8 and 0.9 systems, no significant changes in the Mn-O peak shape occur with temperature.

Detailed first-shell fits were performed on x = 0.8 and 0.9 as well as on the x = 1.0 and these results are reported in Table 6.1. For high Bi content ($x < 0.8$) the spectra can not be modeled by Gaussian distributions or cumulants (expansion does not converge) because of the high level of local structural distortions. This is consistent with the very large distribution of Mn-O distances found by neutron diffraction in the x = 0 endmember, $BiMnO_3$. [195]

TABLE 6.1 XAFS Derived Structure at x = 0.8, 0.9, and 1.0

Sample	T(K)	R(Å)	σ^2	C3	C4
$Bi_{0.2}Ca_{0.8}MnO_3$	50	1.898 ± 0.002	0.0038 ± 0.0001	$-8.00 \times 10^{-6} \pm 6.75 \times 10^{-6}$	$-5.02 \times 10^{-6} \pm 4.14 \times 10^{-6}$
T_{CO} = 190K	100	1.905 ± 0.004	0.0037 ± 0.0003	$-6.00 \times 10^{-6} \pm 6.08 \times 10^{-5}$	$-2.18 \times 10^{-7} \pm 1.12 \times 10^{-5}$
S_0^2 = 0.81	150	1.908 ± 0.005	0.0032 ± 0.0002	$-1.10 \times 10^{-5} \pm 7.80 \times 10^{-5}$	$-2.50 \times 10^{-5} \pm 1.06 \times 10^{-5}$
	160	1.903 ± 0.006	0.0037 ± 0.0004	$-6.20 \times 10^{-5} \pm 7.23 \times 10^{-5}$	$-6.50 \times 10^{-6} \pm 1.08 \times 10^{-5}$
	170	1.905 ± 0.008	0.0038 ± 0.0004	$-5.30 \times 10^{-5} \pm 1.07 \times 10^{-4}$	$-3.16 \times 10^{-6} \pm 1.28 \times 10^{-5}$
	180	1.924 ± 0.008	0.0031 ± 0.0005	$2.17 \times 10^{-4} \pm 1.11 \times 10^{-4}$	$-2.24 \times 10^{-5} \pm 1.49 \times 10^{-5}$
	190	1.910 ± 0.005	0.0034 ± 0.0004	$1.30 \times 10^{-5} \pm 7.10 \times 10^{-5}$	$-1.71 \times 10^{-5} \pm 1.39 \times 10^{-5}$
	200	1.918 ± 0.007	0.0034 ± 0.0004	$1.26 \times 10^{-4} \pm 1.07 \times 10^{-4}$	$-1.51 \times 10^{-5} \pm 1.13 \times 10^{-5}$
	210	1.927 ± 0.010	0.0031 ± 0.0002	$2.46 \times 10^{-4} \pm 1.40 \times 10^{-4}$	$-1.96 \times 10^{-5} \pm 5.93 \times 10^{-6}$
	220	1.922 ± 0.011	0.0031 ± 0.0008	$1.40 \times 10^{-4} \pm 1.69 \times 10^{-4}$	$-3.03 \times 10^{-5} \pm 1.21 \times 10^{-5}$
	230	1.918 ± 0.008	0.0035 ± 0.0006	$1.04 \times 10^{-4} \pm 1.12 \times 10^{-4}$	$-1.90 \times 10^{-5} \pm 1.33 \times 10^{-5}$
	240	1.920 ± 0.003	0.0034 ±0.00004	$1.10 \times 10^{-4} \pm 4.75 \times 10^{-5}$	$-1.77 \times 10^{-5} \pm 2.37 \times 10^{-6}$
	250	1.915 ± 0.003	0.0036 ± 0.0003	$4.13 \times 10^{-4} \pm 4.88 \times 10^{-5}$	$-1.77 \times 10^{-5} \pm 1.45 \times 10^{-5}$
	300	1.918 ± 0.007	0.0040 ± 0.0004	$9.40 \times 10^{-4} \pm 1.04 \times 10^{-4}$	$-1.54 \times 10^{-5} \pm 1.37 \times 10^{-5}$
$Bi_{0.1}Ca_{0.9}MnO_3$	10	1.895 ± 0.002	0.0053 ± 0.0002	$-3.40 \times 10^{-4} \pm 1.47 \times 10^{-5}$	$4.47 \times 10^{-5} \pm 2.34 \times 10^{-7}$
S_0^2 = 0.88	50	1.898 ± 0.008	0.0050 ± 0.0002	$-2.78 \times 10^{-4} \pm 1.01 \times 10^{-4}$	$4.55 \times 10^{-5} \pm 4.84 \times 10^{-6}$
	85	1.897 ± 0.005	0.0062 ± 0.0001	$-2.77 \times 10^{-4} \pm 9.18 \times 10^{-5}$	$7.83 \times 10^{-5} \pm 1.50 \times 10^{-5}$
	100	1.902 ± 0.012	0.0056 ± 0.0004	$-2.37 \times 10^{-4} \pm 2.38 \times 10^{-5}$	$5.01 \times 10^{-5} \pm 4.95 \times 10^{-6}$
	125	1.889 ± 0.015	0.0062 ± 0.0004	$-3.89 \times 10^{-4} \pm 9.27 \times 10^{-5}$	$5.46 \times 10^{-5} \pm 1.62 \times 10^{-5}$
	150	1.902 ± 0.002	0.0057 ± 0.0011	$-2.50 \times 10^{-4} \pm 5.73 \times 10^{-5}$	$5.19 \times 10^{-5} \pm 1.62 \times 10^{-5}$
	220	1.903 ± 0.003	0.0056 ± 0.0003	$-2.01 \times 10^{-4} \pm 7.81 \times 10^{-5}$	$5.31 \times 10^{-5} \pm 7.81 \times 10^{-5}$
	300	1.898 ± 0.003	0.0054 ± 0.0004	$-3.26 \times 10^{-4} \pm 1.63 \times 10^{-5}$	$5.20 \times 10^{-5} \pm 6.10 \times 10^{-6}$
$CaMnO_3$	300	1.885 ± 0.003	0.0037 ± 0.0001	$-1.79 \times 10^{-4} \pm 5.69 \times 10^{-5}$	$7.91 \times 10^{-6} \pm 2.57 \times 10^{-6}$
S_0^2 = 0.90					
$CaMnO_3$ XRD (Ref. of 216)	300	1.899			

Referring again to the BCMO results in Fig. 6.10, the higher shell Mn-Bi/Ca and Mn-Mn coordination peaks are seen to be systematically reduced in amplitude with increased Bi content and in Fig. 6.11 they were compared to the LCMO system. This implies that the higher Bi concentration samples are increasingly disordered. Again the potential role of charge/orbital ordering in this disordering-effect must be considered. Work in our group has shown that the third shell (Mn-Mn) feature is strongly reduced in the ordered (low temperature) phase of the $La_{0.5}Ca_{0.5}MnO_3$ material. Thus the increasing higher shell disorder (with increasing Bi-content) in BCMO system would appear to involve a charge/orbital ordering contribution in addition to the local Bi-distortion contribution. Hence, local disorder induced by the Bi $6s^2$ lone pairs stabilize charge ordering over a large doping (x) range and suppresses the e_g hopping mediated metallic state.

6.7 Conclusion

Systematic structural, magnetic, and transport studies on the BCMO system were reported for the doping range $x \geq 0.4$. These measurements were correlated with x-ray absorption spectroscopy measurements. The XAS measurements clearly indicate that increasing Bi content in $CaMnO_3$ stabilizes increasing Mn^{3+} character similar to the LCMO system. However, the XAS results also indicate that very substantial local distortions about the Mn sites accompany the Bi substitution in contrast to the LCMO system. Indeed, the x-ray diffraction data reveal splittings consistent with lower symmetry cells as Bi content increases.

The phase diagram of the BCMO system (and the magnetic and transport properties on which it is based) resembles the LCMO system in some aspects, and differs from others. The similarities to be noted are as follows. At room temperature FM interactions and enhanced electrical conductivity (decreased resistivity) are rapidly stabilized by small levels of A^{3+} substitution. FM fluctuations dominate the high temperature region for $x \leq 0.95$. A robust FM component is incorporated into the AF ground state with the maximum of this FM component correlating with the maximum conductivity enhancement near $x = 0.875$. A charge/orbital plus AF ordered phase onsets near $x = 0.83$ below which a line of CO ordering transition temperatures (T_{CO}) rises steeply, with decreasing x, in the phase diagrams.

A strong disparity with the LCMO system lies in the substantially more robust character of the charge-ordered state in the BCMO system. Specifically, the charge ordering temperature rises to the 330K range as opposed to about 250K in the LCMO

system. This remains high for x extending down to 0.4 as opposed to T_{CO} declining and the ground state converting to a FM metal below x = 0.5 in the LCMO system. Presumably the local Mn-O distortions stabilize the local charge/orbital ordering process.

In general the FM-metal to CO-ordered insulator transition manifests the most precipitous field sensitive conductivity change in manganite materials. Bi-substitution appears to most efficiently stabilize the CO-ordering to above room temperature. Thus the use of Bi-admixture in materials with high temperature FM-metal transition temperatures may be an avenue to bring these two phenomena into competition in the room temperature range.

CHAPTER 7

EVIDENCE FOR SPIN CLUSTERS AND GLASSY BEHAVIOR IN $Bi_{1-x}Ca_xMnO_3$ ($x \sim 0.875$)

7.1 Introduction

Compared to the $x < 0.5$, colossal magnetoresistance FM region, the $x > 0.5$ region has been less extensively studied. In the range $0.50 < x < \sim 0.875$, one finds a charge/orbital (CO) and AF ordered ground state with insulating behavior. For x above about 0.9, the CO order disappears and the G-type AF order, observed in CaMnO3, appears. [75,76] However, a substantial ground state FM component, originally ascribed to canted AF behavior, appears in this high x range and peaks with significant magnitude near $x = 0.875$. [41(a)-(b),42,43, 44,120,126, 199,200,172,140] More recently, the notion of FM clusters and local phase segregation have been invoked to explain the FM response in this composition range. [201,136, 202] A reduction in the resistivity, yielding values typical of semiconductors, accompanies the peak in the FM moment near $x = 0.875$.

Because of the enhanced moments found in this region of the phase diagram, more recent work has focused on understanding this high Ca region. Neumeier *et al.* [126] suggested that electron-doped $CaMnO_3$ in $0.8 \leq x \leq 1.0$ of $La_{1-x}Ca_xMnO_3$ exhibits magnetic phase segregation with strong competition between the local FM and the long range AFM order, as compared to the standard model of CAF order in this region of the phase diagram. Troyanchuk *et al.* [138(a)] showed that the $Eu_{1-x}Ca_xMnO_3$ system also manifested a FM component in the $0.8 \leq x \leq 1.0$ range. Again, FM/AF phase coexistence was inferred, based on the observed saturation moments. Maignan *et al.* [201] showed that the electron-doped manganite $Sm_{1-x}Ca_xMnO_3$ ($0 < x \leq 0.2$) behaves like a semimetal in

the temperature range 200-300 K. In addition, based on magnetic susceptibility and magnetization measurements, they found evidence for cluster glass behavior for $0.88 \leq x < 1.0$. For example, no saturation of the magnetization was found in fields as high as 5 T. A systematic study of a broad range of materials in the system $L_{1-x}A_xMnO_3$ (L = Pr, Sm; A = Ca, Sr) was performed by Martin, Hervieu, and Raveau. [58] In direct contrast with the hole doped Mn^{3+} rich region results [83], they found that large magnetoresistance in the Mn^{4+} rich region required a small cationic radius. $Sm_{1-x}Ca_xMnO_3$ (SCMO) and $Pr_{1-x}Ca_xMnO_3$ (PCMO) were observed to fall into a class of manganites which are insulators over the entire doping region while $Pr_{1-x}Sr_xMnO_3$ mimics the behavior of the classic $La_{1-x}Ca_xMnO_3$ system. The small-Ca-ion doped systems $Sm_{1-x}Ca_xMnO_3$, $Pr_{1-x}Ca_xMnO_3$ and $La_{1-x}Ca_xMnO_3$ all show a peak in low temperature magnetization near $x \sim 0.9$. The high net moments in these systems were attributed to cluster glass formation based on ac susceptibility measurements. It should be emphasized, however, that neutron scattering measurements on the material clearly showed the presence of G-type AF order coexisting with this FM-cluster glass behavior. [138(a)] Interestingly even in the end-member, $CaMnO_3$, weak ferromagnetism is observed a long with G-type AF order.[138]

In $Bi_{1-x}Ca_xMnO_3$, Chiba *et al.* [140] observed that the low temperature resistivity drops continuously when $CaMnO_3$ is electron-doped with Bi^{3+}, and reaches a minimum at $x = 0.875$ with magnitude characteristic of a semiconductor. At this doping, the Néel temperature approaches the paramagnetic Curie temperature (θ) and a maximum saturation magnetization of $1.1\mu_B$ per Mn site (compared to the theoretical saturation value of 3.1 μ_B per Mn site) is observed.

Thus, the substitution region near x ~ 0.875 exhibits anomalous and not yet clearly understood properties in a range of manganite systems. In particular, it is not clear if the large moment found per Mn ion is due to spin canting, spin glass or spin cluster behavior or some more novel magnetic structure.

Extending our recent work on the $Bi_{1-x}Ca_xMnO_3$ (BCMO) system [172], we have focused the present investigation on the anomalous magnetic/transport properties near x ~ 0.875. Low and high field (up to 30 T) magnetization and resistivity measurements were reported. The long-time and frequency dependence of the magnetization have been studied in detail to probe for glass-like behavior. The combined experiments evidence cluster and glasslike behavior (in addition to AF correlations) in this x ~ 0.875 BCMO material (and by inference in the more general class of electron doped manganites).

7.2 Experimental Procedure

Polycrystalline samples of BCMO at x = 0.875 were synthesized by the standard solid-state reaction method. Stoichiometric mixtures of Bi_2O_3, $CaCO_3$ and MnO_2 were ground and pressed into pellets that were then calcined at 1000 °C for 5 hours. After calcination, the samples were reground and sintered at 1200 °C in air. This was repeated at 1250 °C.

DC magnetization measurements were performed with a Quantum Design SQUID magnetometer (MPMS-XL) between 4.2 K and 300 K in fields up to 50 Oe. AC susceptibility was measured by a Quantum Design MPMS (1 Tesla model with ultra-low field options).

The high field magnetization and resistivity measurements (up to 30 T) were performed using the Cell #8 32 mm bore magnet at the National High Magnetic Field

Laboratory. A vibrating sample magnetometer (VSM) was used for magnetization measurements and the standard four-probe method for resistivity was employed.

7.3 RESULTS

7.3.1 Low Field Magnetic Response

Recent interest in hole doped (Mn^{3+} based) manganate materials stems from their ferromagnetic and magnetoresistive properties. The occurrence of FM-like interactions has naturally broadened this field to electron doped (Mn^{4+} based) manganates. We have chosen the x = 0.875 composition, of the $Bi_{1-x}Ca_xMnO_3$ system for study since it represents the optimal composition with maximum magnetic moment. [140] The sharply peaked magnetization is emphasized in the inset of Fig. 7.1 where we show the magnetization (in Bohr magnetons per Mn ion at H = 1 T) as a function of doping. The data from this work (solid squares) are compared to the previous work of Chiba *et al.* [140] For the LCMO system, a similar maximum in the magnetization was also reported. [126,143,199]

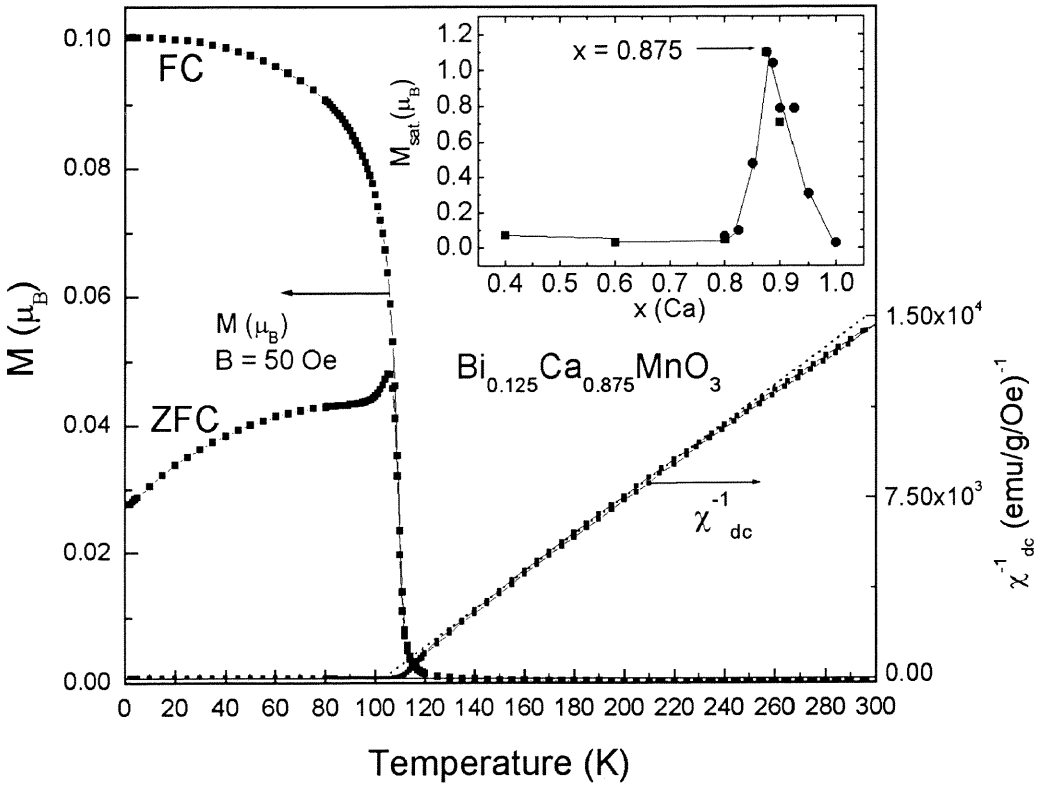

Fig. 7.1 The magnetization curves, taken with increasing temperature, under zero-field cooled (ZFC) and field cooled (FC) for $Bi_{1-x}Ca_xMnO_3$, x = 0.875. The FC curve shows the onset of the FM-like moment below the ordering temperature. The inverse magnetic susceptibility (χ^{-1}) versus temperature illustrates the Curie Weiss behavior with a FM θ where the slightly upper curve is cooling down and lower one is warming up in temperature. Inset shows magnetization (Bohr magneton) versus Ca doping x at 1T. Note that the highest moment is found at x = 0.875. Note that the filled squares are our data and the filled circles are from the data from Chiba *et al.* [140]

The thermal behavior of the ferromagnetic component for this x = 0.875 material is illustrated by the in Fig. 7.1 where the temperature dependence of the low field (50 Oe) magnetization and inverse magnetic susceptibility, χ^{-1} are shown. Fitting the high temperature (170K-300K) χ^{-1} behavior to a Curie-Weiss ([χ = C/(T+θ)]) form one finds with a θ = -100 K. Importantly this FM-θ value is quite close to (but slightly below) the AF ordering temperature T_N=109 K. Below the AF ordering temperature the field-cooled

(FC) magnetization (Fig. 7.1) follows a temperature dependence reminiscent of magnetic order parameter behavior. Indeed T_N = 109 K has been chosen from the negative inflection point of the magnetization rise. The zero-field cooled (ZFC) magnetization has a much more complicated thermal behavior emphasizing the role of thermal/field history in this material, which will be discussed below.

7.3.2 High Field and Small Remnant Magnetization

In Fig. 7.2 we present high field (to 30 T) hysterysis loop magnetization measurements below and above the transition temperature. The magnetization is clearly strongly nonlinear at all temperatures below 175 K. In the 5 to 50 K range, the magnetization appears to be made up of two components: a strongly nonlinear component which saturates (at about 1.25 μ_B) in the 10-15 T range, and a smaller linear component of about 0.0052 μ_B/T. Even at 30 T the full magnetization is 1.41 μ_B far less than the theoretical limit of 3.1 μ_B. Reducing the field from 30 T to 0 yields a very small remnant (see Fig. 7.2(b)), of about 0.08 μ_B, which is suppressed by just a 70 Oe field in the opposite direction. Figure 7.2(b) also displays the partially completed hysteresis loops at a number of temperatures. Neglecting the small remnant, the shape of the nonlinear component of the magnetization below T_N resembles somewhat that of a Brillouin function with varying large moment.

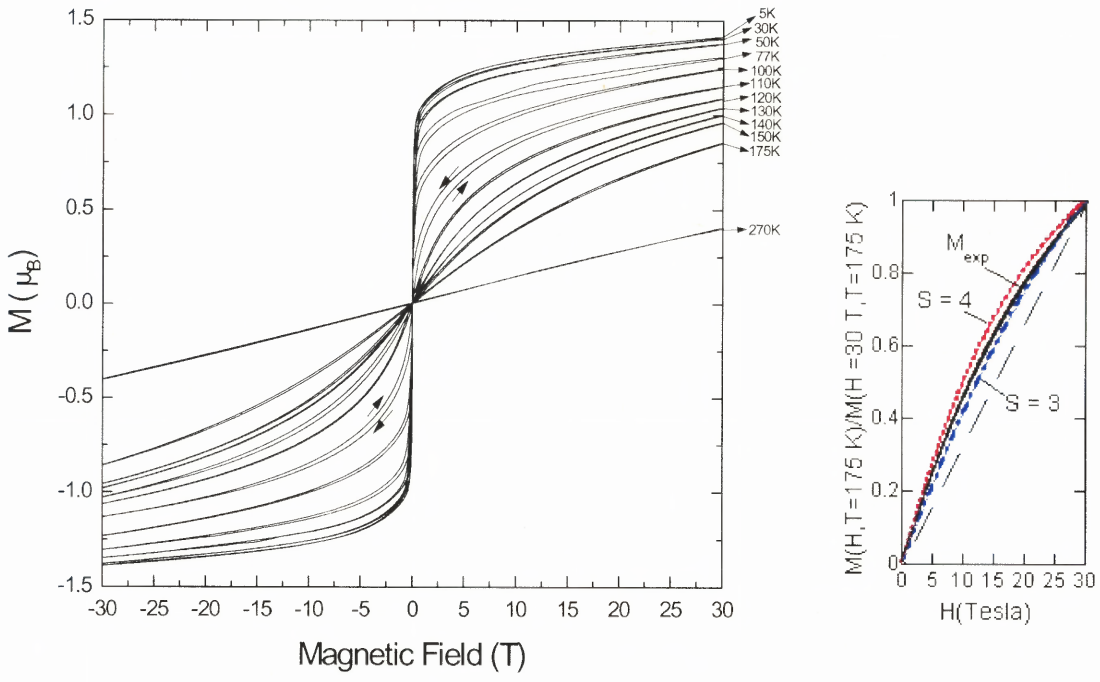

Fig. 7.2a Magnetization (Bohr magneton per a Mn ion) versus magnetic field swept up and swept down to 30T with different temperatures. It clearly shows the magnetic phase transition, i.e., from paramagnetic to ferromagnetic before and after 109 K.(left box) Right Panel: The experimental magnetization, M_{exp}, (normalized to its value at 30 T) at T-175 K versus magnetic field. Also shown for comparison, are the mean-field results calculated for a simple FM material with T_c = 109 K, with spin S = 3 and S = 4.

The strongly nonlinear field dependence of the magnetization persists (albeit decreasing with increasing T) for temperatures well above T_N. Specifically, the M(H) curve at T = 175 K deviates strongly from linear H dependence in the 10 T range. Indeed comparison of the experimental M(H, T = 175 K) data to a mean field ferromagnetic model with an effective spin (S_{eff}) and a Curie temperature T_c=109 K would require S_{eff} > 3 to replicate the curvature of the experimental data. Thus the T = 175 K nonlinearity of

the high field magnetization is clearly inconsistent with the ~ 1.41 μ_B (S ~ 0.8) ferromagnetic component at low temperatures.

7.3.3 Thermal High Field Magnetization

To better understand the behavior exhibited in Fig. 7.2, we display magnetization vs. temperature plots, at a fixed field, in Fig. 7.3.

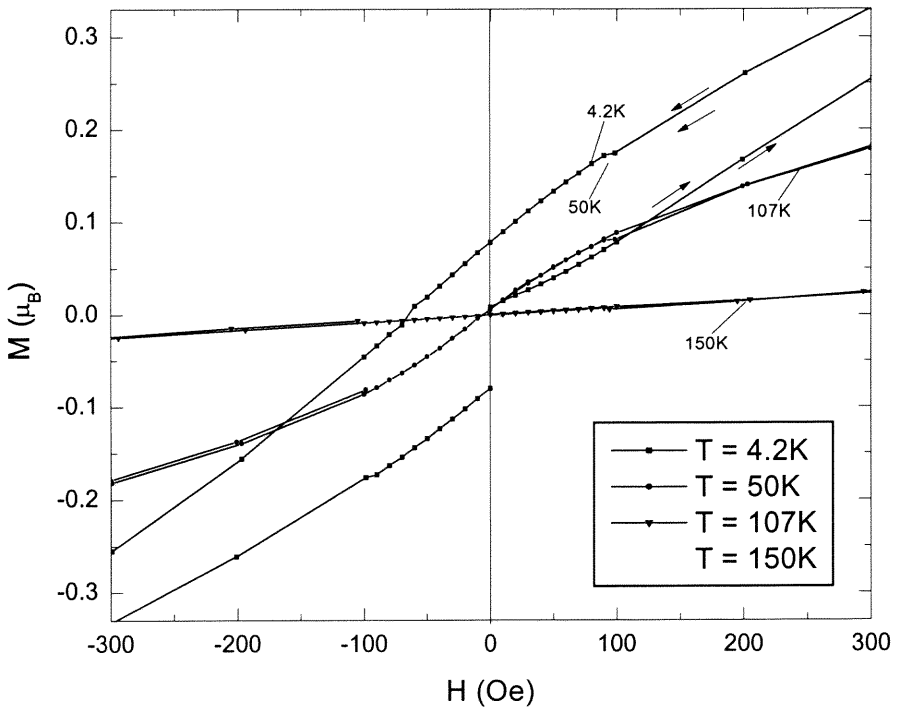

Fig. 7.2b The detailed hysteresis loops with symmetry shape at 4.2 K, 107 K, and 150 K, varying from 1T → 0T → -1T→ 0T →1T. Note that the magnitude of the 150 K curve is 10 times greater than the original curve.

To first order, for H $\leq$ 1T, an order-parameter-reminiscent shape of the M(T) curves is seen, as it was in Fig. 7.1 It should be noted that the saturation values of M(T = 5K,H)

increase substantially in increasing H. For $H \geq 5T$ the vestiges of the order-parameter dependence persist for $T < T_N$ it "rides" on a strongly increasing magnetization in the $T > T_N$ range. A break in the M(T,H) curves near T_N ~105-110 K also appears to persist up to 30 T, suggesting that the ordering onset is surprisingly field insensitive for a material with a strong AF component. Additionally the very substantial field response, for $H \geq 5$ T, appearing at temperatures far above T_N is inconsistent with simple AF order. In a FM material, H is thermodynamically conjugate to the order parameter (the DC magnetization), and accordingly a large field response is induced well above the ordering temperature. Since the susceptibility of our x = 0.875 material is ferromagnetic-like, this large higher-T response is not unexpected despite the AF component in the ground state. In the discussion section we will return to this point.

The inset in Fig. 7.3 displays the magnetoresistance (MR), defined as $MR = (\rho_H - \rho_0)/\rho_0$, where ρ_H and ρ_0 are the resistivities at fields H and zero, respectively. The MR is increasingly negative below T_N = 109 K. The MR at H = 4 T and at H = 30 T were found to be approximately -55% and -90%, respectively.

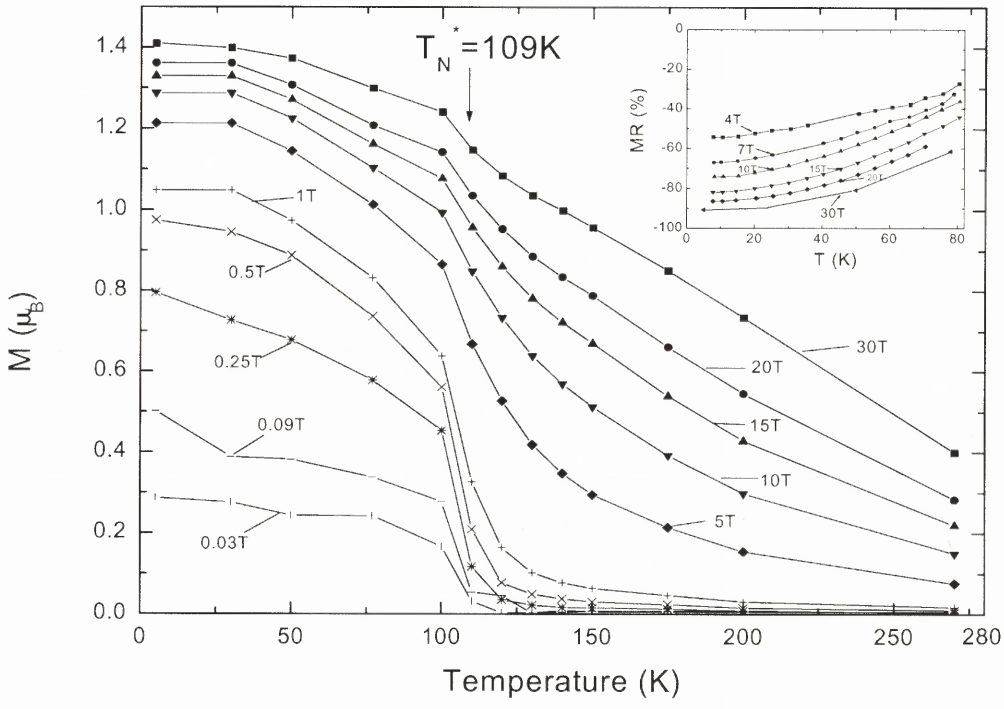

Fig. 7.3 Temperature dependence of the magnetization induced the magnetic field up to 30T. The magnetic transition occurs at T = 109 K. The inset displays magnetoresistance (MR). It is noticeable that MR at H = 4T is 55% but at H = 30T is about 90%.

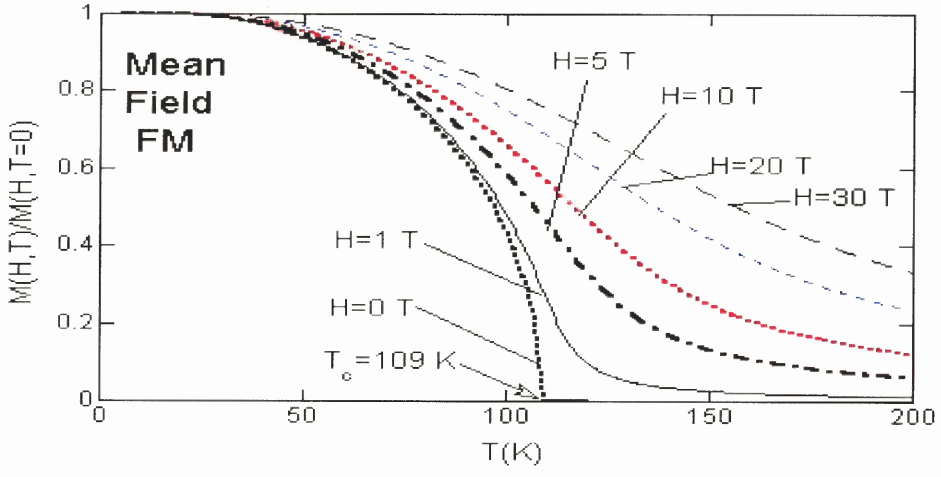

Fig. 7.3b Simulation of magnetiztion by mean field theory.

7.3.4 High Field Magnetization-Magnetoresistance Correlation

The correlation between the field dependence of the magnetization and the resistivity (at temperatures below T_N) is further explored in Fig. 7.4. Note that, as T decreases below T_N, the maximum magnetization does not vary significantly, while the zero field resistivity, and magneto resistance increase enormously. Also while the magnetization is nearly saturated at 2 T, the resistivity manifests large changes out to 15-20 T. The large low field magnetoresistance typical of inter-grain tunneling in ferromagnetic materials appears not to be important in this material. [29, 203]

To clarify the magnetoresistance of this material we show the resistivity in fields up to 30 T as a function of temperature (for $T < T_N$) in Fig. 7.5. At $H = 0$ the resistivity appears similar to a doped semiconductor with some localization operative for the doped electrons. The absence of a $T \rightarrow 0$ K divergence in the resistivity indicates itinerant (albeit strongly scattered) electronic states. The largest field effect is the dramaticreduction in the low temperature resistivity-rise. This effect would be consistent with a field-induced reduction in the degree of doped electron localization (a reduction in scattering). If one views the localization as electrons retarded (but not trapped) by local pinning site potentials, then the field effect could be seen as lowering the depth of these potentials and extending the spatial range of the electronic states. Greater electron hopping and a lower resistivity would result from such a mechanism.

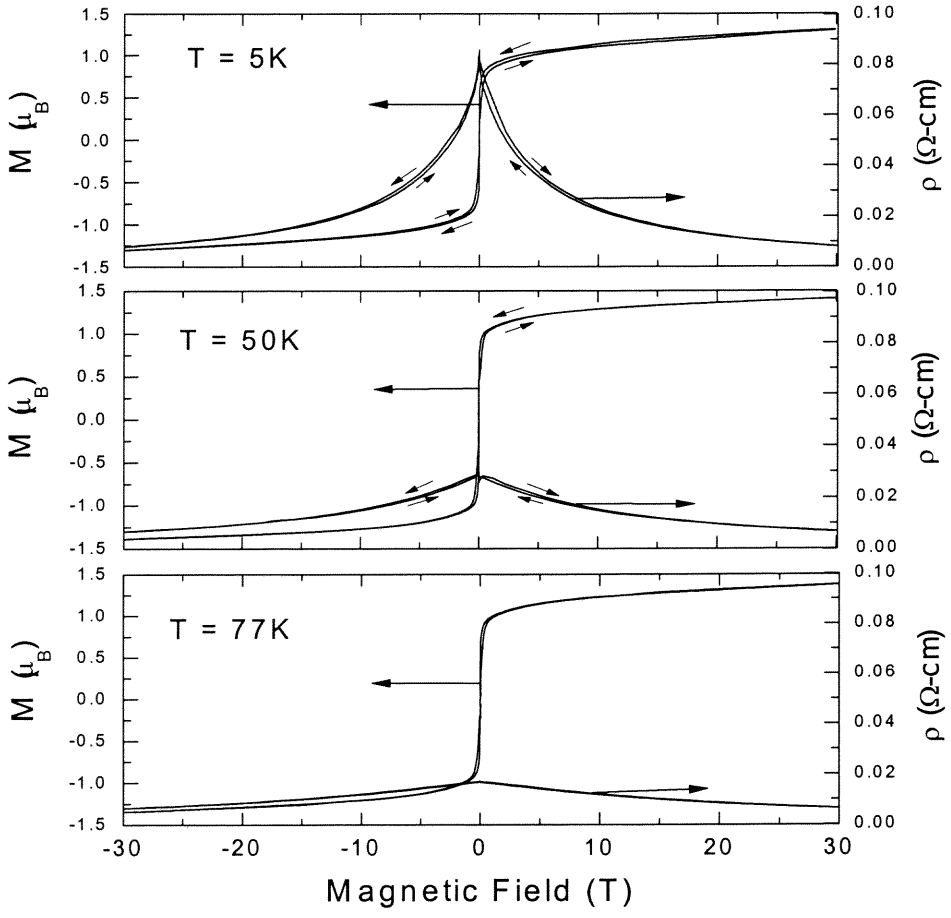

Fig. 7.4(a) Magnetization (Bohr magneton per a Mn ion) and Resistivity correlation at 5K applied fields: 0T → 30T → 0T→ -30T → 0T. (b) Magnetization (Bohr magneton per Mn ion) and Resistivity correlation at 50K applied fields: 0T → 30T → 0T→ -30T → 0T. Note that while the magnetization is constant, the resistivity is reduced. (c) Magnetization (Bohr magneton per Mn ion) and Resistivity correlation at 77K applied fields: 0T → 30T → 0T→ -30T → 0T. Note that while the magnetization is constant, the resistivity is largely reduced.

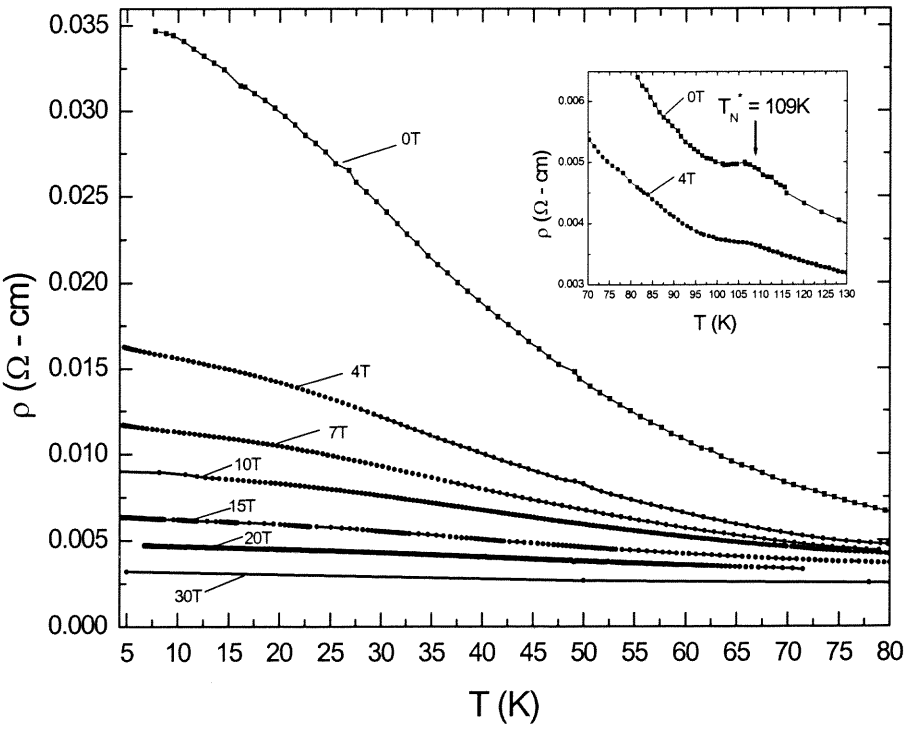

Fig. 7.5 Electrical resistivity versus temperature when applied up to 30T. The magnitude of resistivity near 30T indicates semiconductor-type behavior. No negative magnetoresistivity up to 30T was found. The inset shows the anomalies of resistivity at 106K in 0T and 4T with tiny shoulder. Note that the transition temperature is near 109K.

In the inset of Fig. 7.5, small but reproducible structures in the resistivity curves near the AF ordering temperature, at 0 and 4 T, are shown. The downturn in the resistivity upon entering the AF state is reminiscent of the critical resistivity anomalies at the AF ordering temperature caused by the loss of spin disorder scattering. The small size of this effect is consistent with the probable dominance of localization over spin disorder scattering in these materials. The field degradation of this anomaly would be

consistent with a field induced suppression of spin scattering above the ordering temperature.

7.3.5 AC Susceptibility and Time Tependent Magnetization

In general, history/time dependence of the magnetization (e.g. see the FC and ZFC magnetization curves in Fig. 7.1) is often invoked as evidence for magnetic-glass behavior such as spin glass, cluster-glass or mictomagnetism. While very similar behavior is typical of what some authors have referred to as a cluster glass [201, 202, 204, 205, 206, 207, 208, 209, 210, 211], this issue is clearly still an open one. (For comparison see a recent example of cluster glass behavior: the Co based perovskites $La_{0.5}Sr_{0.5}CoO_3$ [202, 205, 209, 210]). To experimentally address the potential glassy character in our x = 0.875 BCMO material, we have measured both the frequency dependent AC susceptibility (see Figures 6a and 6b, and the time evolution of the ZFC moments (see Fig. 7.7). As we will see our ac-χ results indicate a strong coupling of the magnetization to the AF order parameter. Whether this coupling arises through AF spin canting or a more sophisticated ferromagnetic cluster coupling is not clear. The results will also show time dependent and dissipative behavior which could be related to either AF-domain or glassy effects. In our discussion we will lean toward a canted AF-domain interpretation.

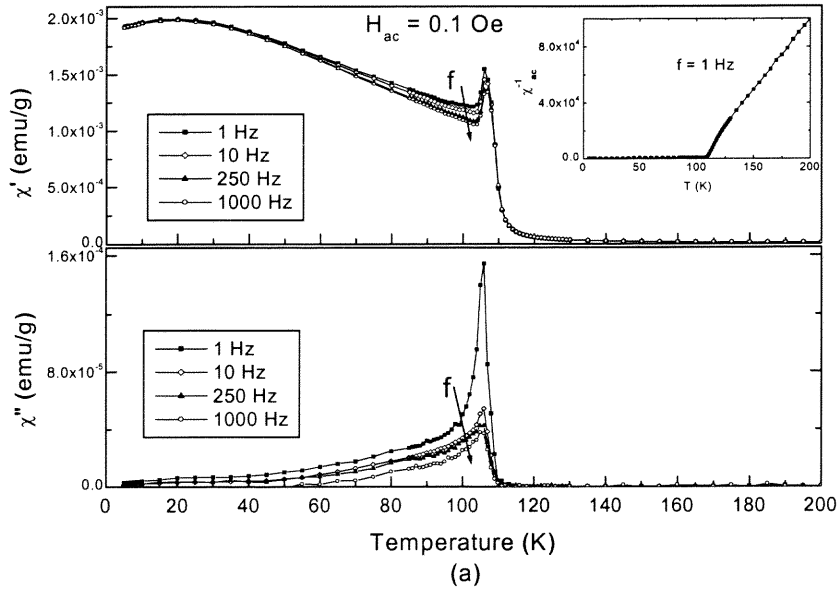

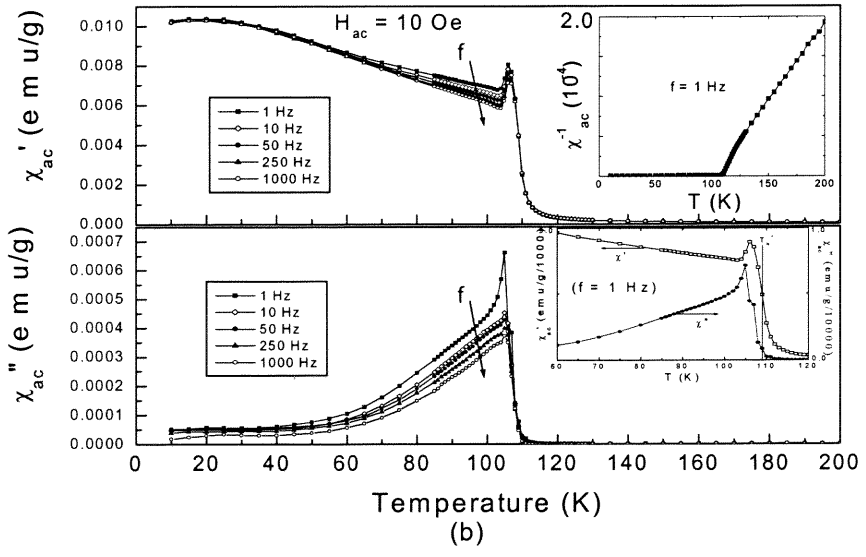

Fig. 7.6 The temperature dependence of the real part χ' and imaginary part χ'' of the ZFC. Ac magnetic susceptibilities in varying frequencies, 1 Hz, 10 Hz, 250 Hz, and 1000 Hz under H = 0.1 Oe (a) and 1 Hz, 10 Hz, 50 Hz, 250 Hz, and 1000 Hz under H = 10 Oe (b).

The AC susceptibility $\chi_{ac}(\omega,T)=\chi'(\omega,T)-i\chi''(\omega,T)$, where the χ' is the in-phase and χ'' the out-of-phase susceptibility components.[212] The in–phase, χ' term is the frequency dependent extension of the DC susceptibility in Fig. 7.1 (except of course + to – swings in the field are used). The out-of–phase, χ'' term is a measure of the magnetic energy dissipation in the sample and is often associated with the degree of hysteresis loop energy absorption.

The connection of χ to the $\omega = 0$, DC results is manifested in a number of ways. In the plot of χ^{-1} vs. T, shown in Fig. 7.6(a) (top-inset), the FM-like CW high temperature behavior is clear in precise analogy to the DC-χ^{-1} behavior in Fig. 7.1. Indeed even the details of the estimated ordering temperature of 109 K, and the downward departure of the data, just above T_N, are faithfully replicated in the ac-χ'^{-1} and DC-χ^{-1} behavior. There is also a qualitative similarity in structure between the below-T_N χ' results in Fig. 7.6 and the DC-ZFC magnetization curve in Fig. 7.1: in both, one observes a negative inflection at 109 K, a peak within 5 degrees below T_N; and a change from sharp-concave to slowly-varying-convex curvature between 10-15 K below T_N. The strongly nonlinear increase in magnetic response, with field, (seen in all of the DC results) is also evident even in these low ac-fields. Specifically, comparing the vertical scales in Fig. 7.6(a) and 7.6(b) one finds that χ'(10 Oe) is nearly 5 fold larger than χ' (0.1 Oe). The modest decreases in χ' at higher frequencies are appreciable only in the 50 K< T < T_N range, where the dissipation (χ'') is also large. Finally it is worth noting that the magnitude of χ' at low temperatures reaches (and remains near) a maximum near 20 K. This would

suggest that there appear to be a population of spins/spin-clusters that are free enough to respond to small fields far below T_N.

The behavior of χ'' is related to the dependence of the magnetic energy dissipation in the ordered phase. Figure 6(b)-inset in bottom panel compares the detailed temperature dependence of χ' and χ'' near T_N. The nonlinear onset of χ'' is displaced slightly lower in temperature relative to the χ' onset. Moreover, the sharp peak in the dissipation appears to coincide with the positive inflection point on the low-T side of the χ' peak. This relation is consistent with the growth of ordered AF domains (and therewith the domain uncompensated net moments) below T_N. The downturn in χ' reflects the AF locking of some of the spins and the peaking of χ'' reflects the concomitant onset of hysteresis loop energy dissipation. Here the field coupling to the AF domain is through its net uncompensated moment. As the T is further lowered, the order-parameter and coercive-field for domains increase to far above the ac-field. This leads to the low-T quenching of χ'' as the domain reorientation dissipating freezes out. Similarly comparing the χ'' (0.1 Oe) and χ'' (10 Oe) results one notes a 10-15 fold increase in magnitude which extends over a much wider temperature range in the higher field case. This would be consistent with the large field-induced enhancement of the magnetic response, and with it the ensemble of domains active in hysterysis-loop energy dissipation.

The strong frequency/temperature dependence of χ'' (relative to χ') can also be discussed in terms of the domain effects. Specifically the smaller clusters/domains will have a more rapid response time whereas the larger domains will respond more ponderously. Thus the higher frequency degradation of χ'' should follow the loss of the

number domains able to respond at shorter response times. The precipitous decay of the χ'' (H = 0.1 Oe, f = 1Hz) below its peak perhaps best illustrates both the rapid freezing out of available domains with low-coercive fields and short response times. These detailed correlations should be incorporated into a proper theory of the AF-domain, and of cluster and glass-like effects in this material, however, such a model is not clear at this time.

Certainly some of the ac susceptibility features exhibited here are similar to those exhibited in CG systems; however, there are also disparities. Indeed, it should be noted that there are also substantial disparities (in ac susceptibility behavior) between different so called "cluster glass" systems. [209, 211] Thus portions of the ac susceptibility would appear to fit into the somewhat broadly defined cluster glass category. The presence of a strong underlying AF order would appear also to set this system apart from other CG systems.

An additional measurement to probe for magnetic-glassy behavior is the slow-long term response of the system to an applied magnetic field. In Fig. 7.7 bottom we show the evolution of the ZFC magnetization for wait times t_w = 0, 30, and 300 minutes. The measurements were performed by cooling in zero field, waiting for time, t_w, before applying a 20 Oe magnetic field, and then recording the magnetization as a function of time.

The magnitude of these glassy effects can be seen from the figure to be modest (i.e. a few percent). The magnitudes of the magnetization are also uniformly smaller for longer wait times after the temperature "quench". This indicates a slow relaxation (upon cooling) into a more magnetically frustrated state, which is less responsive to external

field. The magnitude of the time dependent magnetization as a function of waiting time is consistent with that observed in the $La_{0.5}Sr_{0.5}CoO_3$ CG system. [209]

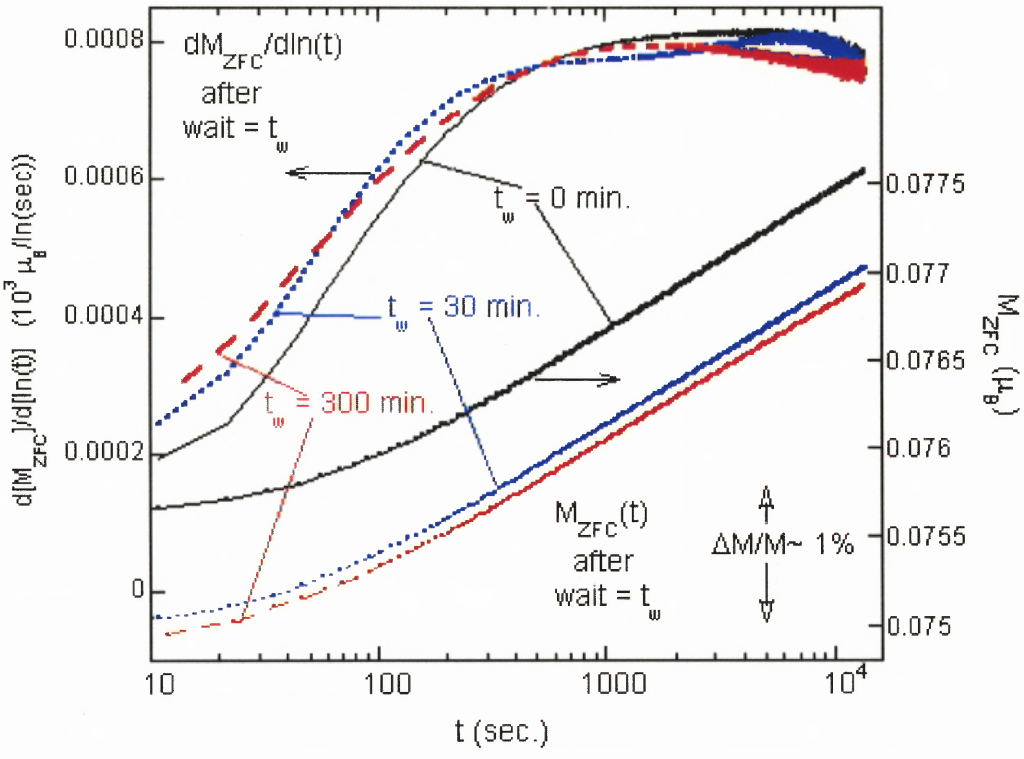

Fig. 7.7 The temporal evolution (logarithmic scale) of the magnetization, and its relaxation rate {d M_{ZFC} / d ln (t) vs log (t)} for 3 different "waiting times" t_w = 0, 30, and 300 min. The sequence of this measurement entailed: cooling the material in zero field to T = 20K; allowing a "waiting time" to transpire; raising the field to H = 20 Oe; and measuring the temporal evolution of the magnetization.

The logarithmic time evolution of the magnetization appears to support a distribution of time scales in the relaxation. The logarithmic-time derivative or the ZFC magnetization evolution is shown in Fig. 7.7 (upper curves). These derivative curves do

not show a characteristic maximum occurring at the wait time, as seen in the SG $La_{0.91}Sr_{0.09}CoO_3$. [202]

Thus the time/frequency dependent magnetic behavior of the x = 0.875 BCMO material does exhibit glassy effects in addition to cluster effects. The observed trends are broadly consistent with cluster glass behavior [202, 213] with the broadness and somewhat imprecise definition of such behavior being recognized.

7.4 DISCUSSION

7.4.1 Cluster Behavior

Several points are worth noting regarding the magnetic properties of electron doped manganites like the $Bi_{1-x}Ca_xMnO_3$ x = 0.875 material studied in this work. G-type AF order in $CaMnO_3$ has been shown to persist in these materials with doping up to levels similar to our x = 0.875 material. Indeed the AF ordering temperature in these electron-doped materials is changed-but-little from that found in the undoped parent compound (i.e., T_N is in the 109-120 K range). Although a substantial net moment does appear at low fields in these materials, the onset of this moment is precisely coincident with the AF ordering temperature (as opposed to higher or lower). Thus G-type AF interactions with an energy scale ~ T_N would appear to be an important component in understanding the magnetic properties of these materials.

The saturation of the resistivity at a finite (though large) low temperature limit would suggest a population of partially electron itinerant doped electrons. The coexistence of electron hopping and AF order are the key ingredients for DeGenes model

of canted antiferromagnetism in these types of materials. One must therefore carefully consider the canted-AF explanations for this materials behavior. Certainly local deviations from a homogeneous canted-AF state would be present, however the occurrence of a distinct glassy state is an open question.

In our discussion of Fig. 7.1 we noted the similarity of the field-cooled magnetization, $M_{FC}(T)$, to a temperature dependence the order parameter below a magnetic transition. We have critically compared the rise in the magnetization below T_N in Figure 1, to the critical behavior $(1-T/T_N)^{\beta}$ with the mean field $\beta = 1/2$, and with $\beta = 1/3$ which is closer to the experimental estimate.[see Fig. 7.8(a)] [214] The $M_{FC}(T)$ is found to rise and saturate more quickly than either of these. Including nonlinear effects in mean field case, by iteratively solving the Brillouin function for the spontaneous field, steepens the temperature dependence toward the experimental data but not sufficiently. Nonlinear effects within a non-mean field $\beta = 1/3$ model should improve still more the notion of a coupling (to first order only) of the low field moment M_{FC} (T) to the order parameter. However, the full, detailed dependence of $M_{FC}(T)$ on the order parameter (as well as T and H) is certainly much more complicated.

This notion would suggest a first order coupling of the low field magnetization (or the effective magnetic moment u_{eff}) to the order parameter for a G-type AF, the staggered magnetization ($M_S = M_A - M_B$, where the A and B refer to the AF sub-lattices). Recall also that we noted, for temperatures well above T_N, the magnetic susceptibility can be fit to a CW-type susceptibility $\chi = C/(T+\theta)$ with θ close to $-T_N$ (rather than the $+ T_N$ value expected for a G-type AF). The below T_N behavior could result from the canted-moment component coupled to the AF order. An explanation in terms of phase segregated FM

regions would appear more demanding. At this juncture we will consider extending the notion of a first order linear coupling between M_S and u_{eff} to $T > T_N$ purely phenomenologically.

Above T_N there is no average sublattice magnetization and no static AF domains. However, there are temporal and spatial AF fluctuations. As T approaches T_N from above, the AF fluctuation divergence is governed by the staggered susceptibility $\chi_S \sim (T-T_N)^{-\gamma}$ [with the $\gamma = 1$ for the mean field value assumed here]. Within our first order coupling assumption, the magnitude of the magnetization should track this divergence, qualitatively explaining the $\chi \sim (T- T_N)$ behavior observed.

To be more quantitative, after Landau and Lifshitz [215] and directly from the fluctuation dissipation theorem, the mean squared order parameter fluctuations above T_N go like

$$< (\delta M_S)^2 > \sim \chi_S. \qquad (1)$$

Since in this high-T-range $\overline{M}_S = 0$, one should have

$$< (M_S)^2 > \sim \chi_S \sim [T - T_N]^{-1}.$$

Invoking the ordered sate behavior, a given AF fluctuation/domain would have an uncompensated effective DC magnetic moment (u_{eff}), with the bigger the M_S the bigger the moment. Specifically, the u_{eff} of such a AF fluctuation, should be coupled linearly to the local staggered magnetization. Thus one would expect the average susceptibility of an ensemble of such moments, each associated with an AF fluctuation, to have a Curie susceptibility,

$$\chi_c = \frac{C_{eff}}{T} \qquad \text{, where } C_{eff} \sim \mu_{eff}^2 .$$

But with a temperature dependent Curie constant given approximately by

$$C_{eff} \sim \mu_{eff}^2 \sim < (M_S)^2 > \sim \chi_S \sim [T - T_N]^{-1}$$

Therefore the explicit T-dependence of this contribution to the susceptibility should approximately be

$$\chi_c = \frac{C_2}{T} \frac{1}{[T - T_N]}$$

The overall susceptibility also should contain a term due to the AF interacting spins (not involved in the uncompensated moments) yielding an overall susceptibility

$$\chi = \frac{C_1}{[T + T_N]} + \frac{C_2}{T[T - T_N]}$$

Given a sufficient number of uncompensated moments, the susceptibility is dominated by the second diverging term, thereby yielding CW behavior with the "wrong" sign for the Weiss-temperature for an AF.

To illustrate the viability of the above notion we show in Fig. 7.8(b)-(c), the experimental inverse susceptibility, along with the predictions of our model. $T_N = 109$ K was fixed and the C1 and C2 were adjusted to track the data. The model-experimental agreement is quite encouraging despite the simplicity of the model. Note that for χ^{-1} the model correctly replicates the high temperature FM-like CW parameter and the

downward curvature away from CW behavior as T approaches T_N from above (see Figure 7.1 and Figure 7.6a-inet).

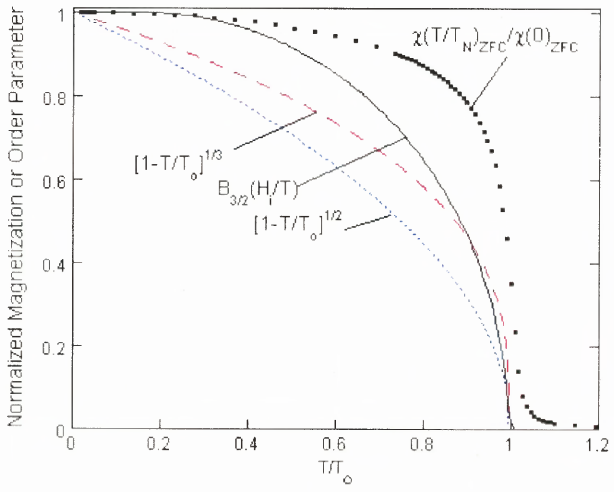

(a)

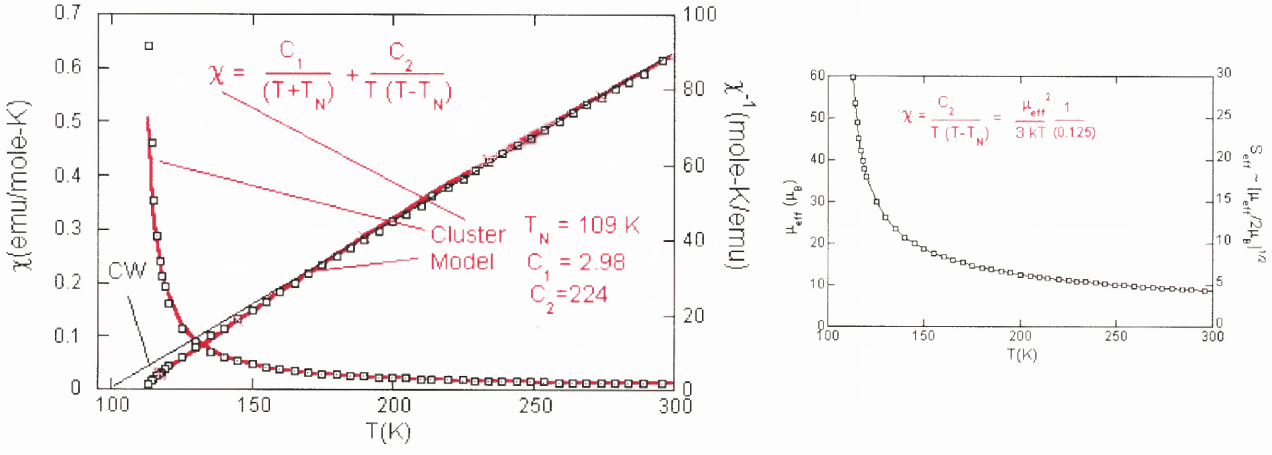

(b) (c)

Fig. 7.8a. Normalized magnetization or order parameters vs. T/T_0.

Fig. 7.8b. The experimental magnetic susceptibility (ψ) and its inverse (ψ^{-1}) plotted as open squares. The heavy solid lines are the model (formula shown in the figure). T_N = 109 K was fixed in accordance with the observed ordering temperature. The C1 and C2 parameters were adjusted to follow the data. The high temperature CW [ψ=C/(T+ϑ)] fit to the data yields ϑ = 99.6 K and C = 2.23 emu/mole-K (or μ_{eff} = 4.23 μ_B).

Fig. 7.8c. The value of μ_{eff} (per doped electron) and S_{eff} in the cluster term from Figure 8a. Note $\mu_{eff} = g^2 S_{eff}(S_{eff}+1) \sim g^2 S_{eff}^2$ has been used.

Using the value of C2 one can estimate the temperature dependence of the effective cluster spin (per dopped electron) is shown in Figure 7.8(c). The notion of the existence of an effective cluster moment (in each AF fluctuation) is also supported by the strongly nonlinear field dependence of the magnetization at 175 K (65 K above the ordering temperature) noted in the discussion of Fig. 7.2(a).

Turning to the below T_N behavior, we note that the strongly nonlinear high field magnetization curves (neglecting the very small remnant) are in fact reminiscent of superparamagnetism exhibited by large collectives of moments acting as clusters (See Figures 7.2(a) and 7.2(b)). To illustrate this we first estimate the linear field response from the highest field slope of the low temperature magnetization data. After subtraction of this linear term, our experimental magnetization curve at 65 K was normalized to its value at 30 T and plotted versus H/T in Fig. 7.9. For comparison plots of the Brillouin function vs. H/T for differing spin values are also shown in Fig. 7.9. Clearly the field dependence must be more complicated however, based on the saturation-shoulder in this comparison, the experimental results would appear to be consistent with an effective uncompensated spin clusters with S on the order of ~ 200.

Within the canted-AF interpretation these moments would be associated with single-AF-domains, each with its own canting direction. The zero-field randomly oriented domains would become aligned with the canting direction along a sufficiently large external field. The magnitude of the canting component of the spin would also be expected to be enhanced in field, upon decreasing the field the domains would have to de-align to produce the low remnant magnetization.

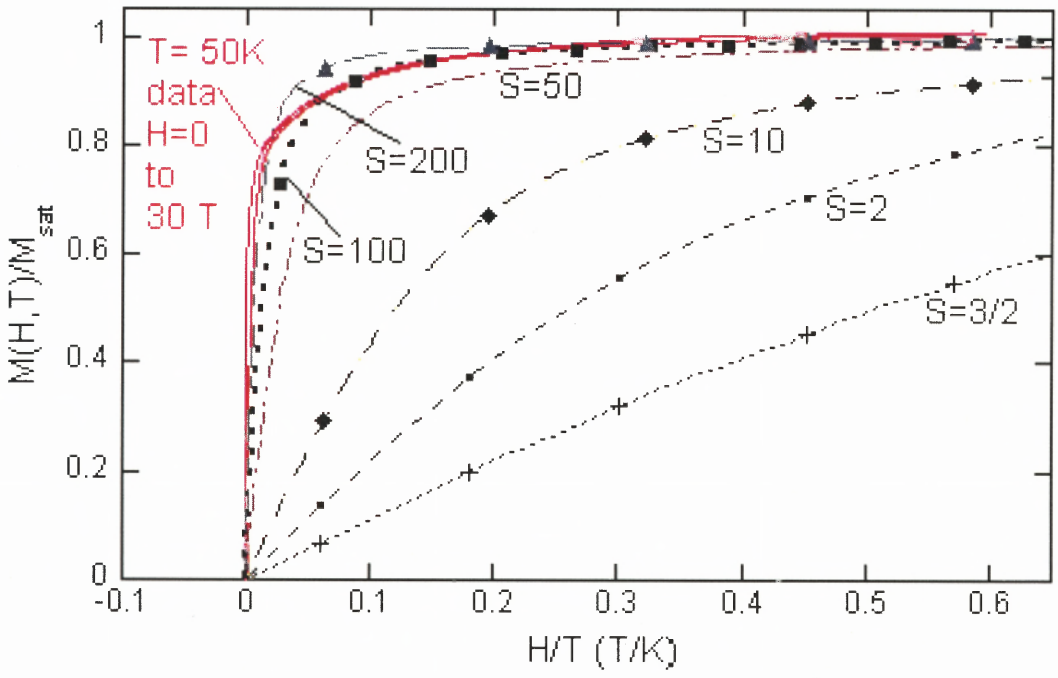

Fig. 7.9 The linear-corrected and normalized experimental magnetizaton (solid line) at T = 50 K and $0 \leq H \leq 30$ T, plotted vs H/T. The linear correction involves subtracting a linear-background term, determined from the high field slope, from the experimental data, M_{exp} {i.e. $M(H,T = 50K) = M_{exp} - H\ (0.0052\ \mu_B/T)$}. The corrected magnetization is then divided by its saturation value at H = 30T (1.21 μ_B in this case) for comparison to the Brillouin function $B_S(H/T)$ with differing spin values S. The Brillouin function plots are all non-solid lines to differentiate them from the experimental results.

Thus above and below T_N the magnetic response would appear to be consistent with the respective presence of AF fluctuations and domains with large net moments. This consistency follows from the first order coupling of the DC magnetization to the AF order parameter (the staggered magnetization). It should be noted that such a liner, $M \alpha M_s$, coupling is explicitly present in the theory of canted antiferromagnetism. [217]

7.5 Conclusions

In this paper we have studied extensively the low-field, high-field magnetic and transport properties of the electron doped BCMO x = 0.875 material. In addition the frequency dependence of the ac susceptibility and time evolution in the low field magnetization have been reported. Experimental evidence of both magnetic clusters and glassy-magnetic behavior in this BCMO for x = 0.875 material was found. Further, the magnetoresistance of this material supports a field-induced enhanced delocalization of the doped electrons in this system.

Extensive magnetic and transport properties of the electron doped $Bi_{0.125}Ca_{0.875}MnO_3$ materials are reported over the temperature range 5 - 300 K and magnetic field range 0 - 30 T. Low field magnetization measurements evidence both an antiferromagnetic state below T_N^* = 109 K in which a ferromagnetic component develops rapidly in modest fields, and ferromagnetic Curie- Weiss behavior at higher temperatures. High field ($-30\ T \leq H \leq 30\ T$) DC magnetization measurements over the 5 K to 300 K temperature range show strongly nonlinear field response below and far above the ordering temperature. The residual magnetic moment and coercive field, in the ordered state, are, however, exceptionally small. These results are discussed in terms of the FM coupling spins into large moment clusters. The possible coupling of these clusters to the AF staggered magnetization (below T_N) and to AF fluctuations (above T_N) is discussed. The high field magnetoresistance (up to 30 T) appears to be governed by a field-induced reduction in the doped carrier localization. The glassy character of the cluster magnetic response was investigated by measuring the frequency dependent ac

susceptibility and time/history evolution of the low field magnetization. Glassy behavior in the cluster response is indeed observed and is discussed in terms of the field modification of the multiple degenerate frustrated-magnetic/doped-carrier states of the system in zero field being modified in finite field. Cluster and Glassy behavior motivation is discussed in Appendix section.

CHAPTER 8

FUTURE WORK

Present work needs to be expanded in further studies as follows:

1. Prepare and study samples in the region ($0.0 < x < 0.25$) to determine the onset of the ferromagnetic insulating state.

2. Study carefully the CO to FM cross over region near $x \sim 0.3$ (make a the sample set for $x = 0.35$ to 0.25 in small steps) using the same experimental approach implemented for the $x = 0.875$. Compare this with the LCMO and PCMO systems at the same doping.

3. Perform temperature dependent x-ray diffraction measurements to probe the charge ordering behavior.

4. Model the energetics of the magnetic ordering by LSDA calculations on $BiMnO_3$ (FM), $LaMnO_3$ (AF) and other Mn^{3+} endmembers. (How does structure influence the stability of the magnetic phase?).

5. Measure the anisotropy of transport in single crystals or films of the BCMO systems. (How are the current flow directions and the magnetic field directions related?)

APPENDIX

Cluster and Glassy Behavior Motivation

In order to illustrate the potential cluster and glassy behavior in these materials we consider a few configurations for a highly simplified, one-dimensional block (domain) of 9 spins, all with magnitude S. We include in this domain two doped interstitial electrons (dots), and two associated preferred pinning sites for the electrons (boxes). An electron between spins causes a ferromagnetic interaction ($-J_F$). Having an electron hop one site away from its preferred site costs an energy E, and hopping further than one site is excluded. All other magnetic interactions are AF of magnitude J. The magnetic field energy is $\pm \mu HS$ per spin aligned/anti-aligned with the external field.

State B in the figure indicates a case where the magnetic and hopping energies are optimized in zero field but which will pay an energetic price in increasing the field. State A maintains the optimum magnetic interaction energy, which is further stabilized in an external field, but at the cost of an electron displaced from its pinning site potential. State C has the highest external field response but at the expense of flipping one AF spin interaction.

In a system made up of a generalization of such blocks, the response to an external field could reasonably be expected to show glassy behavior as the electron hopping and spin flipping occurred by tunneling through their energy barriers. Moreover, the AF ordering can also be viewed as mediating an effective long range interaction between FM defects (i.e. a sort of static-non-damped generalization of the oscillating RKKY interaction in metals). This interaction could be AF or FM depending on the odd or even number of intervening AF bonds (i.e. on the inter-cluster distance). Thus in zero

external field substantial magnetic frustration in the inter-FM-defect interaction would be present leading to additional glassy behavior. In a magnetic field the presence of low energy excitations (i.e. electron displacement or single spin flipping), which induce inter-defect FM interactions, would allow the rapid formation of large clusters of defects all ferromagnetically aligned into a super cluster.

It is worth noting that the field-induced electron hopping excitations (as in the B to A case above) would constitute a broadening of the trap-site potential in an external field. Such a field induced decease in the doped electron localization would provide a mechanism for the large-high-field magnetoresistance. The presence of a large linear component in the M vs. H data at 30 T (below T_N) would also suggest that the spin flip mechanism (case C) is rather unimportant at the fields considered here. Thus the electron hopping induced inter cluster FM coupling would appear to be most important in our system.

REFERENCES

[1] O. A. Kenyon, http://www.cinemedia.net/SFCV-RMIT-Annex/rnaughton/ POULSEN_BIO.html

[2] Eric D. Daniel, C. Denis Mee and Mark H. Clark, Magnetic Recording: The First 100 Years (IEEE Press, New York, 1998).

[3] An original photo from EMTEC, Ludwigshaven, Germany; http://history.acusd.edu/gen/recording/tape.html

[4] J. P. Harris, W. B. Phillips, J. F. Wells, and W. D. Winger, "Innovations in the Design of Magnetic Tape Subsystems, " IBM J. Res. Dev., **25**, 691 (1981).

[5] N. Kihara, F. Kohno, and Y. Ishigaki, "Development of a New System of Cassette Tape Consumer VTR, " IEEE Trans. Consum. Electron., **22**, 26 (1976); Y. Shiraishi and A. Hirota, "Video Cassette Recorder Development for Consumers, " IEEE Trans. Consum. Electron., **CE-24**, 468 (1978).

[6] M. L. Lesser and J. W. Haanstra, "the Random-Access Memory Accounting Machine. I. System Organization of the IBM 305, " IBM J. Res. Develop., **1**, 62 (1957); T. Noyes and W. E. Dickinson, "The Random-Access Memory Accounting Machine. II. The Magnetic-Disk, Random-Access Memory, " IBM J. Res. Develop., **1**, 72 (1957).

[7] D. L. Noble, "Some Design Considerations for an Interchangeable Disk File, " IEEE Trans. Magn., **MAG-10**, 571 (1974);J.T. Engh, "The IBM Diskette and Diskette Drive, " IBM J. Res. Dev., **25**, 701 (1981).

[8] J. W. Toigo, Scientific American, May 2000, p. 59.

[9] S. X. Wang and A. M. Taratorin, Magnetic Information Storage Technology (Academic, New York, 1999), p.188

[10] IBM websites: http://www.almaden.ibm.com/st/projects/magneto/giantmr/; http://www.research.ibm.com/research/demos/gmr/cyberdemo1.htm

[11] J. W. Toigo, Scientific American, May 2000, p. 66.

[12] P. Grunberg, R. Schreiber, Y. Pang, M. B. Brodsky, H. Sowers, Phys. Rev. Lett. **57**, 2442 (1986).

[13] M. B. Salamon, S. Sinha, J.J. Rhyne, J. E. Cunningham, R. W. Erwin, J. Borchers, C. P. Flynn, Phys. Rev. Lett. **56**, 259 (1986); C. F. Maykrzak, J. W. Cable, J. Kwo, M. Hong, D. B. Mc Whan, Y. Yafet, J. V. Waszczak, C. Vettier, Phys. Rev. Lett. **56**, 2700 (1986).

[14] U. Hartmann, Magnetic Multilayer and Giant Magnetoresistance fundamentals and Industrial Applications (Springer, New York, 2000), p.62

[15] M. N. Baibich, J. M. Broto, A. Fert, F. Nguyen Van Dau, and F. Petroff, Phys. Rev. Lett. **61**, 2472 (1988).

[16] S.S.P. Parkin, N. More, K.P. Roche, Phys. Rev. Lett. **64**, 2304 (1990).

[17] G. Binasch, P. Grunberg, F. Saurenbach, W. Zinn, Phys. Rev. B **39**, 4828 (1989).

[18] S.Yamamoto, Y. Nakamura, S. Iwasaki: IEEE Trans. MAG 23, 2070 (1987); A. Berkowitz (Ed.) Magnetic Recording Materials MRS Bulletin XV, 23-72 (1990).

[19] For example, H. Yamamoto and T. Shinjo, "Magnetoresistance of multilayers," IEEE Translation Journal on Magnetics in Japan, **7**, 674, 1992.

[20] S. S. P. Parkin, (unpublished, 1997).

[21] P. Bruno and C. Chappert, Phys. Rev. Lett. **67**, 1602 (1991).

[22] D. M. Edwards, R. P. Erickson, J. Mathon, R. B. Muniz, and M. Villeret, Materials Science & Eng. **B31**, 25 (1995).

[23] S. X. Wang and A. M. Taratorin, Magnetic Information Storage Technology (Academic, New York, 1999), p.165

[24] B. Dieny, V. S. Speriosu, S. S. P. Parkin, D. A. Gurney, D. R. Wilhoit, and D. Mauri, Phys. Rev. B **43**, 1297 (1991).

[25] T. C. Anthony, J. A. Brug, and S. Zhang, IEEE Trans., Magn. **30**, 3819 (1994).

[26] W. F. Egelhoff, Jr., P. J. Chen, C. J. Powell, M. D. Stiles, R. D. McMichael, J. H. Judy, K. Takano, and A. E. Berkowitz, J. Appl. Phys. **82**, 6142 (1997).

[27] S. X. Wang and A. M. Taratorin, Magnetic Information Storage Technology (Academic, New York, 1999), p.166

[28] A. Barthelemy, A. Fert. M. N. Baibich, S. Hadjoudj, and F. Petroff, J. Appl. Phys. **67**, 5908(1990); C. Haas, Phys. Rev. **168**, 531(1968); G. Binasch, P. Grunberg, et al., Phys. Rev. B, **39**, 4828(1989).

[29] H.W. Hwang, S-W. Cheong, N.P. Ong, and B. Batlogg, Phys. Rev. Lett. **77**, 2041 (1996).

[30] J. Belleson and Ed Grochowski, "The era of giant magnetoresistive heads." http://www.storage.ibm.com/hdd/technolo/gmr/fig8.gif

[31] R. L. White, IEEE Trans. Magn. **28**, 2482 (1992); D. M. Edwards, J. Mathon and R. B. Muniz, IEEE Trans. Magn. **27**, 3548 (1991).

[32] J. I. Gittleman, Y. Goldstein, and S. Bozowski, Phys. Rev. B **5**, 3609 (1972).

[33] J. S. Helman and B. Abeles, Phys. Rev. Lett. **37**, 1429 (1976).

[34] Y. Okimoto, T. Katsufuji, T. Ishikawa, A. Urushibara, T. Arima, and Y. Tokura, Phys. Rev. Lett. **75**, 109(1995).

[35] J. C. Phillips, Phys. Rev. **133A**, 1020 (1964); P. M. Tedrow and R. Meservey, Phys. Rev. B **7**, 318 (1973).

[36] A. E. Berkowitz, J. R. Mitchell, M. J. Carey, A. P. Young, S. Zhang, F. E. Spada, F. T. Parker, A. Hutten, and G. Thomas, Phys. Rev. Lett. **68**, 3745 (1992); J. Q. Xiao, J. S. Jiang, and C. L. Chien, Phys. Rev. Lett. **68**, 3749 (1992); A. Milner, A. Gerber, B. Groisman, M. Karpovsky, and A. Gladkikh, Phys. Rev. Lett. **76**, 475 (1996).

[37] J. Brown, Sensors, September 1994, p. 42.

[38] J. M. Daughton, thin Solid Films **216**, 162 (1992).

[39] D. E. Speliotis, J. Magn. Magn. Mater. **193**, 29 (1999); E. Grochowski, IDEMA Adv. Heads and Media Symposium, Santa Clara, CA December (1997).

[40] NIST GMR technology by W. F. Egelhoff *et al.*: http://www.metallurgy.nist.gov/magnet/GMR.htm

[41] (a) S. Jin, T. H. Tiefel, M. McCormack, R. A. Fastnachit, R. Ramesh, and L. H. Chen, Science **264**, 413 (1994); (b) R. von Helmolt, J. Wecker, B. Holzapfel, L. Schultz, and K. Samwer, Phys. Rev. Lett. **71,** 2331 (1993); (c) C. N. R. Rao, Anthony Arulraj, A. K. Cheetham, and Bernard Raveau, J. Phys.: Condens. Matter **12**, R83 (2000); (d) A. P. Ramirez J. Phys.: Condens. Matter **9**, 8171 (1997); (e)Y. Tokura, Y. Tomioka, J. Magn. Magn. Mater. **200**, 1 (1999); (f) C. N. R. Rao and B. Raveau, Colossal Magnetoresistance, Charge Ordering Related Properties of Manganese Oxides (World Scientific, Singapore, 1998); (g) J. M. D. Coey, M. Viret, and S. von Molnar, Adv. Phys. **48**, 167 (1999).

[42] G. Jonker, and J. van Santen, Physica, **16**, 337 (1950).

[43] J. van Santen and G. H. Jonker, Physica, **16**, 599 (1950).

[44] G. H. Jonker, Physica, **16**, 707 (1956).

[45] J. Volger, Physica, **20**, 49 (1954).

[46] C. W. Searle and S. T. Wang, Can. J. Phys., **47**, 2703 (1969); C. W. Searle and S. T. Wang, Can. J. Phys., **48**, 2023 (1970).

[47] A. H. Morrish, B. J. Evans, J. A. Eaton, and L. K. Leung, Can. J. Phys., **47**, 2691 (1969).

[48] L. K. Leung, A. H. Morrish, and C. W. Searle, Can. J. Phys., **47**, 2697 (1969).

[49] R. von Helmholt, J. Wecker, B. Holzapfel, L. Schultz, and K. Samwer, Phys. Rev. Lett. **71**, 2331 (1993).

[50] K. Chahara, T. Ohno, M. Kasai, Y. Kozono, Appl. Phys. Lett., **63**, 1990 (1993).

[51] C. L. Chien, J. O. Xiao, J. S. Jiang, J. Appl. Phys. **73**, 5309 (1993); S. S. P. Parkin, R. Bhadra, K. P. Roche, Phys. Rev. Lett. **66**, 2152 (1991).

[52] E. E. Fullerton, M. J. Conover, J. E. Mattson, C. H. Sowers, and S. d. Bader, Appl. Phys. Lett. **63**, 1699 (1993).

[53] S. Mori, C. H. Chen and S-W. Cheong, nature **392**, 473 (1998).

[54] P. G. Radaelli, D. E. Cox, M. Marezio, S-W. Cheong, P. E. Schiffer, and A. P. Ramirez, Phys. Rev. Lett. **75**, 4488 (1995).

[55] K. Knížek, Z. Jirák, E. Pollert, and F. Zounová, J. Solid State Chem. **100**, 292 (1992).

[56] Y. Tomioka, A. Asamitsu, Y. Moritomo, H. Kuwahara, and Y. Tokura, Phys. Rev. Lett. **74**, 5108 (1995).

[57] Z. Jirák, S. Krupička, Z. Šimša, M. Dlouhá, and S. Vratislav, J. Magn. Magn. Mater. **53**, 153 (1985).

[58] M. Hervieu, A. Barnabé, C. Martin, A. Maignan, and B. Raveau, Phys. Rev. B **60**, R726 (1999).

[59] S.Y. Wu, W.-H, Li, K. C. Lee, J. W. Lynn, R. S. Liu and J. B. Wu, and C. Y. Huang, J. Appl, Phys. 83, 7345 (1998).

[60] H. Kuwahara, Y. Tomioka, A. Asamitsu, Y. Moritomo,and Y. Tokura, Science **270**, 961 (1995).

[61] J. Blasco, J García, J. M. de Teresa, M. R. Ibarra, J. Pérez, P. A. Algarabel, C. Marquina, and C. Ritter, J. Phys.: Condens. Matter. **9**, 10321 (1997).

[62] B. J. Sternlieb, J. P. Hill, and U. C. Wildgruber, G. M. Luke, B. Nachumi, Y. Moritomo and Y. Tokura, Phys. Rev. Lett. **76**, 2169 (1996).; Y. Murakami, H. Kawada, H. Kawata, M. Tanaka, T. Arima, Y. Moritomo, and Y. Tokura, Phys. Rev. Lett. **80**, 1932 (1998).

[63] J.-S. Zhou, J. B. Goodenough, A. Asamitsu, and Y. Tokura, Phys. Rev. Lett. **79**, 3234 (1997).; Y. Yamada, O. Hino, S. Nohdo, R. Kanao, T. Inami, and S. Katano, Phys. Rev. Lett. **77**, 904 (1996).

[64] C. H. Chen and S-W. Cheong, Phys. Rev. Lett. **76**, 4042 (1996).

[65] S-W Cheong, C. M. Lopez and H. Y. Hwang *Preprint* (1997).

[66] H. Kuwahara, Y. Moritomo, Y. Tomioka, A. Asamitsu, M. Kasai, Y. Tokura, J. Appl. Phys. **81**, 4954 (1997).

[67] R. Maezono, S. Ishihara, N. Nagaosa, Phys. Rev. B **58**, 11583 (1998); Y. Tomioka (Unpublished).

[68] H. Kuwahara, T. Okuda, Y. Tomioka, T. Kimura, A. Asamitsu, and Y. Tokura, *Phase Diagram and Anisotropic Transport Properties of* $Nd_{1-x}Sr_xMnO_3$ *Crystals,* MRS symposia Proceedings No. 494 (Material Reseaerch Society, Pittsburgh, 1998), p.

[69] A. P. Ramirez, P. Schiffer, S-W. Cheong, C. H. Chen, W. Bao, T. T. M. Palstra, P. L. Gammel, and D. J. Bishop, and B. Zegarski, Phys. Rev. Lett. **76**, 3188 (1996).

[70] F. Galasso, and J. Pyle, Inorg. Chem. **2**, 482 (1963).

[71] S. Geller, J. Chem. Phys. **24**, 1236 (1956).

[72] P. M. Raccah, and J. B. Goodenough, Phys. Rev. **155** 932 (1967).

[73] B. W. Brown, E. Banks, Phys. Rev. **84**, 609 (1951); H.R. Shanks, P.H. sidles, G.C. Danielson, Pap. 22 in Nonstoichiometric Compunds: Advances in Chemistry Series 39, ed. R Ward. Washington, DC: Am. Chem. Soc. (1963).

[74] C. Zener Phys. Rev. **81**, 440 (1951).

[75] E. O. Wollan, W. C. Koehler, Phys. Rev. **100** 545 (1955).

[76] J. B. Goodenough, Phys. Rev. **100**, 564 (1955).

[77] V. M. Goldschmidt, Geochemische Verteilungsgesetze der Elemente VII, VIII, 1927/28.

[78] R. D. Shannon, and C. T. Prewitt, Acta Crystallogr. A **32** 785 (1976).

[79] J. B. Goodenough and J. M. Longo, Landolt-Bornstein Tabellen New Series Group III/4a, ed. K. H. Hellwege, pp. 126-314. Berlin. Springer-Verlag (1970).

[80] F.W. Lytle, J. Appl. Phys. **35**, 2212 (1964).

[81] A. Wold, B. Post, and E. Banks, J. Am. Chem. Soc. **79**, 4911(1957).

[82] S. Geller, E.A. Wood, Acta Cryst. **9**, 1019 (1956).

[83] H. Y. Hwang, S-W. Cheong, P. G. Radaelli, M. Marezio, and B. Batlogg, Phys. Rev. Lett. **75**, 914 (1995).

[84] J. B. Goodenough, Annu. Rev. Mater. Sci. **28**, 1 (1998).

[85] R. Mahendiran, S. K. Tiwary, A. K. Raychaudhuri, T. V. Ramakrishnan, R. Mahesh, N. Rangavittal, and C. N. R. Rao, Phys. Rev. B **53**, 3348 (1996).

[86] A. Asamitsu, Y. Moritomo, Y. Tomioka, T. Arima and Y. Tokura, Nature **373**, 407 (1995); Y. Tokura., A. Urushibara, Y. Moritomo, T. Arima, A. Asamitsu, G. Kido and N. Furukawa, J. phys. Soc. Japan **63**, 3931 (1994).

[87] S. Jin, M. McCormack, T. H. Tiefel, R. Ramesh, J. Appl. Phys. **76**, 6929 (1994).

[88] G. Briceno, H. Chang, X. Sun, P. G. Schultz, and X. D. Xiang, Science **270**, 273 (1995).

[89] H. Woo, T. A. Tyson, M. Croft, S-W. Cheong and B. L. Brandt will be submitted to PRB.

[90] K. I. Kobayashi, T. Kimura, H. Sawada, K. Terakura and Y. Tokura, Nature **395**, 677 (1998); T. Manako, M. Izumi, Y. Konishi, K. Kobayashi, M. Kawasaki, and Y. Tokura, Appl. Phys. Lett., **74** 2215 (1999).

[91] M. A. Subramanian, B. H. Toby, A. P. Ramirez, W. J. Marshall, A. W. Sleight, G. H. Kwei, Science **273**, 81 (1996).

[92] R. Laiho, K. Lisunov, V. Stamov, and V. Zahvalinsky, J. Magn. Magn. Mater., **140-**

144, 2021 (1995).

[93] H. A. Kramers Proc. Acad. Sci. Amst. **33**, 959 (1930).

[94] H. A. Jahn and E. Teller, Proc. Roy. Soc. (London) **A161**, 220 (1937); H. A. Jahn, Proc. Roy. Soc. (London) **A164**, 117 (1938).

[95] M. D. Kaplan, B. G. Vekhter, Cooperative phenomena in Jahn-Teller Crystals (Plenum Press, New York and London, 1995).

[96] I. B. Bersuker, Chem. Rev. **101**, 1067 (2001).

[97] I. B. Bersuker (Isaak Borisovich), The Jahn-Teller effect and vibronic interactions in modern chemistry (Plenum Press, New York, 1984); L. D. Landau and E. M.Liphshitz, Kvantovaya Mekhanika. Nerelativistskaya Teoriya, Nauka, Moscow (1974); R. M. Hochstrasser, Molecular Aspects of Symmetry, Benjamin, New York, Amsterdam (1966).

[98] L. D. Landau and E. M. Liphshitz, Kvantovaya Mekhanika. Nerelativistskaya Teoriya, Nauka, Moscow (1974)

[99] I. B. Bersuker, in Electronic Structure and Properties of Transition Metal Compounds. Introduction to the Theory, (Wiley: New York, 1996).

[100] I. B. Bersuker (Isaak Borisovich), The Jahn-Teller effect and vibronic interactions in modern chemistry (Plenum Press, New York, 1984).

[101] J. H. Van Vleck, J. chem.. Phys. **7**, 72 (1939).

[102] A. J. Millis, Boris I. Shraiman, and R. Mueller, Phys. Rev. Lett. **74**, 5144 (1995).

[103] R. M. Kusters, J. Singleton, D. A. Keen, R. McGreevy, and W. Hayes, Physica (Amsterdam) **155B**, 362 (1989).

[104] A. J. Millis, R. Mueller, and Boris I. Shraiman, Phys. Rev. B **54**, 5405 (1996).

[105] J. Zang, A. R. Bishop, and H. Roder, Phys. Rev. B **53**, R8840 (1996).

[106] H. Roder, J. Zang, and A. R. Bishop, Rev. Lett. **76**, 1356 (1996).

[107] S. Satpathy, J. Phys.: Condens. Matter **10**, L501 (1998).

[108] L. J. Zou, D. K. Campbell, and H. Q. Lin, J. Appl. Phys. **87**, 5499 (2000).

[109] J. W. Lynn, R. W. Erwin, J. A. Borchers, Q. Huang, and A. Santoro, Phys. Rev. Lett. **76**, 4046 (1996); L. Vasiliu-Doloc, J. W. Lynn, Y. M. Mukovskii, a. A. Arsenov, and D. A. Shulyatev, J. Appl. Phys. **83**, 7342 (1998).

[110] W. A. Harrison, "Solid State Theory" (Dover, New York, 1979).

[111] W. A. Harrison, "Solid State Theory" (Dover, New York, 1979) p. 470.

[112] L. Brillouin, J. Phys. Radium. **8**, 74 (1927).

[113] N. W. Ashcroft, N. D. Mermin, "Solid State Physics", Saunders College Publishing, NY, 1976, p. 696.

[114] J. A. Mydosh, in Spin Glasses (Taylor & Francis, London, 1993).

[115] C. Kittel, "Introduction to Solid State Physics", John Wiley and Sons, Inc., NY, 1986, p. 444.

[116] A. H. Morrish, "The Physical Principles of Magnetism", John Wiley and Sons, Inc., NY, 1965, p. 449.

[117] D. Chowdhury, in Spin Glasses and Other Frustrated Systems (Princeton University Press, New Jersey, 1986).

[118] P. A. Beck, Prog. Mat. Sci., **23**, 1 (1978).

[119] W. Bao, J. D. Axe, C. H. Chen, and S-W. Cheong, Phys. Rev. Lett. **78**, 543 (1997).

[120] P. Schiffer, A. P. Ramirez, W. Bao, and S-W. Cheong, Phys. Rev. Lett. **75**, 3336 (1995).

[121] P.G. Radaelli, D.E. Cox, M. Marezio, S-W. Cheong, Phys. Rev. B **55**, 3015 (1997).

[122] P. W. Anderson and H. Hasegawa, Phys. Rev. **100**, 675 (1955).

[123] M. Croft (personal communication).

[124] Uehera, Kim and Cheong (Unpublished).

[125] J. M. D. Coey, M. Viret, and S. von Molnar, Adv. Phys. **48**, 167 (1999), p.174

[126] J. J. Neumeier and J. L. Cohn, Phys. Rev. B **61**, 14319 (2000).

[127] C. Rettori, D. Rao, J. Singley, D. Kidwell, S. B. Oseroff, M. T. Causa, J. J. Neumeier, K. J. McClellan, S-W. Cheong, and S. Schultz, Phys. Rev. B **55**, 3083 (1997).

[128] Y. Tomioka, A. Asamitsu, Y. Moritomo, H. Kuwahara, and Y. Tokura, Phys. Rev. Lett. **74**, 25 (1995)

[129] Z. Jirak, S. Krupicka, Z. Simsa, M. Dlouha, and S. Vratislav, J. Magn. Magn. Mater. **53**, 153 (1985)

[130] T. Mizokawa and A. Fujimori, Phys. Rev. B **54**, 5368 (1996).

[131] H. A. Kramers, Physica **1**,191 (1934).

[132] C. Zener, Phys. Rev. **82**, 403 (1951).

[133] J. M. D. Coey, M. Viret, and S. von Molnar, Adv. Phys. **48**, 167 (1999), p.173

[134] S. Satpathy, Zoran S. Popovic and Filip R. Vukajlovic, J. Appl. Phys. **79**, 4555 (1996).

[135] (a)D. Louca and T. Egami, J. Appl. Phys. **81**, 5484 (1997).; (b) S. J. L. Billinge, R. G. DiFrancesco, G. H. Kwei, J. J. Neumeier, and J. D. Thompson, Phys. Rev. Lett. **77**, 715 (1996).; (c) C. H. Booth, F. Bridges, G. J. Snyder and T. H. Geballe, Phys. Rev. B **54**, R15606 (1996).; C. H. Booth, F. Bridges, G. H. Kwei, J. M. Lawrence, A. L. Cornelius, and J. J. Neumeier, Phys. Rev. Lett. **80**, 853 (1998).; C. H. Booth *et al.*(unpublished).; (d) T. A. Tyson, J. Mustre de Leon, S. D. Conradson, A. R. Bishop, J. J. Neumeier, H. Röder, and Jun Zang, Phys. Rev. B **53**, 13985 (1996).; (e) Changes in the long range structure with temperature were found by M. R. Ibarra, P. A. Algarabel, C. Marquina, J. Blasco, and J. García, Phys. Rev. Lett. **75**, 3541 (1995).

[136] C. Martin, A. Maignan, M. Hervieu, and B. Raveau, Phys. Rev. B **60**, 12 191 (1999).

[137] L. M. Rodriguez-Martinez and J. P. Attfield, Phys. Rev. B **54**, 15 622 (1995); A. Maignan, Ch. Simon, V. Caignaet, and B. Raveau, Solid State Commun. **96**, 623 (1995); R. Mahesh, R. Mahendiran, A. K. Raychaudhuri, and C. N. R. Rao, J. Solid State Chem. **114**, 297 (1995); **120**, 204 (1995).

[138] (a) I. O. Troyanchuk and N. V. Samsonenko, H. Szymczak, and A. Nabialek, J. Solid State Chem. **131**, 144(1997); (b)H. Taguchi, Phys. Stat. Sol. (a) **88**, K79 (1985).

[139] V.A. Bokov, N. A. Grigoryan, and M. F. Bryzhina, Physica Status Solidi **20**, 745 (1967).

[140] H. Chiba, M. Kikuchi, K. Kusuba, Y. Muraoka, Y. Syono, Solid State Commun.**99**, 499(1996).

[141] H. Chiba, T. Atou, H. Faqir, M. Kikuchi, Y. Syono, Y. Murakami, D. Shindo, Solid State Ionics **108,** 193 (1998).

[142] E. I. Turkevich and V. P. Plakhtii, Soviet Physics – Solid State, **10**, 754 (1968).

[143] S-W. Cheong and Harold Y. Hwang, Colossal Magnetoresistance Oxides, ed, by Y. Tokura (Gordon & Breach, Monographs in Condensed Matter Science, 2001).

[144] E. I. Turkevich and V. P. Plakhtii, Soviet Physics – Solid State, **10**, 754 (1968).

[145] H. L. Liu, S. L. Cooper, and S-W. Cheong, Phys. Rev. Lett. **81**, 4684 (1998).

[146] Y. Murakami and D. Shindo, H. Chiba, M. Kikuchi, and Y. Syono, Phys. Rev. B **55**, 15043 (1997).

[147] F. Sugawara, and S. Iida, J. Phys. Soc. Jpn. **20**, 1529 (1965).

[148] Y. Murakami, D. Shindo, H. Chiba, M. Kikuchi, and Y. Syono, Phys. Rev. B **59**, 6395 (1999).

[149] H. Faqir, H. Chiba, M. Kikuchi, and Y. Syono, M. Mansori, P. Satre, and A. Sebaoun, J. Solid State Chem **142**, 113 (1999).

[150] S. Matsumoto, H. Faqir, H. Chiba, M. Kikuchi, Y. Syono, Materials Letters **39,** 36(1999).

[151] E. Ohshima, Y. Saya, M. Nantoh, M. Kawai, Solid State Commun. 116, 73 (2000).

[152] E. Abrahams, Physica E **3**, 69 (1998).

[153] (a) N. F. Mott, Proc. Phys. Soc. London, Ser. A **62**, 416 (1949); (b) N. F. Mott, Can. J. Phys. **34**, 1356 (1956); (c) N. F. Mott, Philo. Mag. **6**, 287 (1961); (d) N. F. Mott, Metal-Insulator Transitions (Taylor and Francis, London/Philadelphia, 1990).

[154] L. D.Landau, Sov. Phys. JETP **3**, 920 (1957); L. D.Landau, Sov. Phys. JETP **5**, 101 (1957); L. D.Landau, Sov. Phys. JETP **8**, 70 (1958); P. W. Anderson, Basic Notions of Condensed Matter Physics (Benjamin/Cummings, London, 1984).

[155] E. Abrahams, P. W. Anderson, D. C. Licciardello, T. V. Ramarkrishnan Phys. Rev. Lett. **42**, 673 (1979); A. MacKinnon, B. Kramer, Phys. Rev. Lett. **47**, 1546 (1981).

[156] J. Hubbard, Proc. R. Soc. London, Ser. A **276**, 238 (1963); J. Hubbard, Proc. R. Soc. London, Ser. A **277**, 237 (1964); J. Hubbard, Proc. R. Soc. London, Ser. A **281**, 281 (1963); J. Kanamori, Prog. Theor. Phys. **30**, 275 (1963).

[157] Kittel, "Introduction to Solid State Physics", John Wiley and Sons, Inc., NY, 1986, p. 158).

[158] P. W. Anderson, Phys. Rev. **109**, 1492 (1958).

[159] Igor Lerner: http://www.th.ph.bham.ac.uk/ivl/And-mes.html

[160] M. Imada, A. Fujimori, and Y. Tokura, Rev. Mod. Phys. **70** 1039 (1998).

[161] Y. Tokura, H. Kuwahara, Y. Moritomo, Y. Tomioka, and A. Asamitsu, Phys. Rev. Lett. **76**, 3184 (1996).

[162] N. Tsuda, K. Nasu, A. Yanase, K. Siratori, Electronic Conduction in Oxides (Springer-Verlag New York Berlin Heidelberg1983).

[163] Y. Sakai, K. Kawakami, N. Tsuda, M. Tanaka J. Phys. Soc. Jpn. 55, 3181 (1986).

[164] A. N. Bloch, R. B. Weisman, c. M. Varma Phys. Rev. Lett. **28**, 753 (1972).

[165] Manual of QUICKPRESS 3.0-piston cylinder apparatus: the high pressure and high temperature material company, "Depths of the Earth Company".

[166] G. Bunker's lecture notes web site: http://gbxafs.iit.edu/training/xafsoverview.pdf

[167] (a) C. A. Ashley and S. Doniach, Phys. Rev. B **11**, 1279(1975); (b) P.A. Lee and J. B. Pendry, Phys. Rev. B **11**, 2795 (1975); (c) E. A. Stern, Phys. Rev. B **10**, 3027 (1974); (d) E. A. Stern, J. Vac. Sci Technol. **14**, 461 (1977) (e) D. C. Koningsberger and R. Prins, "X-Ray Absorption", John Wiley and Sons Inc., New York,1988, p. 12.

[168] T. A. Tyson, K. O. Hodgson, C. R. Natoli and B. Benfatto, Phys. Rev. B **46**, 5997 (1992).

[169] R. L. Liboff, Introductory Quantum Mechanics (Holden-Day, Inc., 1980) p.610.

[170] C. R. Natoli, M. Benfatto, and S. Doniach, Phys. Rev. A **34**, 4682 (1986).

[171] M. Newville, P. Livins, Y. Yacoby, E. A. Stern, and J. J. Rehr Phys. Rev. B **47**, 14126 (1993).

[172] H. Woo, T. A. Tyson, M. Croft, S-W. Cheong, and J. C. Woicik, Phys. Rev. B **63**, 134412 (2001).

[173] Grant Bunker, Nuclear Instruments and Methods **207**, 437-444 (1983).

[174] G. Dalba, P. Fornasini, and F. Rocca, Phys. Rev. B **47**, 8502 (1993); A. B. Edwards, D. J. Tildesley, and N. Binsted, molecular physics, **91**, 357-369 (1997).

[175] G. Dalba, P. Fornasini, and F. Rocca, Phys. Rev. B **47**, 8502 (1993); A. B. Edwards, D. J. Tildesley, and N. Binsted, molecular physics, **91**, 357-369 (1997).

[176] M. I. McCarthy, G. K. Schenter, and M. R. Chacon-Taylor, J. J. Rehr, G. E. Brown, Jr., Phys. Rev. B **56**, 9925 (1997).

[177] J. J. Rehr, R. C. Albers and S. I. Zabinsky, Phys. Rev. Lett. **69**, 3397 (1992).

[178] Johnny Kirkland (personal communication).

[179] H. M. Rietveld, Acta Cryst. **22**, 151 (1967); H. M. Rietveld, J. Appl. Cryst. **2**, 65 (1969).

[180] D. E. Cox, Handbook on Synchrotron Radiation, Elsevier Science Publishers, G. Brown & D. E. Moncton, eds. Vol. **3**, 155 (1991).

[181] A. L. Bail, NIST special publication 846. Proceedings of the international conference Accuracy in Power Diffraction II, held at NIST, Gaithersburg, MD, May 26-29 (1992).

[182] A. C. Larson and R. B. Von Dreele, GSAS General Structure Analysis System, LAUR 86-748, (1985-1994).

[183] J. E. Lenz, Proc. IEEE **78**, 973 (1990).

[184] J. E. Lenz, Proceedings of the IEEE 78, 973 (1990).

[185] J. E. Lenz, Proceedings of the IEEE 78, 973 (1990).

[186] National High Magnetic Laboratory (NHMFL): http://www.magnet.fsu.edu/users/facilities/dcfield/cell8/cell8side.gif

[187] National High Magnetic Laboratory (NHMFL): http://www.magnet.fsu.edu/users/facilities/dcfield/magnetometry/index.html

[188] Z. Zeng, M. Greeblatt, and M. Croft, Phys. Rev. B **59**, 8784 (1999).

[189] J. Fontcuberta, B. Martínez, A. Seffar, S. Piñol, J. L. García-Muñoz, and X. Obradors, Phys. Rev. Lett. **76**, 1122 (1996).

[190] C. M. Varma, Phys. Rev. B **54**, 7325 (1996).

[191] E. I. Turkevich and V. P. Plakhtii, Soviet Physics – Solid State **10**, 754 (1968).

[192] G. Subias, J. Garcia, M. G. Proietti and J. Blasco, Phys. Rev. B **56**, 8183 (1997).

[193] Q.Qian, T. A. Tyson, C.-C. Kao, M. Croft, S -W. Cheong and M. Greenblatt, Phys. Rev. B **62**, 13472 (2000).

[194] N. A. Hill and K. M. Rabe, Phys. Rev. B **59**, 8759 (1999).

[195] T. Atou, H. Chiba, K. Ohoyama, Y. Yamaguchi, and Y. Syono J. Solid State Chem **145**, 639-642 (1999); H. Chiba, T. Atou, and Y. Syono, J. Solid State Chem, **132**, 139 (1997).

[196] F. Farges, G. E. Brown Jr. and J. J. Rehr, J. Phys. IV France, **7**, Colloque C2-191 (1997); M. Croft (unpublished).

[197] N. Sicron, B. Ravel, Y. Yacoby, E.A. Stern, F. Dogan, and J.J. Rehr, Phys. Rev. B **50**, 13168 (1994).

[198] F. Bridges, C. H. Booth, G. H. Kwei, J. J. Neumeier, and G. A. Sawatzky, Phys. Rev. B **61**, 9237 (2000).

[199] A. Moreo, S. Yunoki, and E. Dagotto, Science **283**, 2034 (1999).

[200] A. P. Ramirez, S-W. Cheong, and P. Schiffer, J. Appl. Phys. **81**, 5337 (1997).

[201] A. Maignan, C. Martin, F. Damay, B. Raveau, and J. Hejtmanek, Phys. Rev. B **58**, 2758 (1998).

[202] M. Itoh, I. Natori, S. Kubota, and K. Motya, J. Phys. Soc. Jpn. **63**, 1486 (1994).

[203] Z. Zeng, M. Greenblatt, M. A. Subramanian, and M. Croft, Phys. Rev. Lett. **82,** 3164 (1999).

[204] M. Koyano, M. Suezawa, H. Watanabe and M. Inoue, J. Phys. Soc. Jpn. **63**, 1114 (1994).

[205] S. Mukherjee, R. Ranganathan, R. S. Anilkumar and P. A. Joy, Phys. Rev. B **54**, 9267 (1996).

[206] N. Gayathri, A. K. Raychaudhuri, S. K. Tiwary, R. Gundakaram, Anthony Arulraj, and C. N. R. Rao, Phys. Rev. B **56**, 1345 (1997).

[207] A. Maignan, C. Martin, F. Damay, and B. Raveau, Z. Phys. B **104**, 21(1997).

[208] H. Negishi, S. Ohara, M. Koyano, M. Inoue, T. Sakakibara and T. Goto, J. Phys. Soc. Jpn. **57**, 4083 (1988).

[209] D. N. H. Nam, K. Jonason, P. Nordblad, N. V. Khiem, and N. X. Phuc, Phys. Rev. B **59**, 4189 (1999).

[210] P. S. A. Kumar, P. A. Joy, and S. K. Date, J. Phys.: Condens. Matter **10**, L487 (1998).

[211] D. A. Pejakovic, J. L. Manson, J. S. Miller, and A. J. Epstein, J. Appl. Phys. **87**, 6028 (2000).

[212] J. A. Mydosh, Spin Glasses: An Experimental Introduction (Taylor and Francis, London, 1993).

[213] A. Pejaković, J. L. Manson, J. S. Miller, and A. J. Epstein, Phys. Rev. Lett. **85,** 1994 (2000).

[214] W. A. Harrison, "Solid State Theory" (Dover, New York, 1979), p. 427

[215] L. Landau, E. Lifshitz, Statistical Physics, Part 1, 3rd. edition (Pergamon Press, New York, 1980 - reprinted 1982), p 472 and additional references within that work mentioned on this page.

[216] K. R. Poeppelmeier, M. E. Leonowicz, J. C. Scanlon, J. M. Longo, and W. B. Yelon, J. Solid State Chem. **45**, 71 (1982).

[217] P. G. DEGennes Phys. Rev., **118**, 141 (1960).